Catch $^{9}_{4}$Be If You Can: Exploiting Second-Sphere Hydrogen Bonding Toward Chelation of Beryllium

A thesis presented in partial fulfilment of the requirements of the degree of

Doctor of Philosophy
in
Chemistry

at
Massey University, Manawatu, New Zealand

by

DAVID J. NIXON

MASSEY UNIVERSITY
TE KUNENGA KI PŪREHUROA
UNIVERSITY OF NEW ZEALAND

2019

Abstract

Beryllium is a crucial metal in the automotive, aviation, nuclear and consumer industries. The unique combination of high rigidity, low density, thermal stability and conductivity makes it highly useful in consumer products such as cell phones and computers. However, beryllium is considered to be the most toxic non-radioactive element, a class A carcinogen, and the cause of life-threatening chronic beryllium disease. Even with its poor reputation, its use is continued in commercial, industrial, and governmental applications. In contrast, the efforts to understand beryllium's fundamental chemistry have been severely neglected. We are interested in developing a suite of chemical chelators which show strong and selective binding towards beryllium. These studies will lead to specific applications such as the detection of beryllium in the environment, protocols to remediate its contamination, and therapies for individuals exposed to its toxicity. This work will focus on both the computational studies of tetradentate ligands and their synthesis. These have been designed to bind strongly to beryllium.

Contributions

All the work in this thesis was completed by David Nixon.

Except:

In collaboration with The University of Marburg, Dr. Magnus Buchner and his PhD student Matthias Müller obtained beryllium-containing crystal structures, and ^{9}Be NMR data. This included the ligand **L1cohH**, and the complexes **401**, **402**, and **403**. ^{9}Be NMR data was also collected there.

Computational work was aided by fellow group member, Tyson Dais, as part of his honours project 'Ligand Optimization for Strong and Selective Beryllium Chelation'. This work involved calculations of ligands **L3**, **L4**, and **L5**, as well as the production of Figure 5.31.

Acknowledgements

First, I would like to express my eternal gratitude for my supervisors, Assoc. Profs. Paul G. Plieger and Gareth J. Rowlands. In no capacity can I truly show my appreciation for all that you have done for me – for your support, guidance, knowledge, and patience.

I would like to thank those who worked closely on this project, through thick and thin: Prof. Penny Brothers, Dr. Magnus Buchner, Tyson Dais, Prof. Bill Henderson, Assoc. Prof. Jo Lane, Matthias Müller, Dr. Raymond Onyekachi, and Dr. Lakshika Perera.

Special thanks to my research group and its honourary members: Michael Brown, Jenna Buchanan, Tyson Dais, Leonie Etheridge, Liam M^{c}Garry, Becky Severinsen, Thomas Telford-Muñoz, and Sidney Woodhouse. My gratitude goes out to you not only for the chemistry we did together, but also for the jokes, games, and support.

I am immensely grateful to my friends and colleagues, who have helped me throughout my PhD studies: John Paul Borberg, Hannah Chapman, Bruce Chilton, Simon Dewar, Dr. Pat Edwards, Daniel Farley, Zane Farrow, Graham Freeman, Elise Fon-Lowe, Toff Fon-Lowe, Ben Fox-Munro, Graham Freeman, Dr. Luke Fullard, Dr. Alex Hamilton, Haley Hop Wo, Heather Jameson, Adrian Jull, Dr. Luke Liu, Jamie Love, Dave Lun, Jenn Mann, David Perl, Ben Roff, Mel Roff, Nathan Seagar, Declan Stagg, Prof. Kathryn Stowell, Laura Sutherland, Mark Sutherland, Ann Truter, Yvette Tyler, Duncan Tyler, Dr. Matthew Vanderwerff, Dr. Rob Ward, Assoc. Prof. Mark Waterland, Dr. Jamie Withers, and Sarah Wright.

Thank you to Massey University's School of Fundamental Sciences and the financial support provided by the Marsden Fund Grant administered by the Royal Society of New Zealand. Thanks also to the New Zealand eScience Infrastructure (NeSI) for the use of their high performance computing facilities.

Overwhelming gratitude and appreciation go out to my family: To my Mum and Dad; to my brothers and sister, Michael, Josh, and Katherine; to my grandparents; to the Frith's; and to the Berghofer's. You have shown me every kindness and love, for which I am in your debt.

And to Ashleigh, always, for her friendship, support, and love. Only together was this accomplishment possible, and I am looking forward to every challenge and joy that life offers us.

Dedication

"A little philosophy inclineth man's mind to atheism, but depth in philosophy bringeth men's minds about to religion."

– Francis Bacon

Contents

Figures

Schemes

Tables

Abbreviations

10-HBQS	10-hydroxybenzo[*h*]quinolone-7-sulfonic acid
acac	acetylacetone
AcOH	acetic acid
B3LYP	3-parameter hybrid Becke exchange/Lee-Yang-Parr correlation functional
BSSE	basis set superposition error
CBD	chronic beryllium disease
CCSD	couple cluster method with single and double excitations
CSD	Cambridge Structural Database
CPC	counterpoise correction
cc-pVTZ	correlation-consistent polarized triple-zeta basis set
COSY	correlation spectroscopy
^{13}C NMR	carbon nuclear magnetic resonance
dba	dibenzylideneacetone
DCM	dichloromethane
DEPT-90	distortionless enhancement by polarization transfer (90° pulse angle)
DEPT-135	distortionless enhancement by polarization transfer (135° pulse angle)
DFT	density functional theory
DMAE	dimethylethanolamine
DME	dimethoxyethane
DMEA	dimethylethanolamine
DMF	dimethylformamide
DMSO	dimethylsulfoxide
dppe	1,2-bis(diphenylphosphino)ethane
dppf	1,1'-bis(diphenylphosphino)ferrocene
dppp	1,2-bis(diphenylphosphino)propane
EDG	electron donating group
EDTA	ethylenediaminetetraacetic acid
Et_2O	diethyl ether
EtOAc	ethyl acetate
EtOH	ethanol
EPA	Environmental Protection Agency

ESI	electrospray ionisation
EWG	electron withdrawing group
G09	Gaussian 09 r*ev. D0.1*
GIAO	gauge-invariant atomic orbital
GV5	GaussView 5.0
^{1}H NMR	proton nuclear magnetic resonance
HMBC	heteronuclear multiple bond correlation
HMQC	heteronuclear multiple quantum coherence
HSAB	Pearson acid-base concept
HOMO	highest occupied molecular orbital
IEF-PCM	integral equation formalism polarisable continuum model
IR	infrared
LUMO	lowest occupied molecular orbital
MS	mass spectroscopy
Me	methyl
MeOH	methanol
MM	molecular mechanics
n-Bu	normal butyl
NCI	non-covalent interaction
NIOSH	National Institute for Occupational Safety and Health
NMR	nuclear magnetic resonance
NOESY	nuclear Overhauser enhancement spectroscopy
NTP	nitrilotripropionic acid
R_f	retention factor
RT	room temperature
OLED	organic light-emitting diode
ONIOM	our own n-layered integrated molecular orbital and molecular mechanics
salbn	*N*,*N*'-bis(salicylidene)butylenediamine
SPhos	2-dicyclohexylphosphino-2',6'-dimethoxybiphenyl
TBAI	tetrabutylammonium iodide
t-Bu	tertiary butyl
TEA	triethylamine
THF	tetrahydrofuran

TLC	thin-layer chromatography
TMS	tetramethylsilane
TTBP	tri-tert-butylphosphine
UV-vis	ultraviolet-visible
VMD	visual molecular dynamics
XPhos	2-dicyclohexylphosphino-2′,4′,6′-triisopropylbiphenyl

Chapter 1: Introduction

"Science is organised knowledge. Wisdom is organised life."

– Immanuel Kant

1.1 Introduction to Beryllium

Beryllium (Be) is a rare metal which, due to its unmatched combination of physical and chemical properties, is found all around us in everyday life.[1] It is thermally stable and conductive; highly rigid; a low density metal (1.85 times that of water); and extremely transparent to X-rays and other ionising radiation.[2] These attributes therefore make beryllium an important industrial material for commercial, industrial, and military applications.[1, 3] Unfortunately, it is a Class A EPA carcinogen, and the cause of a fatal lung disease: Chronic Beryllium Disease (CBD).[1, 4] Many industrial operations release beryllium into the environment and so there is a potential to expose both works and the public to toxic levels of Be.[5] This chapter will provide a brief review of beryllium's material properties, hazards, coordination chemistry, and computational chemistry. It will end with a discussion of the proposed ligands for synthetic and computational work, and an outline for the results and discussion of this thesis.

1.2 Beryllium as an Element

Beryllium has been known of since the 3rd century BC, in the mineral beryl, as well as valuable gemstones such as aquamarines and emeralds (Figure 1.1).[6] The element was first named "glucine" for the sweet taste of some of its compounds – but the name "beryllium" came into use in 1828, not long after it was first isolated.[7] No use for beryllium was found until the early 20th century. New industrial processes for its production were developed after discovering that when alloyed with copper as a 2% addition, an alloy six times stronger than copper was formed.[8]

Figure 1.1 Four different beryllium-containing gemstones: emerald (left), heliodor (middle-left), morganite (middle-right), and aquamarine (right). [9]

Beryllium is mined from naturally occurring silicates, including beryl ($Be_3Al_2Si_6O_{18}$) and bertrandite ($Be_4(OH)_2Si_2O_7$).[7b] Each different structure of beryl which can be found have different physical and structural properties, and a characteristic colour (Figure 1.2).[10] Large cavities within the lattice can hold ions such as Fe^{2+} and Fe^{3+}, which cause the blue and yellow colours of aquamarine and heliodor respectively.

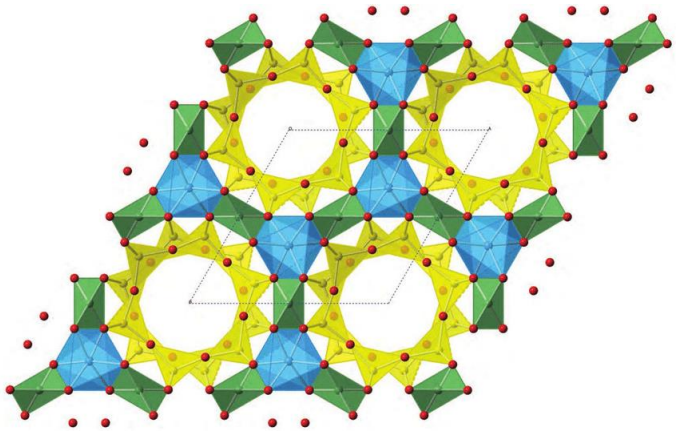

Figure 1.2 The crystallographic structure of beryl ($Be_3Al_2Si_6O_{18}$). Beryllium: Green; Aluminium: Blue; Silicon: Yellow; Oxygen: Red.[11]

Beryllium created within stars is short-lived. This is because it is consumed in the formation of heavy nuclei. Therefore interstellar gases tend to contain little beryllium, and so it is a relatively rare element in the universe and on Earth.[12] It has been estimated that the world's total reserve of beryllium ore is approximately 80,000 tonnes (compared to that of iron, of which there is estimated to be 800 billion tonnes), of which 220 tonnes were used by the United States in 2012, valued at $110 million.[10] In the same year, the

total mine production of beryllium was 230 tonnes, with the United States producing 87% of that, making them by far both the largest consumer and producer.[13]

Beryllium is primarily used as either a pure metal, one of many alloys, or as an oxide ceramic material.[1] It can also be processed into water-soluble salts. Its properties are ideal for its use in automotive, aviation, consumer, medical, nuclear, and space industries.[1-2, 7b, 14] Most of its applications are estimated to be used for military technology, for which more specific information is not easily obtainable.[15] The following is a brief list of examples in which beryllium is essential and irreplaceable:

- In both medicine and the research field, beryllium is used as a pure metal in windows between vacuum chambers and X-ray microscopes (Figure 1.3).[7b] This is because its low atomic number allows it to be essentially transparent to X-rays. The foil provides a window in which the tissue-penetrating X-rays are focused, whilst still maintaining the vacuum within the X-ray tube generator.

- Mammography equipment containing beryllium enables finer tumour resolution scans with lower radiation doses, allowing breast cancer to be detected at its earliest treatable stage.[16]

- A copper-beryllium alloy casing is used to protect fibre-optic cables on the seabed.[17] After decades of use in this high-pressure and corrosive environment, little deterioration has been observed.

- NASA has made extensive use of beryllium in their spacecraft, space telescopes, and rover vehicles.[18] In the late 1950s, the Mercury spacecraft used a beryllium heat shield to protect it during re-entry.[19] The James Webb Space Telescope, scheduled to be launched in 2020, will depend on a 6.5 meter beryllium mirror in order to see objects 200 times fainter than what was previously possible.[20] The

mirror is able to be made very stiff and lightweight, with a defect-free surface, which is crucial for its proper functioning.

- Next to diamond, Be oxide ceramics have the highest thermal conductivity values.[21] This makes them incredibly valuable in high-performance semiconductors, as well as many electrical circuit components. They are therefore found in many common consumer products including cell phones and computers.[1]

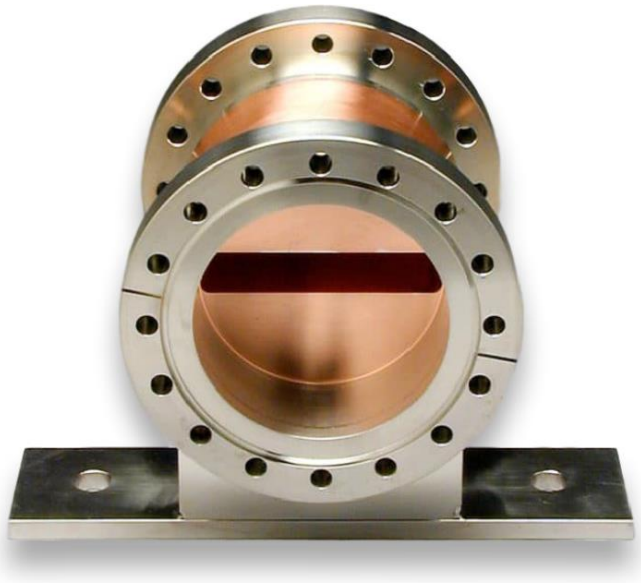

Figure 1.3 A water cooled beryllium window for a synchrotron ring.[22]

1.3 Beryllium as a Health Hazard

In stark contrast to beryllium's value in applied technology, is the fact it presents a significant health risk. Beryllium is the most toxic non-radioactive element found on the periodic table, and is categorised as a Class A carcinogen.[23] It can trigger the debilitating and potentially fatal lung disease, berylliosis, commonly known as chronic beryllium disease (CBD). CBD is a granulomatous lung disease which develops from a cell-mediated immune response to inhaled beryllium in up to 17 percent of exposed individuals.[1] There is currently no clear correlation between the extent of exposure and the severity of the

ensuing disease. Although the symptoms are treatable, the condition is incurable. Acute beryllium disease is similar to CBD in its symptoms, and may develop after a short but heavy exposure of less than one year.

The disease is historically associated with aerospace manufacturing, beryllium mining, and the production of fluorescent light bulbs (which initially made use of a beryllium compound).[8] In the 1930s, cases of bronchitis and pneumonia-like symptoms were reported in Germany and Russia amongst workers involved in beryllium processing. In the 1940s, similar cases appeared in the United States associated with the manufacturing of fluorescent lamps, suggesting that the culprit was beryllium.[24] Upon the discovery of its toxicity, the beryllium in fluorescent bulbs was replaced with the much safer halophosphate-based phosphors. But for many applications, substitutes were, and are still not, available.[8] Over the next decade, engineering controls were implemented in an attempt to protect workers against acute beryllium disease, but it is uncertain as to whether these were sufficient.[1] Since the mid-20th century, there have been few changes in beryllium safety regulations to minimise the risks involved.[25]

With a single or prolonged exposure by inhalation of beryllium particulates, the lungs become hypersensitive to beryllium, causing the development of small inflammatory nodules called granulomas. Like many other occupational lung diseases, patients experience coughing, shortness of breath, chest and joint pain, and fevers. The level of reaction in individuals may vary greatly – with the onset of disease symptoms sometimes not developing until years after exposure. Although the highest risk for contracting CBD is by working directly with the processing of beryllium ores, those who have minimal exposure to beryllium such as secretaries, security staff, and spouses of the workers have also contracted the condition. One study found that 1 percent of the population living within 1 kilometre of a beryllium plant in Ohio had CBD after exposure to concentrations estimated to be less than 1 milligram per cubic metre of air.[1]

The National Institute for Occupational Safety and Health (NIOSH) has carried out research which suggests that skin exposure contributes to sensitisation of workers, which subsequently leaves them more susceptible to the disease.[1] Little research otherwise has been carried out in determining other potential pathways of exposure or sensitization, except via inhalation. It is known however, that inhalation of beryllium dust is the only exposure pathway through which workers can ultimately contract chronic beryllium disease.

The two major factors in the development of CBD are due to both the level of beryllium exposure (whether short-term or long-term), and genetic disposition. A correlation is apparent when different beryllium-related occupations are compared. Beryllium machinists were found to contract CBD at a higher rate (11.8%) than general plant-wide workers (2%). The highest rate is in the beryllium ceramics industry (17%).[26] Exposure to certain compounds (particularly insoluble forms) can be correlated with a higher incidence of sickness. The most common types of exposure occur when beryllium and beryllium-containing materials are processed in such a way that releases airborne dust, fumes, and mist. These observations lead to the conclusion that there is likely an association between the type of exposure and the susceptibility of the individual workers. Regarding genetic disposition, research suggests that there is a strong relationship between individuals with chronic beryllium disease and a mutation in the HLA-DPB1 gene.[27] Machinists who have this gene variation have a rate of CBD eight times that of workers without it. Exposed workers with the mutation are much more likely to develop the disease than others (Figure 1.4).[1]

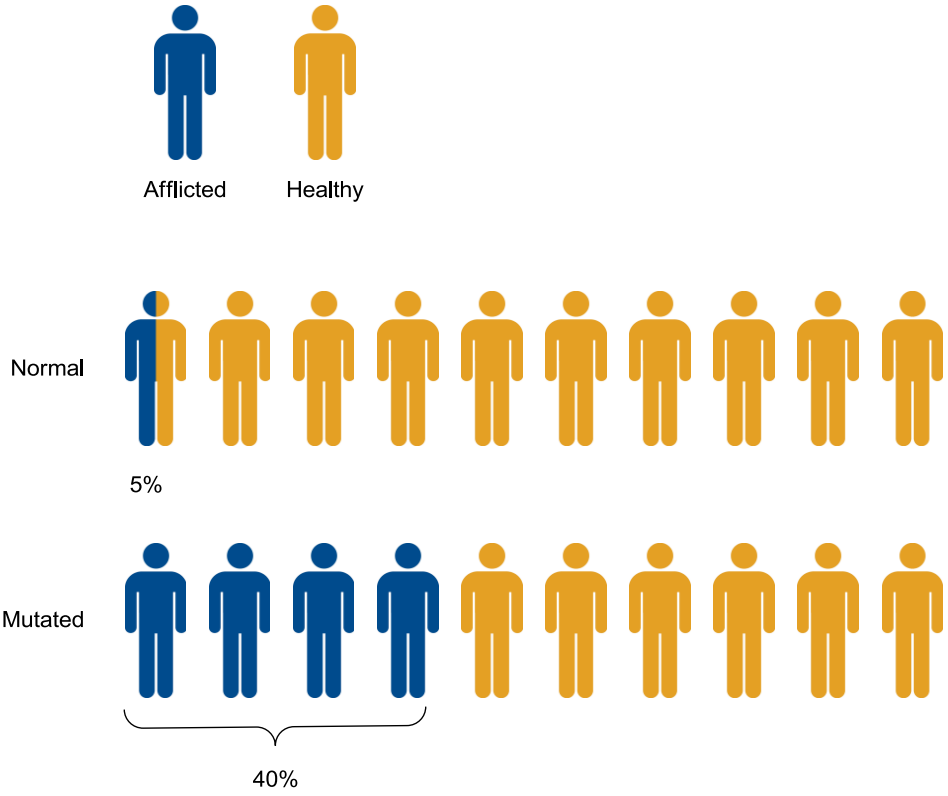

Figure 1.4 This person graph depicts the percentage of exposed normal and mutated-type workers, who have contracted CBD.

The risk of contracting chronic beryllium disease is not confined to those who work in the beryllium industry or those that live in the surrounding area. Beryllium is released into the atmosphere as a consequence of many operations, including oil and coal burning.[5] The general population may potentially be exposed to beryllium because of these actions through either inhalation or contact with beryllium residues in contaminated surface water, ground water, or agricultural products.

Beryllium is dangerously reactive within biological systems. It can bind to sites not normally occupied in biomolecules. Although approximately 35 micrograms of beryllium is found naturally in the human body, this amount is not considered harmful (why this is the case is not yet understood).[7b] Cumulative exposures and sensitisation leads to a build-up of Be in the body (particularly the lungs) – which the body's immune system has no response for. Beryllium is therefore highly cytotoxic.[28]

1.4 Beryllium Coordination Chemistry

Beryllium toxicity was first reported in Europe in 1933 and in the United States in 1943.[29] Nonetheless, because of the wide spread adoption of beryllium in industrial and commercial applications and the severity of the harm that can come to humans, animals, and the environment as a result, it is especially necessary for further understanding of beryllium coordination chemistry.

There are currently four main areas of interest in beryllium coordination chemistry research. The first is geared towards greater detectability of Be^{2+} in the environment in the form of fluorescent sensors,[30] so that contaminated zones may be quarantined and swiftly dealt with. Second, and just as important, is the development of chelation agents and protocols that could separate and sequester beryllium from these sites.[31] Thirdly, one area of increasing research is the development of Be organic light-emitting diodes (OLEDs),[32] which is fast becoming a useful technology for various electronic applications. Lastly, suitable compounds must be developed for medical therapies in the treatment of Chronic Beryllium Disease.[33] The following sections will provide a brief review of the current beryllium coordination and computational research fields.[14, 34] A summary of identified features key for strong or selective beryllium binding will be made at the beginning of the section on beryllium ligand design. These components will be required to design a suite of selective and strong chelators for beryllium.

Beryllium's only available oxidation state is Be^{2+}, which has a high ionisation potential (899.5 kJ mol^{-1}), charge-to-size ratio (5.7), and has the highest electronegativity of the alkali metal and alkaline earth elements (1.57). Its cation form has a radius of 0.41 Å, making it a small and hard Lewis acid. Due to this unique chemistry, there are many groups that may potentially bind to it. It is apparent that the majority of literature is based upon research of *mono*- and *bis*-chelates and beryllium clusters (e.g. basic beryllium acetate, $Be_4O(O_2CMe)_6$), which involve a varying number of oxygen and/or nitrogen

donors.[34d] Our research will not focus on cluster complexes. In solution, beryllium constitutes Be^{2+} ions. In aqueous solutions a series of OH species are formed, including this 4-coordinated tetrahedral species (Figure 1.5).

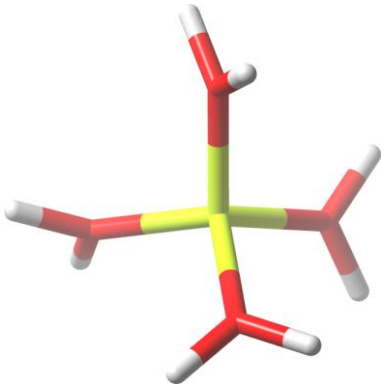

Figure 1.5 A computer model of $[Be(H_2O)_4]^{2+}$ run at CCSD/cc-pVTZ.

The following six complex types will be reviewed. Each of these form 4-coordinate beryllium complexes, where the donors consist of all oxygen through to all nitrogen.

- $[Be(OR)_4]$
- $[Be(OR)_3(NR)]$
- $[Be(OR)_3(XR)]$ where X = O, N, S, or P
- $[Be(OR)_2(NR)_2]$
- $[Be(OR)_1(NR)_3]$
- $[Be(NR)_4]$

1.4.1 [Be(OR)4] Type

For *mono*- and *bis*-chelates of beryllium, the majority of coordination chemistry literature involves oxygen donor ligands. These are often biologically relevant compounds. Functional groups which incorporate oxygen are most often found to be hard bases, according to Pearson's HSAB theory (e.g. CH_3COO^-, RO^-, OH^-). These hard Lewis bases are small, highly solvated, difficult to oxidise, and have high energy HOMOs.

This allows for a strong interaction with hard Lewis acids such as Be^{2+} which is small and positively charged with a low electron affinity, and a high energy LUMO. Therefore complexes of the type $[Be(OR)_4]$ should be very stable.

Beryllium complexes with malonate, succinate acid, 1,1-cyclobutanedicarboxylate and phthalate have been reported (Figure 1.6).[35] These compounds, after deprotonation, offer the Be^{2+} cation two hard oxygen donors each, leading to the formation of both *mono*- and *bis*-complexes. Either two chelating acids can bind to form a tetrahedral geometry, or just one acid with two water molecules. Malonate forms 6-membered rings with the captured metal cation.[35] These have the least ring strain as their geometry is compatible with the tetrahedral ion, and the trigonal planar carbon and oxygen atoms. This being said, complexes with 5-membered and 7-membered (i.e. succinic acid) rings can and do form complexes also.[35]

Malonic Acid **101** | 1,1-Cyclobutanedicarboxylic Acid **102** | Succinic Acid **103** | Phthalic Acid **104**

Figure 1.6 Dicarboxylic acids used to form complexes with beryllium.[35]

Two recent ligands synthesised are 4,5-dicarboxyimidazole and its methyl derivative 1-methyl-4,5-dicarboxyimidzaole (Figure 1.7).[36] These can be bound onto a solid support or form a polymer, whilst binding Be^{2+} with two water molecules.

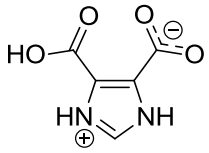

4,5-Dicarboxyimidazole

105

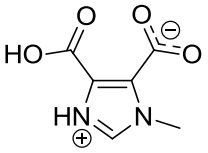

1-Methyl-4,5-dicarboxyimidazole

106

Figure 1.7 Dicarboxylic acids used on solid supports or as part of a polymer in beryllium coordination.[36]

The following diketones (Figure 1.8) bind to Be^{2+} in the same manner as the dicarboxylic acids above.[37] The carbonyl moieties bind beryllium forming two 6-membered rings in a tetrahedral fashion.

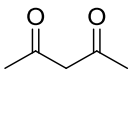

Acetylacetone

107

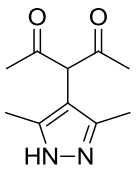

3-(3,5-Dimethylpyrazol-4-yl) pentane-2,4-dione

108

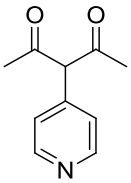

3-(4-Pyridyl) acetylacetone

109

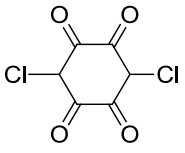

3,6-Dichloro-1,2,4,5-cyclo hexanetetrone

110

Figure 1.8 Diketones used to form complexes with beryllium.[37]

Heterocyclic ligands that contain hydroxyl and keto functionalities have also been utilised for binding beryllium. These have been tested specifically for use as chelating agents. Deferiprone, maltol, kojic acid, and isomaltol (Figure 1.9) have been reported to bind Be^{2+} as the adduct of the type $[BeL(H_2O)_2]^+$.[38] The basicity of the ligands and the stability of their complexes decrease in the order of deferiprone > maltol > kojic acid > isomaltol. A strong correlating factor was the solution pH. Their affinity for beryllium was strongest at high pH. For maltol, there is a fifteen-fold increase in binding strength from pH 3 to 8. Deferiprone is a drug that chelates iron and is used to treat thalassaemia, a major blood disorder.

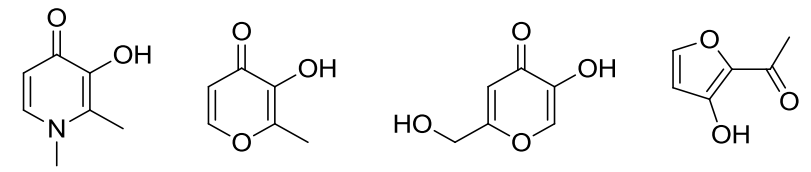

111 Deferiprone **112** Maltol **113** Kojic acid **114** Isomaltol

Figure 1.9 Hydroxyl-keto heterocycles used to form complexes with beryllium.[38]

Salicylic acid is most well-known as an active metabolite of aspirin, as well as being a key ingredient in anti-acne products. The salicylic acid functionality has been extensively studied for use as a beryllium chelation therapy agent (Figure 1.10).[39] This group is a sensible choice because of its formation of stable 6-membered rings, solubility, and strong hard acid-base interaction. This general class of compounds has had countless analogues synthesised, which has allowed for a large suite of ligands to be drawn from for the study. Both the carboxylate and phenolate protons are ionized to form the four-coordinate neutral species: $[BeL(H_2O)_2]$. One derivative incorporates a sulfonate group in order to increase its aqueous solubility – making it useful in applications such as urine tests for urine protein content determination.

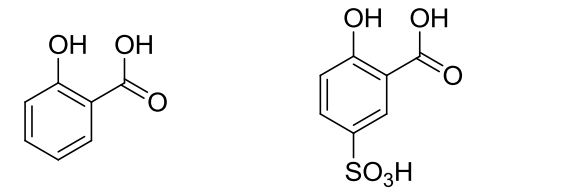

115 Salicylic acid **116** 5-Sulfosalicylic acid

Figure 1.10 Salicylic acid and its sulfonated derivative.[39]

Benzenediols (Figure 1.11) are a class of ligands which have been utilised to bind small cations such as Be^{2+}.[40] They are readily aqueous-soluble compounds, making them ideal for biological systems. The strongest of these is chromotropic acid, which emphasises the importance of beryllium's preference to form 6-membered chelates. The compound 9-

oxidophenalenone forms an adduct of the type $[BeL_2]^{2-}$ and has been used to complex B^{3+} – a cation of similar size to Be^{2+}.

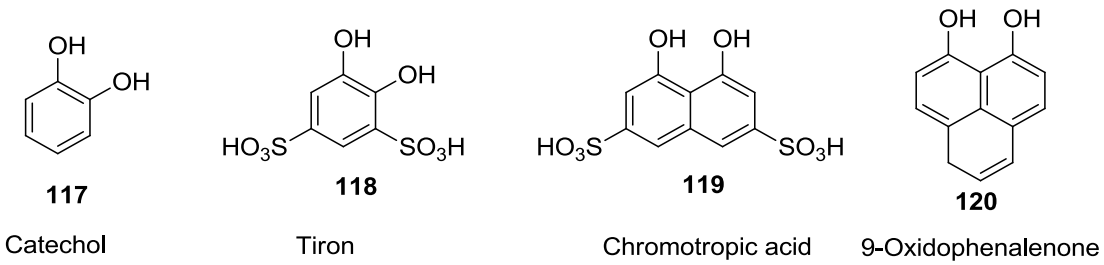

Figure 1.11 Benzenediols used to form complexes with beryllium.[40]

Beryllium phosphonates have been reported with higher binding strengths than their corresponding carboxylate complexes (Figure 1.12).[41] The ligand *P,P'*-diphenylmethylenediphosphinate binds to Be^{2+} as a 1:1 adduct, where there are two beryllium atoms bound to two of the ligand. An amine-based phosphonate was found to form a *mono*-tridentate complex, in which the three phosphonate arms wrap around beryllium to bind it. One water molecule is involved, to complete the favoured tetrahedral geometry. It is likely that the chelate effect helps drive the formation of this complex.

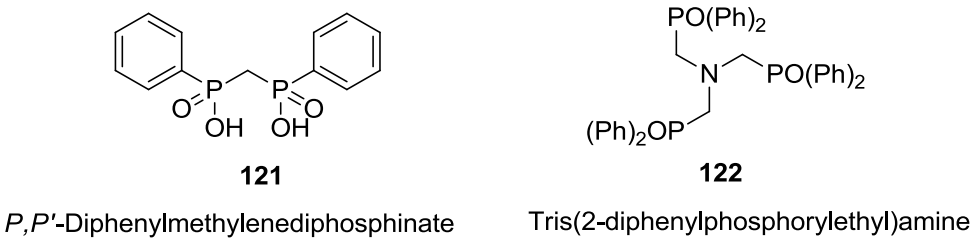

Figure 1.12 Phosphonates used to form complexes with beryllium.[41]

Beryllium forms 5-membered rings with the unusual aromatic compound, tropolone (Figure 1.13).[42] No crystal structures have been observed for this and derivative complexes.

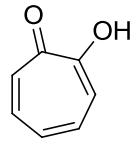

123

Tropolone

Figure 1.13 Tropolone has been used to form a complex with beryllium.[42]

In 2005, the first structurally characterised calixarene-type complex containing beryllium was reported.[43] A dinuclear beryllium complex was formed when *p-tert*-butylcalix[4]arene (Figure 1.14) was treated with $BeCl_2$. Although an interesting complex, for the purposes of this review this species was not examined in any further depth due to it being a cluster complex of two beryllium cations.

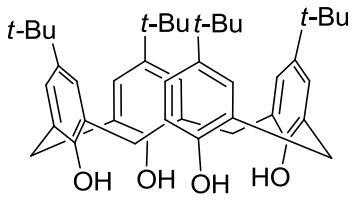

124

p-tert-butylcalix[4]arene

Figure 1.14 Calixarene has been used to form a complex with beryllium.[43]

Aliphatic hydroxycarboxylic acids will form 6-membered rings with beryllium (Figure 1.15).[44] Due to the high pK_a of the aliphatic hydroxyl group, a higher pH is required to deprotonate the ligands.

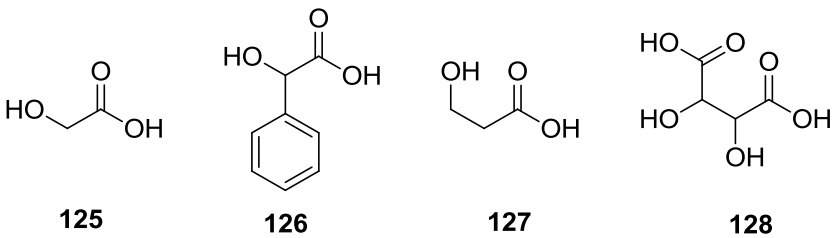

125 Glycolic acid

126 Mandelic acid

127 Hydracyrlic acid

128 Tartaric acid

Figure 1.15 Aliphatic hydroxycarboxylic acids used to form complexes with beryllium.[44]

1.4.2 [Be(OR)$_3$(NR)] Type

While oxygen atoms are the predominant donor group in beryllium chelators, nitrogen atoms have also been employed extensively. When coupled with hard oxygen donors, beryllium coordinates capably with the nitrogen donor. One such compound in which a single nitrogen atom is present is nitrilotripropionic acid (Figure 1.16).[45] Due to the high oxophilicity of beryllium, and because amino groups tend to be weak bases (whereas pyridine moieties are considered as intermediate bases), they are relatively less effective coordinating groups. The apex nitrogen binds to Be^{2+} and the three deprotonated carboxyl groups wrap around to form the fully encapsulated chelate complex. This and other polyamino carboxylic acids successfully coordinated beryllium close to physiological pH – a requirement for beryllium chelation therapy. However, the flexibility of this molecule does allow for the formation of complexes with many sizes of cations – making its selectivity for beryllium unlikely.

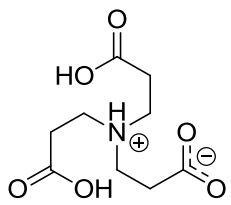

Nitrilotripropionic acid

129

Figure 1.16 Nitrilotripropionic acid has been used to form a complex with beryllium.[45]

1.4.3 [Be(OR)$_3$(XR)] Type

Crown ethers are cyclic compounds containing several ether groups. They are an important and well-studied class of organic compounds. They have been found to be useful in chelation applications and could potentially act as sensors for the detection of cations. A remarkable property that they possess is their ability to almost selectively coordinate and bind to alkali metal ions. For crown-ether complexes, ion-dipole

interactions and hydrogen bonding are the dominant contributing binding forces. The most important reason for the selectivity is considered to be due to the relation between ion and cavity size. Unfortunately, this advantage is also a weakness – as these compounds are highly cytotoxic due to the uptake of essential ions (e.g. Na^+ and K^+).

The below 12-crown-4 ethers (Figure 1.17) have been examined in a computational study,[46] where one of the ether's oxygen atoms has been replaced with another heteroatom (N, S, or P). The heterosubstitution of 12-crown-4 altered the geometry of the cavity size. It was found that aza-12-crown-4 offered the largest metal binding strength to the bivalent beryllium atom forming a cationic, square pyramidal complex. This reflected the predicted geometry offered by the N-containing compound from computation methods. In addition, second-order interaction energies and energy gaps predicted that the aza-12-crown-4 beryllium complex is the most stable of these.

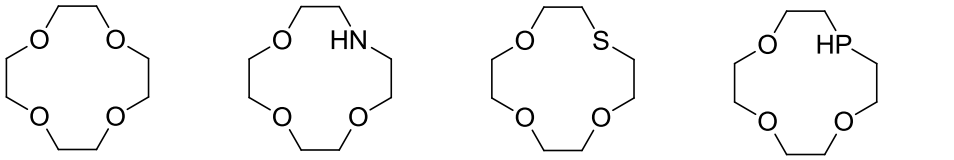

130 12-crown-4 **131** Aza-12-crown-4 **132** Thia-12-crown-4 **133** Phospha-12-crown-4

Figure 1.17 12-crown-4 and its nitrogen, sulfur, and phosphorus containing analogues.[46]

1.4.4 $[Be(OR)_2(NR)_2]$ Type

Beryllium will bind in its typical 4-coordinate fashion to salicylaldimines through the lone pair of the imine nitrogen and the deprotonated phenolic oxygen (Figure 1.18).[47] A distorted tetrahedral geometry is formed as a *bis*-chelate. The imine acts as a weak base. Although its interaction with hard acids such as Be^{2+} is energetically favourable, it is not much stronger than the formation of aqua complexes.[48]

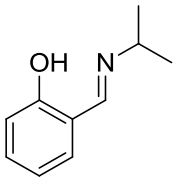

134

N-Isopropylsalicylaldimine

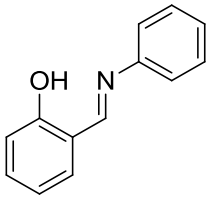

135

N-Phenylsalicylaldimine

Figure 1.18 Salicyclaldimines used to form complexes with beryllium.[47]

Complexes of beryllium with hydroxyphenyl pyridines and azoles form the same type of structures as for salicylaldimines (Figure 1.19).[49] Two 6-membered rings form in a *bis*-chelate. An advantage that these ligands have is they possess photoluminescent properties. The conjugation throughout the ligand allows for an electronic structure suitable for constructing organic light-emitting diodes. For the azole-containing ligand, the heteroatom X can be varied to tune the emitted wavelength.

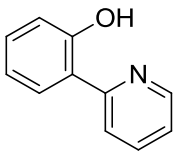

136

Hydroxyphenyl pyridine

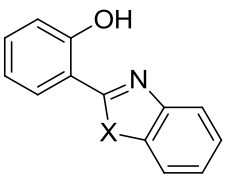

137

Hydroxyphenol azole

Figure 1.19 Hydroxyphenyl type ligands used to form complexes with beryllium, where X = NH, O, or S.[49]

Oxine (8-Hydroxyquinoline) is a monoprotic bidentate chelating agent (Figure 1.20, left). There has been interest in this compound as an anti-cancer drug.[50] It forms *bis*-chelate complexes with both Be^{2+} and Al^{3+} containing 5-membered chelation rings to form a distorted tetrahedral geometry. The latter complex forms tris(8-hydroxyquinolinato)aluminium (Alq_3) – a common component of OLEDs. Varying substituents alter its photoluminescence effects. Commercial testing kits for beryllium contamination detection use a sulfonate analogue of benzo[*h*]quinolin-10-ol (Figure 1.20, right).[51] The resulting complex acts as a colourimetric indicator for the presence of

beryllium. It is not selective for beryllium, however, and requires pre-treatment of the area with EDTA to be surveyed (to bind all other metals present).

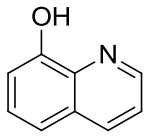

138

8-Hydroxyquinoline

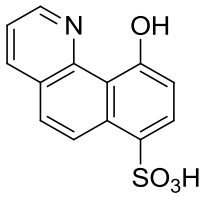

139

10-Hydroxybenzo[*h*]quinoline-7-sulfonic acid

Figure 1.20 Quinolines used to form complexes with beryllium.[50-51]

1.4.5 [Be(OR)(NR)$_3$] Type

Recently, a new ligand has been reported which shows great promise in binding beryllium selectively and strongly.[52] The ligand 2-(6-(dipyridin-2-ylamino)pyridine-2-yl)phenol is the first of this type which offers a *mono*-chelate through an enclosed tetrahedral binding cavity (Figure 1.21). The deprotonated phenolic oxygen would provide initial coordination to Be^{2+}. The three intermediate-base pyridine nitrogen donors would then bind via chelation to encapsulate beryllium fully.

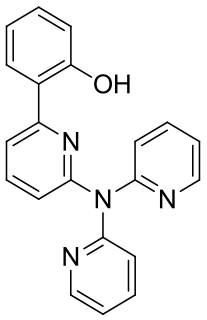

L1nH

Figure 1.21 A synthesised ligand designed specifically for selective chelation of beryllium.[52]

Due to the less strained geometry of this compound, it has greater flexibility when coordinating to small cationic metal ions. The binding cavity supports the formation of the favoured tetrahedral geometry through 6-membered rings. Pearson's HSAB theory supports the hypothesis that strong binding will occur. Thus far, only a computational model of its binding to Be^{2+} has been simulated. Experimental coordination studies have yet to be investigated.

1.4.6 [Be(NR)$_4$] Type

Beryllium complexes consisting of only nitrogen donors have not been studied thoroughly. Without the assistance of a hard oxygen donor, weak bases such as amines and imines typically bind small, highly positively-charged metal cations weakly. There are only a few rare cases where crystal structures of this type of complex have been reported. Often a reactive beryllium salt must be used to form the initial complex.

Silyl imines are an unusual case, where tight 4-membered rings are formed leading to a significant distortion in the characteristic tetrahedral geometry (Figure 1.22).[53] Deprotonation of the nitrogen atom gives a full negative charge which greatly helps in binding cations.

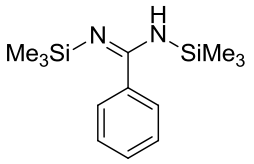

140

N,*N*'-Bis(trimethylsilyl)benzimidamide

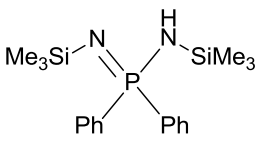

141

P,*P*-diphenyl-*N*,*N*'-bis(trimethylsilyl)phosphinimidic amide

Figure 1.22 Silyl imines used to form complexes with beryllium.[53]

The delocalisation and heavy conjugation of diazabutadiene and indole compounds allows reasonable complexation with Be^{2+} with 5-membered rings in a *bis*-chelate (Figure 1.23, left).[54] Pyridyl indoles act in the same manner (Figure 1.23, right).[55]

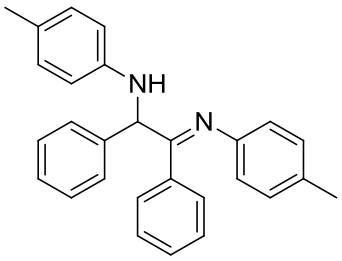

142

N-(1,2-Diphenyl-2-(*p*-tolylamino)ethylidene)-4-methylaniline

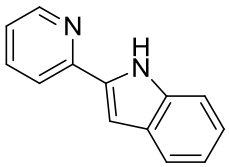

143

2-(2-Pyridyl)indole

Figure 1.23 These two ligands when deprotonated have been used to form complexes with beryllium.[54-55]

One unique complex formed is the adduct of Be^{2+} with phthalocyanine (Figure 1.24).[56] This structure is unstable and prone to hydrolysis. This is due to the beryllium cation adopting an unfavourable planar configuration within the ring.

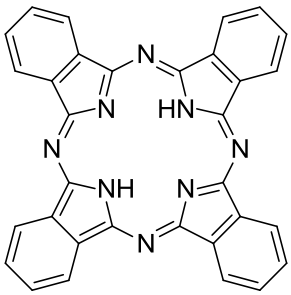

144

Pthalocyanine

Figure 1.24 Phthalocyanine has been used to form a complex with beryllium.[56]

The last class of compounds to be discussed are proton sponges (Figure 1.25).[57] These are ligands which are known to exhibit extremely high basicities and give unique spectroscopic properties. 1,8-Bis(dimethylamino)naphthalene emits a double fluorescence due to a mixture of two ground-state species.[58] These two properties when combined would allow both the sequestering and detection of Be^{2+} ions in an aqueous solution. The high basicity is caused by the rigid distance between the two nitrogen atoms. Each has a lone pair of electrons whose orbitals overlap; this typically causes destabilisation of the

compound. However, this destabilisation can be eliminated by binding a proton between the nitrogen atoms, which forms strong hydrogen bonds – hence their name.

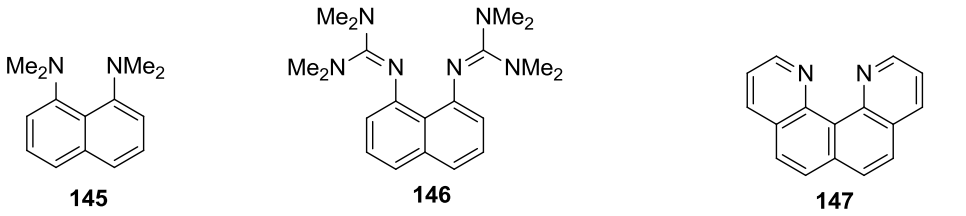

Figure 1.25 Three typical proton sponge structures.[57a, 57d, 57g]

Below in Figure 1.26, benzo[*h*]quinolin-10-amine is the amine analogue of aforementioned benzo[*h*]quinolin-10-ol (Figure 1.20) which is used in chemical detection tests for beryllium.[57g] Although this compound binds Be^{2+}, it does so much more weakly than when the phenolic oxygen was available. This emphasises the need for a hard oxygen donor for the initial binding of beryllium. The dichloro quinoquinoline derivative (Figure 1.26, right) confirms this as it is reported to bind to a number of transition metals strongly, but only weakly to Be^{2+}.[52]

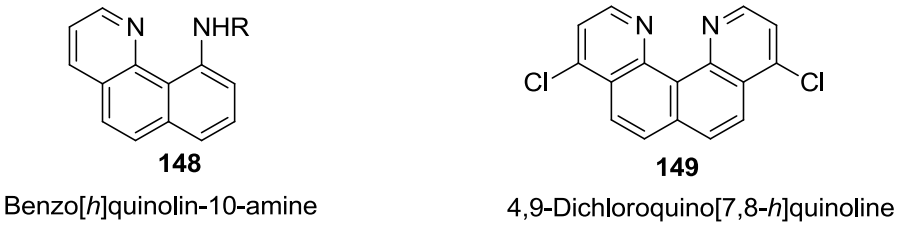

Figure 1.26 Two proton sponges, where R = $SO_2C_6H_4NO_2$, C_6H_5, or CH_3CO.[52, 57g]

The ligand quino[7,8-*h*]quinoline was shown to form a *mono*-complex with BF_2^+ in a tetrahedral fashion, but not with Be^{2+}.[59] Although the bite size is ideal for small cations, the nitrogen donors by themselves are not hard enough bases to bind strongly with a very hard acid without the proton sponge effect.

1.5 Beryllium Computational Chemistry

The number of computational investigations published on beryllium chemistry far outweighs that of experimental studies.[60] This is likely due to the interesting bonding properties that arise from beryllium's position on the periodic table, and the safety risks involved in experimental study. Research is usually focused on beryllium bonds forming through its two empty p-orbitals and subsequent high Lewis acidity.[61] Literature also covers the use of beryllium in carbon nanotubes (CNTs),[62] noble-gas and gaseous compounds,[63] Be clusters,[64] coordination chemistry,[65] NMR studies,[66] as well as its biological interactions.[67] Of particular interest to this thesis is the published work on binding studies.[46, 68] The following section will provide a summary of recent research in these areas.

Biological studies have shown that the body's response to beryllium is caused by an autoimmune reaction. This was discovered by the finding of beryllium-sensitive T-cells in berylliosis patients.[69] Recent theoretical investigations have highlighted the mechanism responsible for these actions.[67b-d] The HLA-DP protein is a peptide-antigen receptor found on the surface of T-cells, which has a high affinity for Be^{2+}. It is suggested that complexation occurs by Be^{2+} displacing hydrogen-bond involved protons between two amino acid side-chains (Figure 1.27).[70] A mutation study of this protein offers that it is these side-chains that are modified in berylliosis-susceptible individuals.[71]

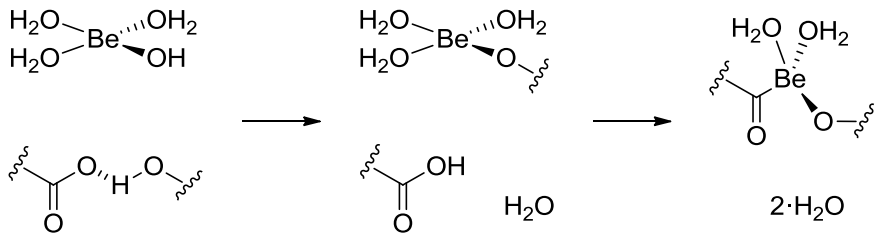

Figure 1.27 Proposed mechanism for beryllium-protein binding.[70]

One beryllium containing metallocene (Figure 1.28) is predicted to be a stable species by DFT methods.[72] Natural Bond Orbital (NBO) analysis gave an electronic structure that indicates a single metal-metal bond and ionic bonding between the beryllium atoms and cyclopentadienyl rings. The calculated Be-Be bond length of 2.057 (B3LYP) is considerably smaller than the experimental value for the diatomic beryllium bond (2.45 Å). Natural population analysis with natural localised molecular orbitals (NPA/NLMO) gives a calculated Wiberg Bond Index (WBI) of 0.926 for the Be-Be bond, indicating a σ bond. The charge on each beryllium atom is 0.849, indicating an ionic bond to the Cp ring, making use of the empty p-orbitals.

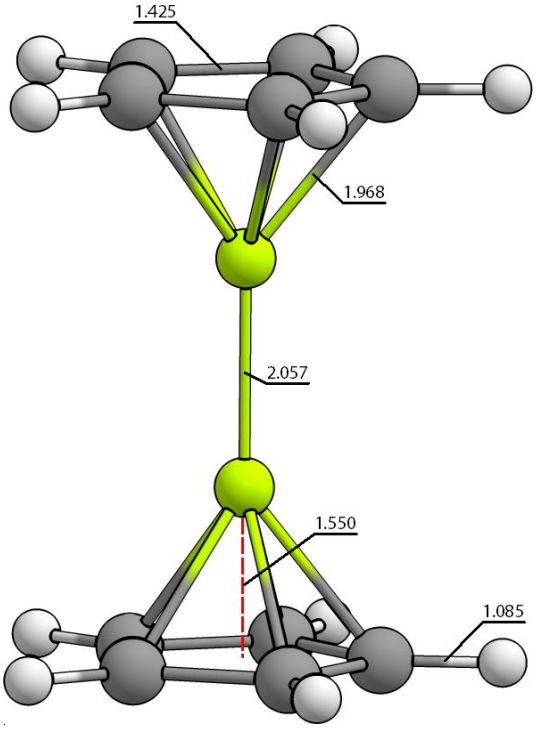

Figure 1.28 DFT optimised geometry for C_5H_5Be-BeC_5H_5. Bond distances are in Å.[72]

In 2015, a noble-gas study was undergone where 1-tris(pyrazoyl)borate beryllium complexes were investigated in their effectiveness to bind to noble gas atoms (He-Rn) (Figure 1.29).[63b] Owing to the large positive charge on the Be cation, the complex was able to bind in a partially covalent manner to argon, krypton, xenon, and radon atoms. The degree of covalency increased with heavier noble gases. The Be-Ng atom bonds were investigated by their WBI (Table 1.1). The WBI values around 0.5 imply significant

covalent character, due to electron transfer from the p_z orbital of the noble gas atom to the empty p_z orbital of the beryllium.

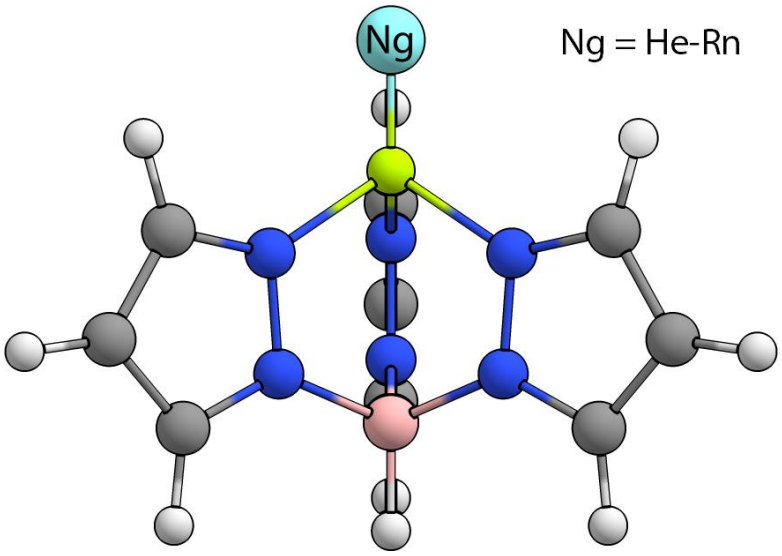

Figure 1.29 The 1-tris(pyrazoyl)borate beryllium cationic complex binds to noble gas atoms. Ng = Noble gas.[63b]

Table 1.1 Wiberg Bond Index values for noble-gas atom bonds.[63b]

Complex	WBI
TpBeHe$^+$	0.19
TpBeNe$^+$	0.13
TpBeAr$^+$	0.33
TpBeKr$^+$	0.41
TpBeXe$^+$	0.51
TpBeRn$^+$	0.53

Cukrowski *et al.* have in recent years published binding studies of beryllium complexes.[73] A direct comparison was made between nitrilotriacetic acid (NTA) and nitrilotripropionic acid (NTP). By using the molecular fragment energy terms as defined in the Interacting Quantum Atoms/Fragments (IQA/F) framework, an accurate model of complexation was found that fit experimental trends (Figure 1.30). PBE1PBE, B3LYP, and X3LYP methods were used with the basis set 6-311++G(d,p) with the IEFPCM-UFF solvation model using water as the solvent.

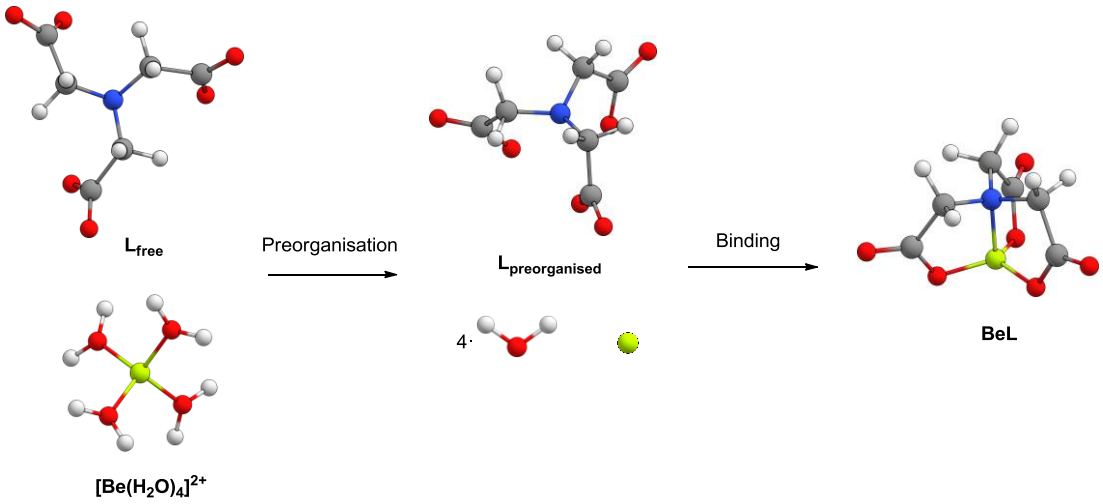

Figure 1.30 A depiction of the complex formation process for hydrated beryllium binding to NTA.[73]

DFT methods have also been used to accurately determine binding energies of complexation. Pavlov *et al.* examined group 2 metals (Be, Mg, Ca) and a group 12 metal (Zn) with B3LYP and the large double-ξ basis set 6-311+G(2d,2p).[68b] In order to obtain accurate metal-water binding energies, they investigated a successive series of $M(H_2O)_n^{2+}$ clusters. For highly accurate results, the dipole moment and polarisability of the water molecules are required to be well described by the computational method. Using this method and basis set, errors of these values were 6% and 17%, respectively. However, when these calculations are run using a basis that includes the basis functions of the metal atom, these errors drop to 2% and 4%, respectively. These errors would be representative of any error in the computed binding energies of the same systems.

1.6 Beryllium Ligand Design

It is necessary to have further understanding of beryllium coordination because of its widespread adoption and the severity of the harm it causes. A new suite of ligands will be designed that will bind selectively and strongly to beryllium. These could be used to remove or recover beryllium from waste sources, hazardous environments. Later,

chelators of this type may have the potential to be used in medical remediation of those who suffer from beryllium sensitivity or chronic beryllium lung disease.

1.6.1 Current Chelation of Beryllium

Both essential and non-essential metals can cause predictable toxic effects when exposure surpasses the concentration and duration of a critical dose.[74] The effect may be acute or chronic, and depending on the metal involved, will manifest in different organs including respiratory and central nervous systems. In such cases, chelation therapy is administered to remove excess metal from the poisoned body. This medical procedure can have unwanted side-effects, including death; therefore care is taken to reduce the risks involved. The first chemical used in medicine for its ability to chelate was dimercaprol (Figure 1.31).[75] Chronic berylliosis is assessed similarly to silicosis, asbestosis, and sarcoidosis.[74]

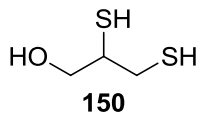

150

Dimercaprol

Figure 1.31 Dimercaprol, also known as British anti-Lewiste (BAL), was the first chemical used in chelation therapy during WWII as an antidote to the chemical weapon Lewisite.[75]

It is unfortunately the case that all known chelators coordinate not only to beryllium but even more strongly to a vast array of other metals – principally, commonly found metals such as copper, iron, and magnesium. It has been identified that this is due primarily to two reasons; the functional groups present in the ligand (in particular hard oxygen donors), and the size of the binding cavity. Several explicit examples of desirable ligand properties will be given below. The chosen designs will focus on these ideas to provide a ligand that would bind to beryllium selectively over other present metals.

The most essential properties of a chelating agent based on biological and chemical considerations are the following:[74]

- High stability of the formed complexes.
- Selectivity toward the target metal ion; the chelating agent must not perturb the essential metal status.
- Favourable toxicity profile of the chelating agent and its complexes.

Few experimental chelation studies have been made since the discovery that the metal caused berylliosis in the 1950s. In 1982, Jones *et al.* investigated 11 water soluble chelating agents as antidotes for mice and found the most effective to be sodium 4,5-dihydroxy-1,3-benzenedisulfonate (Tiron).[76] Later animal studies by Gupta *et al.*,[77] Shukla *et al.*,[78] and Mathur *et al.*,[79] included the following chelators: ethylenediaminetetraacetic acid (EDTA), N-(2-hydroxyethyl)ethylenediaminetriacetic acid (HEDTA), *meso*-2,3-dimercaptosuccinic acid (DMSA), 2,3-dimercapto-1-propanesulfonic acid (DMPS), and dimethyl cysteine (DPA) (Figure 1.32). From what has been investigated, Tiron and DPA were found to be the most effective, closely followed by DMPS, but no extensive comparison study has been completed.

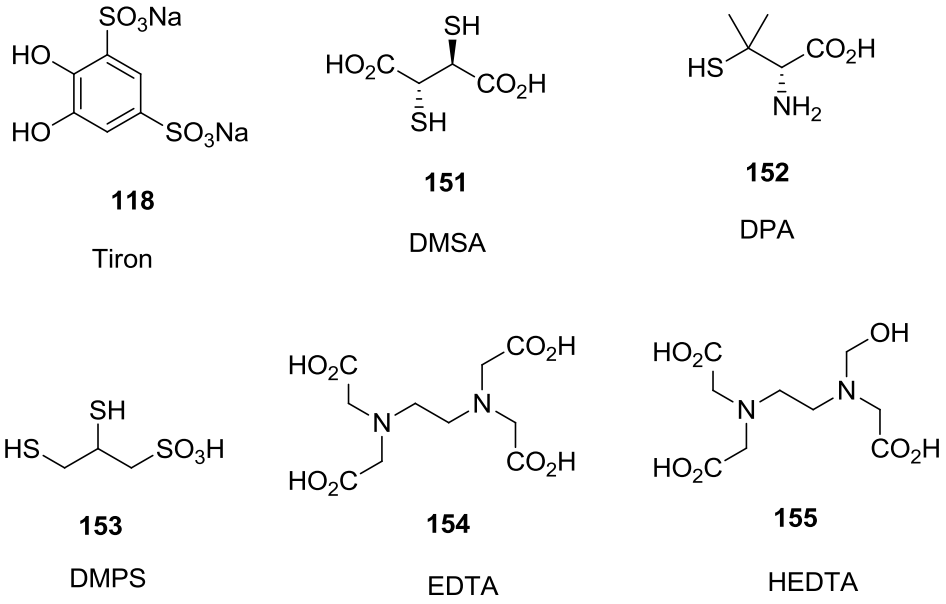

Figure 1.32 Biologically tested chelators for beryllium.[76-79]

A single short-duration clinical study was performed in 1959 on two patients suffering from occupationally induced berylliosis.[80] One was administered Na_3HEDTA, and the other Ca_2EDTA; but no comments were made on the clinical effects of these chelators. A conclusion on which is the best choice of chelator cannot be made due to insufficient data. Similarly, it is difficult to determine if these would be effective in chelating beryllium in various environments, particularly because these compounds were chosen based off their previous ability to chelate other metal ions. It is likely that Be^{2+} binds to many of these ligands via strong Be-O bonds, due to the ion's preference for hard donors. The ability of EDTA and HEDTA to fully encapsulate metal ions is advantageous due to the chelate effect, but they are found to bind beryllium poorly.

Each of these dicarboxylic and dihydroxyaromatic derivatives provide two hard oxygen donors, which, when bound to beryllium, form a tetrahedral donor arrangement with a second ligand of the same type (Figure 1.33).[14] The equilibrium table suggests that of these, chromotropic acid is the strongest chelator for beryllium (Table 1.2). Malonic acid has an increased stability over oxalic acid, which is unlikely to be due solely to the difference in ionization constants. Instead, this points to beryllium's preference for 6-

membered chelate rings over 5-membered chelate rings. The ligand design in this thesis will attempt to take advantage of this preference. Also, the sulfonate residues of Tiron and chromotropic acid provide increased water solubility and reduced oxidation to their quinone analogues. The addition of this functionality could prove useful.

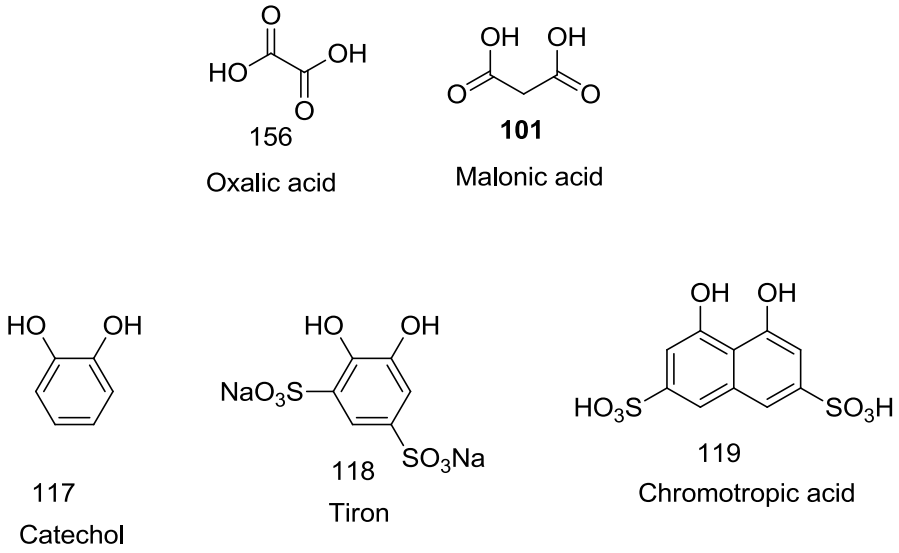

Figure 1.33 Dicarboxylic and dihydroxyaromatic ligand derivatives.[14]

Table 1.2 Formation constants of some dicarboxylic and dihydroxyaromatic derivatives of beryllium.[14]

Ligand	$\log_{10}K_1$	$\log_{10}K_2$	Ring formation
Oxalic acid	4.08 3.26		5
Malonic acid	5.73 5.35		6
Catechol	13.70 13.52	12.02 9.83	5
Tiron	13.5±0.1 12.88 12.20	12.5±0.1 9.37 9.30	6
Chromotropic acid	16.34 16.20	11.85 12.00	6

The detection of beryllium has been researched primarily for the testing of contaminated sites. Ligands containing mixed N and O donors have been a recent target for metal

chelation studies to this end. 10-hydroxybenzo[h]quinolone-7-sulfonic acid (10-HBQS) is a fluorophore and the standard for trace detection of beryllium (Figure 1.34, left).[81] Beryllium binds strongly to this compound. The method first involves using EDTA to remove the other metals present, which then allows quantitative analysis of beryllium without interference.[82] The estimated detection limit for the most recent analytical technique is less than 0.1 ng per air filter or wipe sample.[83] This compound shows strong photoluminescent effects, as do many of the previously reviewed ligands. Similarly, 1,1'-binaphthalene(salicylaldimine)beryllium displays both photoluminescent and fluorescent properties due to its highly aromatic structure (Figure 1.34, right).[84] It is possible that by introducing aromatic systems to a mixed donor tetradentate coordination, our ligand motif will also display these characteristics, and potentially be used as a detector itself. A *mono*-binding chelating agent has a lower intrinsic entropic energy, therefore will be best suited for high binding strength complexes.

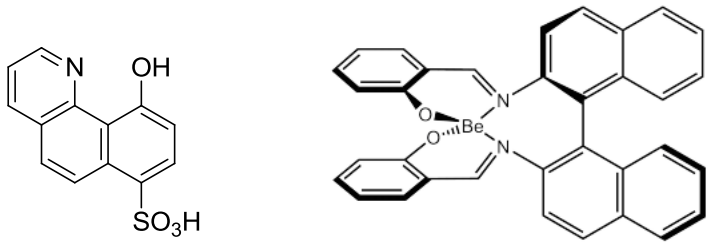

157 **158**

Figure 1.34 10-hydroxybenzo[*h*]quinolone-7-sulfonic acid (left) and 1,1'-binapthalene(salicylaldimine)beryllium (right).[81,84]

1.6.2 Primary Motif Design

By analysis of the previously reported work on beryllium complexes, a number of key principles essential for selective and strong binding chelators are:

- Pearson's HSAB theory
- Provision for a small binding pocket

- Tetradentate coordination
- An arrangement of tetrahedral positioned donor atoms
- *Mono*-chelation
- The formation of 6-membered rings on chelation
- Mixed O-N donors

To fulfil these, a series of basic motif structures were designed to best take these into account (Figure 1.35).

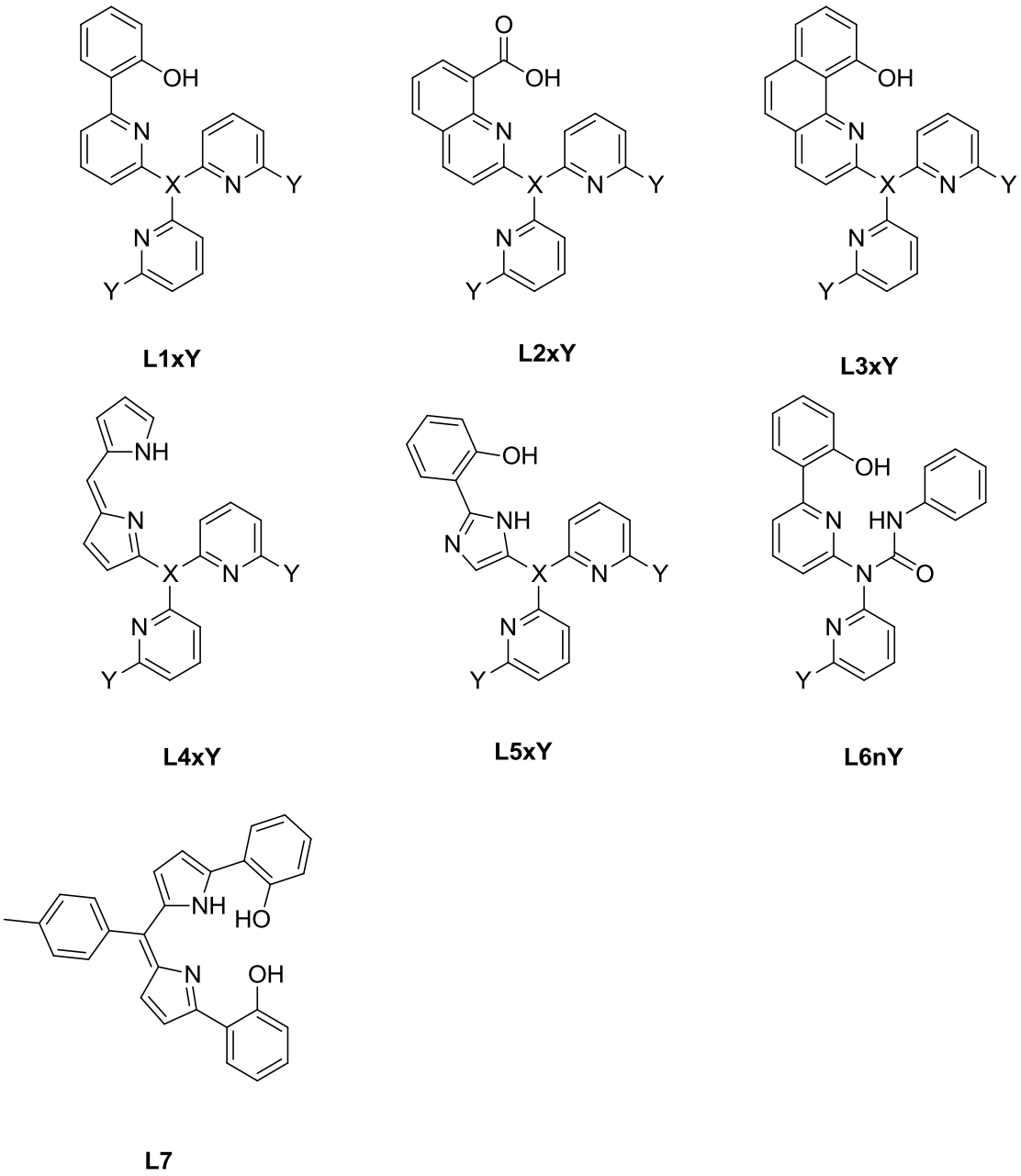

Figure 1.35 Designs for an encapsulating ligand, where X is an apex group (CH, COH, or N), and Y is a group that may offer the potential of intramolecular hydrogen bonding.

Pearson's acid base concept is fulfilled by introducing bases in the form of a phenol, a hard oxygen donor (except **L4**), and pyridyl moieties (intermediate nitrogen donors). Because Be^{2+} is a small and hard acid, it favours interactions with functionality such as these. Whilst oxygen-containing functional groups are best suited for this, they will also form strong or stronger complexes with many metals, and so selectivity is greatly reduced. However, at least one negatively charged oxygen donor was required to successfully bind

beryllium strongly. We will avert reduced selectivity by making the other three donors pyridyl nitrogens, which will form a conformationally strained backbone. These are intermediate Lewis bases, and thus favour bonding to beryllium to a lesser extent. Initial association will occur between the Be^{2+} ion and the deionised oxygen, followed by complexation via chelation of the pyridines. This is particularly important in aqueous environments, in order to displace the protective solvent shell of water molecules around beryllium. This will allow the ligand to form a strong complex with Be^{2+}.

The sixth encapsulating ligand, **L6nY**, is a derivative of **L1xY**, when x = N, and one pyridyl unit is substituted for a urea-like functionality (Figure 1.36). This provides the ligand a second weaker oxygen donor that could bind to a metal in place of an aromatic nitrogen atom. This type of ligand was considered later in the project after the DFT calculations on the ligands **L1**-**L5**, and **L7** were complete, so only minimal computational work was performed on it. Only the synthetic work will be discussed.

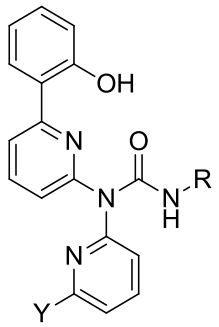

L6nY

Figure 1.36 Sixth ligand design, where R = CH_3, Ph and Y = H, NHBn, NH_2.

Metal ions greatly vary in their ionic radii. A common ion, Fe^{3+} (six-coordinate, low spin), has an ionic radius of 0.69 Å; whereas Be^{2+} (four-coordinate) has an ionic radius of 0.41 Å. Flexible ligands can bind well to large ions as they can more easily encapsulate them. By establishing a more rigid structure, a tight binding pocket is achieved. This should in theory help improve selectivity, as the ligand will be able to fully encapsulate beryllium, but otherwise prevent binding of larger metals.

It was shown that the predominant form beryllium takes in complexes is in a tetrahedral coordination with tetradentate binding. Its preference for this structure is convenient, as most of the metal ions that this ligand would be selecting from have a predisposition to adopt octahedral geometries. Tetrahedral geometries for these result in higher ground state energies than what they would find in typical binding agents like EDTA. Our ligand achieves this motif through its three nitrogen and single oxygen donors. The pyridyl scaffold will allow chelation around a single Be^{2+} ion to form a close-fitting tetrahedral cavity. To minimise steric, torsional, and ring strain, the design is *mono*-chelating, and will bind beryllium with favoured 6-membered rings.

In the literature, only two ligands are known that are similar to the proposed design (Figure 1.37). The ligand 2-(6-dipyridin-2-ylamino)pyridine-2-yl)phenol was synthesised by Shaffer *et al.* and is the first of its type – offering *mono*-chelation through an enclosed tetrahedral binding cavity.[52] The key difference is that it uses an apex nitrogen group rather than a carbon. It was designed for selective chelation of beryllium, and a computational model of it has been simulated. The other compound, 2-(6-(fluorobis(6-methylpyridin-2-yl)methyl)pyridin-2-yl)phenol, was synthesised by Stoessel *et al.*, and was part of a project investigating organic electroluminescent devices containing metal complexes.[85] They successfully formed a *mono*-copper containing complex with this molecule. The synthetic routes to these ligands will form an initial basis for the synthetic schemes used in this thesis.

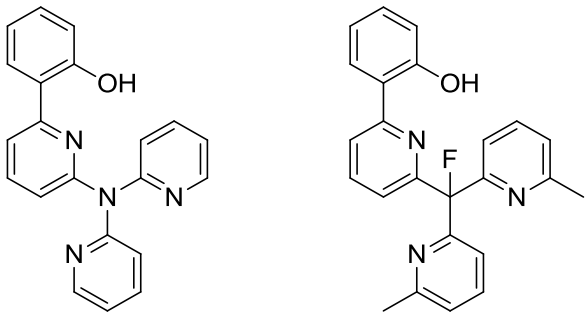

L1nH **L1cfCH$_3$**

Figure 1.37 Previously synthesised ligands that are structurally similar to this proposed design.[52, 85]

1.6.3 Buttressing Components and Modifications

Complementarity and pre-organisation are two fundamental concepts in host-guest chemistry.[86] The *principle of complementarity* is given by Cram as follows: "to complex, hosts must have binding sites which can simultaneously contact and attract the binding sites of the guests without generating internals strains or strong non-bonded repulsions." This important feature is required for any complexation, as without it the targeted molecule or ion would not be recognised by the ligand. The *principle of pre-organisation* states: "the more highly hosts and guests are organised for binding and low solvation prior to their complexation, the more stable will be their complexes". Taking advantage of this will provide improved energy efficiency and perhaps more selective binding. A rigid host has a smaller range of conformations than a flexible host. The latter must overcome an entropic and enthalpic cost, which reduces the overall binding energy. By pre-forming the binding cavity, this 'cost' is already paid, resulting in higher complexation binding energies. The free ligand differs to the coordinated ligand in terms of conformation and protonation state. The deprotonation required for tetradentate binding of a metal will result in a small conformation change in its structure.

These fundamental host-guest concepts can be taken advantage of by making modifications to the primary motifs, thereby creating a library of ligand derivatives. By

attaching new functional groups, the ligands can be tuned specifically for beryllium binding, as well as altering how they will interact in various environments. These ideas involve:

- Buttressing
- Solubility
- Detection

In order to maximise binding and selectivity, buttressing components will be investigated. These are either inherent or additional components of a ligand that provide a secondary shell of hydrogen bonding that is not directly involved in the metal-ligand bonding. They can provide both increased stability and selectivity for complexes by providing a pre-organized structure. The choice of buttress can be varied to tune the binding site for the desired metal.

The proof of concept of complex stabilization via secondary sphere hydrogen bond coordination was shown by Tasker *et al.* (Figure 1.38).[87] The separation of specific metals from aqueous solutions is an essential part of hydrometallurgy and efficient solvent extraction is required for kiloton scales used by industry. Intermolecular forces between chelates and solvent contribute a significant amount to the stability of complex formation. By introducing hydrogen bonding capable buttresses, the strength and selectivity of metal extraction could be manipulated to our advantage. This work will frame our initial approach to introducing a secondary coordination sphere to our complexes.

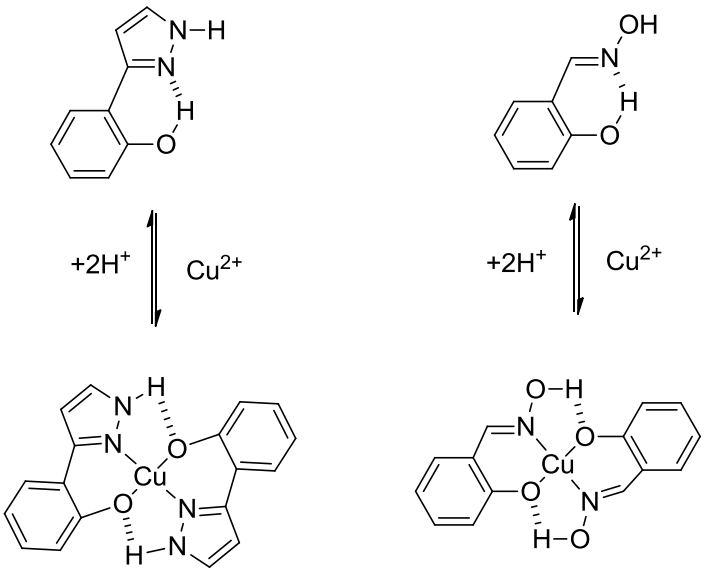

Figure 1.38 Hydrogen bonds form a secondary sphere of coordination that enhances the stability of these phenolic pyrazole and phenolic oxime copper complexes.[87a]

Our design will incorporate amine functionalities to the 6-position of the two pyridyl arms (Figure 1.35, group Y). This position will offer an N-H bond capable of forming hydrogen bonds with the opposing phenolic oxygen in 6-membered rings. The increased stability of the formation of these, as well as the pre-organization, will offer a lower ground state energy for a beryllium complex, compared to the non-buttressed complex form. Optimal tuning of the binding cavity site can be tested by investigating a series of buttress groups such as methyl amines, formamides, and urea, as well as including bulkier substituents.

Although not directly in the scope of this thesis, future work on these ligands would involve examining how these ligands interact in different systems, be it aqueous, organic, or colloidal. For extraction of beryllium from aqueous systems, the metal needs to be either quenched within an aqueous phase or to be moved into an organic phase. For the former, the ligand would need to be water soluble. This could be introduced through attaching sulfonate residues. The later method would require a non-specific prior complexation agent to move beryllium into the organic layer, where our ligand would then aid in full complexation and subsequent removal.

Some of the reviewed ligands had functional groups and conjugation, which resulted in a photoluminescent effect. Our designs have similarities to them, and any photoluminescence observed would be useful for the detection of beryllium in the environment.

1.7 Scope of Research

The aim of this research is to examine and explore the use of secondary sphere hydrogen bonding interactions for chelating ligands in the formation of beryllium complexes. Our motivation for this research is our desire to find a selective and strong binder of beryllium. Such a ligand is necessary due to beryllium's wide use in applications across industries and its inherent toxicity. As knowledge of the fundamental chemistry of beryllium, compared to other small metals, is underwhelming, our approach to this field is multifaceted. Initially, computational work will evaluate ligand preference of Be^{2+}, which will be followed by ligand synthesis and complexation with small cations. These will be complexed and analysed with electrospray ionisation mass spectrometry (ESI-MS), competition studies, and crystallization.

Chapters 2, 3, and 4 form the first half of this thesis. These will discuss the computational work of non-buttressed ligands, outline the experimental synthesis towards non-buttressed ligands of type **L1**, and investigate X-ray structures for determined Be^{2+} complexes of non-buttressed ligands. Chapter 4 will also make a comparison of the experimental and the computational data.

Chapters 5 and 6 form the second half of this thesis. They will explore the computational work of buttressed ligands, their NCIPlots, wider studies of metals, as well as considering the synthetic routes to buttressed ligands of type **L1**.

Chapter 7 will contain the synthetic experimental procedures, and Chapter 8 will lay out the overall conclusions made.

Chapter 9 will list the references. This is followed by appendices A and B, which will contain the experimental spectra and crystallographic details. Appendix C contains the computational data and X-ray data, and can be found in the supplementary information. Appendix D provides a fold-out sheet of the studied ligands, including the naming system used.

This project was part of a Marsden grant involving two other research groups in New Zealand. These were at the University of Waikato (Prof. Bill Henderson), and at the University of Auckland (Prof. Penelope J. Brothers). More recently, collaboration has been taken up with The University of Marburg (Dr. Magnus R. Buchner).

Chapter 2: Computation of Non-buttressed Ligands

"We are reaching the stage where the problems we must solve are going to become insoluble without computers. I do not fear computers. I fear the lack of them."

– Isaac Asimov

2.1 Introduction

One of the first project goals was to use computational chemistry as a tool to screen potential ligands of the tri-pyridyl variant that are most likely to bind beryllium strongly. Theoretical calculations can be run to make reasonable judgements of this. These calculations can be a powerful tool to explain the chemistry behind selective capture and transportation of metal cations.[46, 88] However, as far as we know, no theoretical investigation has been reported in which the binding capabilities of ligands to beryllium were specifically examined. This thesis will provide such an investigation, incorporating second-sphere coordination through buttressing (Chapter 5). This will involve the addition of functional groups that will not take part in the binding of a metal cation but will instead form strong hydrogen bonds that will help to further stabilize the complex. The designed suite of ligands and their buttressed derivatives were evaluated, using theoretical calculations and binding energies were calculated for Be^{2+}, and compared with similar calculations of B^{3+} and Al^{3+}. These ions were chosen as they share a similar size and tend to adopt the same geometries as Be^{2+}, and therefore they should give an indication towards relative binding strengths for each ligand.

Once preliminary calculations have established that the new ligands will theoretically bind to Be^{2+}, a complimentary computational *metal* binding study will be carried out (Chapter 5). This will involve calculating binding strength data for a ligand and its buttressed form, then compared against the computed binding data for three known chemicals that bind to beryllium (NTP, EDTA, and HBQS). For this study, a series of metals have been chosen

that are commonly found in the environment or are essential metals in the human body. This study will help identify the relative strength of binding that each metal has towards these. A full analysis of this investigation will provide data as to how effective our ligands are in contrast to known binders.

The last computational section will examine non-covalent interactions within each complex (Chapter 5). Graphical visualisations of these forces will be presented to aid in the interpretation of the effects of binding metals in the ligand cavity, as well as key changes due to the introduction of buttressing functionality.

The strengths and weaknesses of these initial ligand designs will be evaluated to determine the best candidates for organic synthesis and complexation with Be^{2+}, Al^{3+}, B^{3+} and other small cations. By doing so, synthetic work would take a more directed and efficient approach. Due to the inherent toxicity of beryllium, it was desirable to limit the synthesis of beryllium containing binders to just those that are theoretically optimal.

2.1.1 Binding Energies

Intermolecular binding energy is defined as the energy difference found in a system after the combination of individual molecules. It can be positive (destabilising), or negative (stabilising). The below bimolecular reaction is the simplest case, but these can often be more involved. Our bindings also involve the expulsion of water. A general model is created by calculating the thermal ground state energies for each component involved; A and B, the reactants; and AB, the product (Equation 1).

$$A + B \rightarrow AB \quad (1)$$

From this, a general equation for binding energy is found (Equation 2):

$$\Delta E_{bind} = E(AB) - E(A) - E(B) \quad (2)$$

E(AB), E(A), and E(B) each represents the energy of the complex and each monomer. ΔE_{bind} is the calculated binding energy. Therefore, three separate calculations are required in order to determine this energy.

Unfortunately, in computational studies it is common to find an associated strengthening of intermolecular interactions and therefore an artificial shortening of intermolecular distances. These are called *basis set superposition errors* (BSSEs), and manifest as increased complex stabilisation. They arise due to an artificial stabilisation of each monomer when they are in close proximity by borrowing extra basis functions from neighbouring components (which they otherwise could not use when at larger intermolecular distances). This occurs because each molecule wants to best improve its electron distribution by utilising orbitals belonging to other molecules, in order to minimise its ground state energy. The effect is particularly pronounced when smaller basis sets are used, wherein the basis set approximates all orbitals to be the same shape. Using a large triple-zeta basis set gives a more accurate representation of each orbital by treating each orbital separately during the Hartree-Fock calculation, through using the sum of three Slater-type orbitals. Other factors that contribute to BSSEs are if the systems in question are particularly large or if Van der Waal dispersion interactions are especially important. In the limit of a complete basis set, the BSSE would be eliminated completely.

The Boys and Bernardi counterpoise correction is the most commonly proposed method for correcting basis set superposition error.[89] The method alters Equation 2 by estimating the amount of artificial stabilisation of each monomer through the use of ghost functions on each monomer. Deformation of the monomers upon complexation can also be considered (particularly for strongly interacting molecules).

The general form of the calculation used to determine the binding energy of a ligand to a specific metal (Equation 4) was derived from the following general reaction (Equation 3):

$$L^- + [M(H_2O)_n]^{x+} \rightarrow [LM]^{x-1} + n.H_2O \quad (3)$$

Where L^- is the deprotonated ligand, $[M(H_2O)_n]^{x+}$ is the hydrated charged metal cation, and $[LM]^{x-1}$ is the formed complex (n = 4 or 6, x = 2 or 3, and M = Al^{3+}, B^{3+} or Be^{2+}).

$$\Delta E_{bind} = E([LM]_{x-1}) + E(n.H_2O) - E(L^-) - E([M(H_2O)_n]^{x+}) \quad (4)$$

2.1.2 Geometry Optimisation and Frequency Calculations

Geometry optimisation calculations try to achieve minimisation of the global potential energy for a given system. It does so by determining the optimal spatial arrangement of atoms through analysis of its potential energy surface (PES). The PES of a molecule is the relationship between a molecule's geometry and its total energy. An initial guess is made for the geometry, and the calculation carries out an iterative process. This is where a small change is made in the geometry, and a convergence calculation is made, depending on the criteria outlined by the method used. Convergence is found when the last optimisation step meets the criteria. When it does, the calculation is complete, and the geometry is said to be optimised. If, however, convergence fails, this step is repeated. If no convergence is found within a set number of steps, the calculation will fail. Many solutions are available in such cases. Within this thesis, the initial guess for the starting geometry will be built using a chemically intuitive idea of the final expected geometry.

Once the optimal geometry has been calculated, a single-point frequency calculation is performed to compute force constants, vibrational frequencies and intensities, and the thermal data for the system. The two primary functions of a frequency calculation used here are:

- To confirm that the optimised geometry is at the global minima energy position on the PES.
- To calculate the structure's free energy in solution.

Frequency calculations output all vibrational frequencies for the given structure. Imaginary frequencies (negative frequencies) are nonsensical, and do not exist in nature. Therefore, if these are present, this indicates that the geometry found is at a saddle point on the PES and must be further optimised. To confirm that the found solution is the global minima, multiple starting geometries are used. If they converge to the same geometry, it can be said that the solution is good. The Gibb's free energy of the molecule in solution is calculated by combining the free energy of the gas-phase molecule with the free energy of solvation. This solvation energy is obtained using a Self-Consistent Reaction Field (SCRF) calculation of the optimised structure.

To calculate binding energies for the complexation reactions of our ligands to the selected metal cations, solution phase computation methods are required. This is to best mimic a real-world scenario. Standard DFT methods for geometry optimisation and frequency calculation are performed in the gas-phase. To correct them for our use, a SCRF calculation is required. This additional technique models the solvent as a reaction field. A solvent is modelled by applying a continuum of uniform dielectric constant, ε, around a solute cavity, where the molecule is placed. The Integral Equation Formalism Polarisable Continuum Model (IEF-PCM) method will be used during both the geometry optimisation and single-point frequency calculations. This is the most common recommended method for calculating the free energy of solvation for general purposes. Here, water is used as the solvent ($\varepsilon = 78.3553$).

2.1.3 Gaussian and Visualisation Software

Computational chemistry is most widely practised with the computation packages provided by Gaussian.[90] Its flexible and thorough features have a long standing history in the literature, which provides not only a wide berth of scrutinised topics and novel techniques, but also offers many examples of computational chemistry which can be used as a benchmarking tool for future research.

Within this thesis, all calculations performed to optimise ligand geometry and frequency calculations were run using the Gaussian 09 (Revision D.01) package, either on a Linux CentOS workstation, or through the New Zealand eScience Infrastructure (NeSI) high performance computing facility.[90]

In order to enhance discussion concerning the non-covalent interactions of the complexes, the systems will be analysed with the tool NCIPlot (non-covalent interaction plot). NCIPlot is a piece of software that enables a graphical visualization of inter- and intra-molecular non-covalent interactions based on electron density and its derivatives. This qualitative method is convenient to create depictions of both attractive and repulsive forces. This tool will give regard to the hydrogen bonds formed in the secondary coordination sphere by the amine buttresses to the phenolic oxygen of the core binding site (Chapter 5).

The geometric structures of each ligand and complex were prepared with the GaussView 5.0 package on a Windows desktop.[91] They were initially constructed such that they were close to the expected minimised geometry before being submitted for calculation. The frequencies of each optimised structure were checked to ensure no negative values were observed, confirming that the structures are minima geometries. To ensure that the solutions are at global minima energies, multiple starting geometries were tested, which all converged on the same geometry.

Visualisation, examination, and the depiction of these molecules throughout this thesis were obtained through using ChemCraft 1.8.[92]

2.1.4 Geometry and Pre-Organisation Indices

Two parameters will be used to help describe the geometry of ligands and complexes. The first of these are the geometry indices or structural parameters (τ_4 and τ_4'), which distinguishes the geometry found in the coordination centre of a four-coordinate complex.[93] These parameters have values in the range of 0 to 1. They quantify how close the geometry is to a square planar geometry ($\tau_4 = \tau_4' = 0.00$), seesaw geometry ($\tau_4 \approx 0.43$, $\tau_4' \approx 0.24$), or tetrahedral geometry ($\tau_4 = \tau_4' = 1.00$) (Figure 2.1).

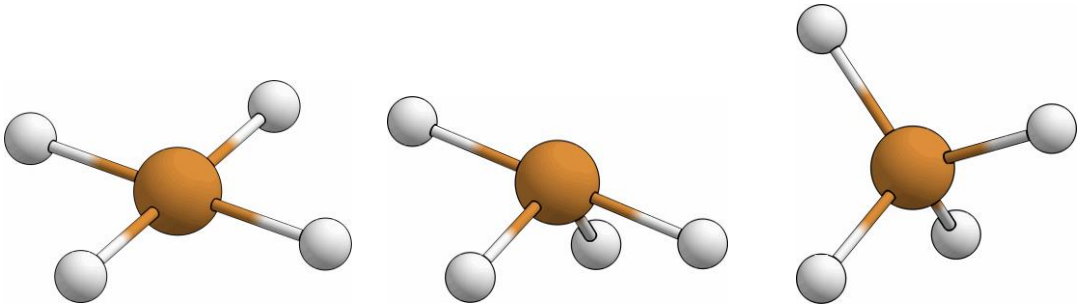

Figure 2.1 Square planar geometry (left), seesaw geometry (middle), and tetrahedral geometry (right)

Equations 5 and 6 describe their calculation:

$$\tau_4 = \frac{360° - (\alpha_1 + \beta_1)}{360° - 2\theta_1} \tag{5}$$

$$\tau_4' = \frac{\beta_1 - \alpha_1}{360 - \theta_1} + \frac{180° - \beta_1}{180° - \theta_1} \tag{6}$$

Where α_1 and β_1 are the two greatest valence angles of the coordination centre, and θ_1 is the ideal tetrahedral angle (109.5°).

The pre-organisation indices or Nixon parameters (η_α and η_β) indicates the extent of pre-organisation that a tetradentate ligand has. These parameters have values in the range of 0 to 1. A value of 1 corresponds with the donor atom being in the ideal location, whereas a value of 0 corresponds with the donor atom being positioned away from the binding site through an inversion operation. Figure 2.2 shows an example of this, where in orange and pink are shown dihedral angles that are used in this calculation. Its η_α and η_β values are 0.98 and 0.15 respectively. This result is interpreted to mean that one pyridyl arm is pre-organised to a high degree, whereas the other is not.

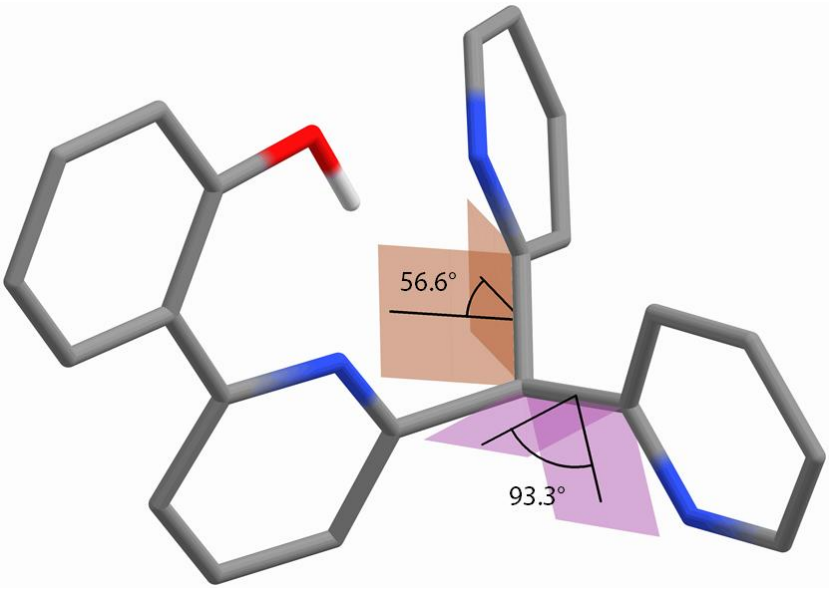

Figure 2.2 Example of the dihedral angles of a tetradentate ligand that are used to calculate the Nixon parameters.

Equations 7 and 8 describe their calculation:

$$\eta_\alpha = 1 - \frac{|\alpha_2 - 60°|}{240°} \tag{7}$$

$$\eta_\beta = 1 - \frac{|\beta_2 + 60°|}{240°} \tag{8}$$

Where α_2 and β_2 are the dihedral angles found through the apex and donor atom of one pyridyl arm respectively.

2.1.5 Level of Theory

It was determined that the most appropriate computational theory to employ in calculating binding energies for this suite of ligands was density functional theory (DFT). It has been previously shown that Becke's three-parameter hybrid exchange correlation functional containing the non-local gradient correlation of Lee, Yang, and Parr (B3LYP)[94], with a 6-31G(d) basis set gives accurate geometry calculations for proton sponge and proton sponge-like molecules.[52, 94-95] At this level of theory, bond lengths and bond angles are within an acceptable range of the experimental results, and so this level of theory has been used to find initial geometries for the ligand and resulting complex structures. Accurate thermochemical data and ground state energies are required for the calculation of binding energies.[46, 68b, 68c, 96] All thermal chemical data has been calculated at 298.15 K.

The binding study methodology has been previously justified in a comparison study of known complexes of beryllium (Figure 2.3).[97] A series of aminopolycarboxylic acids NTA, NADP, NDAP, and NTP were shown experimentally to bind Be^{2+}, as shown below (Table 2.1). Figure 2.4 gives an example reaction used to obtain a binding energy value (ΔG) using equations 3 and 4. In a collaborative effort with Lane and Onyekachi at the University of Waikato, a reproduction in the trend was attempted by using two DFT functionals (B3LYP, M06-2X), each with and without a solvation model. Regardless of functional, the best fit to the previous study was obtained when the IEF-PCM solvation model was used. The opposite trend was observed in the gas-phase calculations. Further extensive calculations and manipulation is required to convert these binding energies into comparative log$K$ values. So, although these binding energies cannot be quantitatively

compared with the experimental log*K* values, they are qualitatively comparable. Mederos *et al.* found the B3LYP functional to provide better values than M06-2X.[98]

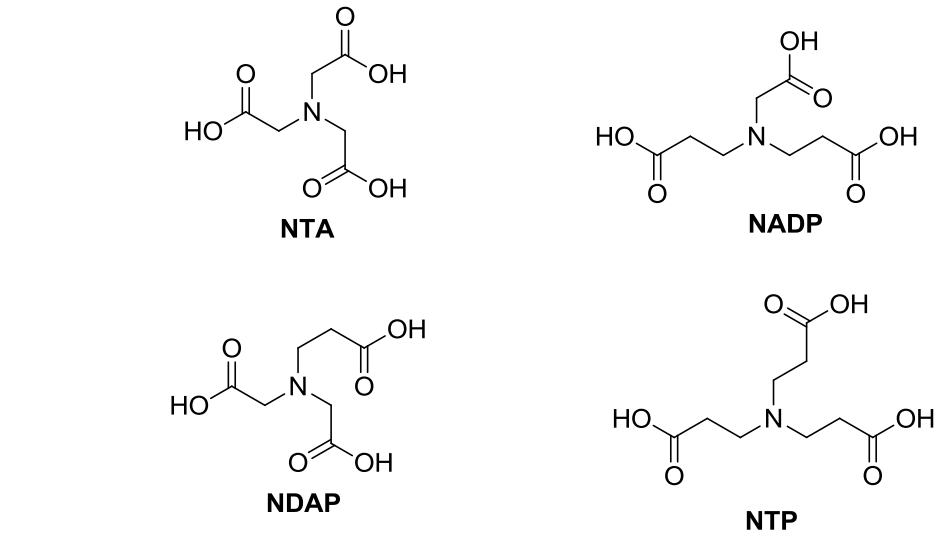

Figure 2.3 Known aminopolycarboxylic acids that form complexes with beryllium.[98]

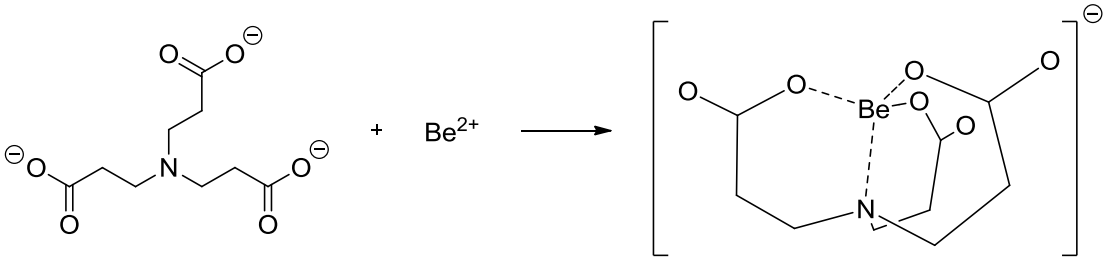

Figure 2.4 Reaction of $[NTP]^{3-}$ with Be^{2+}.

Table 2.1 Comparison of two DFT methods for aminopolycarboxylate ligands for the formation of beryllium complexes with their experimentally deduced equilibrium constants.[48, 97]

	ΔG_{gas} / kJ mol^{-1}		ΔG_{aq} / kJ mol^{-1}		Experimental
	B3LYP	M06-2X	B3LYP	M06-2X	log *K*
[BeNTP]$^-$	-2157	-2171	-314	-349	9.23
[BeNADP]$^-$	-2222	-2235	-310	-344	9.25
[BeNDAP]$^-$	-2231	-2299	-299	-329	8.12
[BeNTA]$^-$	-2347	-2361	-290	-317	6.62

Based on this trend and the previous literature studies,[48, 97] it was decided that the optimised structure of [Be(NTP)]$^-$ using B3LYP, the large triple-zeta Pople basis set 6-311++G(d,p), and the solvation model IEF-PCM, gave a good estimate of the experimental parameters (Figure 2.5). To further evaluate the most appropriate computational method to determine binding energies for our ligand systems, the B3LYP functional was tested against B3LYP-D3, M06-2X, and ωB97X-D.[99] For each method, calculations were performed with an unbuttressed ligand and two buttressed ligands, all with Be^{2+}. It was found that each functional gave the same interaction energy trend, where the magnitude of the trend varied on average by only 3%. As this work involved a large array of ligands and metals, and was desirable to be further extended, economical calculations were required. Therefore the B3LYP functional was chosen as it provided efficient use of computer time as well as giving quantitative results of the expected trends.

These results were used to provide a rationale for using this level of computational study for the research contained in this thesis. The chosen basis set contains sufficiently diffuse functions and is flexible enough to give a good account for any occurrences of hydrogen bonding, including second sphere interactions formed due to the presence of a buttressing group. Given our complexes are roughly 40 atoms in size, this basis set is sufficient to reduce BSSE to an acceptable level. Calculations were made with and without a counterpoise correction, and the non-corrected energies were found to be 0.9-1.2% greater than the corrected energies. This was found to be comparable to similar calculations in the literature, and has been a recommended functional/basis set combination for this for the prediction of hydrogen bonded systems. Therefore in the limit of this basis set, the extra calculations required to reduce the BSSE were unnecessary.[89] This level of theory allows reliable predictions to be made in regards to the metal-ligand binding strength.

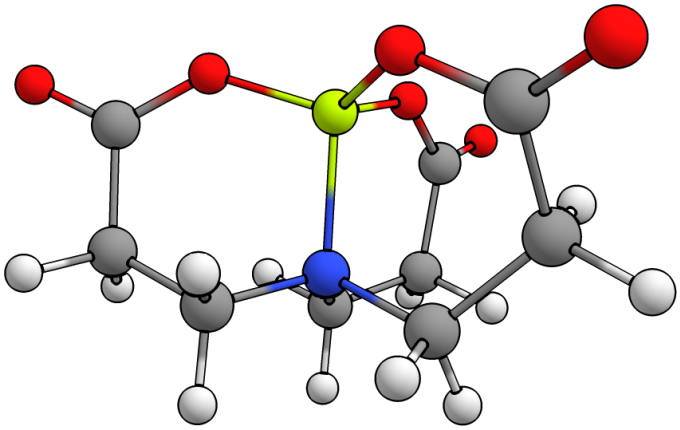

Figure 2.5 Geometry optimized complex of $[BeNTP]^-$, at B3LYP/6-311++G(d,p).

2.1.6 Computational Studies of Ligands 1-7

To examine the binding of ligands to the metal cations Be^{2+}, B^{3+}, and Al^{3+}, free energies for the selected metals were calculated in their hydrated forms as $[Be(H_2O)_4]^{2+}$, $[B(H_2O)_6]^{3+}$, and $[Al(H_2O)_6]^{3+}$ respectively (Table 2.2). The aluminium species is inherently more stable than the others are. The gas-phase and solvent-phase data have been compared for illustration purposes. This chapter will discuss only the results and trends of the solvent-phase calculations, as these will give the most realistic depiction of experimental coordination.

Table 2.2 Calculated free energies of water and the hydrated cations.

	ΔG_g / kJ mol^{-1}	ΔG_{aq} / kJ mol^{-1}
$[Al(H_2O)_6]^{3+}$	-1838.27	-1839.98
$[B(H_2O)_6]^{3+}$	-864.71	-866.68
$[Be(H_2O)_4]^{2+}$	-840.29	-841.13
H_2O	-200.72	-200.75

2.2 Primary Motifs

Six non-buttressed capable ligands will be examined in this chapter (buttress capable ligands are presented in Chapter 5) (Figure 2.6). These ligands are capable of binding

small cations within a tetrahedral coordination geometry of tetradentate donor atoms. **L1-5** will bind through two pyridyl groups, and either a phenol, carboxylic acid, dipyrrin, or a phenol and imidazole moieties. **L7** is somewhat unique, in that its geometry may allow for a wider range of encapsulation, and geometry preferences.

Each of these ligands and their complexes had geometries first calculated using the DFT functional B3LYP and the basis set 6-311++G(d,p) in the gas-phase. After this, their optimisation was refined using the solvation method IEF-PCM (using water as the solvent). A single-point frequency calculation is made in both the gas-phase and solvent-phase to determine thermochemical data.

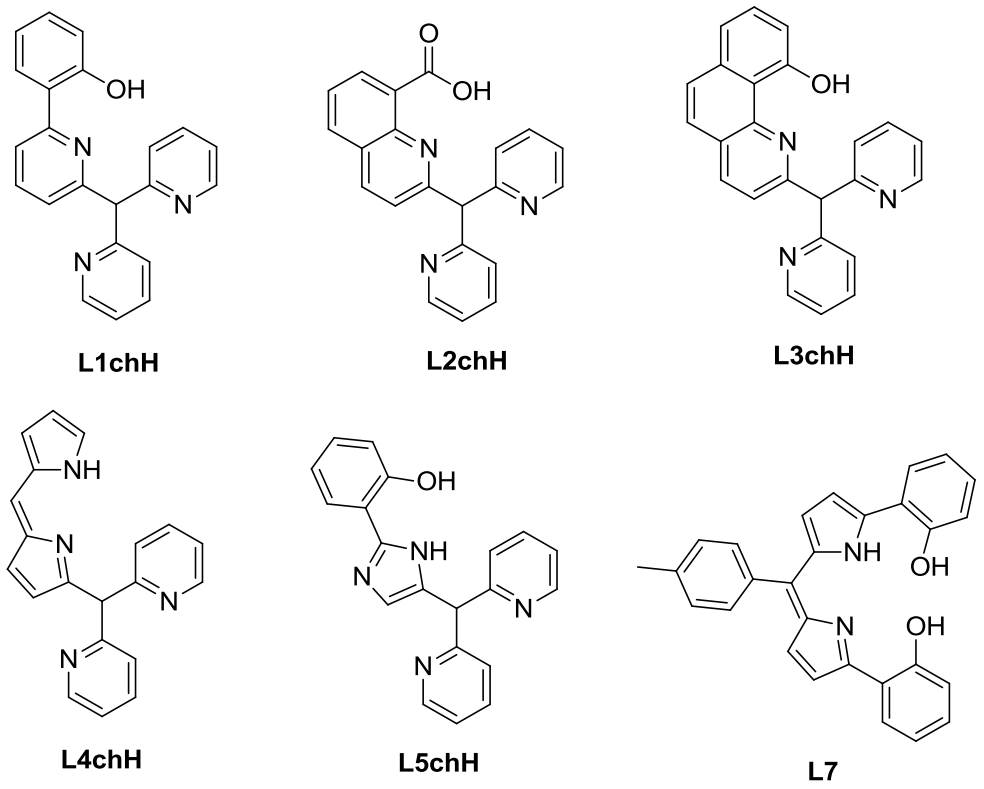

Figure 2.6 Primary motifs investigated.

2.2.1 Ligand Geometries

Pre-organisation of the ligands in this study are noted to roughly increase stepwise from **L1** < **L2** < **L4** < **L5** < **L3** < **L7** (Figure 2.7). The flexible nature of **L1** allows a great degree

of rotational freedom, which has resulted in none of the donor atoms appearing to point towards a central cavity. There is a small attractive interaction between the phenolic oxygen atom and the closest proton (C-H) of the same ring. There is perhaps some pre-organisation present in the two furthest pyridyl rings, which are orientated in the same direction. **L2** displays a higher amount of order, as its carboxylic acid moiety forms a very strong, mostly covalent, hydrogen bond (O-H···N, 1.663 Å) with the pyridyl nitrogen of the same ring system. One pyridyl arm is orientated towards the acid, forming a moderate hydrogen bond (2.739 Å). In **L4**, all four donor atoms are directed towards a central cavity. Three hydrogen bonds are present, occurring with the protonated pyrrole nitrogen. The first hydrogen bond is strong, being with the adjacent pyrrole nitrogen (2.053 Å), and the other two are weaker, with the nearby pyridyl nitrogens (2.692 Å and 2.660 Å). The next most pre-organised is **L5**. In its structure, a moderate, mostly electrostatic, hydrogen bond occurs between the OH moiety of the hydroxyphenol group and imidazole nitrogen (2.404 Å). Its pyridyl groups face towards this hydrogen bond, and although the ligand is elongated, it does tend towards a cavity space. The second highest order of pre-organisation is in **L3**, where all four donor atoms fold around a central cavity. Aided by its greater level of structural rigidity, there is a strong hydrogen bond between its phenol and adjacent pyridyl nitrogen (1.692 Å), a moderate hydrogen bond to one pyridyl arm (2.844 Å), and a very weak, electrostatic, hydrogen bond to the third nitrogen atom (3.953 Å). The highest level of order is found in **L7**, which has a significantly different conformation, due to its two phenolic arms. These result in a particularly tight cavity, in which all four donor atoms are involved in a near-planar configuration. The strongest hydrogen bond present is between one phenolic proton and the adjacent pyrrole nitrogen (1.691 Å). Like **L4**, the two other important bonds present are also formed with the protonated pyrrole nitrogen. These are with the other phenolic oxygen (1.982 Å) and the other pyrrole nitrogen (2.276 Å). The last hydrogen bond present is between the two phenolic groups (1.989 Å). The varying degrees of pre-organisation in each ligand will result in smaller or greater amounts of deformation when

binding to a metal cation. This entropic factor will contribute adversely to the overall binding energies.

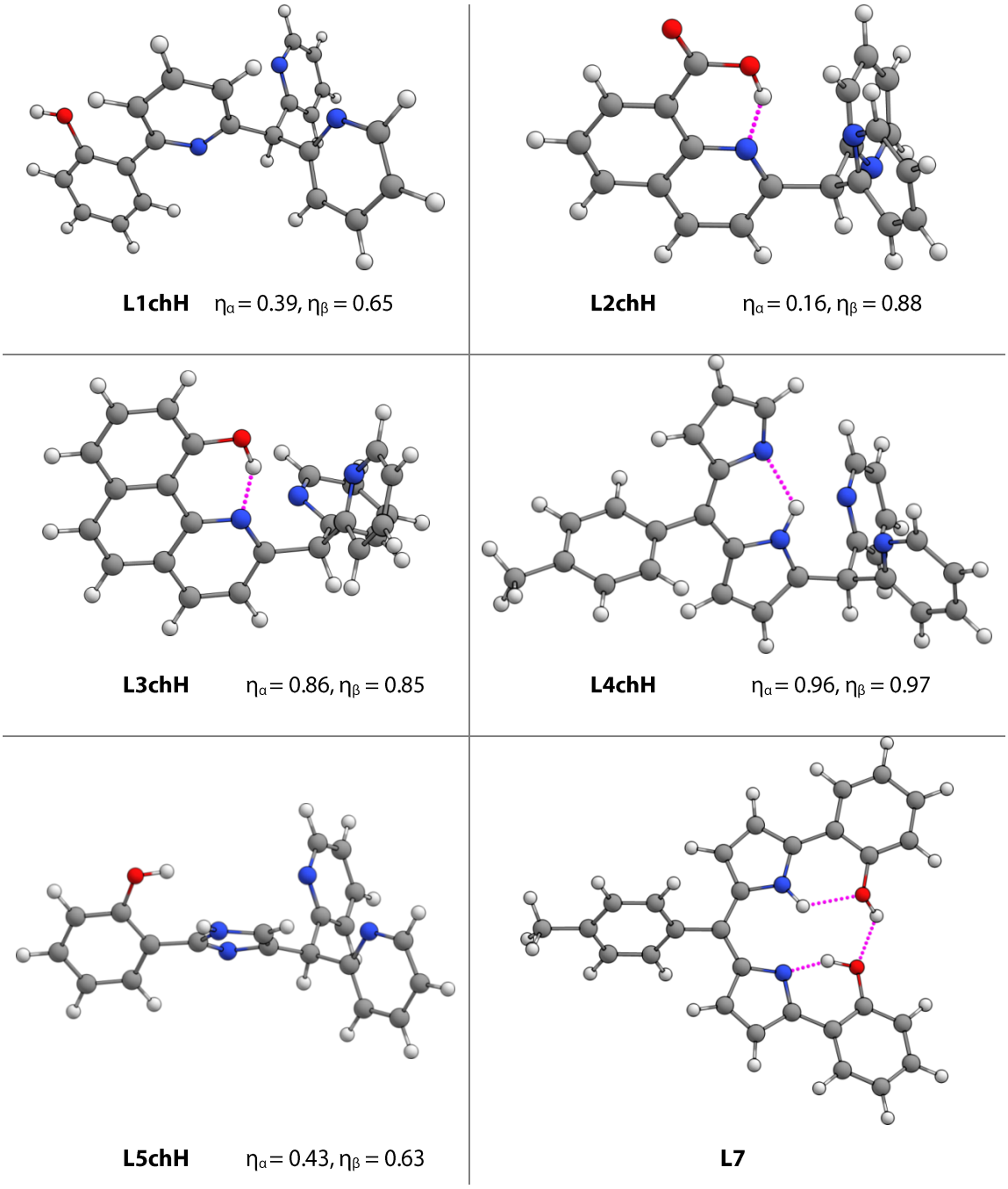

Figure 2.7 Aqueous phase geometry optimised ligands in their primary motif at B3LYP/6-311++G(d,p).

2.2.2 Complex Geometries

Each metal cation adopts relatively identical complex geometries (Figures 2.8-2.10). They are tetradentate *mono*-chelating, with tetrahedral cavities. Data for each ligand, including key bond lengths, angles, and their geometry index, have been listed in the following tables (Tables 2.3-2.8). **L1**, **L2**, and **L5** in particular have deformed the most in order to form a complex, which will correspond to a deformation energy which will contribute negatively in their calculated binding strengths.

The average length of coordinating bonds to the metal cation was found to be shortest for B^{3+}, with an average O-B bond length of 1.44 Å, and N···B bond length of 1.56 Å. The next shortest is for the Be^{2+} cation, with an average O···Be bond length of 1.59 Å, and N···Be bond length of 1.73 Å. The Al^{3+} cation has the longest bonds to the metal centre, with an average O···Al bond length of 1.75 Å, and N···Al bond length of 1.89 Å. These values are reflected in the binding strengths observed, which increase with shorter (stronger) bonds (all other variables kept the same).

Of **L1**-**L5**, **L3chH** has the shortest bond lengths to Be^{2+} (Table 2.5). Its O···Be bond is 1.535 Å, and the three N···Be bonds are 1.700-1.762 Å. Its angles are converging on being tetrahedral with one angle of 109.4° and the others averaging to be 10.8° away from ideal tetrahedrality. A good indicator for molecular geometry is through the calculated geometry indices, τ_4 and τ_4'. These values will be equal to 1.00 for perfectly tetrahedral geometries, and they will be equal to 0.00 for square planer complexes. For **L3chH_Be**, its τ_4 value is 0.82. This indicates good tetrahedrality. However, its imperfection comes from part of the coordination tending towards a plane (O, N_2, N_3, Be). This suggests that the binding pocket is not tight enough for the Be^{2+} cation. It is predicted that a better geometry will be obtained through the second sphere of interactions provided by the buttress groups introduced in Chapter 5. **L1chH** and **L2chH** have close to the same τ_4

values (τ_4 = 0.83 and 0.82 respectively) when bound to Be^{2+}, but weaker bonds to the metals.

The higher ionic charge for aluminium and boron puts beryllium at a disadvantage in the metal-ligand attraction due to their increased electrostatic attraction. Also, the size of the metal cation likely plays a significant role, with a better cation to cavity fit in each ligand. B^{3+} is the smallest cation, with an ionic radius of 0.25 Å. Be^{2+} is the next smallest cation with an ionic radius of 0.41 Å. And the Al^{3+} cation has an ionic radius over 2 times larger than that of B^{3+}; being 0.68 Å. These radii correspond to the observed trend in bond angles of each system. A tetrahedral bound cation prefers angles of 109°, and 6-membered rings typically prefer angles of 120°. The key bond angles in the coordination centre for B^{3+} (average of 114.1°) are closest to the ideal angles. Be^{2+} complexes have consistently larger bond angles than this, and even larger for Al^{3+}.

Seesaw and distorted tetrahedral geometries are found between the extreme values of τ_4 and τ_4'. This helps explain the altered trend for binding Al^{3+} over Be^{2+} in **L5** and particularly **L7**. The τ_4 values are much lower for **L4chH_Al** (τ_4 = 0.69), **L5chH_Al** (τ_4 = 0.69), and **L7_Al** (τ_4 = 0.49) (Tables 2.7-2.8), which are far closer to the ideal values for a distorted or seesaw geometry (τ_4 = 0.43). For aluminium and beryllium, this is clear in their complex geometries, where **L5** has a trigonal pyramidal-like shape, and **L7** tends towards a square planar geometry. These geometries have more space surrounding the binding site, which means they have larger bite sizes. This enables **L5** and **L7** to exhibit a higher binding strength to Al^{3+} over Be^{2+}. It is noted that the boron complexes all have high τ_4 values, with an average value of 0.91. The last consideration to make is in regard to the donor atoms involved. The involvement of two oxygen donors is more favourable than pyridyl nitrogens due to their level of electronegativity and hardness. The dipyrrin moieties also bind strongly to the metals, where they are in fact shorter than the O-M bonds in **L7** complexes.

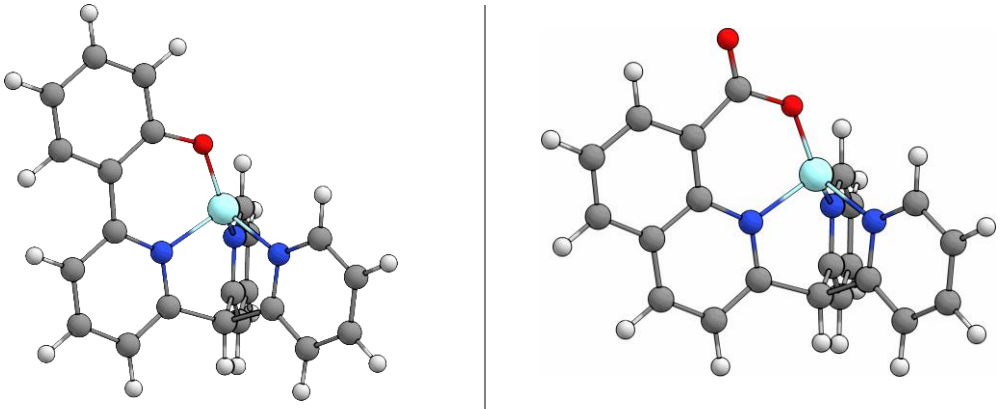

L1chH_Al

L2chH_Al

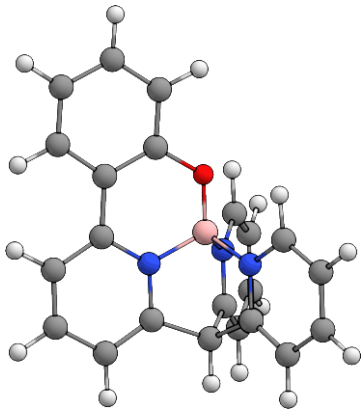

L1chH_B

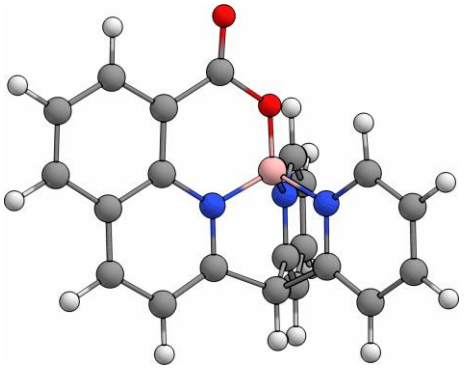

L2chH_B

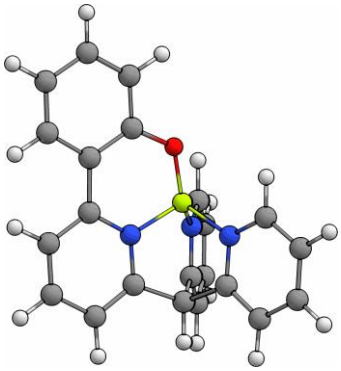

L1chH_Be

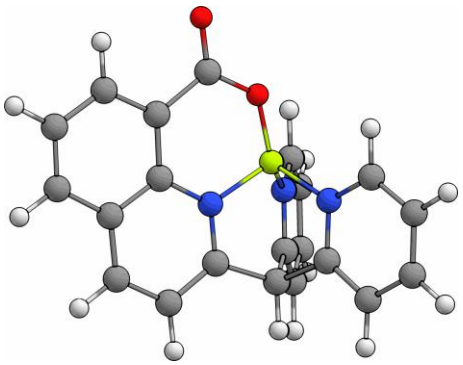

L2chH_Be

Figure 2.8 Aqueous phase geometry optimised complexes **L1** and **L2** formed with the metal cations Al^{3+}, B^{3+}, and Be^{2+}, in their primary motif at B3LYP/6-311++G(d,p).

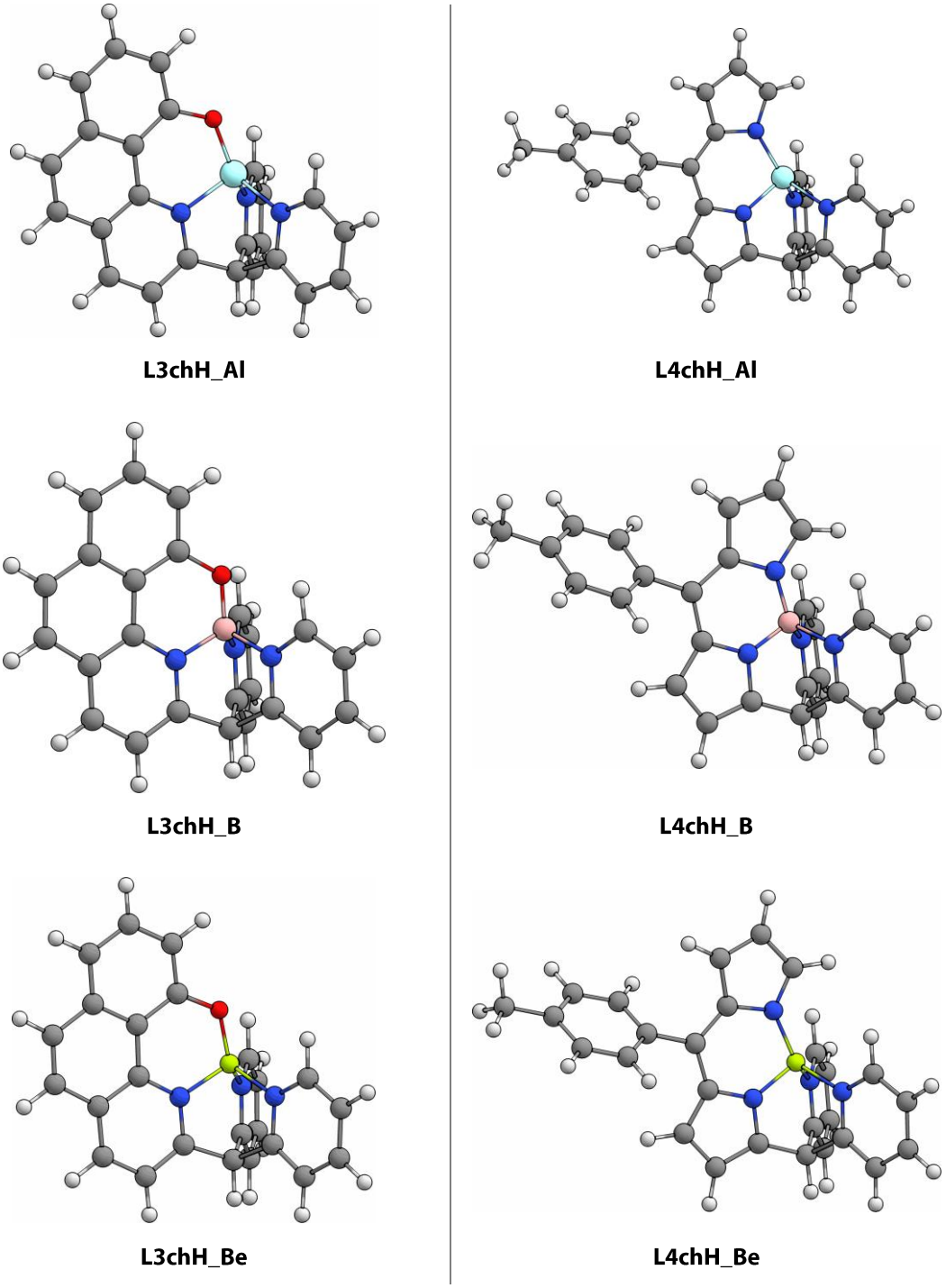

Figure 2.9 Aqueous phase geometry optimised complexes **L3** and **L4** formed with the metal cations Al^{3+}, B^{3+}, and Be^{2+},, in their primary motif at B3LYP/6-311++G(d,p).

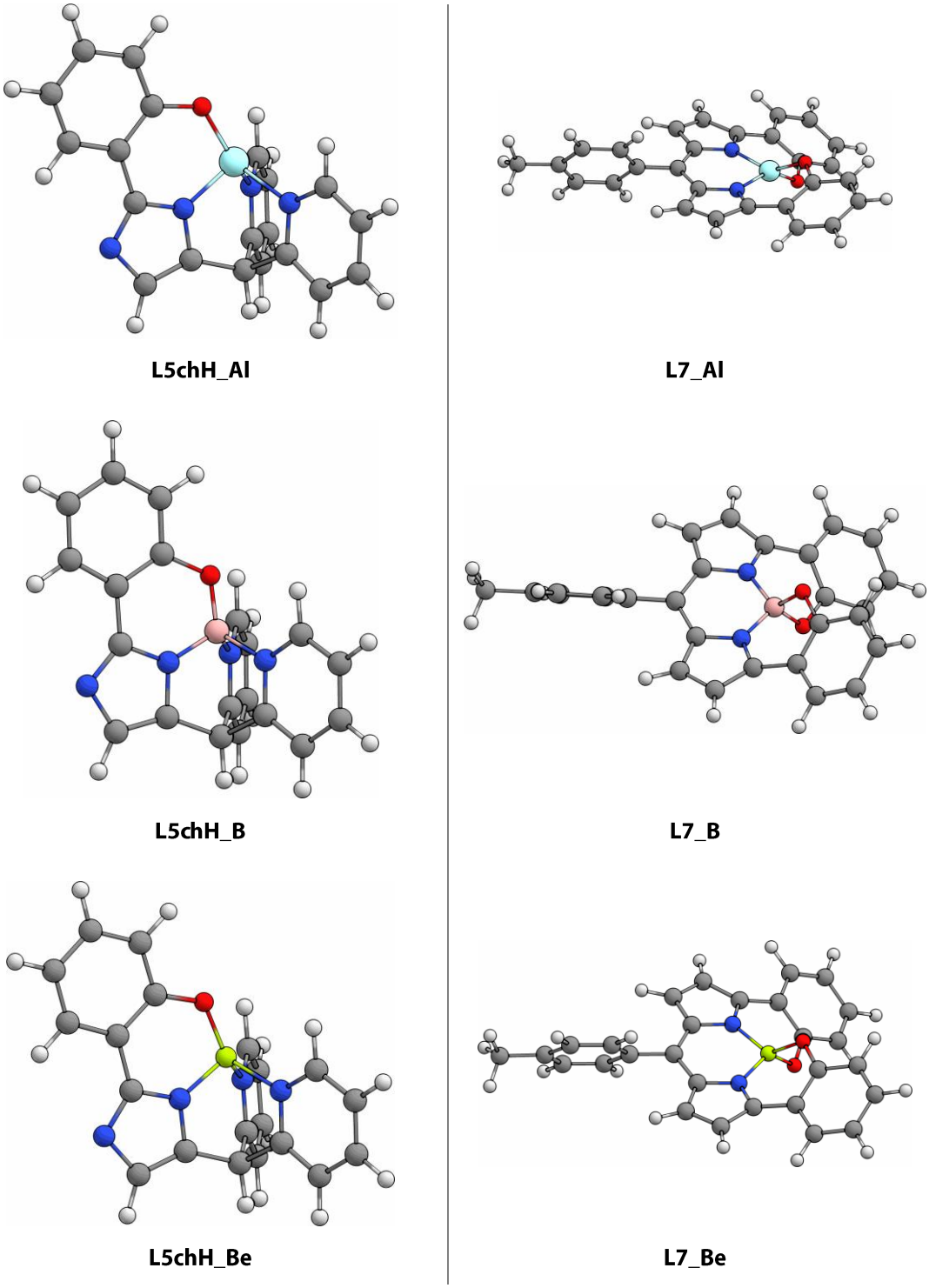

Figure 2.10 Aqueous phase geometry optimised complexes **L5** and **L7** formed with the metal cations Al^{3+}, B^{3+}, and Be^{2+},, in their primary motif at B3LYP/6-311++G(d,p).

Table 2.3 Geometric parameters for **L1chH**.

L1chH				
		Al	**B**	**Be**
Bond /Å	O-M	1.708	1.394	1.530
	N_1-M	1.884	1.554	1.701
	N_2-M	1.918	1.589	1.760
	N_3-M	1.919	1.590	1.760
Angle /°	O-M-N_1	102.0	115.0	109.5
	O-M-N_2	128.4	114.4	121.5
	O-M-N_3	127.2	114.5	121.5
	N_1-M-N_2	97.9	104.5	101.1
	N_1-M-N_3	97.9	104.5	101.1
	N_2-M-N_3	95.9	102.6	98.7
Index	τ_4	0.74	0.93	0.83

Table 2.4 Geometric parameters for **L2chH**.

L2chH				
		Al	**B**	**Be**
Bond /Å	O-M	1.721	1.405	1.547
	N_1-M	1.884	1.551	1.701
	N_2-M	1.917	1.583	1.753
	N_3-M	1.917	1.583	1.753
Angle /°	O-M-N_1	101.7	114.6	109.1
	O-M-N_2	128.1	114.7	122.0
	O-M-N_3	128.1	114.7	122.0
	N_1-M-N_2	97.3	104.2	100.4
	N_1-M-N_3	97.3	104.2	100.4
	N_2-M-N_3	96.1	103.0	99.2
Index	τ_4	0.74	0.93	0.82

Table 2.5 Geometric parameters for **L3chH**.

L3chH				
		Al	**B**	**Be**
Bond /Å	O-M	1.710	1.399	1.535
	N_1-M	1.882	1.553	1.700
	N_2-M	1.920	1.590	1.762
	N_3-M	1.920	1.590	1.761
Angle /°	O-M-N_1	101.8	115.0	109.4
	O-M-N_2	128.1	114.9	122.1
	O-M-N_3	128.1	114.9	122.0
	N_1-M-N_2	97.6	104.0	100.4
	N_1-M-N_3	97.5	104.0	100.5
	N_2-M-N_3	95.7	102.3	98.6
Index	τ_4	0.74	0.92	0.82

Table 2.6 Geometric parameters for **L4chH**.

L4chH				
		Al	**B**	**Be**
Bond /Å	O-M	1.841	1.493	1.664
	N_1-M	1.823	1.499	1.643
	N_2-M	1.943	1.606	1.781
	N_3-M	1.940	1.603	1.779
Angle /°	O-M-N_1	97.3	108.2	102.8
	O-M-N_2	129.1	118.0	124.6
	O-M-N_3	133.2	119.4	127.1
	N_1-M-N_2	97.1	104.3	100.3
	N_1-M-N_3	95.8	103.6	99.5
	N_2-M-N_3	93.2	101.6	97.0
Index	τ_4	0.69	0.87	0.77

Table 2.7 Geometric parameters for **L5chH**.

L5chH				
		Al	**B**	**Be**
Bond /Å	O-M	1.732	1.404	1.555
	N_1-M	1.805	1.480	1.618
	N_2-M	1.951	1.612	1.808
	N_3-M	1.951	1.612	1.808
Angle /°	O-M-N_1	98.5	112.5	105.9
	O-M-N_2	131.6	117.5	126.1
	O-M-N_3	131.8	117.5	126.1
	N_1-M-N_2	95.7	103.7	99.2
	N_1-M-N_3	95.7	103.7	99.2
	N_2-M-N_3	92.1	99.9	94.7
Index	τ_4	0.69	0.89	0.76

Table 2.8 Geometric parameters for **L7**.

L7				
		Al	**B**	**Be**
Bond /Å	O-M	1.875	1.517	1.691
	N_1-M	1.875	1.517	1.691
	N_2-M	1.778	1.481	1.645
	N_3-M	1.778	1.481	1.644
Angle /°	O-M-N_1	93.7	105.6	99.4
	O-M-N_2	93.7	106.2	99.9
	O-M-N_3	145.4	116.0	129.0
	N_1-M-N_2	145.4	116.0	129.0
	N_1-M-N_3	93.7	106.2	99.9
	N_2-M-N_3	99.0	107.1	103.4
Index	τ_4	0.49	0.91	0.72

2.2.3 Binding Energies

An example chemical equation using equations 3 and 4 to solve for binding energy is given below (Figure 2.11). For each ligand, the binding energy towards Al^{3+}, B^{3+}, and Be^{2+} was determined (Table 2.9, Figure 2.12). Each ligand formed stable structures, with the metal cations binding to the ligand through four donor atoms as predicted. The general trend in ligand strength was found to be **L2** < **L4** < **L1** < **L3** < **L5** < **L7**. It was found that the strongest stabilisation energy occurred with the B^{3+} cation. The trend for preferred metal cation for **L1**-**L4** was Al^{3+} < Be^{2+} < B^{3+}, and for **L5** and **L7** it was Be^{2+} < Al^{3+} < B^{3+} (Table 2.9). The binding energy towards Al^{3+} ranged from -279.80 to -675.17 kJ mol^{-1}, Be^{2+} ranged from -318.76 to -523.83 kJ mol^{-1}, and B^{3+} ranged from -673.82 to -1034.71 kJ mol^{-1}. Whilst the binding was always observed to be strongest towards B^{3+}, often the binding energy of Al^{3+} was comparable to that of Be^{2+}. The difference in binding energy between these metals ranged from as low as 8.66 kJ mol^{-1} to moderate differences of 38.96 kJ mol^{-1}. Although in the case of **L7**, the difference was 151.34 kJ mol^{-1}.

$$[L1chH]^- + [Be(H_2O)_4]^{2+} \rightarrow [L1chH\_Be]^+ + 4.H_2O$$

Figure 2.11 The chemical equation for the calculation of the binding energy (Δ*G*) of the deprotonated ligand L1chH with the tetra-aqua beryllium(II) ion.

Table 2.9 Calculated binding energies of complexes in their primary motif.

	ΔG_{aq} / kJ mol^{-1}		
Ligand	**Al**	**B**	**Be**
1	-326.85	-734.07	-352.15
2	-279.80	-673.82	-318.76
3	-360.83	-762.21	-382.89
4	-331.50	-733.17	-340.16
5	-424.99	-831.82	-390.51
7	-675.17	-1034.71	-523.83

Notably the trend for binding strength, although not perfect, does show some similarity to the trend in pre-organisation. **L1**, **L2** and **L4** are in the lower half, and **L3**, **L5**, and **L7** in the higher half. This was expected to a small extent, as the entropic factor in chelation will result in easier binding modes when a cavity is pre-arranged. But it is clear that the functional groups and structure play the largest role in determining their binding strengths.

2.2.4 Comparison

The binding energies for each complex have been graphically depicted below (Figure 2.12). Each ligand binds most strongly to B^{3+}. Previously used binders of beryllium typically consist of two oxygen donors and two nitrogen donors. The mixed donor complexes, in particular **L7**, have high binding strengths. This is both advantageous, and disadvantageous, as the ligands can adopt strong preferences for other metals over beryllium. Although ligands **L1**, **L2**, **L3**, and **L4** bind boron more strongly than beryllium, they retain high binding strengths, and bind more strongly to the Be^{2+} cation over the Al^{3+} cation. Of these, the best binder of Be^{2+} is **L3**. The chelator bite size correlates strongly with the observed trend in metal cation preference. Altering this through modifications to these motifs may result in stronger binding to Be^{2+} relative to the others (see Chapter 5).

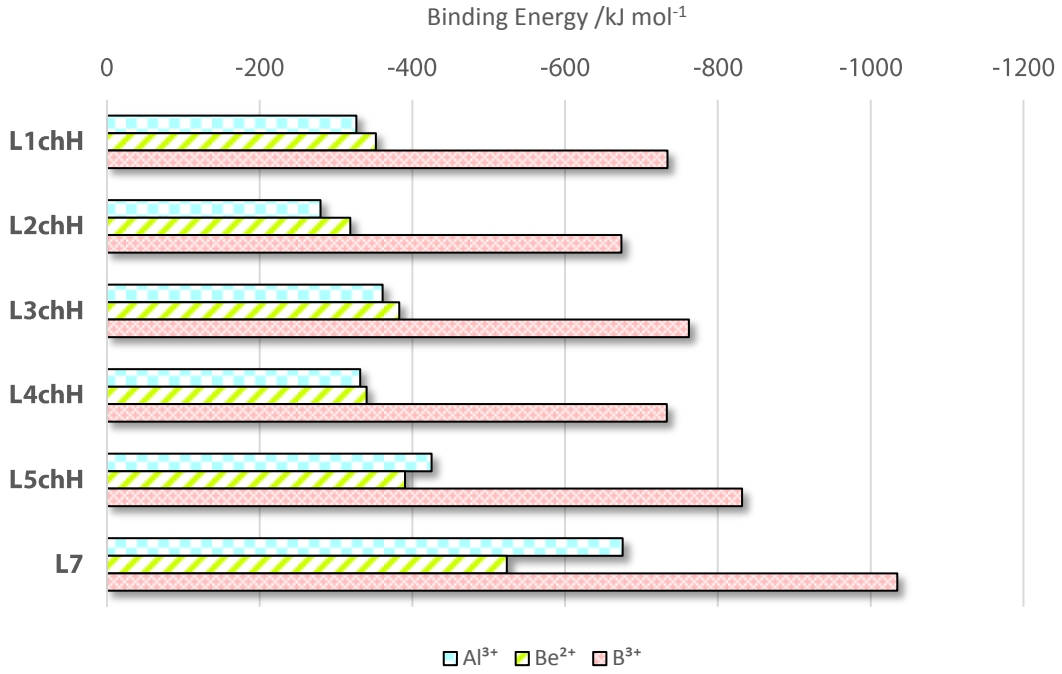

Figure 2.12 Binding energies of examined ligands in the aqueous phase.

No hydrogen bonds are present in any of the complexes. It is predicted that an addition of one or more of these will have a significant effect on cavity size and conformation, therefore altering binding strengths and preference. Computational work on hydrogen bond enabled buttresses will be discussed in Chapter 5.

2.3 Apex Groups

The next variable in the structure to be investigated was the apex group of ligands **L1**-**L5** that connect the two pyridyl arms to the rest of the molecule. This takes up the rear position of the chelating site, so this group may be optimised for its angles in the multiple 6-membered rings it is a part of. In comparison to the **ch** apex already studied, two further functional groups were chosen for analysis. These are a tertiary alcohol and a tertiary amine (Figure 2.13). One additional reason for their investigation is that they have the advantage of being synthetically easier targets. However, they each have their own respective disadvantages. The alcohol of the **coh** apex may interfere in complexation, and

the lone pair of electrons of the **n** apex may result in unfavourable pre-organisation or apex geometry.

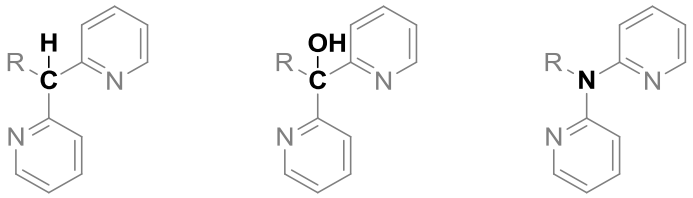

ch **coh** **n**

Figure 2.13 Apex groups investigated.

2.3.1 Ligand Geometries

The new apex groups have caused both significant and trivial alteration to the ligand geometries (Figures 2.14-2.15). The tertiary alcohol apex in ligands **L2** and **L3** have disrupted some of the pre-organisation previously observed. This is due to the possibly of new intramolecular hydrogen bonding with the proton of the alcohol. **L4** and **L5** both have a net reduction in pre-organisation due to the alcohol proton forming a hydrogen bond to a neighbouring pyridyl or imidazole nitrogen (1.839 Å and 1.711 Å respectively). It is expected that this will cause reduced binding energies to each of Al^{3+}, B^{3+}, and Be^{2+}. **L1** is an exception, in which its hydrogen bond of 1.868 Å has resulted in an increase in pre-organisation, with three of its donor atoms orientated in a preferred manner. However, the complexation process will have to overcome the energy of this new hydrogen bond, which may negate any advantage gained by its overall structure.

Dissimilarly, the ligand scaffolds did not alter much when the apex was replaced with a tertiary nitrogen group. The pyridyl arms in each case were observed to tilt further away from a binding cavity. This is seen to the greatest extent in the geometry change between **L4chH** (Figure 2.7) and **L4nH**, in which its pyridyl rings are pointed away from the primary backbone at more dihedral angles of 42.7° and 139.6°.

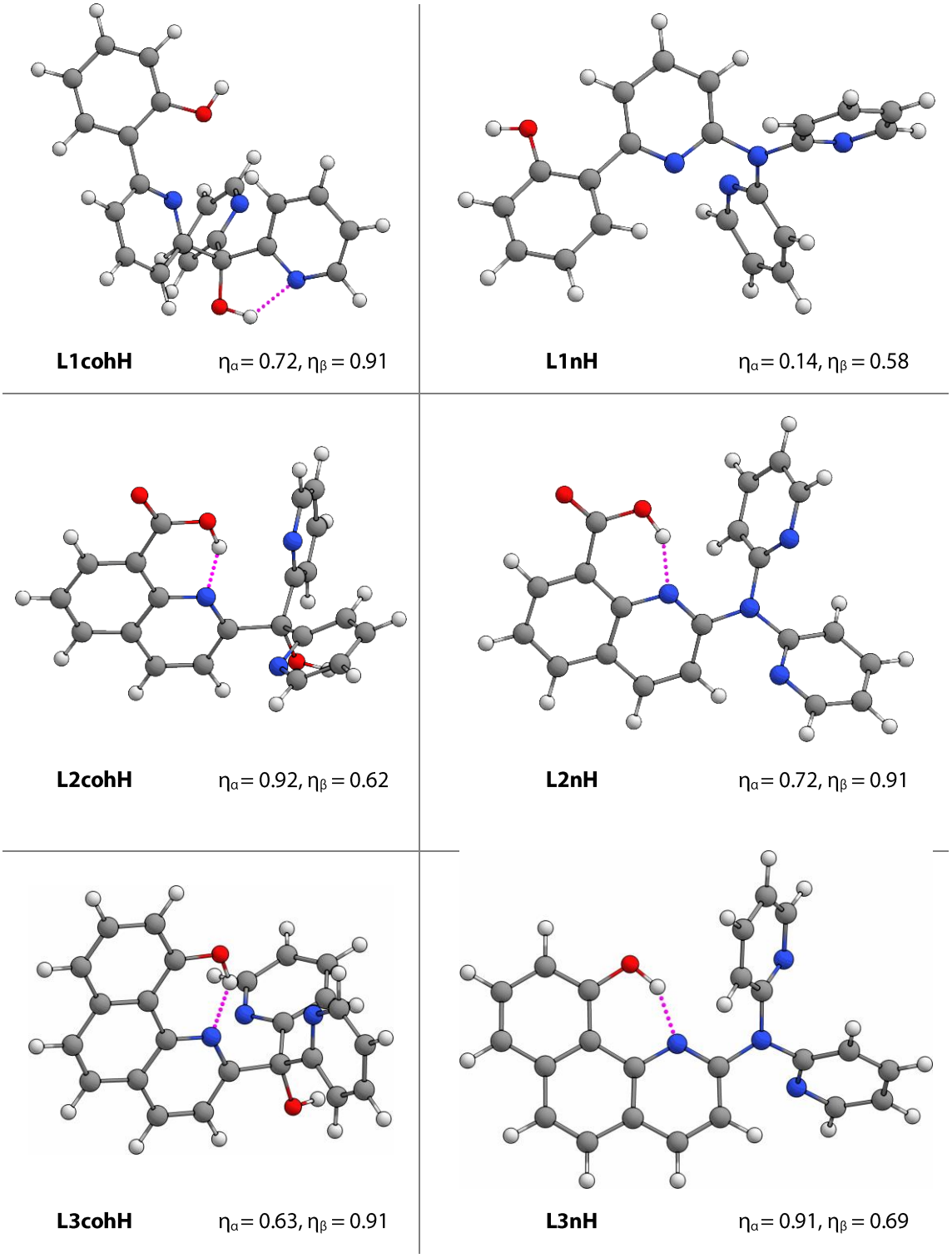

Figure 2.14 Aqueous phase geometry optimised ligands **L1**-**L3** with **oh** and **n** apex at B3LYP/6-311++G(d,p).

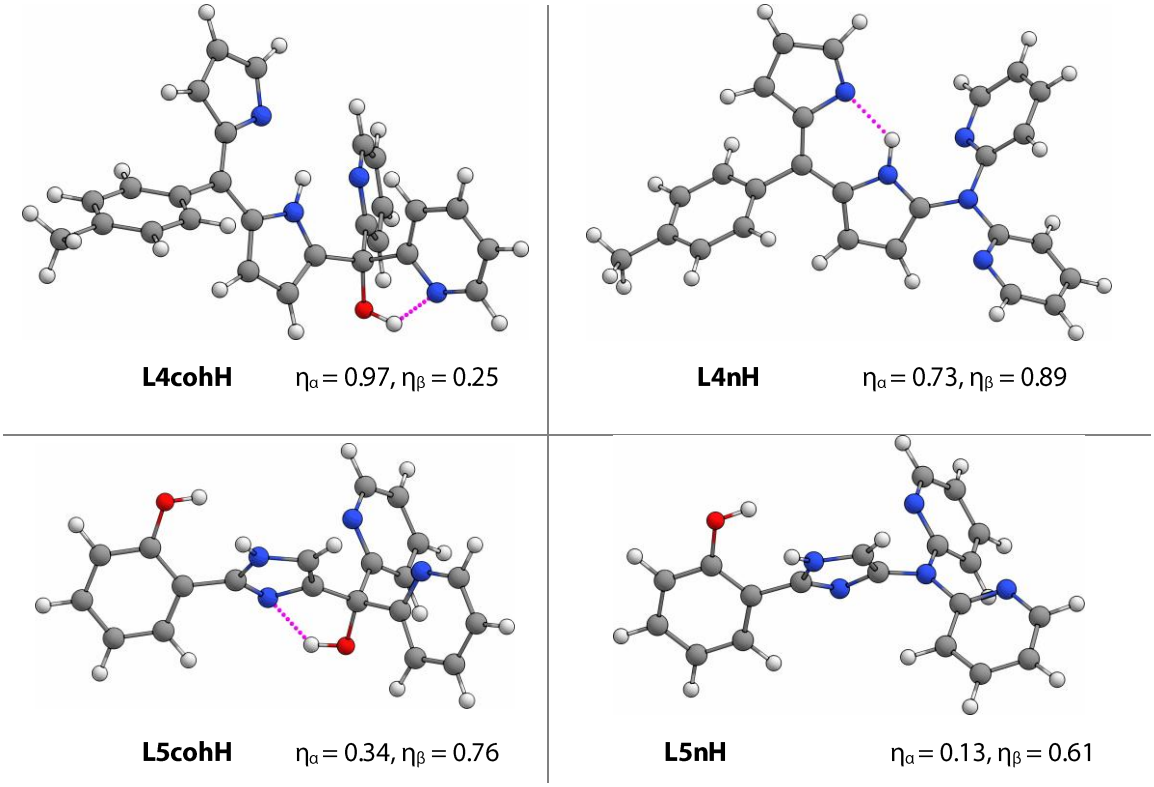

Figure 2.15 Aqueous phase geometry optimised ligands **L4**-**L5**, with **oh** and **n** apex at B3LYP/6-311++G(d,p).

2.3.2 Complex Geometries

The geometric parameter data for the new apex ligands with the B^{3+}, Be^{2+}, and Al^{3+} cations are listed in Tables 2.11-2.20, but only the structures for **L1** and **L3** with the tertiary alcohol and nitrogen apexes have been presented, as these illustrate the typical geometries found (Figures 2.16-2.17). The bond lengths and angles of the binding site across each apex differ by about 0.02 Å and 2.3°. The geometry index (τ_4) of each is slightly higher for the **ch** and **coh** apexes compared with the **n** apex. This is observed most easily in the aluminium complexes, where the metal adopts a trigonal pyramidal-like conformation. These differences caused by the tuning of the ligand structures could lead to significantly differing binding strength values.

L3chH and **L3cohH**, when compared to their **n** apex analogue, have the closest to ideal tetrahedral values (Table 2.10). Their O···Be bond length is comparable (1.530 and 1.532

Å respectively). The N···Be bond lengths are shorter for **L1cohH_Be** but result in angles that are even further away from ideal.

Table 2.10 Geometric parameters for **L1chH_Be**, **L1cohH_Be**, and **L1nH_Be**.

		L1chH_Be	**L1cohH_Be**	**L1nH_Be**
Bond /Å	O-M	1.530	1.532	1.534
	N_1-M	1.701	1.702	1.700
	N_2-M	1.760	1.752	1.751
	N_3-M	1.760	1.752	1.774
Angle /°	O-M-N_1	109.5	109.7	108.5
	O-M-N_2	121.5	122.1	123.8
	O-M-N_3	121.5	122.0	123.7
	N_1-M-N_2	101.1	100.3	99.3
	N_1-M-N_3	101.1	100.4	99.4
	N_2-M-N_3	98.7	98.5	97.3
Geometry Index	τ_4	0.83	0.82	0.80

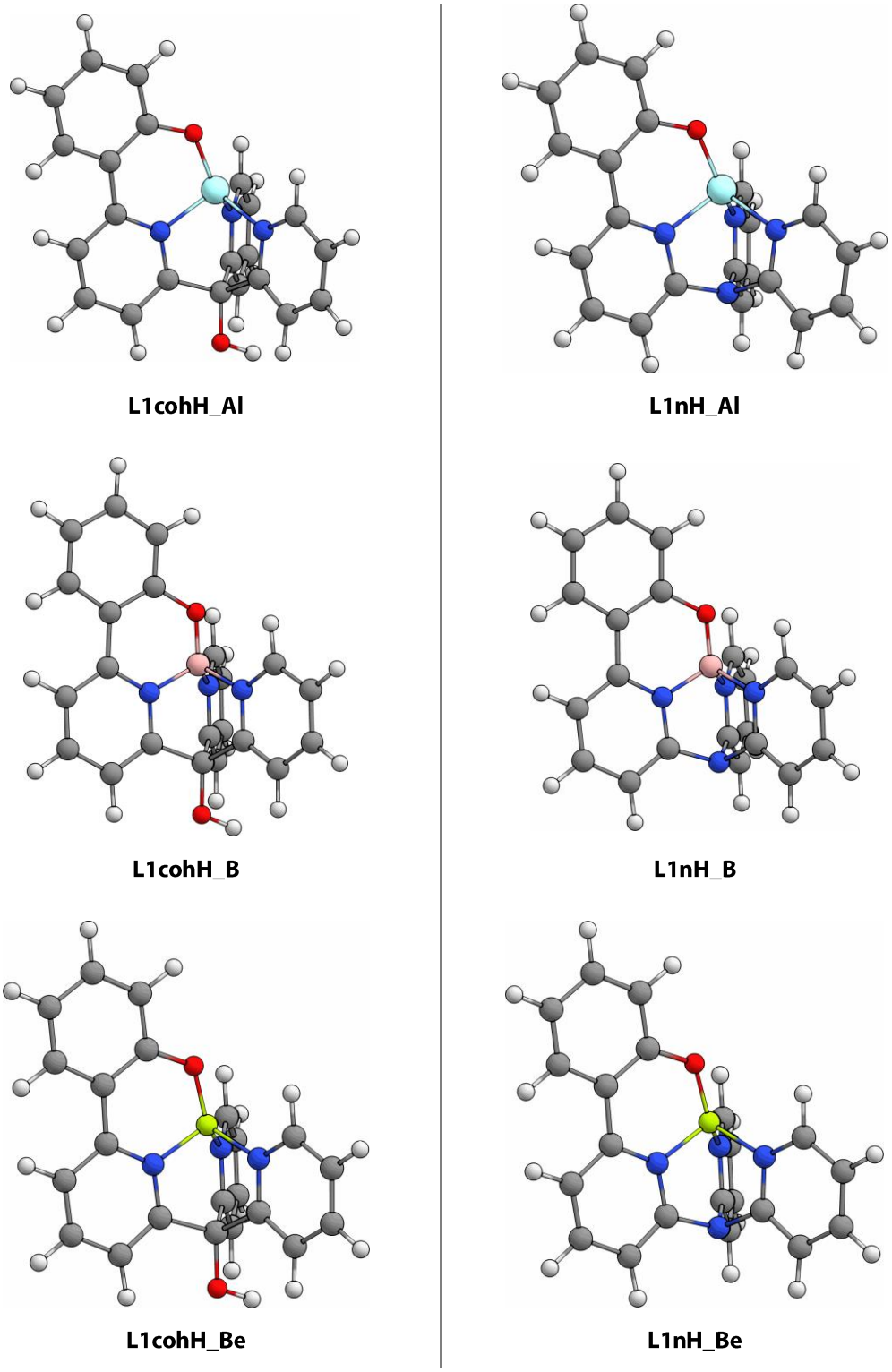

Figure 2.16 Aqueous phase geometry optimised complex **L1** formed with the metal cations Al^{3+}, B^{3+}, and Be^{2+}, with **coh** and **n** apexes at B3LYP/6-311++G(d,p).

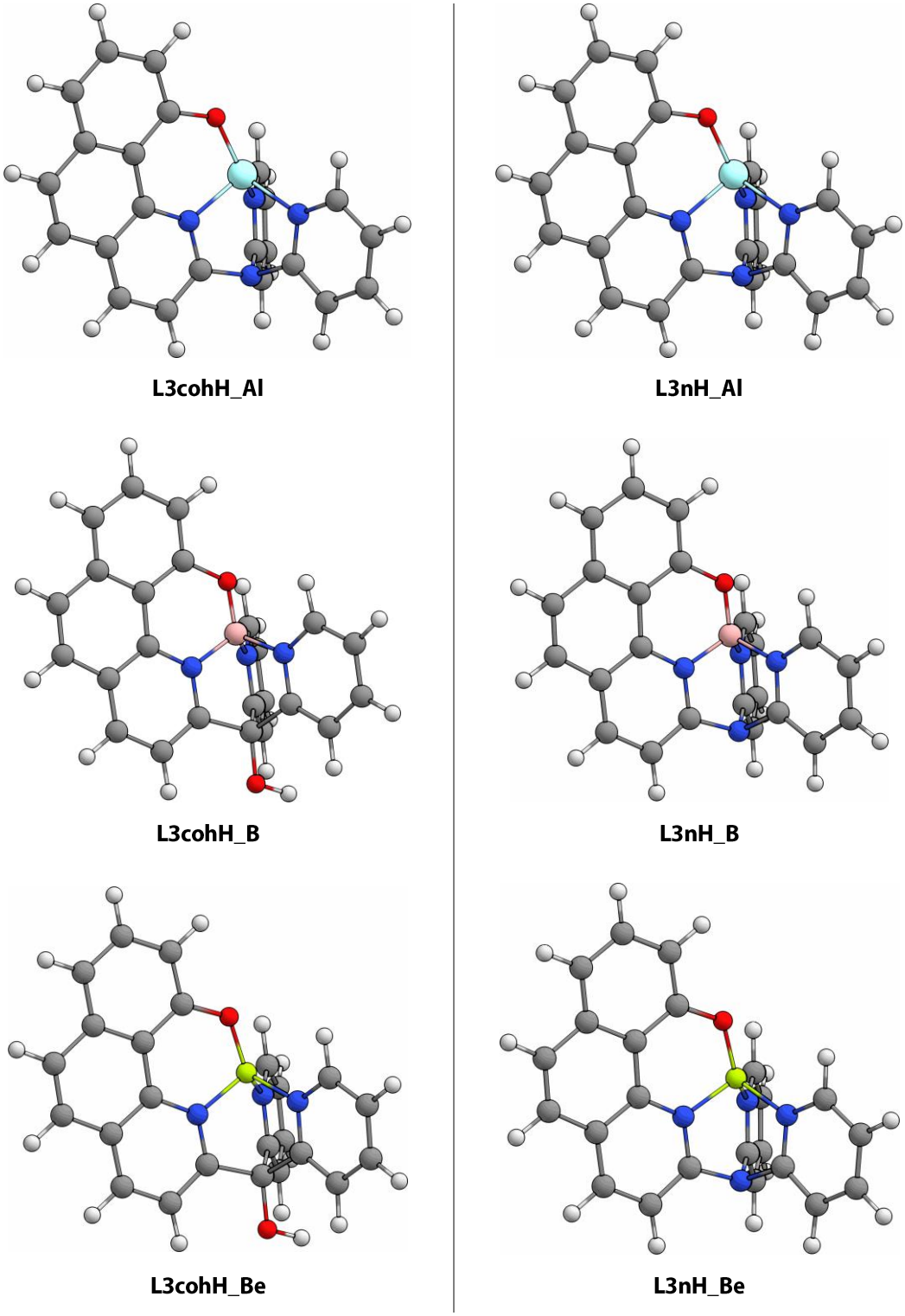

Figure 2.17 Aqueous phase geometry optimised complex **L3** formed with the metal cations Al^{3+}, B^{3+}, and Be^{2+}, with **coh** and **n** apexes at B3LYP/6-311++G(d,p).

Table 2.11 Geometric parameters for **L1cohH**.

L1cohH				
		Al	**B**	**Be**
Bond /Å	O-M	1.704	1.394	1.527
	N_1-M	1.886	1.555	1.703
	N_2-M	1.911	1.586	1.750
	N_3-M	1.911	1.586	1.750
Angle /°	O-M-N_1	102.6	115.0	109.9
	O-M-N_2	127.8	114.5	121.5
	O-M-N_3	128.2	114.5	121.5
	N_1-M-N_2	97.6	104.3	100.9
	N_1-M-N_3	97.5	104.4	100.8
	N_2-M-N_3	95.3	102.7	98.7
Index	τ_4	0.74	0.93	0.83

Table 2.12 Geometric parameters for **L1nH**.

L1nH				
		Al	**B**	**Be**
Bond /Å	O-M	1.710	1.390	1.527
	N_1-M	1.888	1.552	1.702
	N_2-M	1.930	1.594	1.771
	N_3-M	1.931	1.593	1.770
Angle /°	O-M-N_1	100.3	114.8	108.7
	O-M-N_2	129.0	115.7	123.0
	O-M-N_3	128.2	115.6	123.0
	N_1-M-N_2	97.6	103.6	100.0
	N_1-M-N_3	97.7	103.7	100.0
	N_2-M-N_3	95.6	101.6	97.8
Index	τ_4	0.73	0.91	0.81

Table 2.13 Geometric parameters for **L2cohH**.

L2cohH				
		Al	**B**	**Be**
Bond /Å	O-M	1.718	1.404	1.544
	N_1-M	1.886	1.552	1.695
	N_2-M	1.907	1.579	1.753
	N_3-M	1.909	1.580	1.743
Angle /°	O-M-N_1	102.4	114.7	109.6
	O-M-N_2	128.3	114.7	122.1
	O-M-N_3	128.1	114.9	121.6
	N_1-M-N_2	96.9	104.1	100.1
	N_1-M-N_3	96.8	104.0	100.5
	N_2-M-N_3	95.9	103.1	99.1
Index	τ_4	0.73	0.93	0.82

Table 2.14 Geometric parameters for **L2nH**.

L2nH				
		Al	**B**	**Be**
Bond /Å	O-M	1.723	1.401	1.545
	N_1-M	1.887	1.549	1.700
	N_2-M	1.928	1.586	1.765
	N_3-M	1.928	1.587	1.765
Angle /°	O-M-N_1	100.0	114.4	108.2
	O-M-N_2	129.2	116.0	123.6
	O-M-N_3	129.1	116.0	123.5
	N_1-M-N_2	96.8	103.4	99.3
	N_1-M-N_3	96.9	103.2	99.2
	N_2-M-N_3	95.4	102.0	98.1
Index	τ_4	0.72	0.91	0.80

Table 2.15 Geometric parameters for **L3cohH**.

L3cohH				
		Al	**B**	**Be**
Bond /Å	O-M	1.706	1.397	1.532
	N_1-M	1.885	1.554	1.702
	N_2-M	1.911	1.587	1.752
	N_3-M	1.910	1.587	1.752
Angle /°	O-M-N_1	102.5	115.1	109.7
	O-M-N_2	128.2	115.0	122.1
	O-M-N_3	128.2	115.0	122.0
	N_1-M-N_2	97.2	103.9	100.3
	N_1-M-N_3	97.2	103.9	100.4
	N_2-M-N_3	95.4	102.4	98.5
Index	τ_4	0.73	0.92	0.82

Table 2.16 Geometric parameters for **L3nH**.

L3nH				
		Al	**B**	**Be**
Bond /Å	O-M	1.713	1.395	1.534
	N_1-M	1.884	1.550	1.700
	N_2-M	1.930	1.594	1.751
	N_3-M	1.932	1.594	1.774
Angle /°	O-M-N_1	100.3	114.8	108.5
	O-M-N_2	129.1	116.2	123.8
	O-M-N_3	128.9	116.2	123.7
	N_1-M-N_2	97.4	103.2	99.3
	N_1-M-N_3	97.0	103.2	99.4
	N_2-M-N_3	95.1	101.4	97.3
Index	τ_4	0.72	0.91	0.80

Table 2.17 Geometric parameters for **L4cohH**.

L4cohH				
		Al	**B**	**Be**
Bond /Å	O-M	1.838	1.493	1.665
	N_1-M	1.826	1.500	1.646
	N_2-M	1.937	1.603	1.774
	N_3-M	1.935	1.601	1.774
Angle /°	O-M-N_1	97.7	108.3	103.0
	O-M-N_2	129.0	118.0	124.0
	O-M-N_3	133.9	119.4	128.0
	N_1-M-N_2	96.6	104.1	100.0
	N_1-M-N_3	95.4	103.3	99.5
	N_2-M-N_3	92.8	101.8	96.7
Index	τ_4	0.69	0.87	0.77

Table 2.18 Geometric parameters for **L4nH**.

L4nH				
		Al	**B**	**Be**
Bond /Å	O-M	1.844	1.491	1.666
	N_1-M	1.824	1.496	1.642
	N_2-M	1.952	1.610	1.795
	N_3-M	1.948	1.605	1.792
Angle /°	O-M-N_1	96.0	107.8	101.9
	O-M-N_2	129.8	119.0	125.8
	O-M-N_3	134.5	121.0	129.2
	N_1-M-N_2	96.9	103.6	99.3
	N_1-M-N_3	95.0	102.7	98.3
	N_2-M-N_3	92.2	100.4	95.5
Index	τ_4	0.68	0.85	0.74

Table 2.19 Geometric parameters for **L5cohH**.

L5cohH				
		Al	**B**	**Be**
Bond /Å	O-M	1.728	1.403	1.553
	N_1-M	1.807	1.481	1.619
	N_2-M	1.944	1.610	1.799
	N_3-M	1.944	1.610	1.799
Angle /°	O-M-N_1	98.9	112.6	106.1
	O-M-N_2	131.9	117.5	126.1
	O-M-N_3	131.9	117.5	126.1
	N_1-M-N_2	95.4	103.6	99.1
	N_1-M-N_3	95.4	103.6	99.1
	N_2-M-N_3	91.7	99.9	94.6
Index	τ_4	0.68	0.89	0.76

Table 2.20 Geometric parameters for **L5nH**.

L5nH				
		Al	**B**	**Be**
Bond /Å	O-M	1.733	1.400	1.554
	N_1-M	1.804	1.476	1.615
	N_2-M	1.960	1.620	1.824
	N_3-M	1.960	1.620	1.824
Angle /°	O-M-N_1	97.1	112.1	105.0
	O-M-N_2	133.0	119.1	128.1
	O-M-N_3	132.9	119.1	128.1
	N_1-M-N_2	94.9	102.7	97.9
	N_1-M-N_3	94.9	102.7	97.9
	N_2-M-N_3	90.7	98.7	93.0
Index	τ_4	0.67	0.86	0.74

2.3.3 Apex Effect on Binding Energies

As before, the binding energy for each ligand with each of the three metals under examination were calculated (Table 2.21 and graphically in Figure 2.18). It remains the case that each ligand has formed the strongest complex with B^{3+}. In fact, the trend in binding energies has not changed, beyond lowering by a small amount in every case. The alkyl group offers the highest binding strengths, giving an apex strength trend of **n** < **coh** < **ch**. A small deviation from the general observations is found for **L1**. The difference in binding energy between **L1chH** and **L1cohH** is small, at 6.73 kJ mol^{-1}. This is attributed to the improvement in pre-organisation with the alcohol apex for this ligand.

Table 2.21 Calculated binding energies of complexes with each apex group.

		ΔG_{aq} / kJ mol^{-1}		
Ligand	**Apex**	**Al**	**B**	**Be**
1	**ch**	-326.85	-734.07	-352.15
	coh	-308.79	-725.72	-345.42
	n	-265.66	-653.54	-290.51
2	**ch**	-279.80	-673.82	-318.76
	coh	-241.77	-644.37	-294.08
	n	-192.32	-566.74	-233.06
3	**ch**	-360.83	-762.21	-382.89
	coh	-318.94	-729.03	-354.38
	n	-287.47	-669.95	-312.01
4	**ch**	-331.50	-733.17	-340.16
	coh	-298.91	-706.79	-318.92
	n	-241.72	-630.71	-261.84
5	**ch**	-424.99	-831.82	-390.51
	coh	-397.50	-811.69	-374.67
	n	-340.59	-732.81	-313.61

2.3.4 Comparison

The binding energy graph below shows the strength of each apex (Figure 2.18). It is clear that a change in the apex group has not altered any of the binding modes or trends. It is the case that the strongest binding ligands have an alkyl apex. The synthetic target will therefore seek to make ligands with the alkyl apex.

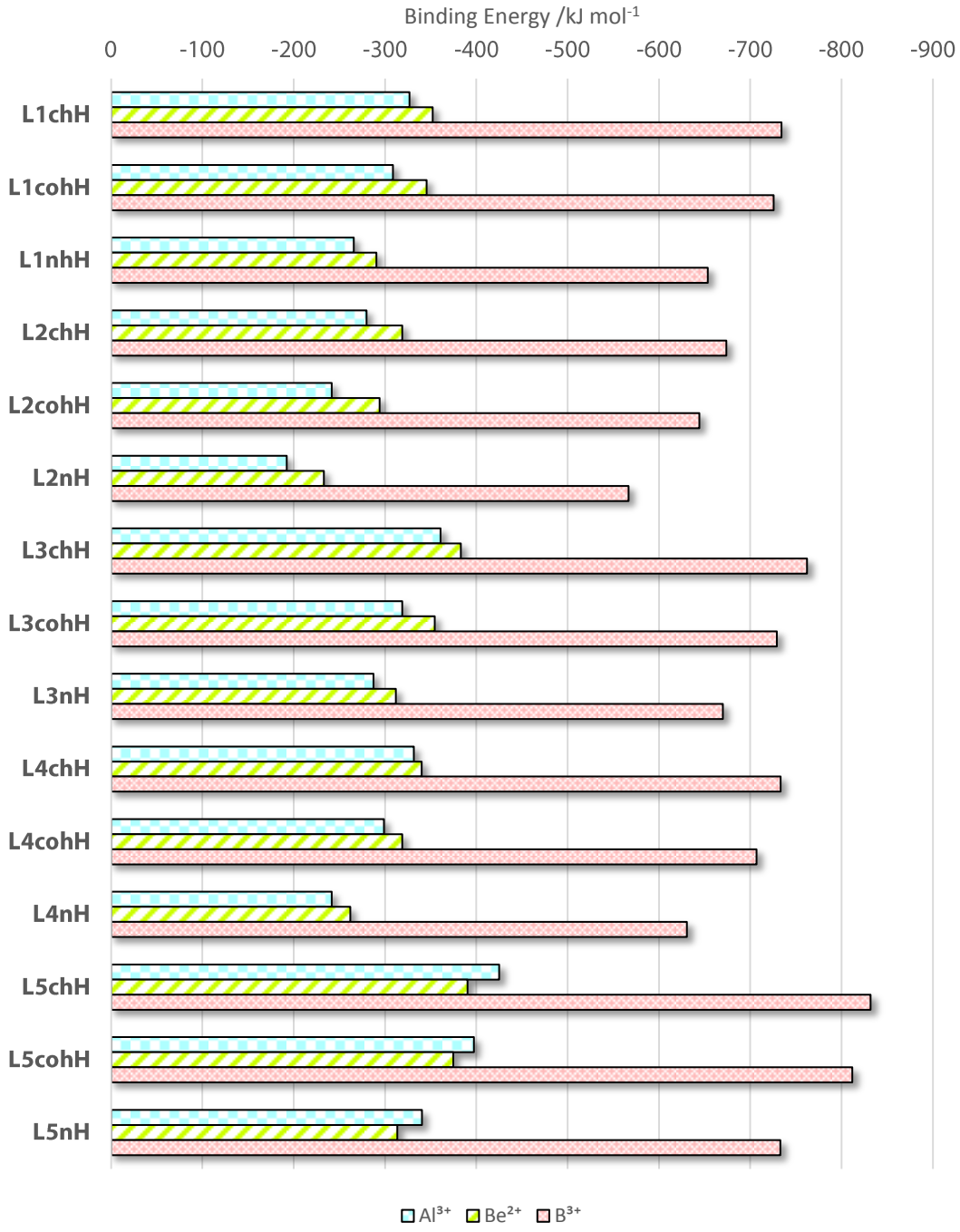

Figure 2.18 Binding energies of the examined ligands with each apex type.

2.4 Summary

Chapter 2 has discussed an investigation of DFT calculations on **L1**-**L5**, and **L7** using the B3LYP method, 6-211++G(d,p) basis set, and IEF-PCM solvation model. They were

tested for their binding capacity to the cations Al^{3+}, B^{3+}, and Be^{2+}. It was found that they all bound to the B^{3+} cation the strongest, and towards the others their trends differed based on ligand motif. **L1**-**L4** had the trend $B^{3+} > Be^{2+} > Al^{3+}$, and **L5**, **L7** had the trend $B^{3+} > Al^{3+} > Be^{2+}$. The strongest of these was **L7**, which bound extremely strongly to B^{3+}, and forms seesaw-like geometries. This is not ideal, as through additional solvation, 5- and 6-coordinate complexes are likely to form, which will further hamper the ability of **L7** to bind to Be^{2+}. **L3** had the highest relative binding energy for Be^{2+} over that of the other motifs.

A further study was conducted to explore the influence of the apex group ion geometry and binding strength. The general binding trends remained the same in each case, although the relative strength was altered, with decreasing binding strengths in the order **ch** > **coh** > **n**.

This study identified that of this series of ligands, the most suitable non-buttressed ligand for beryllium encapsulation is **L3chH** (Figure 2.19). Modifying the apex group does not result in huge changes in the binding energies. The synthetic strategies therefore are not restricted to any one apex, which allows more freedom in ligand choice. However, it is the **ch** apex that should be targeted by any synthetic studies if possible.

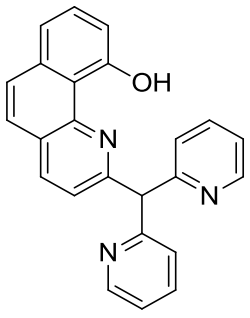

L3chH

Figure 2.19 L3chH was identified as the most suitable non-buttressed binder of the Be^{2+} cation.

Chapter 3: Synthesis of Non-buttressed Ligands

"If you perceive that there are four possible ways in which a procedure can go wrong, and circumvent these, then a fifth way, unprepared for, will promptly develop."

– Murphy's Law

3.1 Introduction to Mixed Pyridine-Phenol Ligands

This chapter will discuss tetra-coordinate ligands capable of providing a tight binding cavity to small hard cations, with the hope that they will bind selectively and strongly to Be^{2+}. Ligands of this scaffold type will provide a tetradentate binding pocket with a tetrahedral arrangement of donor atoms, whilst retaining a limited flexibility due to its pyridyl structure. The motif for **Ligand 1** consists of a phenol-pyridine backbone connected to two pyridine moieties via an apex methylene, tertiary amine, or tertiary alcohol (Figure 3.1). It is thought that Be^{2+} will first associate to the hard phenol oxygen with a strong bond, followed by binding through the three pyridyl nitrogens, fully encapsulating the cation.

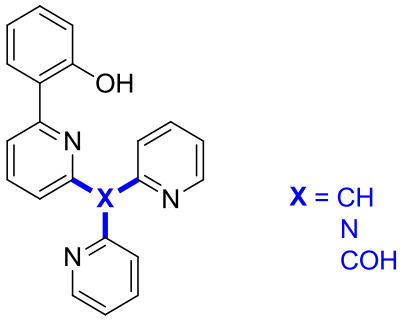

L1xH

Figure 3.1 Ligand type 1.

This type of ligand is relatively unexplored in all areas of chemistry. Although chelators do commonly consist of phenol and/or pyridine units, such as bipyridine, quinoline, and

catechol, it is rare to find a motif that contains an apex carbon or nitrogen that allows for a tetrahedral shaped cavity.[100] Pyridine and phenol-type ligands form complexes with most transition metal ions. These often have distinctive optical properties and are studied for their fluorescence,[101] supramolecular chemistry,[102] and catalysis.[103] New research that involves this more complicated system may yield interesting results.

There are only two ligands in the literature that use this tetra-coordinate motif. The first was synthesised by Shaffer *et al.*, a previous member of the Plieger group (Figure 3.2, left).[52] This molecule could potentially bind Be^{2+} through its three pyridyl N atoms and its phenolic oxygen, providing a tetrahedral cavity. It was designed for selectively chelating beryllium, but this work was not carried out. The other ligand was synthesised by Stoessel *et al.* as work towards novel OLEDs (Figure 3.2, right).[85] A Cu^{+} complex was made of it, demonstrating its binding ability, but there have been no subsequent reports.

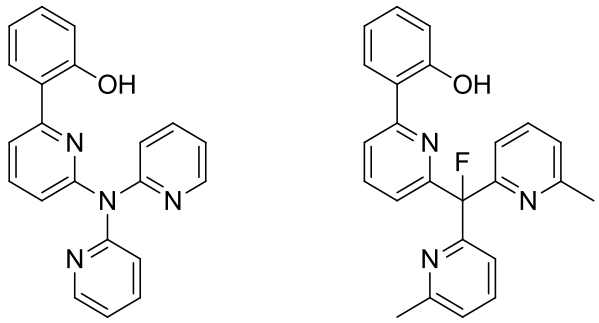

L1nH **L1cfCH$_3$**

Figure 3.2 Related tetra-coordinate ligands.

Three similar ligands can be found that, although not adequate for binding beryllium, do possess certain traits that identify them as useful molecules in both chemistry and biology (Figure 3.3).[104] This suggests that our ligand motifs, as they are similar, are rational targets that do have potential real-world use. The first ligand (left) comes from a patent that discusses polycyclic pyridine for use as potassium ion channel modulators in therapeutic and diagnostic applications.[104b] This compound will be unsuitable in binding Be^{2+} as it

would not provide an optimal tetrahedral geometry for coordination, as well as having no ionisable donor atoms. The next ligand (middle) consists of two 2-(2-pyridyl)phenol units, joined by a bridging gem-dimethyl methylene.[104c] This ligand was found to bind to Pt^{2+} and Zn^{2+}. Although perhaps more useful as it contains two phenol groups, its wider chelating bite angle allows for increased binding affinity towards larger metals than Be^{2+}. The third related ligand (right) was complexed with Fe^{3+} in a study on how a secondary coordination sphere influences its reactivity.[104d] As it provides 6 donor atoms, this is also not appropriate for ideal binding of Be^{2+}.

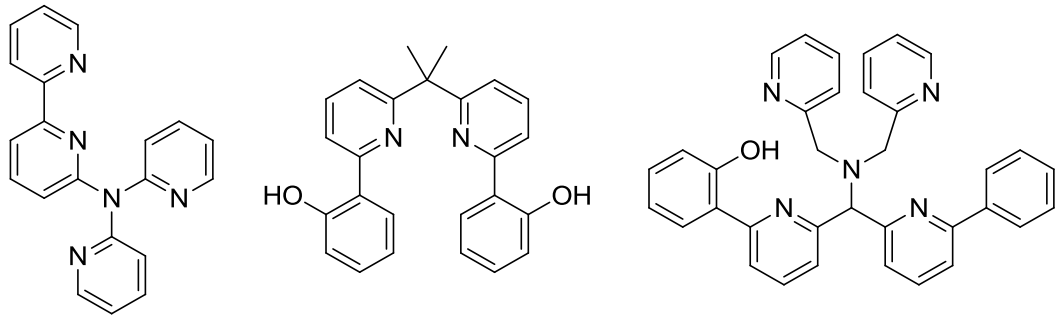

Figure 3.3 Related ligands.

Although the **L1** motif has similarities to these molecules, it is expected to be a much better candidate for binding metal cations. And further, for all the previous reasons discussed, is also likely to selectively bind smaller cations like Be^{2+} over many others. Therefore, this ligand motif is the focus of this thesis.

3.2 L1cohH

3.2.1 First Route towards L1cohH

Our initial target was the ligand with an apex alcohol group (bolded in Figure 3.4). **L1cohH** as it was thought to be the most readily synthesised. The retrosynthetic plan developed gave this ligand in the fewest synthetic steps compared to the other variants. Potentially the alcohol could be removed later if required, and additional functionality

could be added elsewhere to provide tuning to specific metals as well as increased solubility. Two primary routes were identified towards the synthesis of **L1cohH** and **L1chH**. The first involved sequentially building the molecule ring by ring. The second more cogent route involved synthesising the phenol-pyridine backbone, then adding the dipyridyl methylene alcohol. Both schemes had previously been employed by Stoessel and Shaffer to varying degrees of success for similar ligand designs. Adapting the chemistry of Stoessel would involve well-known reactions that were relatively simple, so this became the starting point.

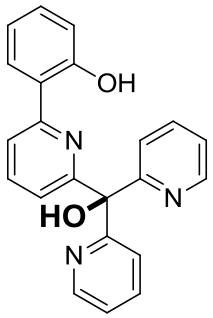

301

Figure 3.4 L1cohH.

The retrosynthetic analysis of **301** first began with disconnection of the phenol to give (2-hydroxyphenyl)boronic acid **302** and (6-bromo-2-pyridyl)-bis-(2-pyridyl)methanol **303** (Scheme 3.1). The forward reaction can be completed with a powerful Suzuki coupling. The boronic acid **302** was commercially available.

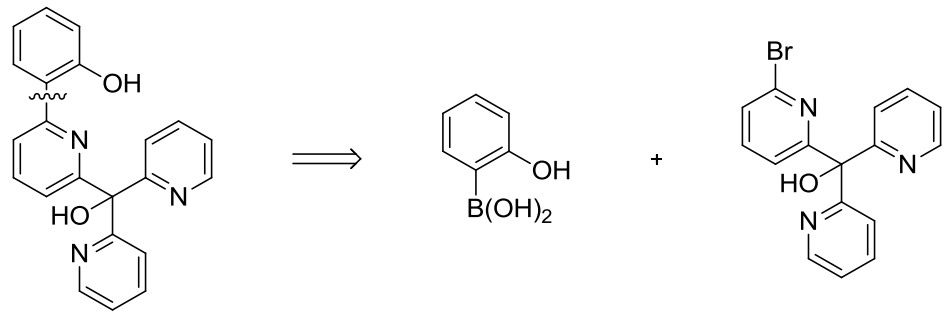

L1cohH, 301 **302** **303**

Scheme 3.1 Disconnection of **301**.

Compound **303**, which is known,[105] can undergo a further disconnection to provide two simple molecules, 2,6-dibromopyridine **304** and dipyridyl ketone **305**, which are both commercially available (Scheme 3.2).

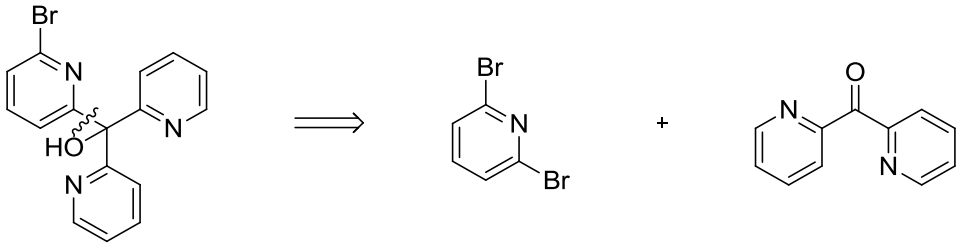

303 **304** **305**

Scheme 3.2 Disconnection and functional group interconversion of **303**.

The overall route would require only two synthetic steps from simple starting materials. Although it was commercially available, it was more expedient to synthesise dipyridyl ketone. Its synthesis was derived from a literature procedure, but with the addition of an atmosphere of argon in order to prevent undesirable side-reactions to provide a cleaner work-up (Scheme 3.3). This reaction proceeded cleanly to give **305** in a 97% yield. Its synthesis and purification was confirmed by comparison of the ^{1}H NMR with literature values.[106]

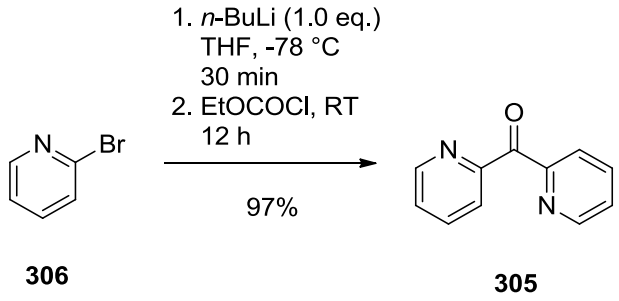

Scheme 3.3 Synthesis of dipyridyl ketone **305**.

After the synthesis of dipyridyl ketone **305**, it was reacted with 2,6-dibromopyridine (Scheme 3.4). This successfully gave the tri-pyridyl bromo **303** in a modest yield (50%) but good purity. The ^{1}H NMR agreed with literature values, confirming its synthesis.[106] The unique advantage to this route compared to that of Stoessel's[85] is that dipyridyl ketone can readily be modified at the 2-position, allowing the introduction of buttress groups. However, the introduction of an alcohol group to the apex carbon could cause two issues. First it may affect the Suzuki coupling negatively by interacting with the catalyst. Secondly, it could cause interference in metal complexation for the final ligand. An additional step to the procedure to reduce or protect the alcohol may be required.

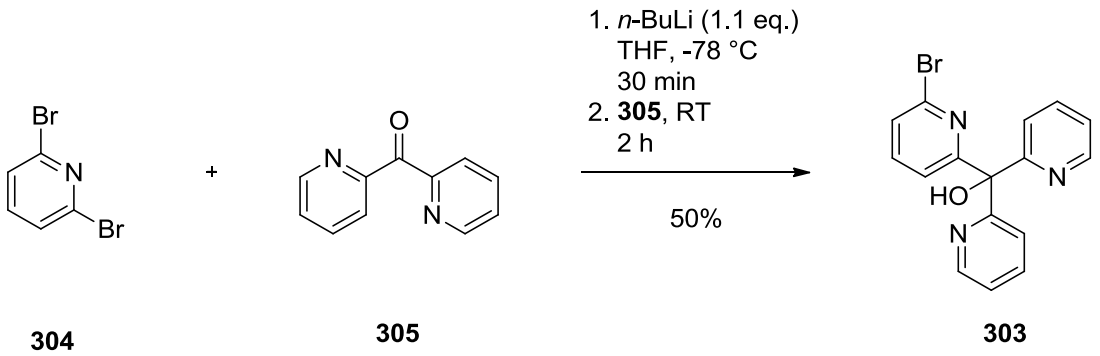

Scheme 3.4 Synthesis of **303**.

X-ray structural information for compound **303** was not known. To further confirm a successful synthesis, to test appropriate solvent systems for the ligand type, and to provide further characterisation, X-ray analysis was carried out. Crystals of **303** were grown by slow evaporation from a solution of diethyl ether and subjected to single crystal X-ray

structural determination (Figure 3.5). Its space group is $P2_1/a$ with an R_1 value of 5.65%. Two of the pyridyl nitrogens are pointed towards each other such that they begin to form a cavity, to minimise electrostatic interactions and possibly to reduce the overall dipole. The third nitrogen atom is involved in a strong hydrogen bond (1.88(7) Å) to the proton of the tertiary alcohol. Weak to moderate electrostatic interactions exist between the proton of C3 to the nearby pyridyl nitrogens (H3···N2, 2.689(4) Å and H3···N3, 2.507(5) Å). The bromo group is structurally unhindered for any subsequent reaction.

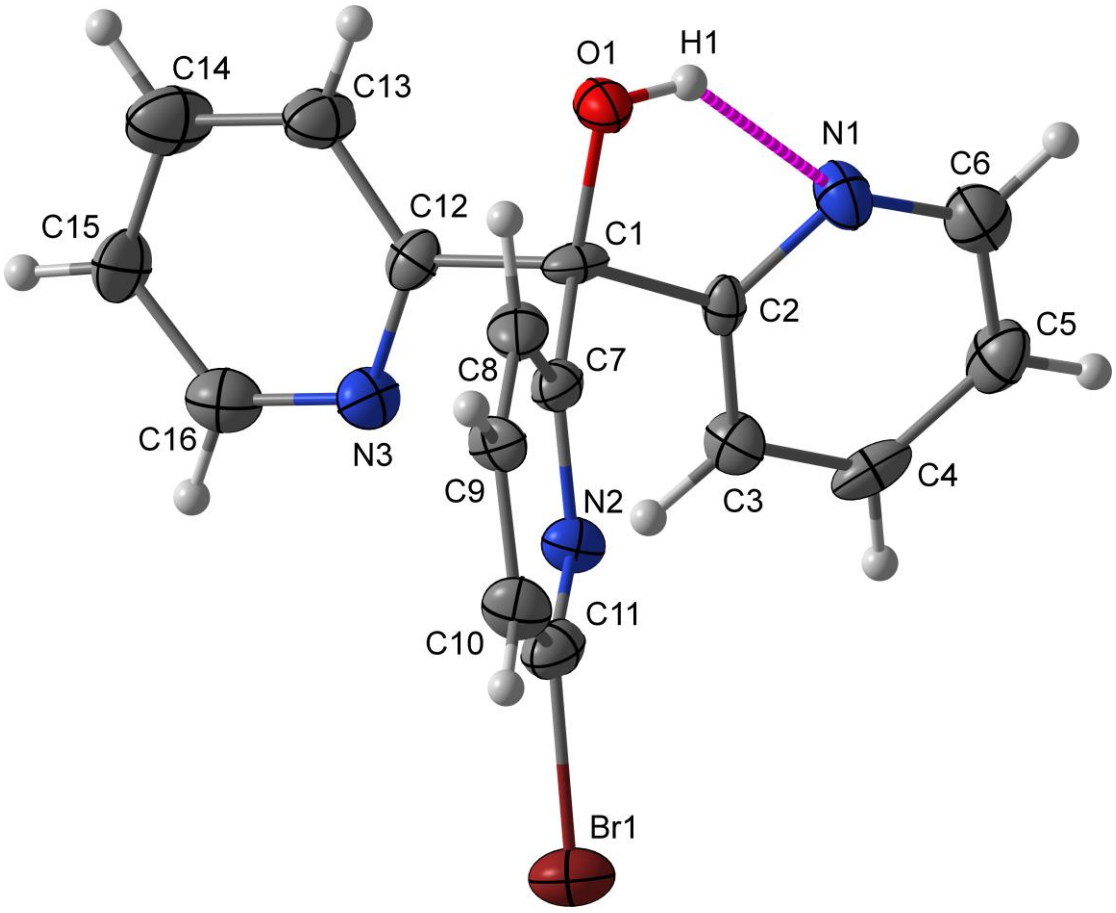

Figure 3.5 X-ray image of **303**, with thermal ellipsoids at 50% probability level.

Suzuki couplings are well-known reactions with established (substrate specific) reaction conditions. The last step of this route was performed using reaction conditions provided by Stoessel (Scheme 3.5).[85] Analysis of the crude product determined the reaction had not proceeded. The ^{1}H NMR indicated that the reaction product consisted of **303** and a new molecule that has more than the 15 unique proton signals expected of **301**. Varying the

reaction conditions by altering solvent (THF, Water/Dioxane, DMF), catalyst ($Pd(OAc)_2$, $Pd(PPh_3)_4$), phosphine (TTBP, PPh_3), and base (CaF_2, $CsCO_3$, K_2CO_3) – were fruitless.

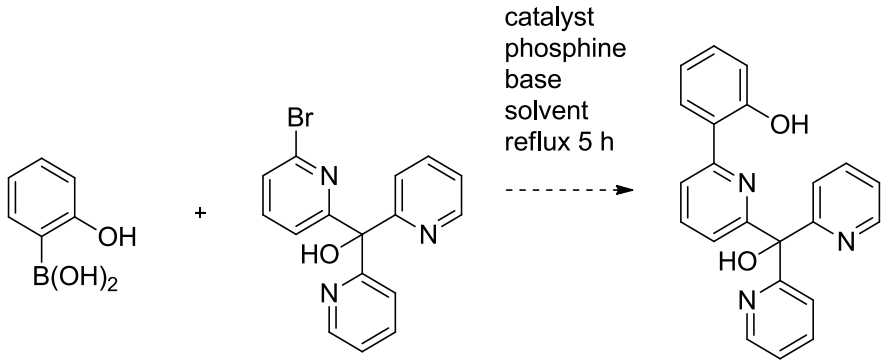

302 **303** **301**

Scheme 3.5 Attempted synthesis of **301**.

Eventually crystals were grown from the slow evaporation out of an EtOAc solution containing the reaction product and subjected to single crystal X-ray structural determination (Figure 3.6). A skeletal structure is given for clarity (Figure 3.7). The quality of data was low so the solved structure had an R_1 value of 14.24%, and was found in a $P2_1/n$ space group. The reaction had formed **306**, a 2:1 adduct of the boronic acid and **303**, by binding through the deprotonated tertiary apex alcohol (1.476(13) Å), and a pyridyl nitrogen (1.602(13) Å). The tertiary alcohol proton of compound **303** has been replaced with a boron atom of one molecule of 2-hydroxyphenyl boronic acid **302** – a result of the basic conditions of this reaction. The other boronic acid molecule has bound to the first boronic acid molecule through its boron atom and one phenolic oxygen (1.359(14) Å), and via a bridging oxo- group (1.359(14) Å). A hydrogen bond completes this network of complexation from the second phenol to the boron-bridging oxygen (1.928(6) Å). Other intramolecular bonds of interest are H8···O1 (2.438(6) Å), H13···O1 (2.461(6) Å), and H24···O3 (1.928(6) Å). An attempt to procure NMR and ESI-MS data for this unique boron complex was made, but was not possible, due to the low purity of the bulk material.

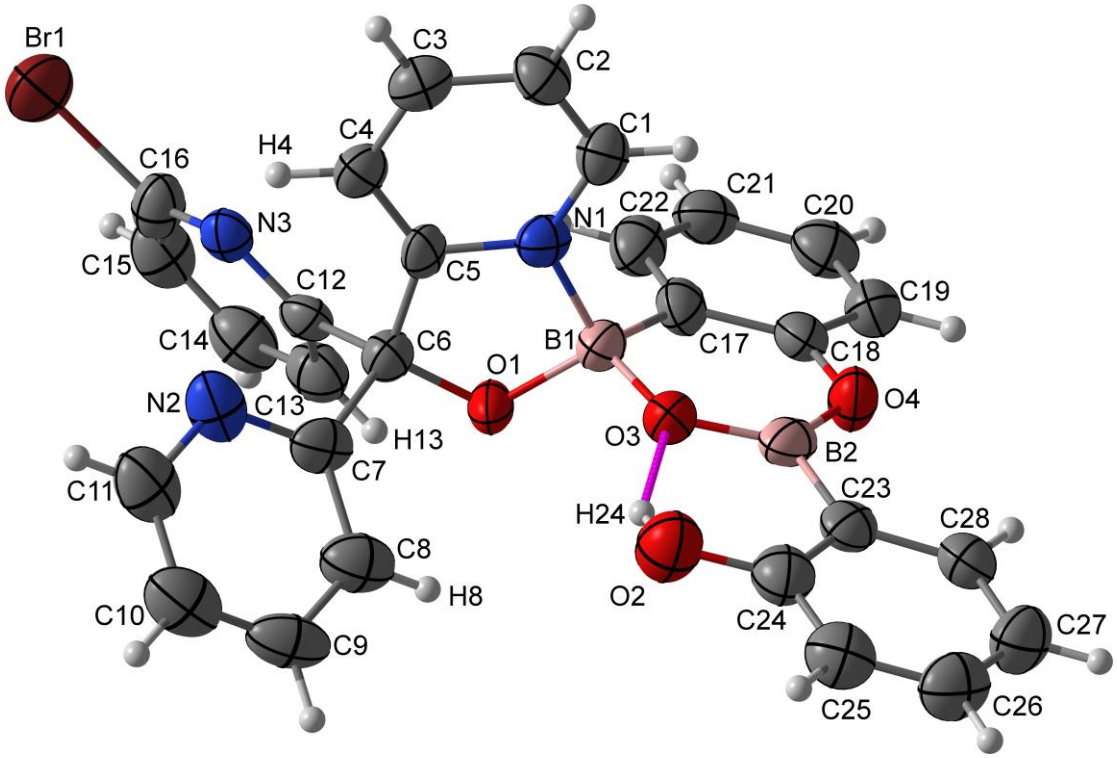

Figure 3.6 X-ray image of **306**, with thermal ellipsoids at 50% probability level.

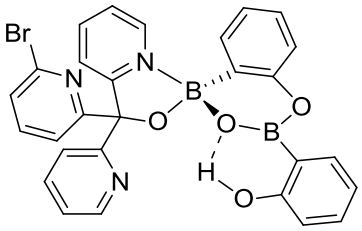

306

Figure 3.7 Chemical structure of the boron adduct **306**.

The formation of this adduct results in the removal of the boronic acid from the reaction mixture, therefore preventing a productive reaction. This problem could be averted by using a large excess of boronic acid, removal of the tertiary alcohol, or protecting either the alcohol or phenol. As reduction of tertiary alcohols analogous to **303** has not been well-studied, it was decided that a protecting group for the tertiary alcohol would be investigated.[107]

There are a large number of alcohol protecting groups, including commonly used *t*-butyl ether, methoxymethyl ether, and benzyl ether. For our system, a protecting group was

required that would not interact with the bromine and was also able to be removed later in the presence of a phenol. Bulkiness could also be advantageous for increased organic solubility, and to avert any interactions with chemicals involved in the Suzuki coupling. For these reasons, a benzyl protecting group was chosen. This can be added simply by deprotonating the tertiary alcohol with a base such as sodium hydride at 0 °C, followed by the addition of benzyl bromide (Scheme 3.6). Tetrabutylammonium iodide (TBAI) was used to catalyse the reaction by way of a Finkelstein reaction. TBAI provides an iodide that may substitute for the bromide of BnBr, thus increasing the reaction rate of the subsequent substitution. This reaction afforded **307** in a 34% yield. Purification of the crude material was possible through column chromatography. Confirmation of the product was made through assignment of the ^{1}H NMR spectrum. The C*H* proton shifts of BnBr (7.09-7.51 ppm) were, on average, shifted downfield (7.28-7.42 ppm), and the distinct chemical shift of CH_2 moved from 4.44 ppm (BnBr) to 4.56 ppm (**307**). ^{13}C NMR, COSY, DEPT-135, HMBC, and HMQC techniques were used to fully assign **307** (Figure A-2).

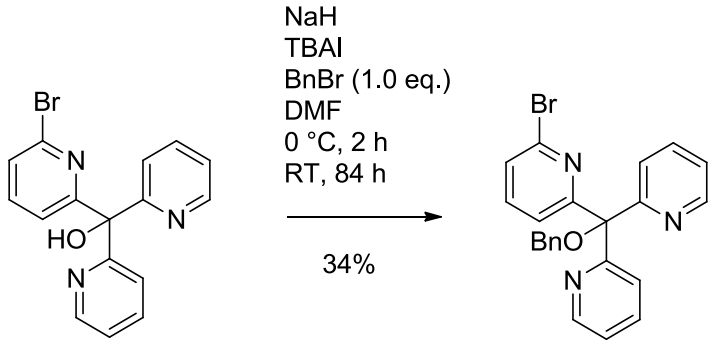

303 **307**

Scheme 3.6 Synthesis of **307**.

Crystals of **307** were grown by slow evaporation from a solution of DCM, and subjected to single crystal X-ray structural determination (Figure 3.8), solved in the space group $P2_12_12_1$ (R_1 = 7.68%). This gave conclusive evidence that the benzyl protection of **303** was a success. The X-ray asymmetric unit contains two independent molecules of **307**, whose

structures have similarities to the non-benzyl-protected starting material, with the major exception that there is no longer a proton available for internal hydrogen bonding. There exists π-π stacking within the asymmetric unit. The bromo group remains structurally unhindered for subsequent reaction.

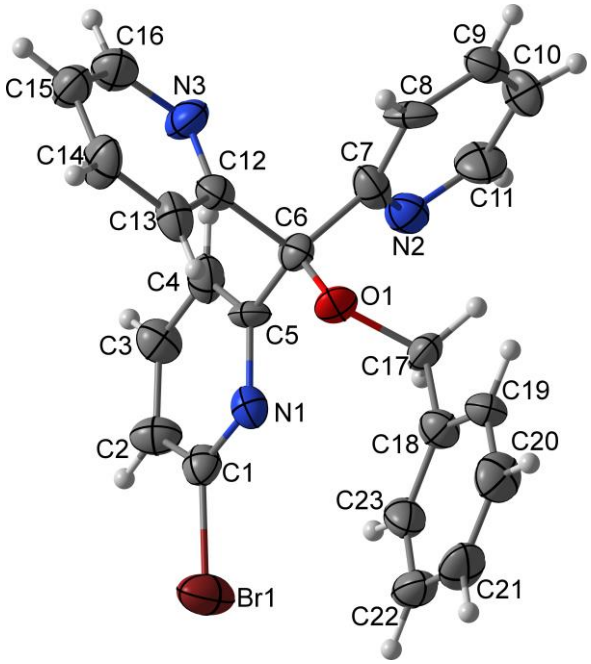

Figure 3.8 X-ray image of **307**, with thermal ellipsoids at 50% probability level.

The benzyl-protected compound **307** was subjected to the Suzuki reaction (Scheme 3.7), using tetrakis(triphenylphosphine)palladium(0) as the catalyst in the presence of caesium carbonate and **302** in DMF. A microwave vessel was initially used at 100 °C for 2 hours for this reaction. NMR analysis showed formation of the product, in a 5:1 ratio with starting material. The chemical shift CH_2 changed significantly (4.56 ppm to 4.82 ppm), as did the benzyl and pyridyl aromatic chemical shifts C*H* (7.19-8.61 ppm to 6.58-7.45 ppm). Increasing the temperature to 120 °C resulted in an increased conversion, affording a 9:1 ratio of product to starting material. Neither further time nor increased temperature improved the yield of this reaction (54%).

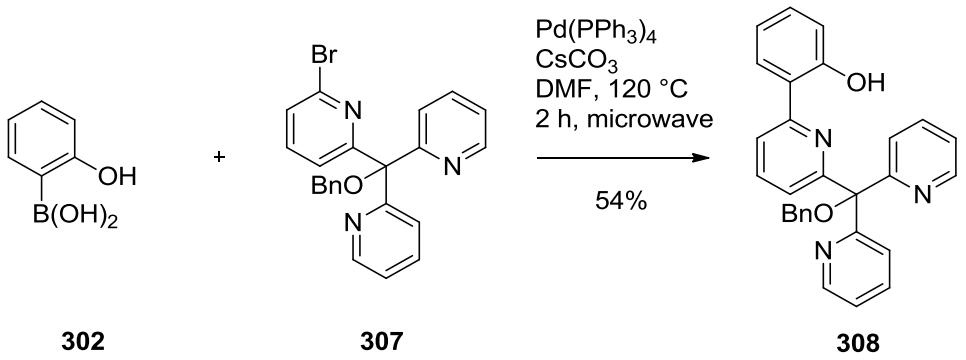

302 **307** **308**

Scheme 3.7 Synthesis of **308**.

Before the next step of deprotection, the intermediate ligand **308** required purification to remove the starting material **307**. A combination of flash column chromatography and slow evaporation was attempted. Unfortunately, the materials moved together on the column for all solvents tested. Crystallisation attempts resulted in the isolation of an unpurified oily material. As purification was not possible, deprotection was not attempted. Given this, and that we had another potential synthetic scheme, this reaction pathway was abandoned.

3.2.2 Second Route towards L1cohH

Our second approach began with a re-examination of the previous synthetic route developed by Shaffer.[52] His plan followed a logical progression but was ultimately unsuccessful. As it was simple, and the chemistry involved was well known, it was reattempted. This scheme would target the ligand **L1chH 309** (Figure 3.9).

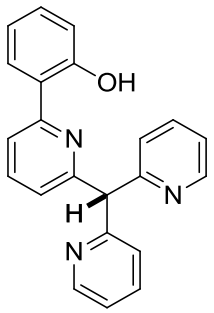

309

Figure 3.9 L1chH 309.

The new target, **309**, lacked the problematic tertiary alcohol. The first disconnection splits the molecule in half by removing the dipyridine methylene (Scheme 3.8). In a forward sense, it was hoped that S_NAr chemistry would give the product. The phenol is methylated to help avoid undesired side-product formation in the coupling of **310** to **311**.

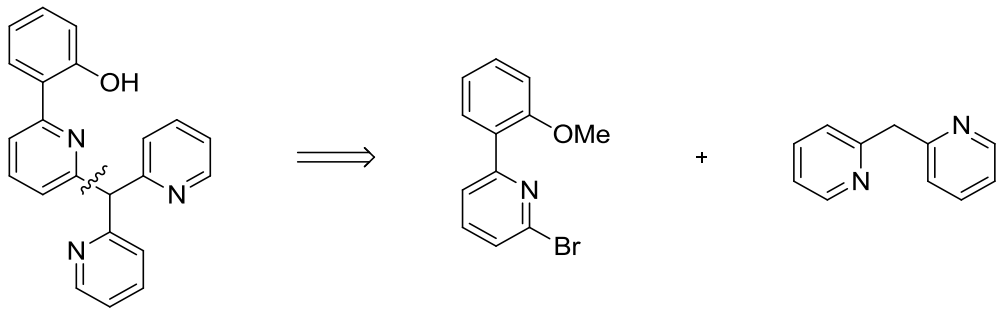

309 **310** **311**

Scheme 3.8 Disconnection of **309**.

In order to synthesise 2-bromo-6-(2-methoxyphenyl)pyridine **315**, a Kumada-Tamao-Corriu coupling can be employed.[108] This was done by forming the Grignard of **312**, which was reacted with **314** to give **315** (Scheme 3.9). This one-pot reaction afforded a good yield (75%). Confirmation of synthesis was achieved by comparing the product NMR spectrum with literature values.[109]

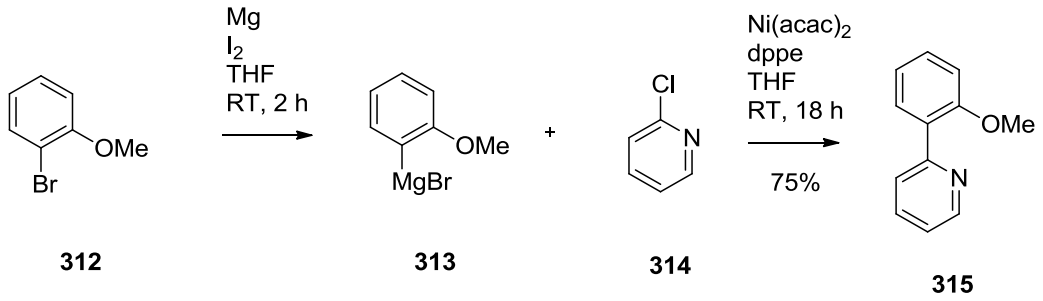

Scheme 3.9 Kumada-Tamao-Corriu coupling using $Ni(acac)_2$ as the catalyst in a one pot synthesis.

The bromo group was installed at the 2-position of **315** by selective deprotonation using the reagent *n*-BuLi-LiDMAE (butyllithium-lithium dimethylaminoethanol), followed by reaction with carbon tetrabromide (Scheme 3.10). The selective substitution has been proposed to occur by chelation of the aggregate *n*-BuLi-DMAE. The product was isolated in an 82% yield. The ^{1}H NMR spectrum agreed with literature values (Figure A-3).[52]

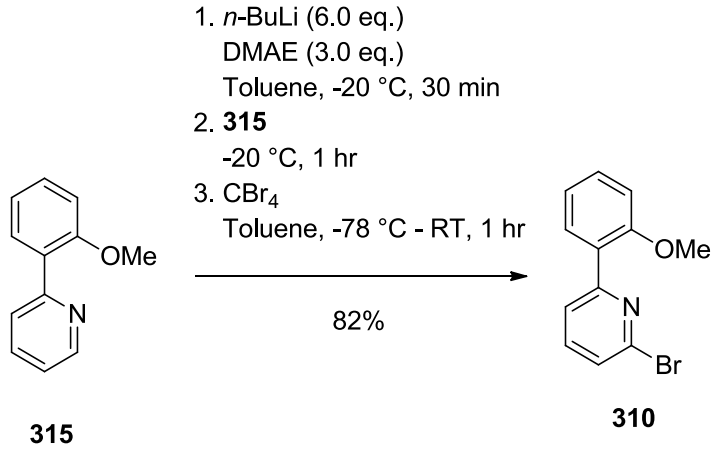

Scheme 3.10 Synthesis of 2-bromo-6-(2-methoxyphenyl)pyridine, **310**.

The other half, compound **311**, was synthesised simply by combining **316** and **317** with *n*-BuLi in THF giving a high yield of 99% (Scheme 3.11). Confirmation of the product's identity was by comparison to literature values.[110]

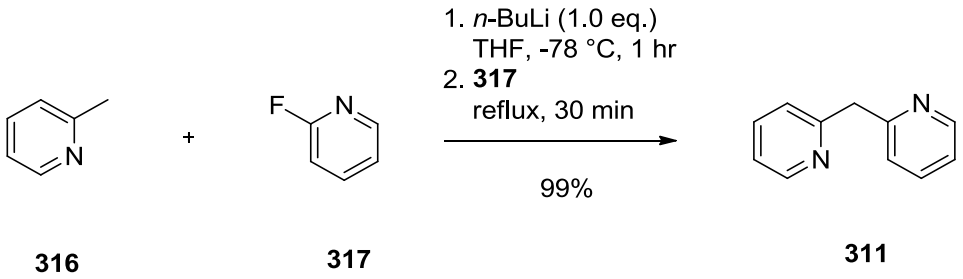

Scheme 3.11 Synthesis of dipyridine methylene, **311**.

The second to last step involved the coupling of **310** to **311** (Scheme 3.12). Although this coupling was previously reported to not proceed, it was deemed worthwhile to reattempt.[52] It was hoped that formation of the carbanion of **311** by treatment with *n*-BuLi would generate a nucleophile that could displace the bromo group. Similar chemistry has previously been used in carbon-carbon bond forming reactions, providing precedence for this substitution.[111]

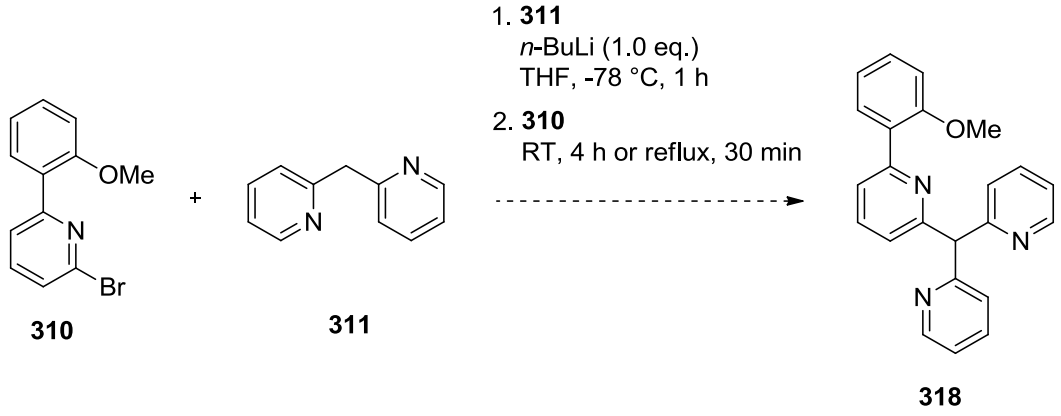

Scheme 3.12 Attempted synthesis of **318**.

Dipyridine methylene in THF with *n*-BuLi was stirred at -78 °C under Ar for one hour, then a solution of 2-bromo-6-(2-methoxyphenyl)pyridine **310** was introduced dropwise over 10 minutes. The reaction vessel was warmed to room temperature over four hours. Detailed examination of the subsequent products revealed that this procedure was unsuccessful. NMR and ESI-MS analysis showed only starting materials.

Multiple attempts were undertaken, involving more forcing conditions, but all to no avail. There are a number of possible issues. Firstly, the methylene bridge may not be acidic enough to undergo deprotonation. Secondly, the resulting anion could be a poor nucleophile due to charge delocalisation over the adjacent pyridines. Finally, it is possible that **310** is a poor electrophile and that a stronger electron withdrawing group like the fluorine in **317** is required.

By reversing the roles of the compounds making **311** the electrophile and **310** the nucleophile, the reaction might proceed. In order to make **311** into an electrophile, a good leaving group is needed. This would be achieved by adding bromine to the methylene position (Scheme 3.13). This was achieved by radical bromination in a 42% yield, and its NMR matched the values given by the literature.[112]

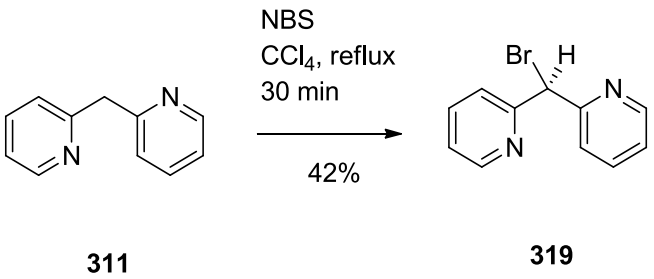

311 **319**

Scheme 3.13 Synthesis of 2,2'-(bromomethylene)dipyridine, **319**.

The compound **310** was converted to a nucleophile by halogen-metal exchange using *n*-BuLi, after which the bromide **319** was added dropwise. The coupling was attempted in refluxing THF, toluene, or DMSO. Unfortunately, again, there was no observed product (Scheme **3.14**). Analysis of the ^{1}H NMR spectrum revealed only starting materials were present. The lack of the protodebrominated form of **319** in the crude reaction material is strong evidence that the lithiated species did not form.

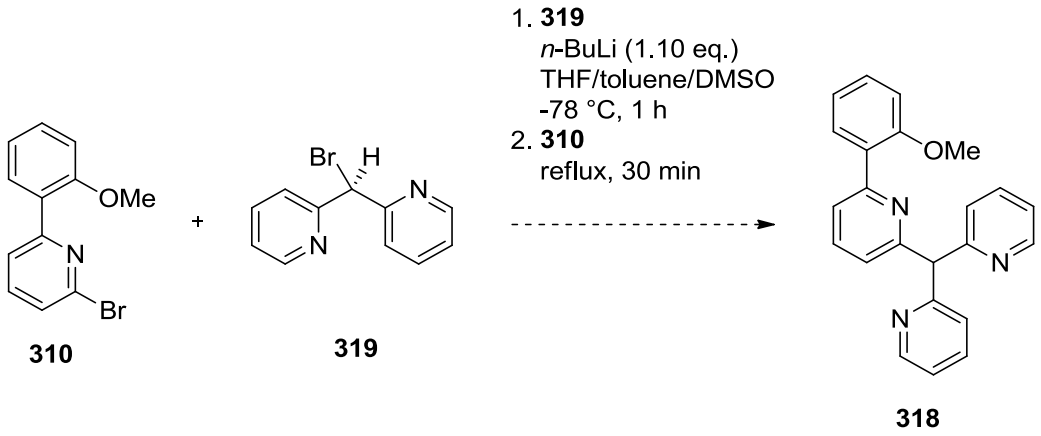

Scheme 3.14 Attempted synthesis of the methylated **310** derivative, 3**18**.

A last attempt was made, this time using dipyridyl ketone **305** instead of **311** or **319** (Schemes 3.12-3.14). The dipyridyl ketone was previously synthesised as part of the first reaction scheme towards **L1cohH** (Scheme 3.3). The reaction was carried out once each with THF, toluene, and DMSO. Although there is precedence for a coupling between **305** and an aromatic bromo group taking place, it may be the case that the 2-methoxyphenyl moiety and pyridine functionality of **310** might be acting as a chelator by binding to the Li^+ cation, thus disrupting any reaction from taking place.

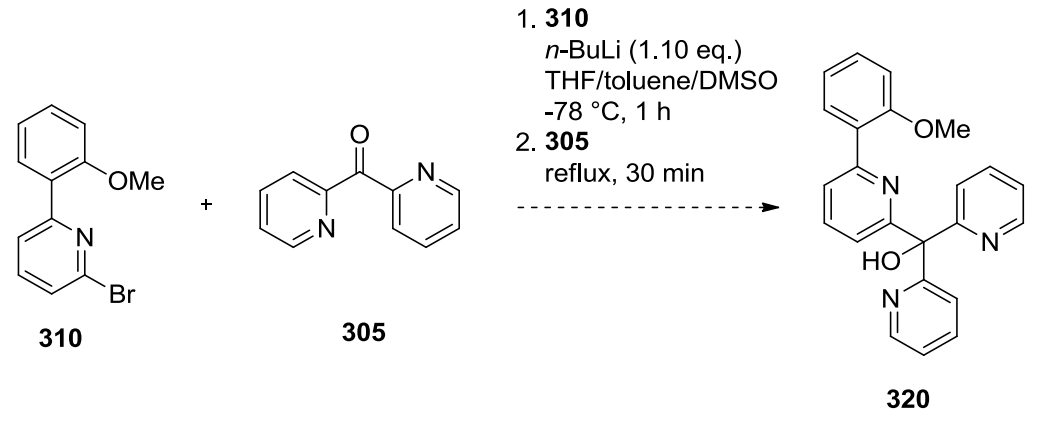

Scheme 3.15 Attempted synthesis of the methylated **310** derivative, **320**.

The last modification to this procedure was to consider a different protecting group for the phenol in compound **321** (Scheme 3.16). This would help ascertain what might be causing trouble for the previous syntheses. As benzyl-group protecting chemistry had

been successfully used previously, this was applied here too. The first new reaction was building the 2-(6-bromo-2-pyridinyl)-phenol molecule from 2,6-dibromopyridine and 2-hydroxyphenol boronic acid (Scheme 3.16). This Suzuki coupling afforded **321** as the major product (67% yield). Although these exact reaction condition used are new, **321** had previously been synthesised in low yields.[113] The ^{1}H and ^{13}C NMR spectra matched that of the literature, confirming its synthesis (Figure A-4). A small amount of the dicoupled pyridine (2,2'-(pyridine-2,6-diyl)bisphenol) was found as a side-product, but was removed during purification using silica gel chromatography. A further advantage to this alternate pathway compared to Scheme 3.10 is that it allows various protecting groups to be used. This would allow optimisation of the protecting group to be readily undertaken.

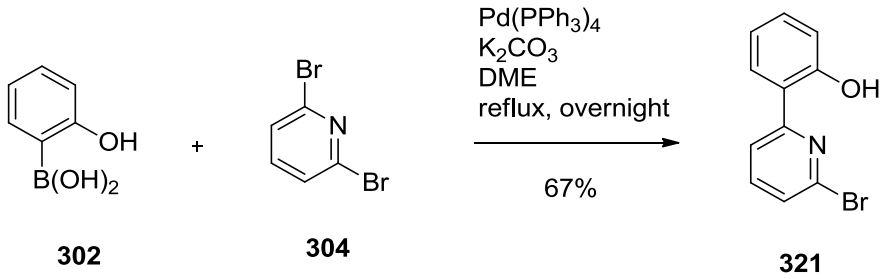

302 **304** **321**

Scheme 3.16 Synthesis of **321**.

Protection of the phenol group was carried out using similar conditions to the standard ones as used previously (Scheme 3.17). Purification by silica gel chromatography yielded 33% of **322**. The success of synthesis for this new compound was determined through analysis and assignment of the spectroscopic data (Figure A-5).

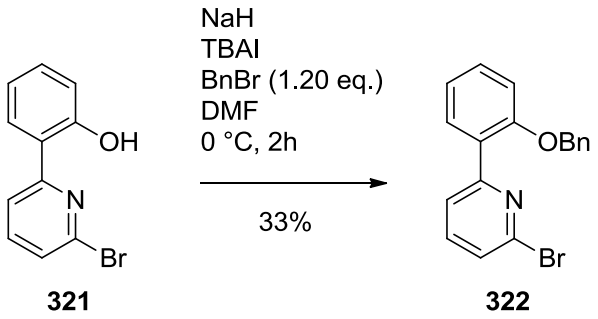

321 **322**

Scheme 3.17 Synthesis of **322**.

The newly benzyl-protected pyridyl phenol was reacted with dipyridyl ketone (Scheme 3.18). This reaction was successful according to NMR and ESI-MS analysis and purification was possible after multiple silica gel chromatography columns (Figure 3.10). The yield for this reaction, however, was poor (11%).

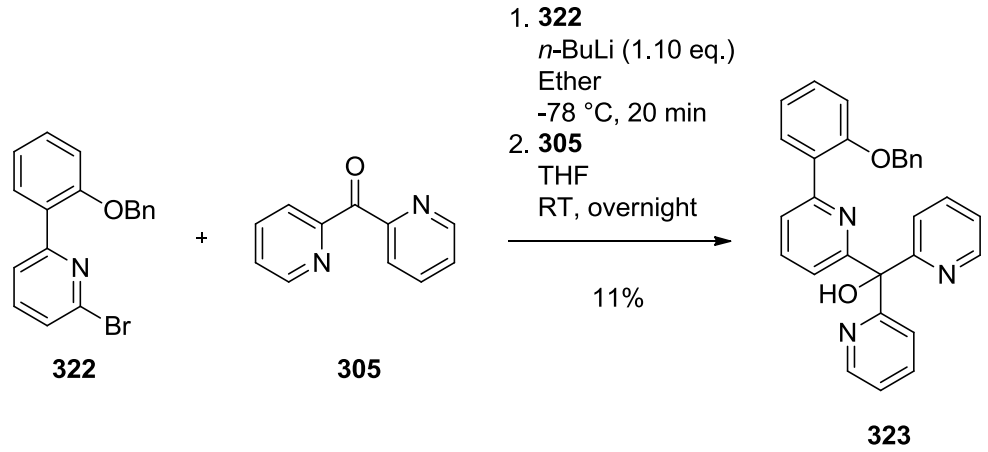

322 **305** **323**

Scheme 3.18 Synthesis of the benzylated **301** derivative, **323**.

The new material **323** was fully analysed and the ^{1}H NMR, ^{13}C NMR, DEPT-135, COSY, HMBC and HMQC spectra were assigned (Figure A-6). The proton of the tertiary alcohol was easily assigned (7.49 ppm) due to its characteristic broadness and integration of one proton. The carbon of this apex group was assigned using HMQC at 81.33 ppm. The other relatively shielded carbon peak (compared to typical aryl and pyridyl carbon shifts) at 70.63 ppm therefore must be due to the benzyl methylene group. Comparison of this peak to the starting material (70.76 ppm) confirms this. Likewise, the ^{1}H NMR singlet at

5.16 ppm, which integrates for two protons, must be due to the benzyl methylene protons. The two most deshielded protons at 8.58 and 7.93 ppm are associated with protons on the pyridyl rings, as are the peaks in the range 7.68-7.76 ppm. The peak at 7.81 ppm, and the upfield protons are all associated with the last remaining rings. HMQC and HMBC were used to assign these protons to the correct carbon atoms.

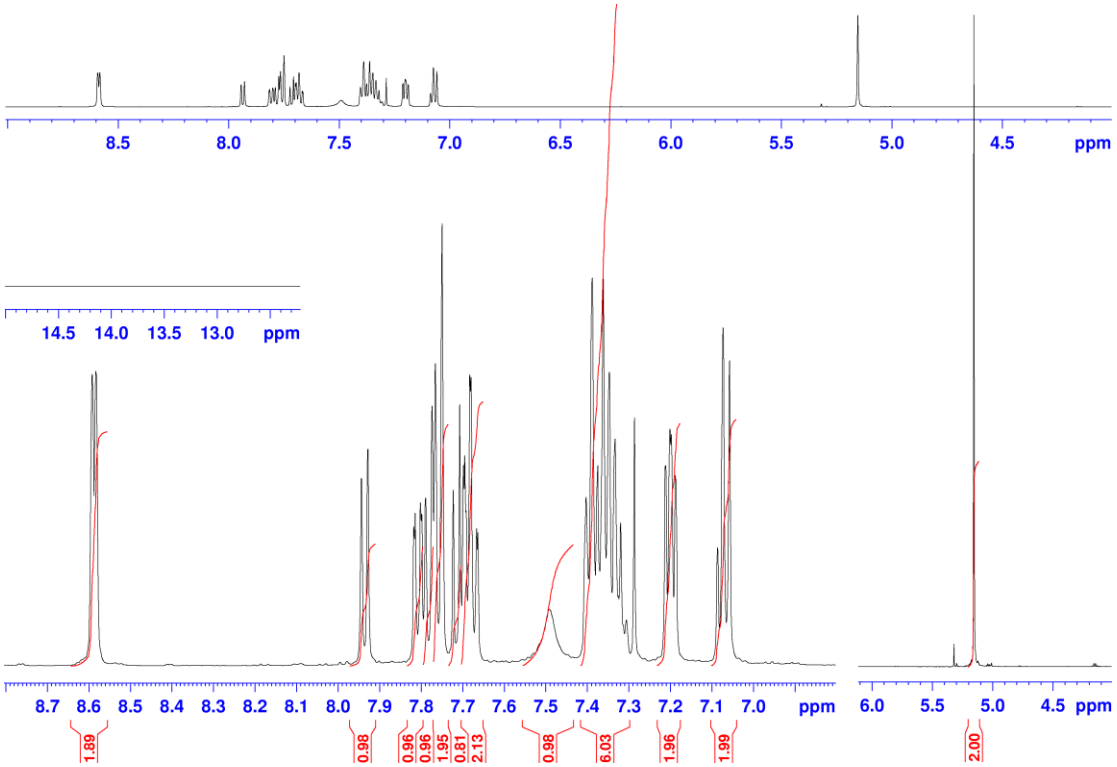

Figure 3.10 ^{1}H NMR spectrum of compound **323**.

The benzyl group could be removed by deprotection to give **301**, the ligand **L1cohH** (Scheme 3.19). The starting material was stirred with boron tribromide in DCM at -78 °C, allowing to warm to room temperature overnight. A yellow precipitate resulted, and following silica gel chromatography, gave the pure ligand as a pale-yellow powder (46% yield). The ligand was fully characterised with NMR, ESI-MS, and CHN analysis (Figure A-1). This ligand was subsequently coordinated to beryllium (see Chapter 4).

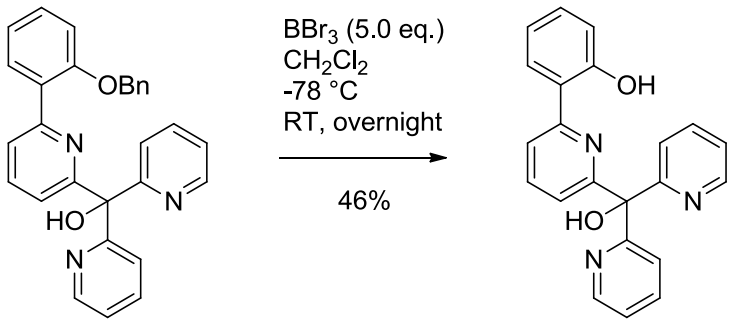

323 **301**

Scheme 3.19 Successful synthesis of the ligand **L1cohH 301**.

The notable differences between the NMR of **323** and **301** are the disappearance of the methylene protons of the benzyl protecting group at 5.16 ppm, and the appearance of the broad and distinctive phenolic proton signal at 13.11 ppm (Figure 3.11). A hydrogen bond between the phenolic proton and the neighbouring pyridyl nitrogen causes the proton to be highly deshielded. This may cause the compound's interaction with Be^{2+} to be more reactive, as the proton has a lower electron density. Elemental analysis confirmed purity of **301**, Expected ($C_{22}H_{17}N_3O_2 \cdot \frac{1}{2}H_2O$): C, 72.48; H, 4.97; N, 11.55; Found: C, 72.90; H, 4.94; N, 11.55. This ligand, which is potentially capable of binding beryllium in tetradentate fashion, was synthesised in an overall yield of 1.1% over 5 steps.

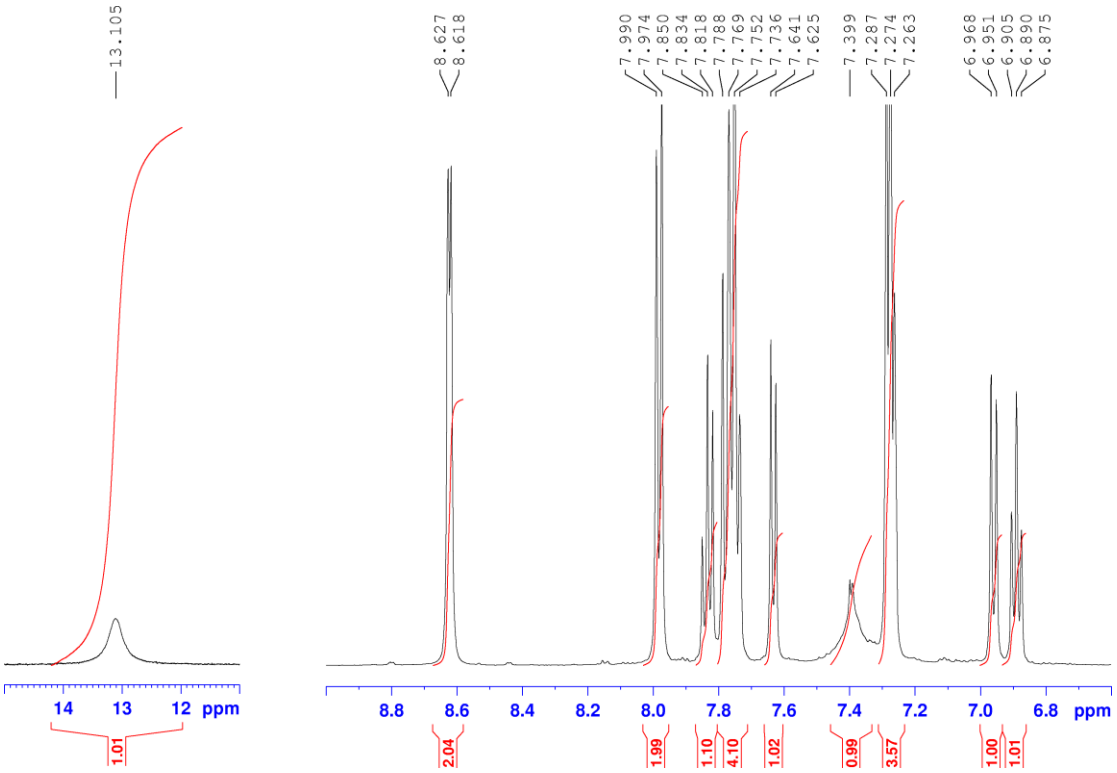

Figure 3.11 ^{1}H NMR spectrum of ligand **301**.

3.2.3 X-ray Crystal Structure of L1cohH

It proved challenging to fully purify **L1cohH 301**. Although any remaining starting material and side products were removed, a small amount of stubborn solvent (H_2O) always remained. However, this did not prevent the growth of block-shaped crystals by the slow evaporation of pentane from a solution of **L1cohH** in benzene left to stand overnight. At the University of Marburg, a suitable crystal was selected and mounted on a Stoe IPDS2T diffractometer and subjected to single X-ray structural determination. The crystal was kept at 100(2) K during data collection. Using Olex2, the structure was solved with the Superflip structure solution program using Charge Flipping and refined with the ShelXL refinement package using Least Squares minimisation (Figure 3.12).

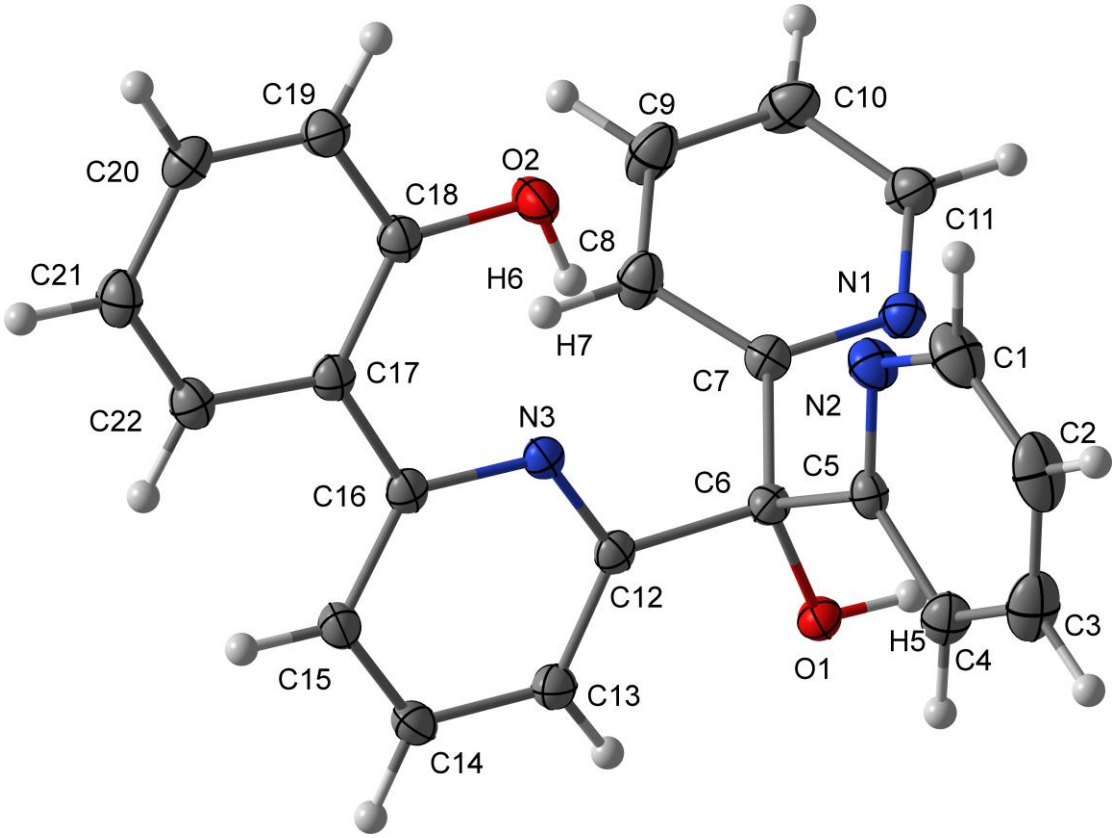

Figure 3.12 X-ray structure of **L1cohH 301**, with thermal ellipsoids at 50% probability level.

The asymmetric unit consists of one molecule in its entirety. Refer to Table B-1 for structural parameters. The crystal had an orthorhombic lattice, and space group of *Pbca* (R_1 = 3.41%). The structure of the ligand mimics closely the hypothesised motif.

The backbone of the ligand consists of a relatively planar pyridyl-phenol unit (3.11° dihedral angle). The other two pyridyl moieties sit freely away from each other, forming a relaxed pocket in the centre of the ligand. A particularly strong hydrogen bond exists between the phenolic proton and the backbone pyridyl nitrogen (1.753(18) Å). The distance between this proton and the next closest pyridyl nitrogen suggests a weak hydrogen bond (2.843 Å), but the last pyridyl nitrogen is at a substantial distance in which any electrostatic interaction is non-dominant (4.366 Å). Three of the potential donors (O2, N2, N3) are pre-organised into a cavity, available for chelation.

The last pyridyl group is twisted away from the potential binding site, as it is part of a strong hydrogen bond (2.066(18) Å) between its nitrogen atom and the proton of the tertiary alcohol belonging to a neighbouring ligand molecule within the crystal lattice (Figure 3.13). Upon complexation with a metal cation, the last pyridyl group can potentially rotate and complete the binding in a tetrahedral fashion.

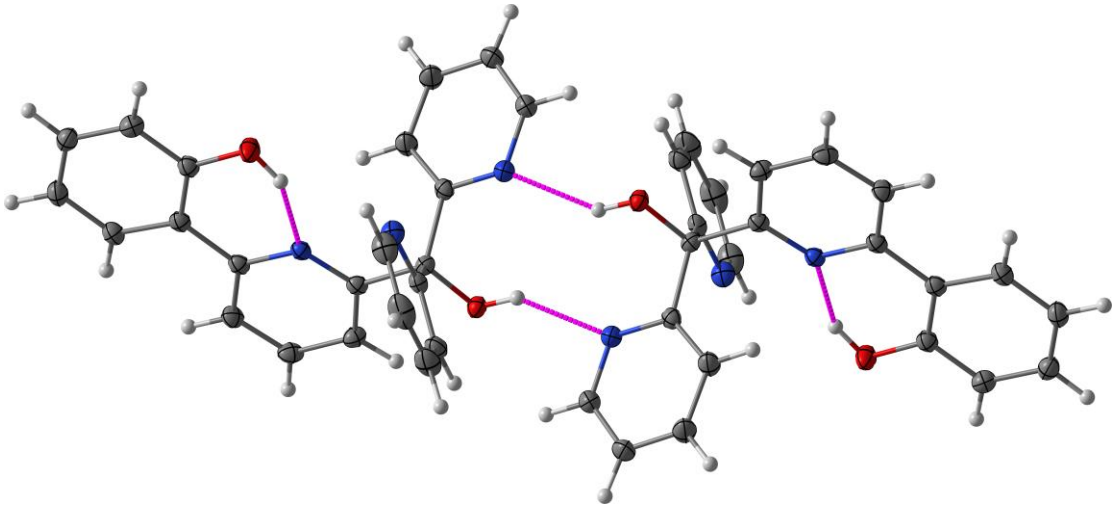

Figure 3.13 Intermolecular hydrogen bonding between two molecules of **301** in the unit cell.

A structural comparison was made between the crystal structure and computational model of **L1cohH** (Figure 2.14, page 65). It was found that there was overall a good agreement between the two structures. The backbone of the X-ray structure had a 3.11° dihedral angle, whereas the computational model has a 21.18° dihedral angle. This deformation is due to an artificially shortened hydrogen bond between the phenol proton and the nearby pyridyl arm (2.339 Å) of the model. The other major difference between the structures is the arrangement of the other pyridyl arm, which is found to be further twisted away from the binding site in the computational model. This unfavourable contortion can be explained due to the model allowing a strong hydrogen bond between the tertiary alcohol proton and the pyridyl nitrogen (1.823 Å). This does not exist in the X-ray structure because of the intermolecular hydrogen bonds (Figure 3.13).

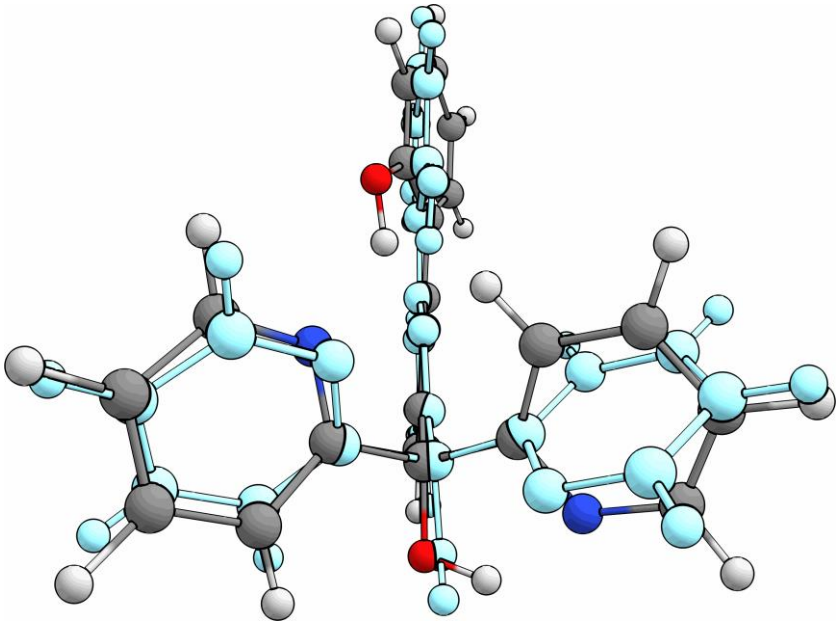

Figure 3.14 Computational structure of **L1cohH** (coloured normally) merged with the X-ray structure for **301** (coloured light-blue).

3.3 L1nH

The second ligand targeted was **L1nH** (Figure 3.15, left). This compound was previously synthesised by Shaffer.[52] His procedure was followed successfully without any significant alterations, and the ^{1}H data agreed with his values.

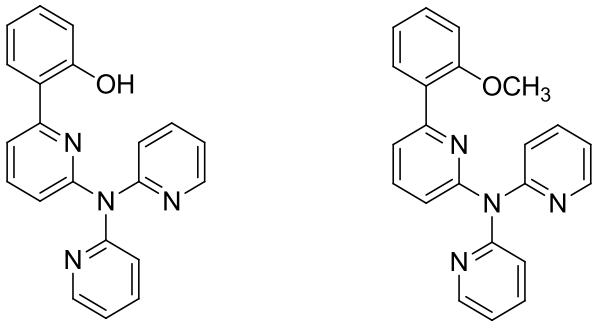

L1nH, 324 **325**

Figure 3.15 **L1nH** (left) and **325** (right).

A single crystal of **325** (Figure 3.15, right), the methyl-protected version of **L1nH**, was obtained by slow evaporation of a DCM/heptane solution, and subjected to a single

crystal X-ray structural determination (Figure 3.16). The crystal had a *Pbca* space group and a low R-factor (R_1 = 4.93%). The structure is in a loose elongated conformation. Every heteroatom is orientated away from each other to minimise electrostatic repulsions – this is the case in the unit cell as well. The central nitrogen N4 is not planar, with each pyridyl unit twisted away from the plane of the backbone, at an average angle of 35°. This is due to the lone pair present on N4. There exist intramolecular hydrogen bonds of a modest strength between the pyridyl nitrogens and opposing protons (N1···H12, 2.8356(17) Å; N2···H4, 2.5876(17) Å; N3···H7, 2.6939(17) Å; N3···H17, 2.5456(16) Å).

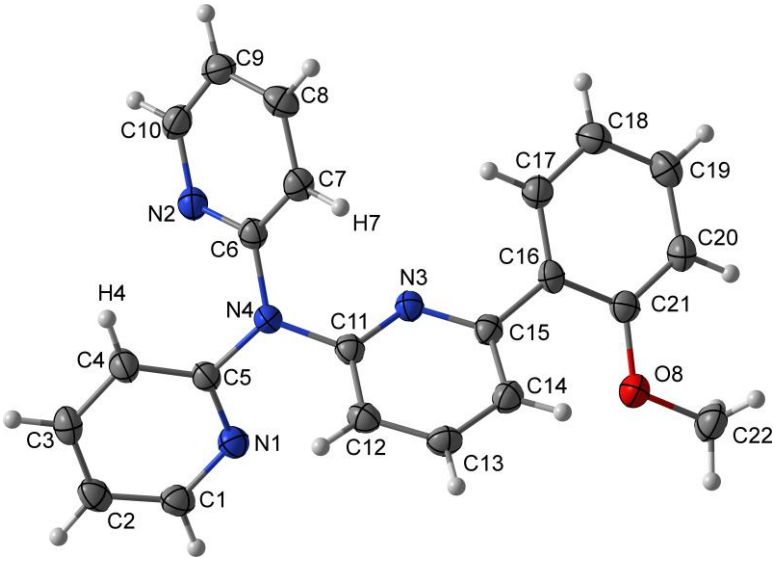

Figure 3.16 X-ray image of **325**, with thermal ellipsoids at 50% probability level.

3.4 Summary

In this chapter, many routes were tried in an attempt to synthesise an non-buttressed ligand. Although these often proved troublesome, great efforts successfully synthesised the ligand **L1cohH 301** (Figure 3.17, left), and this was fully characterised, and its structure was determined by X-ray crystallography. The ligand **L1nH** was also synthesised (Figure 3.17, right), and the intermediate species **325** was characterised by X-ray crystallography.

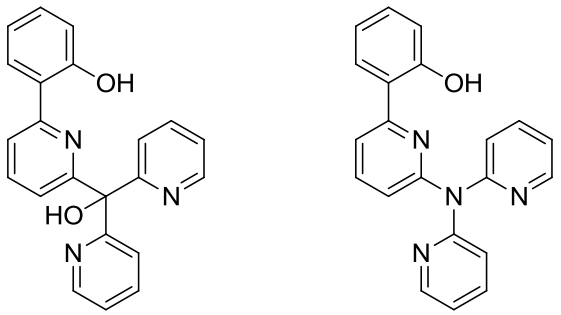

L1cohH **L1nH**

Figure 3.17 Successfully synthesised ligands **L1cohH** and **L1nH**.

3.5 Future Work

During this project, a route was identified to reach the third apex group investigated, **L1chH**. A further step in the reaction pathway can be added which would be the selective reduction of the hydroxyl group of **L1cohH** (Scheme 3.20). There is precedence in the literature that tertiary alcohols can be selectively reduced – particularly in the presence of bulky substituents (in this case, three pyridyl rings).[107] The use of diphenylchlorosilane and $InCl_3$ should result in **L1chH**. If accomplished, this would provide the last remaining apex compound for the non-buttressed **L1** ligand motif. This would be useful in experimental competitive and comparison studies, as well as providing further evidence towards the reliability of the computational work.

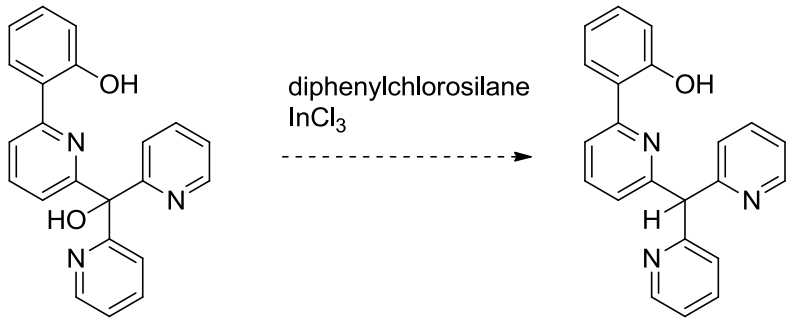

301 **309**

Scheme 3.20 Proposed dehydration of L1cohH 301 to form ligand L1chH 309.

Other attachments may also be made to various positions on the scaffold, including bulky *t*-Bu groups for increased crystallisation reliability or sulfonate residues to increase solubility in aqueous systems.

Chapter 4: Beryllium Complexes

"Research is what I am doing when I don't know what I am doing."

– Werner von Braun

4.1 Introduction

In order to find confidence that the computational work in this thesis is reliable, comparison with experimental study of beryllium-containing complexes is required. This could involve a number of techniques including X-ray crystal structural determination, spectroscopic analysis, and competition studies. The collation of evidence provided by these will provide justification of the computational predictions.

4.2 X-ray Crystal Structural Determination

During this research, a number of compounds were sent to our collaborator Dr. Magnus Buchner at the University of Marburg, Germany. There, reactions were undergone in which each material was reacted with $BeCl_2$ under heating conditions. This was successful for three compounds (Figure 4.1). The first part of this chapter is a structural discussion of the resulting X-ray structural determinations.

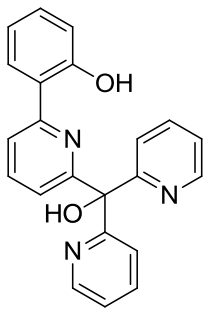

301

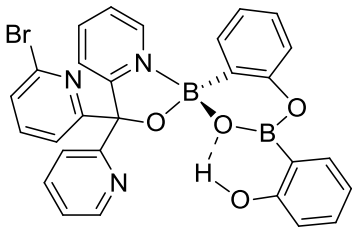

306

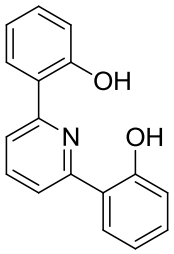

2,2'-(Pyridine-2,6-diyl)bisphenol

Figure 4.1 Ligands **301**, **306**, and 2,2′-(pyridine-2,6-diyl)bisphenol were successfully bound to beryllium.

4.2.1 X-ray Crystal Structure of 401

The ligand **L1cohH 301** was reacted with $BeCl_2$ in a mixture of acetonitrile, 1,2-difluorobenzene, and DMF. The resulting suspension was heated for several days at 80 °C, and colourless rod shaped crystals of **401** formed at the phase interface of a mixture of acetonitrile, 1,2-difluorobenzene, and DMF. A suitable crystal was selected and measured on a Stoe StadiVari diffractometer. The crystal was kept at 97(2) K during data collection. Using Olex2, the structure was solved with Superflip, a structure solution program, using Charge Flipping and refined with the ShelXL refinement package using Least Squares minimisation. This is the first beryllium complex reported of this type (Figure 4.2).

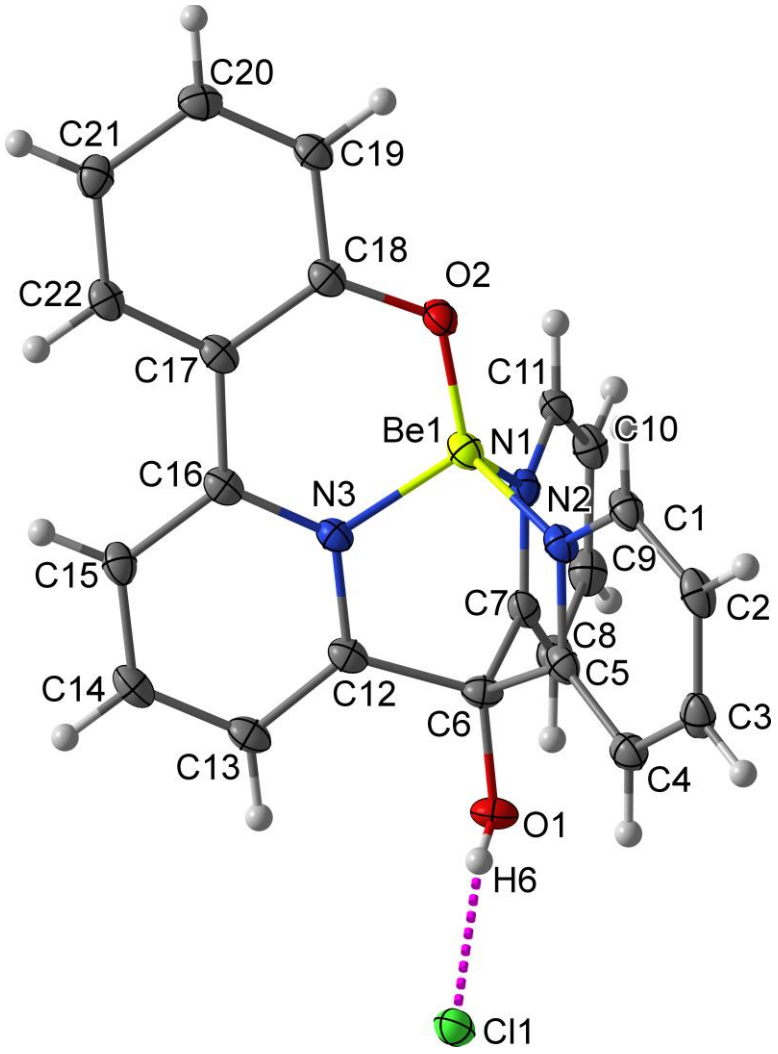

Figure 4.2 X-ray structure of the complex **401**, with thermal ellipsoids at 50% probability level.

This triclinic system has a *P*-1 space group (R_1 = 4.54%). The beryllium(II) centre is in a moderately distorted tetrahedral donor environment with angles subtended within the range 98.66(19)-121.8(2)°. The four donors comprise of three nitrogen donor atoms from each of the pyridyl molecules, and one phenolate oxygen atom. The Be···O bond length is significantly shorter (1.511(3) Å) than the Be···N bond distances (1.687(4), 1.740(4), and 1.744(4) Å). The angles about the beryllium ion are not perfectly tetrahedral, and are found between 98.65(19)-121.9(2)°. The closest angle to the ideal tetrahedral angle is O2···Be1···N3, which is 111.4(2)°. A chloride ion forms a moderately strong hydrogen bond to the tertiary alcohol (2.181 Å). This counter ion balances the -1 charge of the ligand and the +2 charge of the cation.

The asymmetric unit of **401** consists of two complete molecules of the complex (Figure 4.3). The arrangement of each complex is the same, except for the chloride counter ion, which is found to be inverted through the ligand backbone.

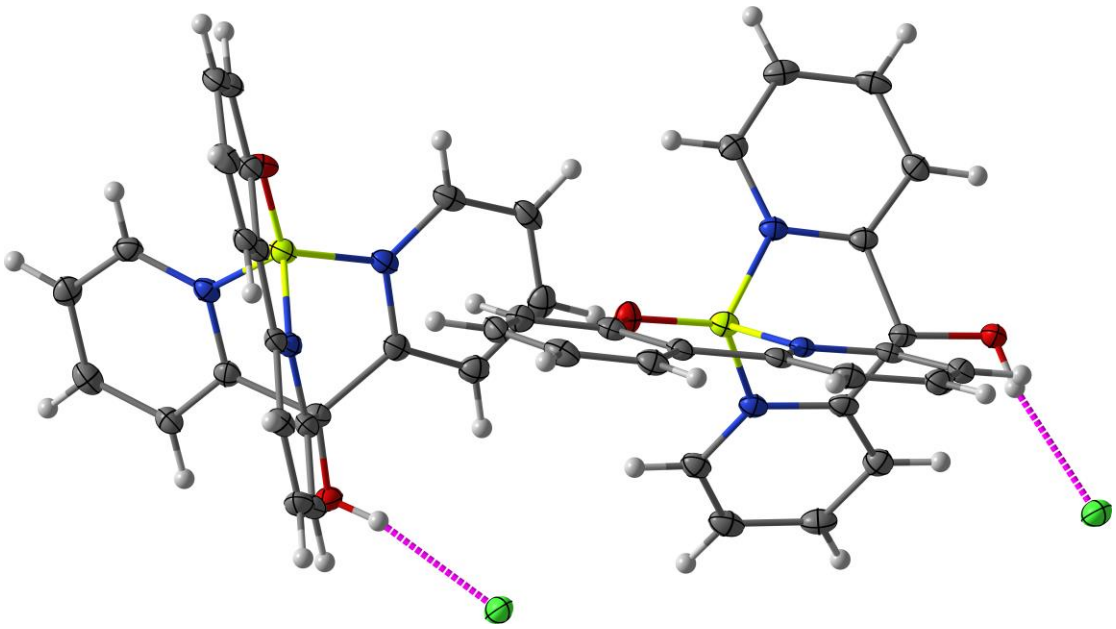

Figure 4.3 Asymmetric unit of **401**, with thermal ellipsoids at 50% probability level.

Only three other organic tetradentate X-ray structures of beryllium complexes are known. Beryllium is in a tetrahedral arrangement in two of these[114] and square planar in the

other.[56] There is no tight binding pocket in either tetrahedral complex like the one found for **401**. The [Be(salbn)] complex has Be···O bond lengths of 1.583(4) Å and Be···N bond lengths of 1.727(4) Å, and the angles about its binding centre are between 103.8(2)-113.8(3)°. The other tetrahedral complex, [Be(NTP)]Na, has Be···O bond lengths of 1.597 Å, a Be···N bond length of 1.780, and the angles about its binding centre are between 108.9-110.1°. The complex **401** has bond lengths shorter than all of these, but its conformation is further from an ideal tetrahedral shape. This implies a ligand constricted coordination environment upon complexation.

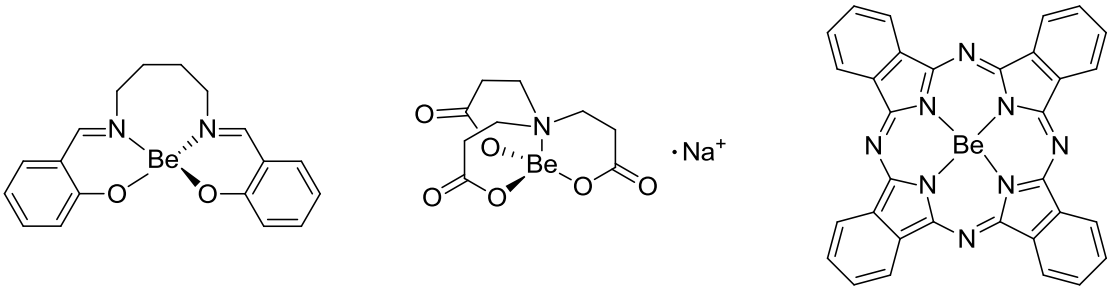

Figure 4.4 Known organic tetradentate binders of Be^{2+} and their CCDC codes.[56, 114]

4.2.2 X-ray Crystal Structure of 402

The compound **306** was reacted with $BeCl_2$ in acetonitrile and triethylamine. The resulting suspension was heated for several days at 95 °C. White needle-like crystals of the beryllium adduct **402** formed at the phase interface. A suitable crystal was selected and measured with the monochromated Cu-Kα radiation of a Stoe IPDS2T diffractometer equipped with a Xenocs Microfocus Source and a Dectris Pilatus 300K Detector. The crystal was kept at 97(2) K during data collection. The structure was solved with the Olex2 structure solution program and refined with the ShelX refinement package (Figure 4.5). The asymmetric unit consists of two complete molecules of the complex. The crystal space system is monoclinic and is in a $P2_1/c$ space group (R_1 = 7.35%).

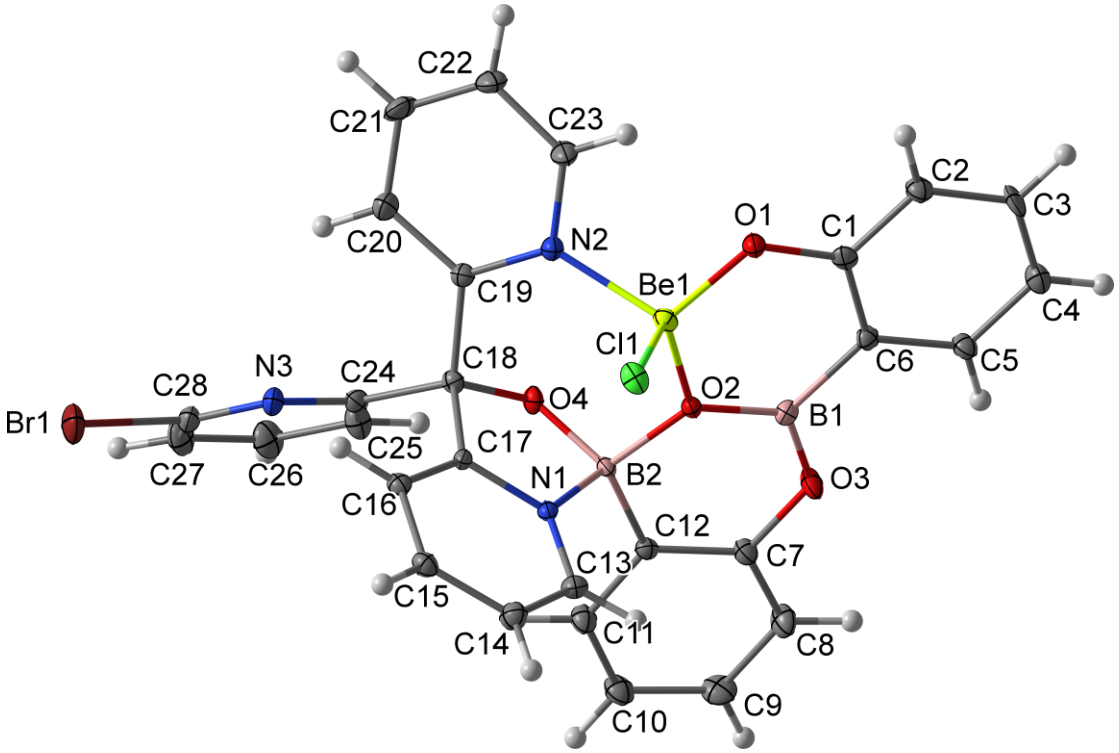

Figure 4.5 X-ray structure of the complex **402**, with thermal ellipsoids at 50% probability level.

This complex, although not targeted, exhibits some interesting properties. The coordination centre gives a slightly distorted tetrahedral geometry. The complex **402** is formed by the replacement of H24 of **306** (Figure 3.6, page 84) with beryllium chloride. The beryllium ion binds to one phenolic oxygen atom, one pyridyl nitrogen atom, one oxo group, and one chloride ion. This oxo group bridges the two boron atoms in this μ_3 complex to the beryllium cation. A pyridyl group of **306** changes its conformation so that in **402** it can bind through its nitrogen atom to the beryllium ion. Around the site of coordination, the two boronic acid-moieties and the coordinating pyridine is relatively planar. A second pyridyl group sits perpendicular to this plane, in a fashion such that a possible π-π interaction is taking place between its aromatic ring system and the lone chloride. The bond lengths of Be1···O1 (1.560(5) Å) and Be1···O2 (1.692(5) Å) are in the typical range found for beryllium-phenolate bonds. However the Be1···N2 bond (1.850(5) Å) is found to be elongated compared to N-donor beryllium complexes.[53, 56] The tetrahedral angles about the beryllium binding site varying from 103.2(2) – 113.1(2)°. This

results in a stable arrangement of donor atoms as the angles about the Be^{2+} atom are near to the ideal angles of a tetrahedral environment (average = 109.6°). This arrangement of nitrogen and oxygen donors provides a suitable tridentate binding pocket for Be^{2+}.[37, 40, 49]

This is the fifth reported structure to contain a Be···O···B bridge.[115] B1 and B3 occupy a trigonal planar and tetrahedral coordination environment respectively. The angles for each of these are found to be close to their expected values: O2···B1···O3 = 121.6(3)° and O2···B1···O4 = 109.3(3)°.

The unit cell is composed of four molecules of **402**. Revealed in the macrostructure is a small extent of packing of the equatorial components. The Be···Cl bonds alternatively point away and towards each other.

4.2.3 X-ray Crystal Structure of 403

The compound 2,2'-(pyridine-2,6-diyl)bisphenol was treated in the same manner as **301** and **306.** Crystals of the tridentate beryllium complex **403** formed, and were subjected to single X-ray structural determination (Figure 4.6). The orthorhombic crystal system is in a *Pbca* space group with a low R_1 index of 3.20%.

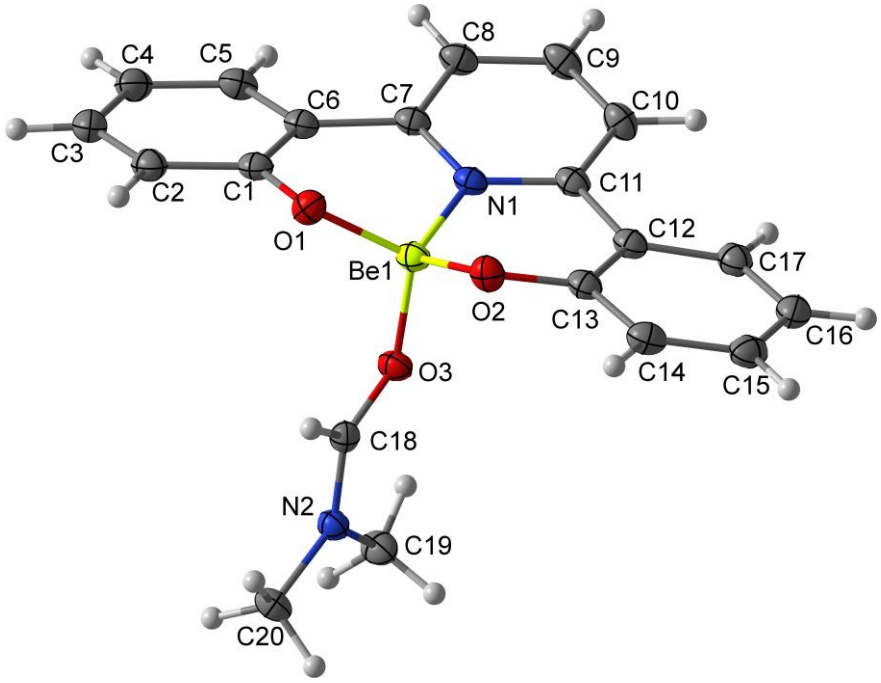

Figure 4.6 X-ray structure of the complex **403**, with thermal ellipsoids at 50% probability level.

The asymmetric unit consists of one doubly deprotonated and tridentate coordinating compound bound to beryllium through two phenolic oxygen atoms, and one pyridyl nitrogen atom. The last coordinating atom comes from the oxygen of the amide DMF. The binding site is in a tetrahedral geometry, with the backbone of the chelating ligand retaining most of its planarity.

A similar complex to **403** is known.[116] This is the same molecule, but the coordinating solvent is water as opposed to DMF (CCDC: **BOHMOB**). The bond lengths and angles of the coordinating atoms are comparative, with the bonds of **BOHMOB** being shorter (Table 4.1). The only significantly different bond is O_3···Be, and this is due to beryllium binding to two different functional groups (amide vs water). With the errors taken into account, the tetrahedrality of **403** and **BOHMOB** are not statistically significant.

Table 4.1 Experimental geometric parameters for **403** and **BOHMOB**.

		403	**BOHMOB**
Bond /Å	N-Be	1.7054(13)	1.687(7)
	O_1-Be	1.5684(15)	1.552(7)
	O_2-Be	1.5560(15)	1.559(6)
	O_3-Be	1.6915(14)	1.641(7)
Angle /°	N-Be-O_1	108.05(8)	107.5(4)
	N-Be-O_2	108.46(8)	107.8(4)
	N-Be-O_3	102.74(7)	104.7(4)
	O_1-Be-O_2	115.72(9)	113.0(4)
	O_1-Be-O_3	110.55(8)	110.8(4)
	O_2-Be-O_3	110.47(8)	112.5(4)
Geometry Index	τ_4	0.948(1)	0.954(6)

4.3 Experimental and Computational Comparison

In addition to the X-ray crystallography, the complex **401** was modelled and its structure optimised by DFT calculations using B3LYP/6-311++G(d,p) (Figure 4.7). Its ^{9}Be NMR was calculated with the GIAO (gauge-including atomic orbital) method. A large basis set is required to obtain good results with all computational NMR methods. Therefore, the same large triple-zeta basis set (6-311++G(d,p) was used. The combination of a structural and spectral comparison of the experimental data to the computational data will give a good indication towards the accuracy and reliability of the computational work.

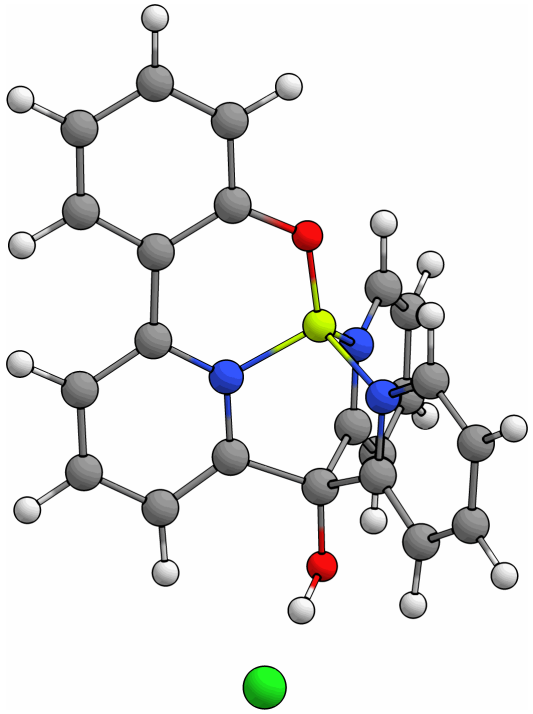

Figure 4.7 Aqueous phase geometry optimised complex **401** at B3LYP/6-311++G(d,p).

4.3.1 Structural Comparison

As done so previously (Figure 4.8, page 100), a comparison was made between the crystal structure and computational model of **401** (Figure 4.9). There is an extremely high degree of agreement for all bond lengths, angles, and dihedrals. Table 4.2 lists the key values of this complex. Most of the calculated values are exactly within the error of the experimentally determined values. Where they differ, they only differ by less than 0.7%. The calculated bond lengths have been slightly overestimated, which differs from what was expected. Usually, it is found that calculated values are underestimated as they are the equilibrium values and experimental values are vibrationally averaged values. The bond angles have converged to be closer to the ideal tetrahedral angles (τ_4(calc.) of 0.840 and τ_4(exp.) of 0.838), but these are within the error parameters. Therefore, their geometries are essentially the same.

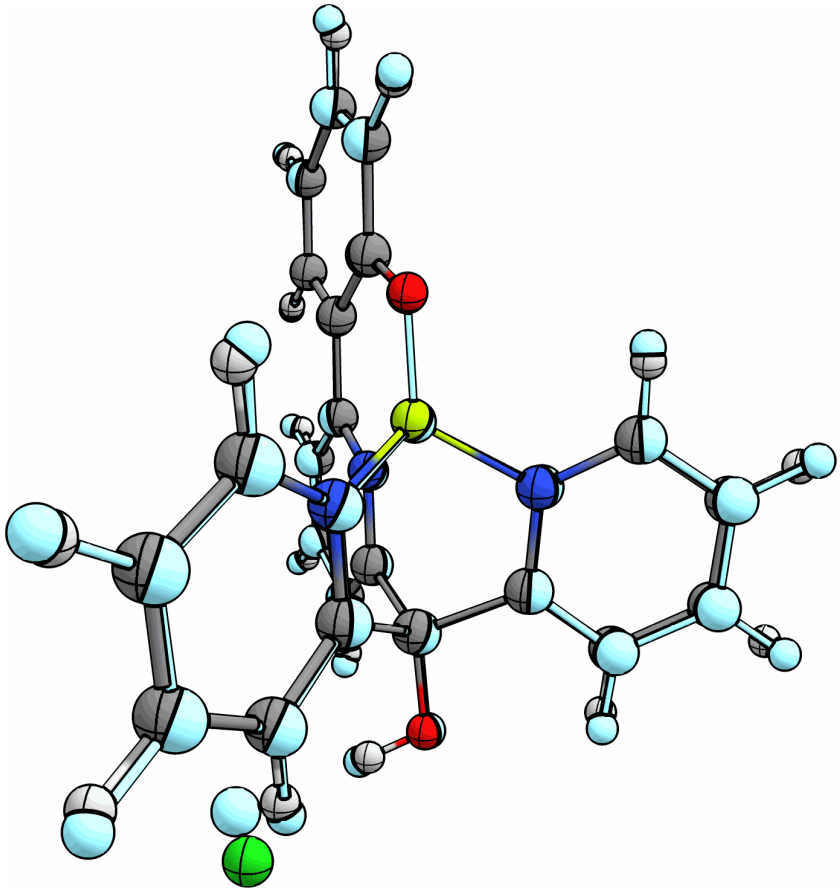

Figure 4.9 Computational structure of **401** (coloured normally, with crosses) merged with the X-ray structure for **401** (coloured light-blue).

Table 4.2 Calculated and experimental geometric parameters for **401**.

		Calc.	Exp.
Bond /Å	O-Be	1.524	1.511(3)
	N_1-Be	1.689	1.687(4)
	N_2-Be	1.755	1.745(4)
	N_3-Be	1.747	1.740(4)
Angle /°	O-Be-N_1	110.7	111.4(2)
	O-Be-N_2	120.2	120.0(2)
	O-Be-N_3	121.4	121.9(2)
	N_1-Be-N_2	100.90	100.58(19)
	N_1-Be-N_3	101.63	100.73(19)
	N_2-Be-N_3	98.70	98.65(19)
Geometry Index	τ_4	0.840	0.838

The two noticeable (but not significant) differences are in the C···H bond lengths, and the placement of the Cl^- ion. The first is explained due to the placement of hydrogens through

the Olex2 program, which is known to estimate artificially long C···H bonds. The displacement of the chloride ion is likely due to either the solvation model used in the calculation (IEF-PCM), or an interaction in the unit cell that has not been taken into account.

It was found that there was overall a good agreement between the two structures. The backbone of the X-ray structure had a 3.11° dihedral angle, whereas the computational model has a 21.18° dihedral angle. This deformation is due to an artificially shortened hydrogen bond between the phenol proton and the nearby pyridyl arm (2.339 Å) of the model. The other major difference between the structures is the arrangement of the other pyridyl arm, which is found to be further twisted away from the binding site in the computational model. This unfavourable contortion can be explained due to the model allowing a strong hydrogen bond between the tertiary alcohol proton and the pyridyl nitrogen (1.823 Å). This does not exist in the X-ray structure because of the intermolecular hydrogen bonds (Figure 3.13).

4.3.2 Spectral Comparison

The ^{9}Be NMR of **401** was obtained at the University of Marburg. The NMR was done in the solvents 1,2-difluorobenzene, DMF, and acetonitrile, prior to its crystallization. The spectrum gave broad signals at 2.68 ppm and 6.17 ppm (using $[Be(H_2O)^{2+}$ as the reference compound). The lower peak at 2.68 ppm is attributed to the $[BeCl(DMF)_3]^+$ species, and the higher peak at 6.17 ppm is attributed to the **401** complex. The broadness of the peaks suggests exchange between the species, so it is plausible that the actual ^{9}Be signal is slightly further downfield. The calculated value for **401** is 6.06 ppm. Few computational studies have investigated the NMR properties of beryllium complexes. Those that have tend towards larger differences between the computational and experimental data.[66b] Other tetradentate complexes of beryllium typically have differences between 0.3 ppm and 2.1 ppm, and as high as 5.3 ppm. The calculated value of 6.06 ppm for the ^{9}Be shift in **401**

is found in the same range as bischelates of beryllium (through alcohol and ketone functionals), which is only a little lower than what was expected. The small difference between the calculated and the experimental value for **401** is only 0.11 ppm (1.8%). Therefore, this degree of preciseness suggests that the computational model can make accurate predictions.

4.4 Summary

Three new beryllium-containing complexes were successfully characterised by X-ray crystallography. Due to the nature of beryllium, relatively few Be^{2+}-containing crystal structures exist. Nonetheless, these new complexes are unique and interesting structures (in particular **401** and **402**). The comparison of experimental and computational data of **401** has shown that there is both a good geometric and spectroscopic fit. Therefore, the computational model appears reliable, allowing further predictions to be made. As a part of future study, it is recommended that competition studies are performed.

Chapter 5: Computation of Buttressed Ligands

"It is unworthy of excellent men to lose hours like slaves in the labour of calculation which could be safely relegated to anyone else if a machine were used."

– Gottfried Wilhelm Leibniz

5.1 Introduction

The thesis of this work is that buttress groups through hydrogen bonding will enhance the binding strength of certain ligand designs towards small cations, and in particular Be^{2+}. Therefore, extensive buttressing types have been considered in this chapter (Figure 5.1). As before, the three apex groups previously examined will be further considered. This chapter also provides a comprehensive metal binding study, which compares two new ligands to known beryllium binders.

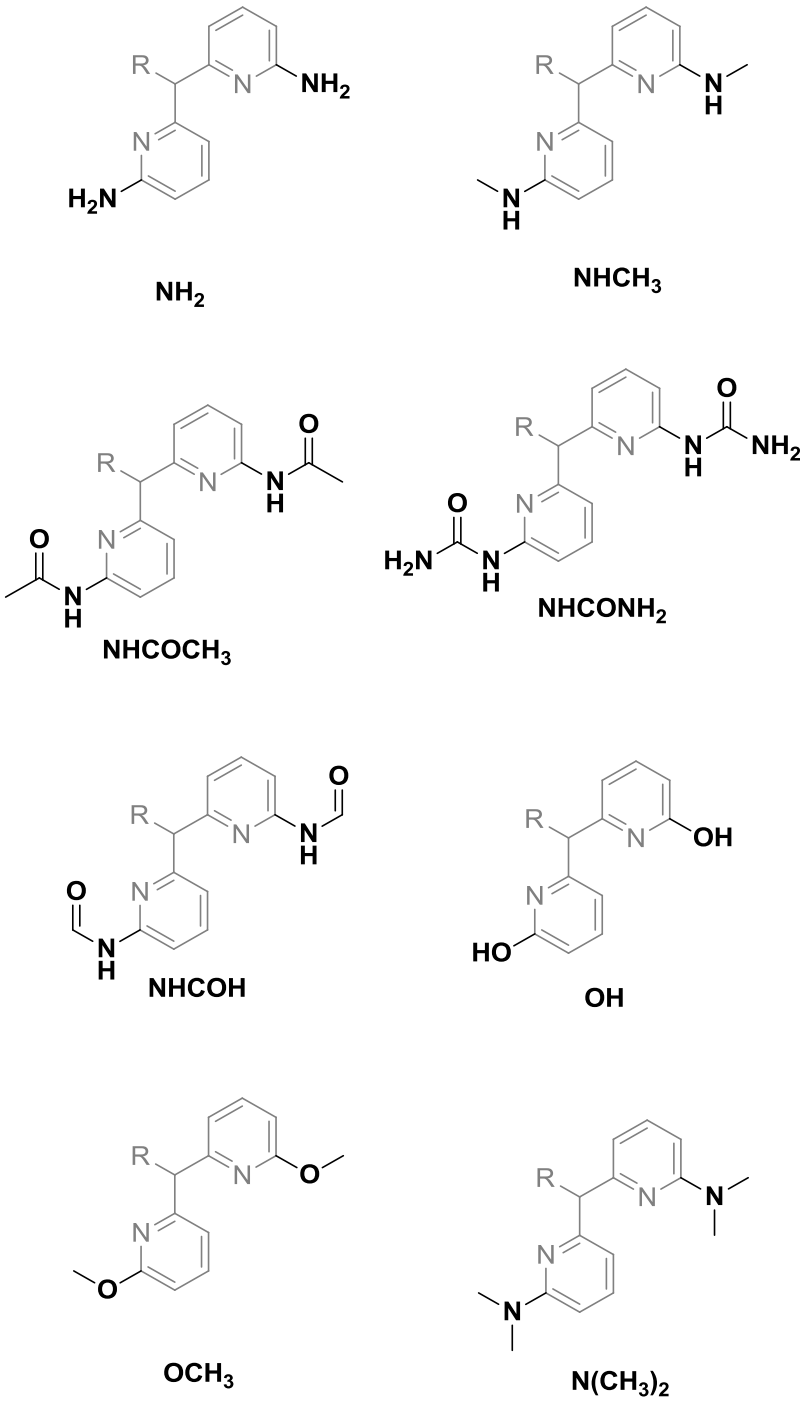

Figure 5.1 Buttress groups investigated, where R denotes the rest of the ligand motif.

5.2 Buttress groups

For every ligand, the following buttress groups have been investigated: NH_2, $NHCH_3$, $NHCOCH_3$, and $NHCONH_2$. **L1** and **L2** were examined further with the buttress group NHCOH. These buttressing groups were designed to provide a secondary sphere of

coordination through a network of intramolecular hydrogen bonds. **L1** was investigated further still with **OH**, **$N(CH_3)_2$**, and **OCH_3**. It should be noted that these last two groups do not contain a hydrogen bond capable proton, therefore are not able to form a secondary sphere of coordination like the others.

5.2.1 Ligand Geometries

The optimised structures of all ligands were calculated as done previously. It would be impractical to present an image of every combination of ligand, buttress, and metal, so the following figure only gives an image of each buttress using **L1ch** as the base ligand (Figure 5.2). Any unique conformations will be discussed separately; otherwise only general trends will be given for each buttress. In theory, the buttress groups should both enhance the binding strength and selectivity of the ligands, as well as helping to pre-organise their binding cavities.

It has been observed to be the case that when capable, each buttress group investigated enables the ligand to assemble itself into its near-complex-like geometry. Pre-organisation has to some extent been observed with each buttress group. This modifies their rigidity, which should in theory lead to reduced conformational freedom – increasing the potential for selective binding of beryllium over other metals.

Hydrogen bonds in **L1chNH$_2$** are found between the phenolic proton and adjacent pyridyl nitrogen (1.748 Å), and one buttress amine proton and the phenolic oxygen (2.286 Å). It is the case however, that one pyridyl arm still faces away from the binding site. The same hydrogen bonds are observed in **L1chNHCH$_3$** (1.744 Å and 2.283 Å respectively). Its geometry is overall the same, but the other pyridyl arm is twisted much further away. The buttress for **L1chNHCONH$_2$** has a more complex arrangement, as the oxygen of one buttress group also participates, forming a hydrogen bond with the phenolic proton (2.048 Å). A weak electrostatic interaction is found between the involved secondary amine

proton and the opposing pyridyl nitrogen (3.485 Å). The result is that all donor atoms point towards a single cavity. It is likely that a steric effect strains the geometry of the larger buttress groups, which prevents the pyridyl arms from coming closer together without a strongly attractive cation present. This is the case for the **L1chNHCOCH$_3$** buttress, where only weak electrostatic interactions are present between the potential hydrogen bond candidates.

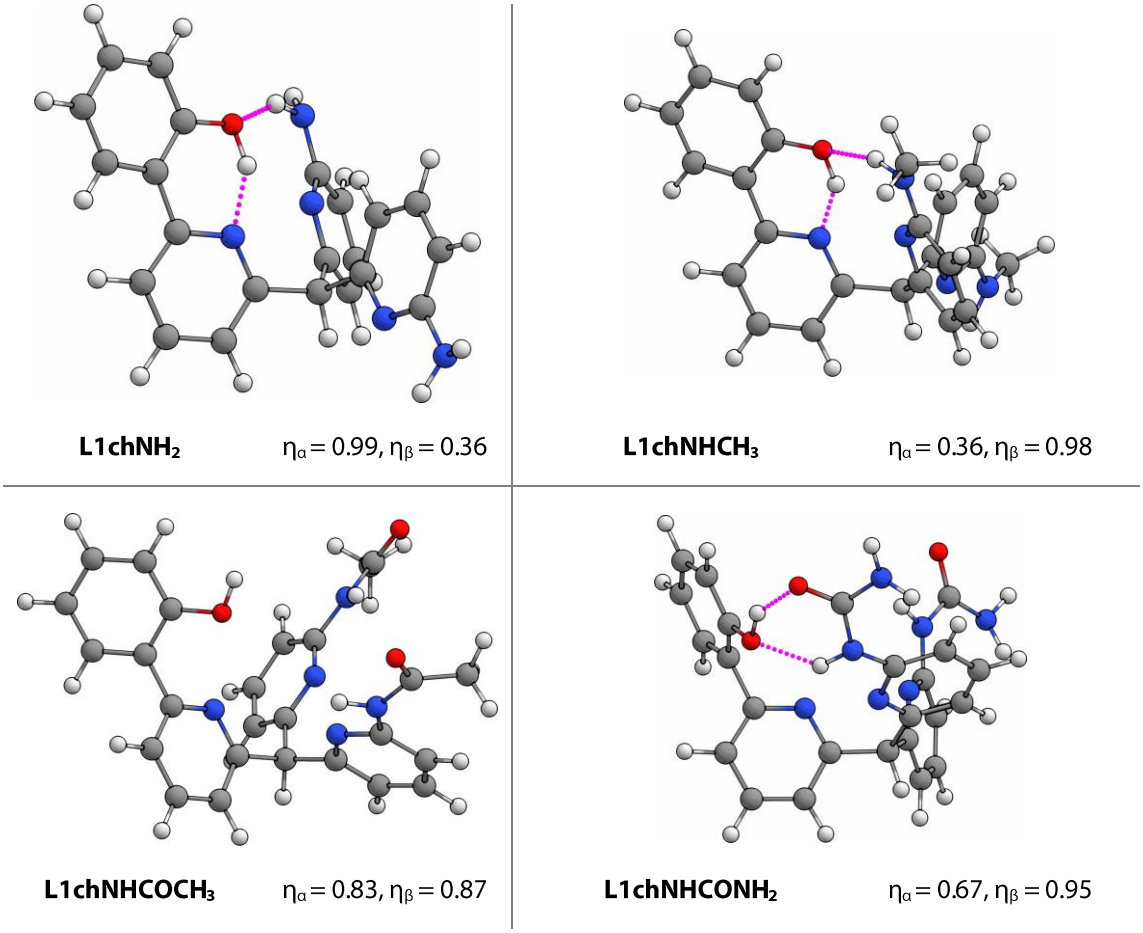

Figure 5.2 Aqueous phase geometry optimised ligand **L1** with each of the four buttresses that have been examined for each ligand type, at B3LYP/6-311++g(d,p).

L1 was further studied with four more groups of various buttressing ability (Figure 5.3). One is another small secondary amine, whilst the other has a hydroxyl group. The ether and tertiary amino groups will not be involved in a secondary coordination sphere, but their steric effects, weak electrostatic interactions, and ring interactions may provide

information about the types of contributions the buttresses have to binding metals. **L1chNHCOH** is pre-organised in the same manner as **L1chNHCH$_3$** except in this case no strong hydrogen-bonds are observed except between the buttress pyridyl nitrogen and the adjacent an amide proton.

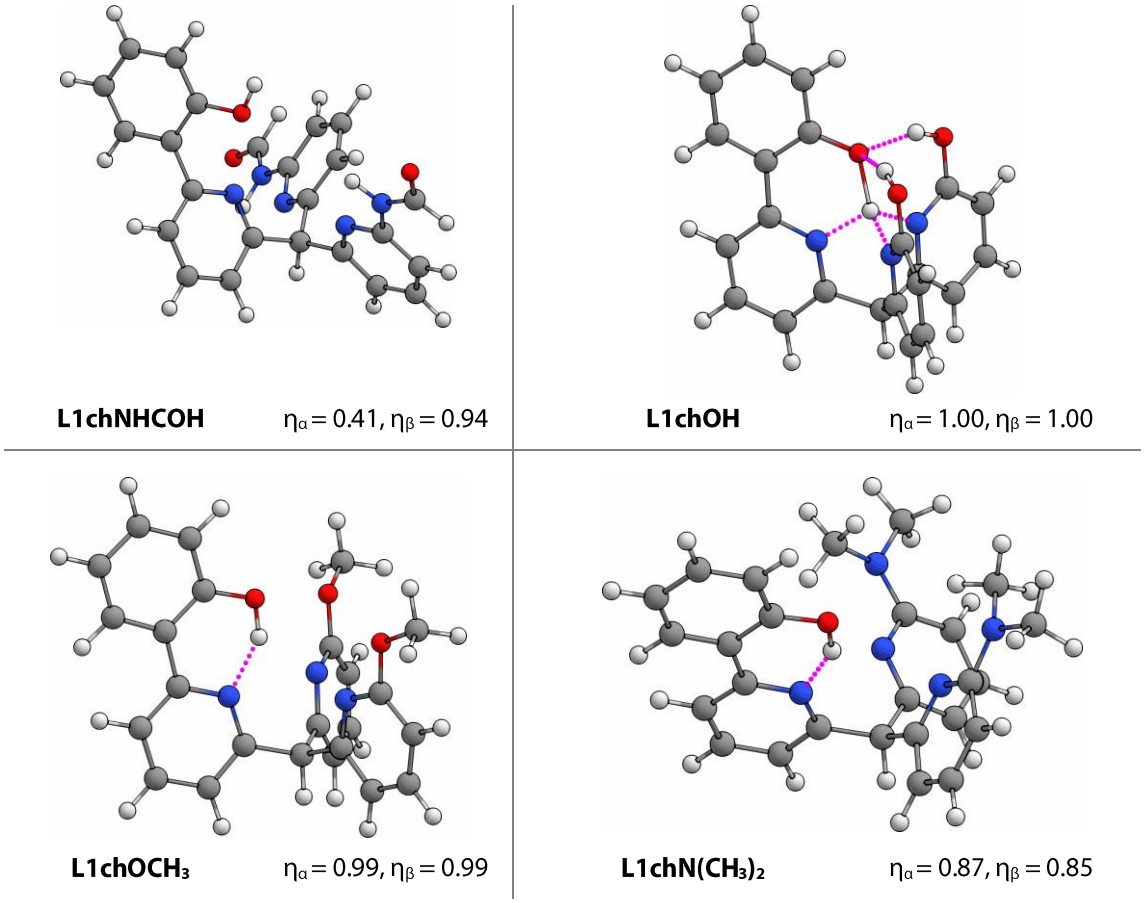

Figure 5.3 Aqueous phase geometry optimised ligand **L1** with the second four buttresses that have been only examined for **L1** and **L2**, at B3LYP/6-311++G(d,p).

It is the case that for all ligand types, partial pre-organisation has taken place. In most cases, one buttress arm comes close to the binding site through a hydrogen bond. This is in stark contrast to the disordered structure of **L1chH** (Figure 2.7, page 54). From these geometries, it is predicted that binding energies towards small cations should increase over that of the non-buttressed ligands. **L4** and **L5** show less pre-organisation, except in the cases with small buttress groups (**NH$_2$** and **NHCH$_3$**). It is with these small 1° and 2° amine components that the highest degree of pre-organisation is observed.

5.2.2 Complex Geometries

Immediately, it is clear from the complex geometries that the buttress groups have – be it favourable or otherwise – significantly altered the complex structures relative to the non-buttressed cases. The **L1** series of calculations have been shown with each of the four buttresses used for all motifs, as well as the four buttresses that were only examined in cases for **L1** and **L2** (Figures 5.4-5.6). All key bond lengths and angles, including present hydrogen bonds, have been listed also (Tables 5.1-5.8). After examining all complex structures, it was found that the **L1** series, overall, fit well the trends observed in the other ligands. Any deviations of note will be discussed later in this chapter.

For the smaller buttresses (e.g. **NH_2** and **$NHCH_3$**), two hydrogen bonds are present. These form a secondary sphere of interaction just beyond the core metal binding site. They occur between the phenolic oxygen bound to the metal, and the nearby labile protons attached to a heteroatom of the buttress. The larger buttresses (e.g. **$NHCOCH_3$** and **$NHCONH_2$**) have either one or two hydrogen bonds present. It is sometimes the case that one buttress arm does not come in close enough proximity with a potential hydrogen bond acceptor to form a strong interaction. The steric bulk of these buttress groups cause large unfavourable proximity interactions with the opposing buttress arm, causing them to lie at significant angles away from what would be ideal as exhibited by the smaller buttresses.

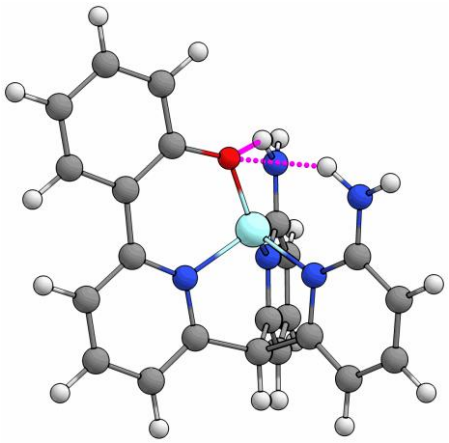

L1chNH$_2$_Al

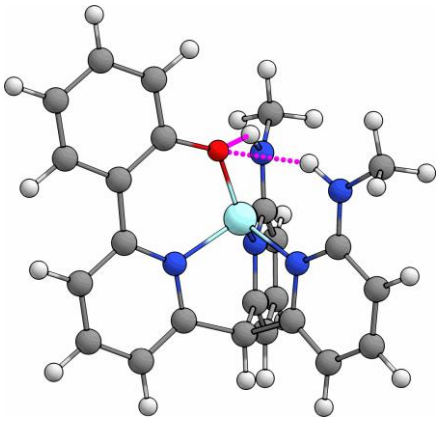

L1chNHCH$_3$_Al

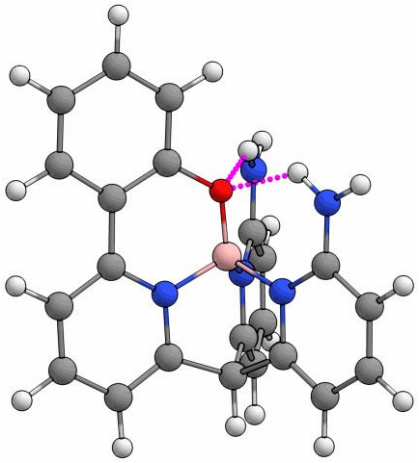

L1chNH$_2$_B

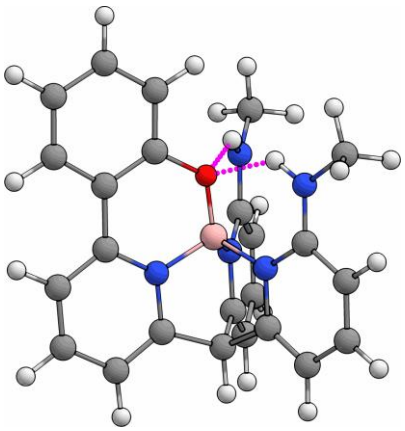

L1chNHCH$_3$_B

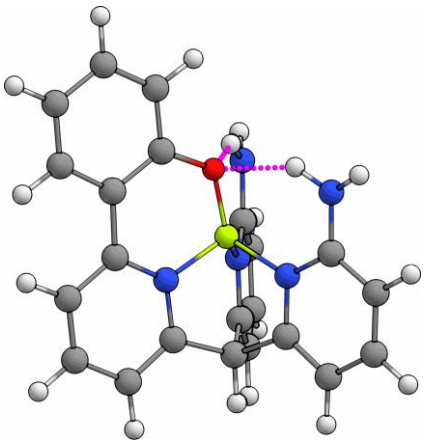

L1chNH$_2$_Be

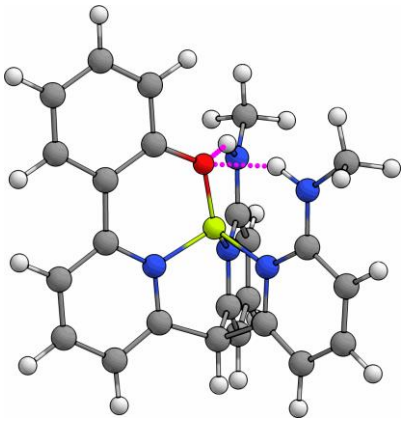

L1chNHCH$_3$_Be

Figure 5.4 Aqueous phase geometry optimised complexes **L1chNH$_2$** and **L1chNHCH$_3$**, formed with Al^{3+}, B^{3+}, and Be^{2+}, examined at B3LYP/6-311++G(d,p).

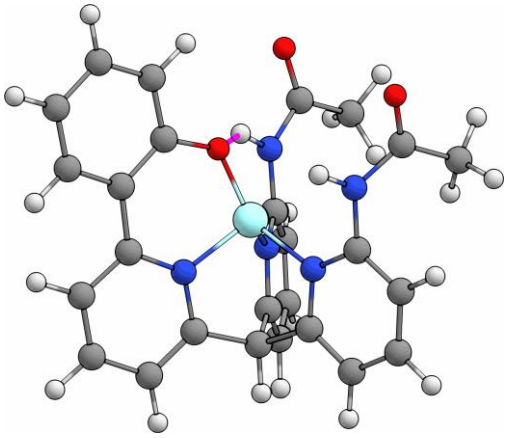

L1chNHCOCH$_3$_Al

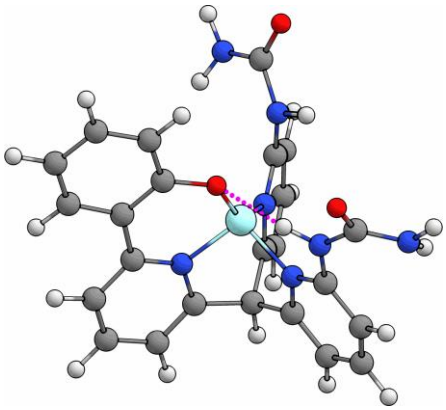

L1chNHCONH$_2$_Al

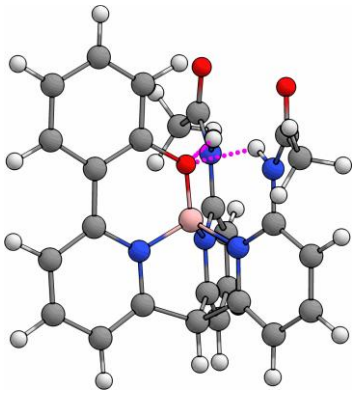

L1chNHCOCH$_3$_B

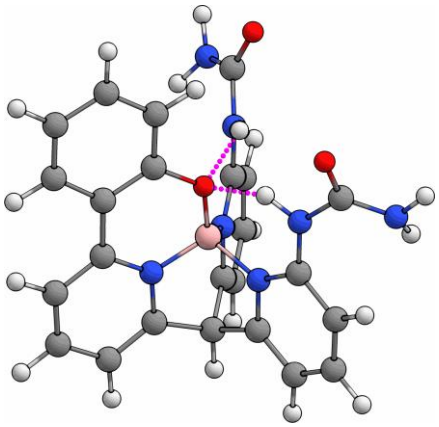

L1chNHCONH$_2$_B

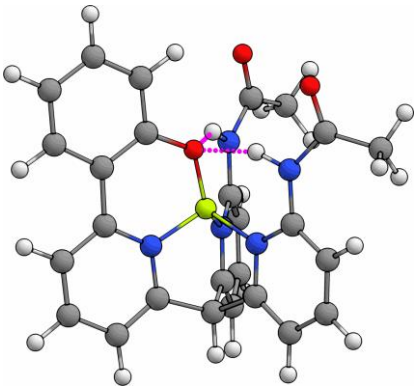

L1chNHCOCH$_3$_Be

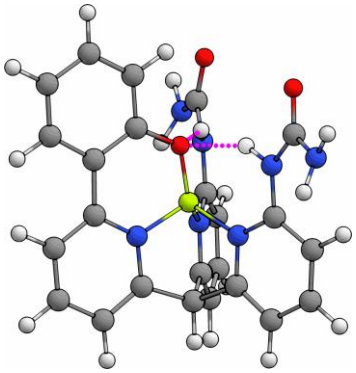

L1chNHCONH$_2$_Be

Figure 5.5 Aqueous phase geometry optimised complexes **L1chNHCOCH$_3$** and **L1chNHCONH$_2$**, formed with with Al^{3+}, B^{3+}, and Be^{2+}, examined at B3LYP/6-311++G(d,p).

The hydrogen bonding interactions range between very strong, mostly covalent bonds (1.852 Å) to slightly weaker, more electrostatic bonds (2.573 Å), and included a small

number of weak hydrogen bonds (3.324 Å). A strong relationship is found between the length of hydrogen bonds present, and the 'tightening' or reduction in cavity size. This involved the bond lengths between metal and binding atoms, as well as the tetrahedrality of the binding site.

The secondary hydrogen bonding causes the phenolic oxygen to be drawn slightly away from the metal. On average, a 1% increase in the length of the O···M bond is observed for buttressed ligands over their non-buttressed forms, which corresponds to a weakening of the bond. Nevertheless, the presence of this secondary sphere of hydrogen bonding stabilises the overall structure over that of the non-buttressed complexes, as evidenced by their binding energies.

L1chNH$_2$ when directly compared with **L1chH** is strictly a stronger chelator as it binds to each metal cation closer and more compactly. Higher τ values are obtained for each complex, which corresponds to a closer tetrahedral binding geometry. The strong attraction of the buttress amine protons to the phenolic oxygen creates a pulling effect on the rest of the pyridyl arm. The result is that the pyridyl nitrogen atoms are all pulled in towards the metal binding site.

The buttress groups **OCH$_3$** and **N(CH$_3$)$_2$** in their neutral states cannot take part in hydrogen bonds as the hydrogen donor, as the previously available proton has been replaced with a methyl group (Figure 5.6). It is expected that these groups will destabilise the complex by introducing groups that will push away from the binding site due to repulsive electrostatic interactions with the phenolic oxygen.

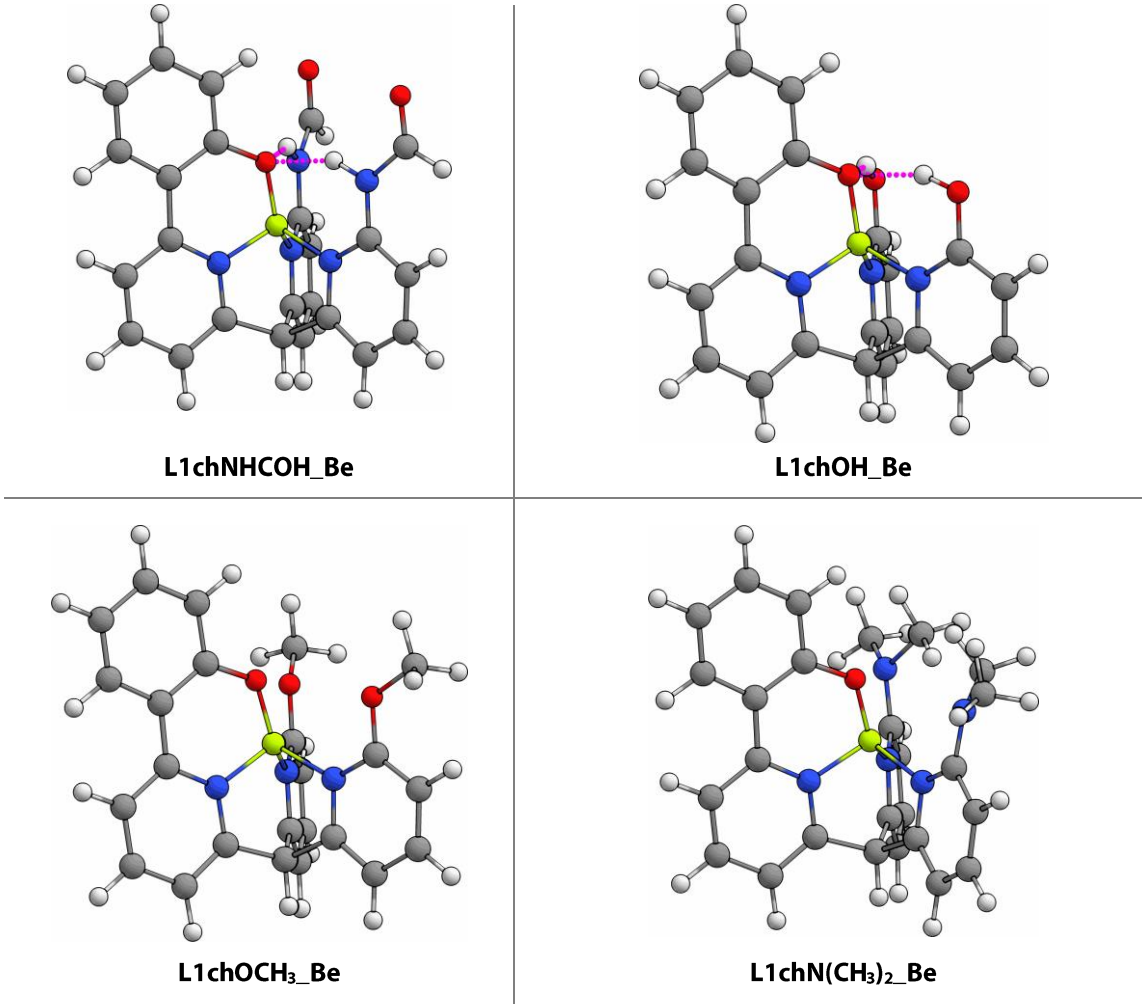

Figure 5.6 Aqueous phase geometry optimised complexes **L1chNHCOH**, **L1chOH**, **L1chOCH$_3$**, **L1chN(CH$_3$)$_2$** formed with Be^{2+}, examined at B3LYP/6-311++G(d,p).

Table 5.1 Geometric parameters for **L1chNH$_2$**.

L1chNH$_2$				
		Al	**B**	**Be**
Bond /Å	O-M	1.714	1.414	1.549
	N_1-M	1.872	1.568	1.697
	N_2-M	1.899	1.597	1.751
	N_3-M	1.899	1.597	1.751
	O-H_1	2.632	2.007	2.115
	O-H_2	2.573	2.007	2.116
Angle /°	O-M-N_1	102.3	112.3	109.0
	O-M-N_2	126.3	114.8	120.5
	O-M-N_3	124.7	114.8	120.5
	N_1-M-N_2	99.3	105.2	102.0
	N_1-M-N_3	99.2	105.2	102.0
	N_2-M-N_3	98.9	103.5	99.9
Index	τ_4	0.77	0.92	0.84

Table 5.2 Geometric parameters for **L1chNHCH$_3$**.

L1chNHCH$_3$				
		Al	**B**	**Be**
Bond /Å	O-M	1.715	1.416	1.550
	N_1-M	1.873	1.569	1.696
	N_2-M	1.897	1.599	1.752
	N_3-M	1.897	1.599	1.752
	O-H_1	2.559	1.952	2.080
	O-H_2	2.524	1.953	2.080
Angle /°	O-M-N_1	102.2	112.0	108.9
	O-M-N_2	125.9	114.9	120.4
	O-M-N_3	124.8	114.9	120.4
	N_1-M-N_2	99.2	105.3	102.0
	N_1-M-N_3	99.4	105.3	102.0
	N_2-M-N_3	99.4	103.5	100.3
Index	τ_4	0.78	0.92	0.85

Table 5.3 Geometric parameters for **L1chNHCOCH$_3$**.

L1chNHCOCH$_3$				
		Al	**B**	**Be**
Bond /Å	O-M	1.542	1.713	1.404
	N_1-M	1.691	1.884	1.556
	N_2-M	1.765	1.921	1.618
	N_3-M	1.765	1.919	1.620
	O-H_1	2.003	2.313	1.955
	O-H_2	1.996	3.324	2.023
Angle /°	O-M-N_1	101.3	113.1	109.1
	O-M-N_2	118.6	114.5	120.4
	O-M-N_3	137.0	114.7	120.6
	N_1-M-N_2	98.1	105.3	102.4
	N_1-M-N_3	97.3	105.1	102.4
	N_2-M-N_3	96.3	102.9	99.3
Index	τ_4	0.74	0.93	0.84

Table 5.4 Geometric parameters for **L1chNHCONH$_2$**.

L1chNHCONH$_2$				
		Al	**B**	**Be**
Bond /Å	O-M	1.715	1.409	1.541
	N_1-M	1.883	1.562	1.680
	N_2-M	1.917	1.613	1.766
	N_3-M	1.918	1.613	1.765
	O-H_1	3.492	2.001	2.014
	O-H_2	2.268	1.894	2.008
Angle /°	O-M-N_1	101.3	112.3	110.3
	O-M-N_2	137.7	115.8	119.8
	O-M-N_3	117.7	114.1	119.6
	N_1-M-N_2	98.0	104.9	102.0
	N_1-M-N_3	98.1	105.9	102.0
	N_2-M-N_3	96.1	102.7	100.4
Index	τ_4	0.74	0.92	0.85

Table 5.5 Geometric parameters for **L1chNHCOH**.

L1chNHCOH				
		Al	**B**	**Be**
Bond /Å	O-M	1.709	1.407	1.542
	N_1-M	1.870	1.556	1.685
	N_2-M	1.913	1.617	1.763
	N_3-M	1.912	1.617	1.761
	O-H_1	2.574	1.935	2.002
	O-H_2	2.536	1.941	1.986
Angle /°	O-M-N_1	102.5	112.9	109.8
	O-M-N_2	126.5	114.9	120.4
	O-M-N_3	125.4	114.6	119.9
	N_1-M-N_2	99.1	105.4	102.2
	N_1-M-N_3	99.0	105.4	102.4
	N_2-M-N_3	98.0	102.6	99.5
Index	τ_4	0.77	0.93	0.85

Table 5.6 Geometric parameters for **L1chOH**.

L1chOH				
		Al	**B**	**Be**
Bond /Å	O-M	1.707	1.421	1.545
	N_1-M	1.861	1.554	1.675
	N_2-M	1.906	1.593	1.735
	N_3-M	1.906	1.593	1.735
	O-H_1	2.617	1.857	1.977
	O-H_2	2.618	1.852	1.977
Angle /°	O-M-N_1	103.6	113.6	111.4
	O-M-N_2	125.1	114.2	119.1
	O-M-N_3	125.1	114.0	119.1
	N_1-M-N_2	99.6	105.4	102.2
	N_1-M-N_3	99.6	105.4	102.2
	N_2-M-N_3	98.5	103.1	100.2
Index	τ_4	0.78	0.93	0.86

Table 5.7 Geometric parameters for **L1chN(CH$_3$)$_2$**.

L1chN(CH$_3$)$_2$				
		Al	**B**	**Be**
Bond /Å	O-M	1.711	1.387	1.532
	N_1-M	1.902	1.567	1.717
	N_2-M	1.920	1.620	1.793
	N_3-M	1.920	1.620	1.793
Angle /°	O-M-N_1	99.3	112.3	106.7
	O-M-N_2	133.0	116.9	123.4
	O-M-N_3	121.7	114.1	119.7
	N_1-M-N_2	97.9	104.7	100.2
	N_1-M-N_3	100.3	104.5	101.5
	N_2-M-N_3	97.5	103.1	101.6
Index	τ_4	0.75	0.92	0.83

Table 5.8 Geometric parameters for **L1chOCH$_3$**.

L1chOCH$_3$				
		Al	**B**	**Be**
Bond /Å	O-M	1.720	1.395	1.532
	N_1-M	1.897	1.571	1.717
	N_2-M	1.924	1.614	1.822
	N_3-M	1.916	1.621	1.817
Angle /°	O-M-N_1	100.7	112.9	107.5
	O-M-N_2	129.8	116.0	123.2
	O-M-N_3	129.8	115.8	123.2
	N_1-M-N_2	96.8	104.3	100.9
	N_1-M-N_3	96.8	104.4	100.9
	N_2-M-N_3	93.6	101.9	97.2
Index	τ_4	0.71	0.91	0.81

Some complexes diverged from the typical geometries observed. For some of the investigated ligand motifs, the large buttresses, which contain multiple available donor atoms, form 5- and 6- coordinate complexes. This is because they allow for further intramolecular bonds to the captured metal through the donor atoms of the buttress (Figures 5.7-5.8). In this case, this is beneficial for the binding of larger metal cations that prefer to adopt coordination geometries larger than the preferred four. This outcome was

not surprising given the geometric preferences of Al^{3+}. In the 5-coordinate case, explicit solvation would likely increase the binding mode to 6-coordinate.

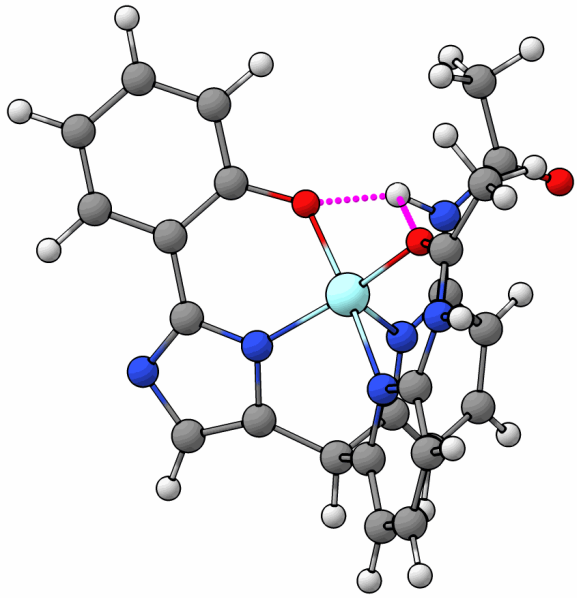

Figure 5.7 L5chNHCOCH3_Al is 5-coordinate.

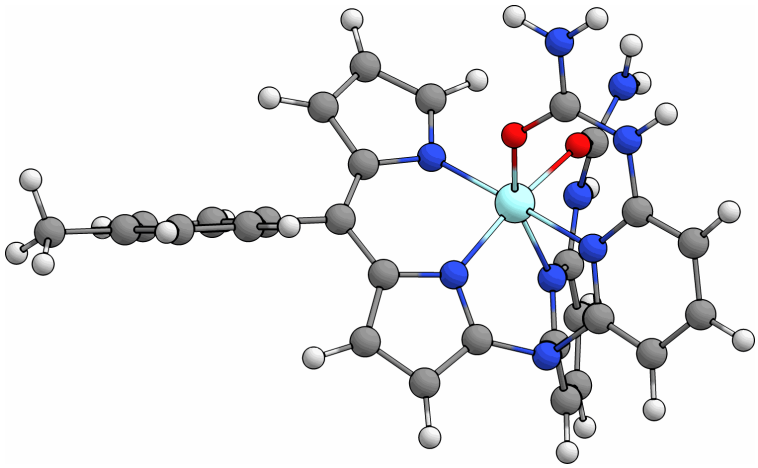

Figure 5.8 L4nNHCONH2_Al is 6-coordinate.

5.2.3 Binding Energies

An extensive series of calculations were made such that the binding energy of each ligand, with each buttress, and with each studied metal, could be identified (Tables 5.9-5.13). It is the case that the NH_2 and $NHCH_3$ buttress groups increased the binding energy towards

all three metal cations over the non-buttressed complexes for all ligands but **L4**. It remains the case that every examined complex binds to boron more strongly than beryllium. In the most favourable case, from **L1chH** to **L1chNHCH$_3$**, binding to Be^{2+} increased by 12.3% (43.49 kJ mol^{-1}), to B^{3+}, a 4.3% increase (31.38 kJ mol^{-1}), and to Al^{3+}, a 13.3% increase (43.56 kJ mol^{-1}).

Table 5.9 Calculated binding energies of **L1ch** complexes with varying buttress groups.

L1ch	ΔG_{aq} / kJ mol^{-1}		
Buttress	**Al**	**B**	**Be**
None	-326.85	-734.07	-352.15
NH$_2$	-358.03	-754.55	-383.71
NHCH$_3$	-370.41	-765.45	-395.64
NHCOCH$_3$	-298.79	-679.70	-347.84
NHCONH$_2$	-308.81	-691.58	-349.35
NHCOH	-286.23	-672.83	-344.98
OH	-279.15	-694.86	-353.69
N(CH$_3$)$_2$	-329.37	-675.86	-296.63
OCH$_3$	-349.87	-710.94	-345.80

Table 5.10 Calculated binding energies of **L2ch** complexes with varying buttress groups.

L2ch	ΔG_{aq} / kJ mol^{-1}		
Buttress	**Al**	**B**	**Be**
None	-279.80	-673.82	-318.76
NH$_2$	-304.23	-691.14	-342.49
NHCH$_3$	-297.23	-642.19	-264.11
NHCOCH$_3$	-237.78	-616.08	-296.46
NHCONH$_2$	-240.30	-605.40	-271.27
NHCOH	-218.49	-601.60	-309.16

Table 5.11 Calculated binding energies of **L3ch** complexes with varying buttress groups.

L3ch	ΔG_{aq} / kJ mol^{-1}		
Buttress	**Al**	**B**	**Be**
None	-360.83	-762.21	-382.89
NH_2	-390.92	-782.11	-413.29
$NHCH_3$	-385.50	-772.91	-406.07
$NHCOCH_3$	-310.64	-685.80	-354.90
$NHCONH_2$	-435.76	-709.48	-361.54

Table 5.12 Calculated binding energies of **L4ch** complexes with varying buttress groups.

L4ch	ΔG_{aq} / kJ mol^{-1}		
Buttress	**Al**	**B**	**Be**
None	-331.50	-733.17	-340.16
NH_2	-325.68	-691.73	-331.91
$NHCH_3$	-331.96	-669.86	-269.37
$NHCOCH_3$	-284.90	-618.25	-286.34
$NHCONH_2$	-300.95	-585.91	-249.01

Table 5.13 Calculated binding energies of **L5ch** complexes with varying buttress groups.

L5ch	ΔG_{aq} / kJ mol^{-1}		
Buttress	**Al**	**B**	**Be**
None	-424.99	-831.82	-390.51
NH_2	-440.36	-841.97	-405.97
$NHCH_3$	-439.48	-847.11	-348.42
$NHCOCH_3$	-505.15	-773.49	-391.01
$NHCONH_2$	-522.06	-783.30	-394.16

The exact binding strength trend differs in each case, but the general observations are the following:

1. Binding strength decreases in the order $B^{3+} > Be^{2+} > Al^{3+}$
2. For B^{3+} and Be^{2+} complexes, small buttresses are preferable
3. For Al^{3+}, after their preference for the **NH_2** and **$NHCH_3$** buttress groups, non-hydrogen bond capable groups are favourable
4. There is often a large drop in energy between the small and large buttresses

It is of note that for **L1**, the **$NHCOCH_3$**, **$NHCONH_2$**, **NHCOH**, and **OH** buttress groups resulted in approximately the same binding strength towards the Be^{2+} cation (-344.98 to -353.69 kJ mol^{-1}), but significantly reduced binding strengths towards the B^{3+} and Al^{3+} cations. This is also the case for **L2chNHCOH**. Of the buttress groups investigated, it was the **$NHCH_3$** buttress group that gave the highest increase in binding energy towards the Be^{2+} cation.

For **L1**, **L2**, and **L4**, the binding energy towards the cations typically decreased when any buttress was used other than **NH_2** or **$NHCH_3$**. In the case of **L3** and **L5**, increases in binding strength were observed. The motif of **L4** does not allow the formation of a secondary sphere like that of the others – therefore any 'buttress' is a substituent that would be disruptive. In the cases of the **OCH_3** and **$N(CH_3)_2$** substituents, their respective complexes had increased binding towards the Al^{3+} cation, and decreased binding towards the others. This is due to the bulkiness and increased availability of donor atoms and aluminium's preference to adopt non-tetrahedral coordinate systems.

5.2.4 Comparison

The best buttresses for increasing binding strength are **NH_2** and **$NHCH_3$**, with the overall best binder towards Be^{2+} being **L3chNH_2**. The binding energies of **L3** with each buttress and metal are compared in Figure 5.9.

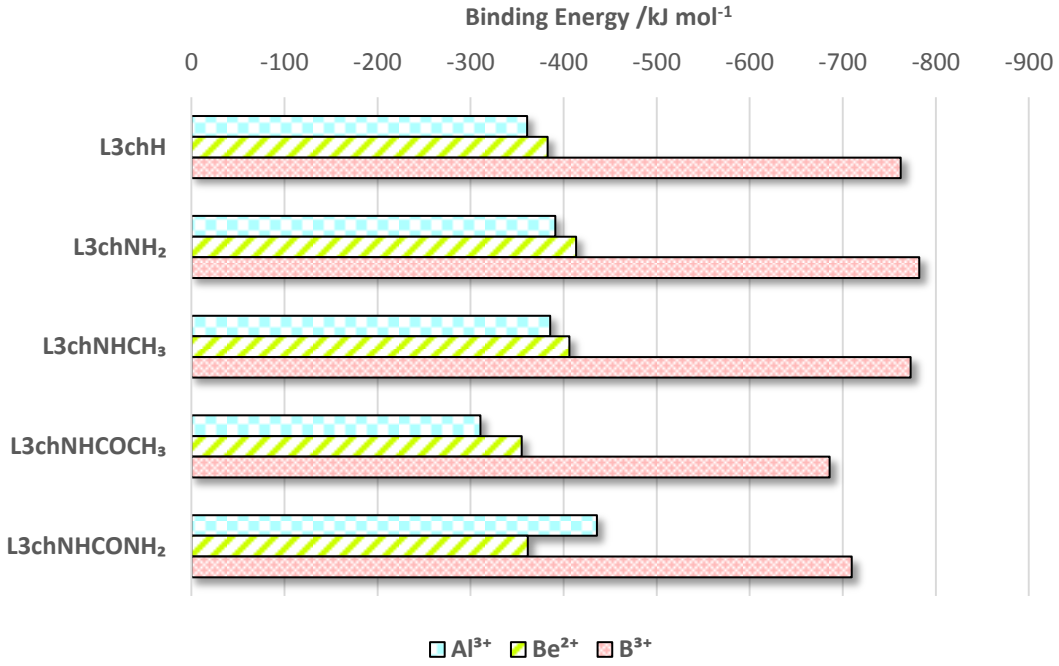

Figure 5.9 Binding energies of **L3** with each buttress type.

The space-filling representations of **L1chH** and **L1chNH$_2$** bound to Be^{2+} show that beryllium fits tightly within the binding cavity of the ligands (Figure 5.10). With the addition of the two amino groups, the Be^{2+} cation is almost completely encapsulated. This demonstrates an advantage that the second-shell hydrogen bonding provides, thus reinforcing the evidence for buttressing leading to stronger binding. A group that protects beryllium from outside interactions after its initial binding has potential to give high binding strengths.

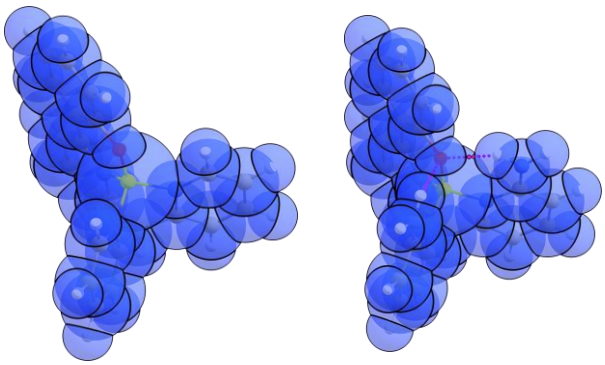

Figure 5.10 Space-filling models of **L1chH_Be** (left) and **L1chNH$_2$_Be** (right) looking down on the binding site with Van der Waals spheres showing.

As **L3chNH$_2$** has been identified as the theoretically strongest binder of Be^{2+}, its data has been presented below.

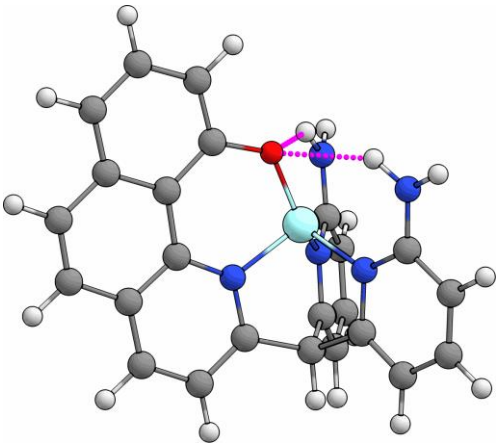

L3chNH$_2$_Al

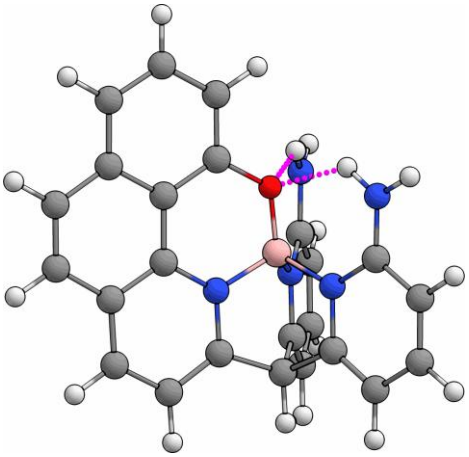

L3chNH$_2$_B

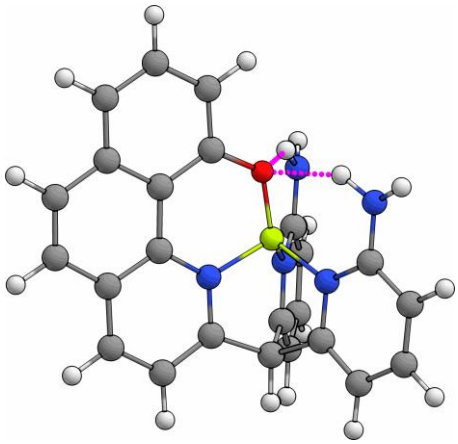

L3chNH$_2$_Be

Figure 5.11 Aqueous phase geometry optimised complex **L3chNH$_2$**, formed with Al^{3+}, B^{3+}, and Be^{2+}, examined at B3LYP/6-311++G(d,p).

Table 5.14 Geometric parameters for **L3chNH$_2$**.

	L3chNH$_2$			
		Al	**B**	**Be**
Bond /Å	O-M	1.716	1.419	1.554
	N_1-M	1.871	1.565	1.695
	N_2-M	1.902	1.597	1.753
	N_3-M	1.901	1.597	1.752
	O-H_1	2.614	2.010	2.136
	O-H_2	2.631	2.007	2.124
Angle /°	O-M-N_1	102.1	112.4	108.8
	O-M-N_2	125.7	115.2	121.2
	O-M-N_3	126.1	115.2	121.0
	N_1-M-N_2	98.5	104.8	101.4
	N_1-M-N_3	98.8	104.7	101.4
	N_2-M-N_3	99.0	103.4	99.8
Index	τ_4	0.77	0.92	0.84

5.3 Apex Groups

The same apex groups have been investigated for buttressed ligands as they were for non-buttressed ligands in chapter 2 (Figure 2.13). With the addition of a secondary sphere of hydrogen bonds from the buttress groups, the geometries of the ligands and complexes could be altered significantly enough that the previously identified trend (**ch** > **coh** > **n**) may change.

5.3.1 Ligand Geometries

As before, there are too many combinations of ligands, buttresses, and apex groups to show them all. **L1** with the buttresses **NH$_2$**, **NHCH$_3$**, **NHCOCH$_3$**, and **NHCONH$_2$** will be considered in this section, with the apexes **coh**, and **n** (Figures 5.12-5.13). It was noted that the same general structures were obtained for the other ligand motifs. The presence of the hydrogen bonds significantly alters the pre-organisation of the ligands. This is the case for both the tertiary alcohol apex as well as the tertiary nitrogen apex.

For the ligands incorporating the **coh** apex, a hydrogen bond is observed in every case between the proton of the alcohol group and nearby pyridyl nitrogen. This prevents complete pre-organisation to occur, as seen with the **ch** apex (Figure 5.2). Increased hydrogen bonding occurs with the two larger buttresses (**$NHCOCH_3$**, and **$NHCONH_2$**), in which the phenol of the backbone interacts strongly with the buttress arm of one pyridyl group (Figure 5.13).

Contrastingly, the **n** apex has resulted in much more planar geometries. The lone pair of electrons on the nitrogen is in a 2p orbital, and thus able to delocalise. Therefore, the atom is sp2 hybridised causing planarity. Each pyridyl arm finds an energy minima by being pointed away at a maximum angle from the ligand backbone. In **L1nNH_2** this allows a network of hydrogen bonds to exist between the backbone donor atoms, pyridyl donor atom, and primary amine (Figure 5.12).

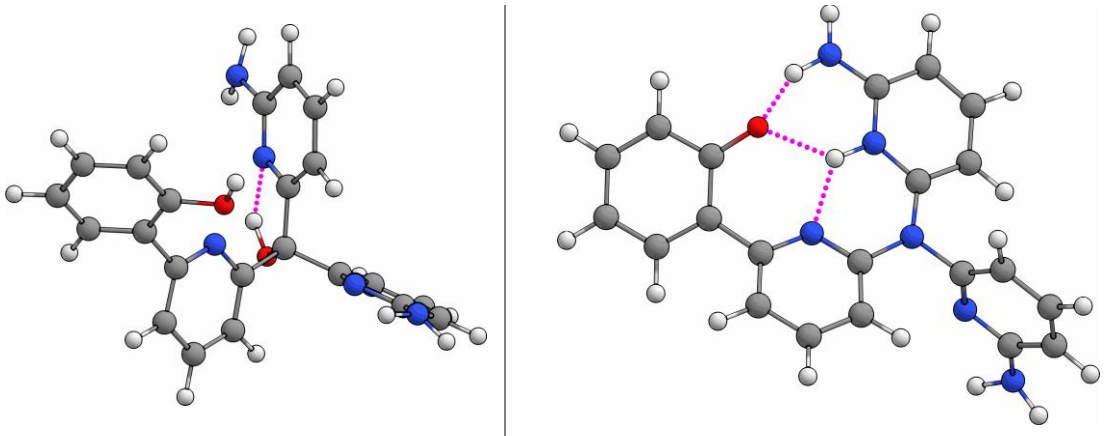

Figure 5.12 Aqueous phase geometry optimised ligand **L1** with **NH_2** buttress, with **oh** and **n** apexes, at B3LYP/6-311++G(d,p).

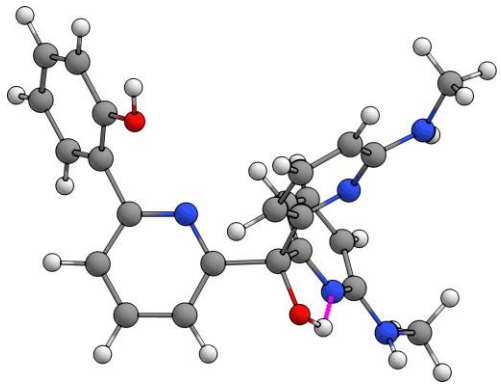

L1cohNHCH$_3$ $\eta_\alpha = 0.20, \eta_\beta = 0.79$

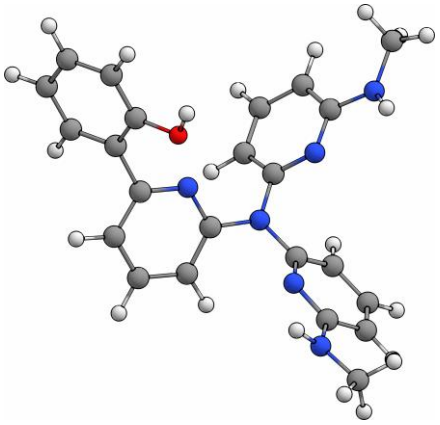

L1nNHCH$_3$ $\eta_\alpha = 0.79, \eta_\beta = 0.90$

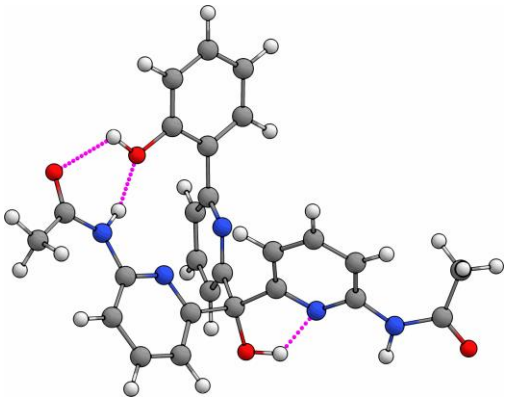

L1cohNHCOCH$_3$ $\eta_\alpha = 0.32, \eta_\beta = 0.90$

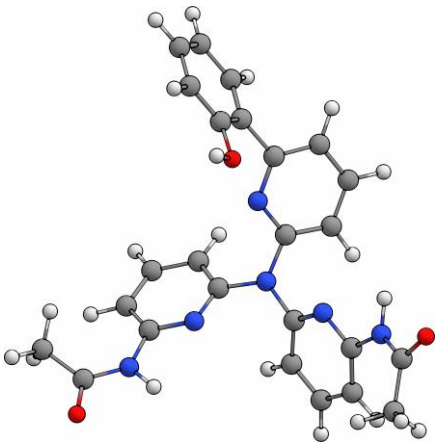

L1nNHCOCH$_3$ $\eta_\alpha = 0.90, \eta_\beta = 0.66$

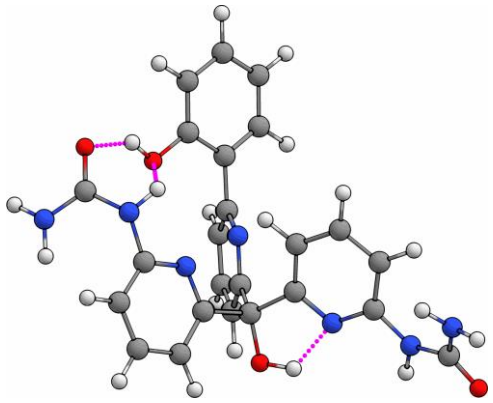

L1cohNHCONH$_2$ $\eta_\alpha = 0.25, \eta_\beta = 0.98$

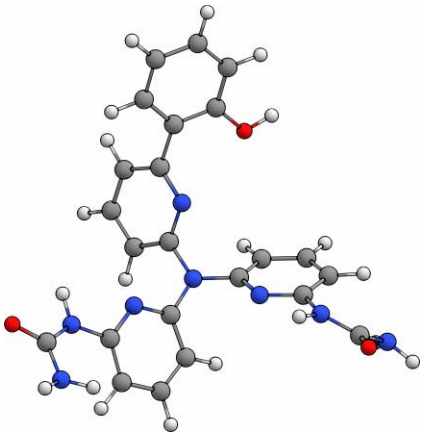

L1nNHCONH$_2$ $\eta_\alpha = 0.67, \eta_\beta = 0.88$

Figure 5.13 Aqueous phase geometry optimised ligand **L1** with **NHCH$_3$**, **NHCOCH$_3$** and **NHCONH$_2$** buttresses, with **oh** and **n** apexes, at B3LYP/6-311++G(d,p).

5.3.2 Complex Geometries

Each of the five ligands, with buttress, each apex, and each metal cation were calculated. Shown below are the **L1** complexes against the each buttress and the **coh** and **n** apexes, bound to the Be^{2+} cation (Figures 5.14-5.15). Each ligand motif is represented well by the geometry adopted by **L1**. The only exceptions to this are for the ligands **L2**-**L5** with the larger two buttresses, which occasionally formed 5- and 6-coordinate geometries when bound to Al^{3+}.

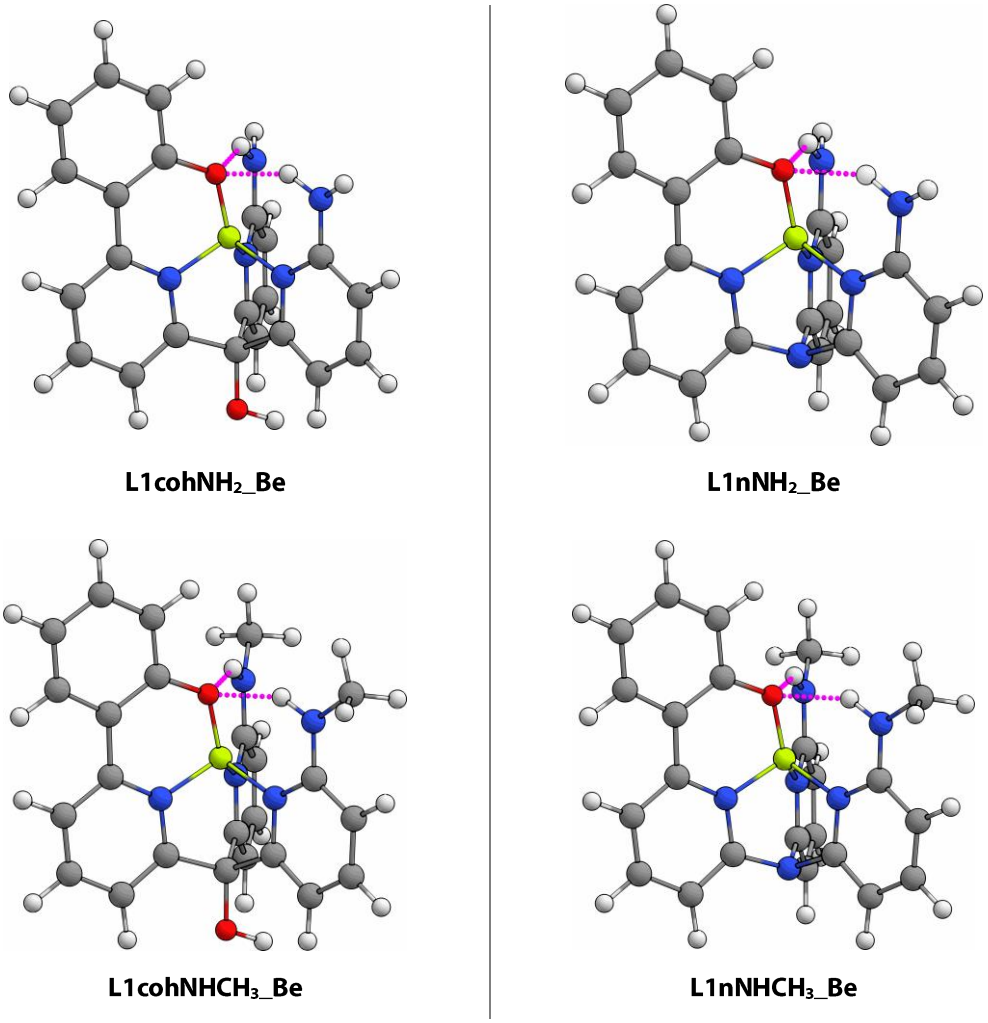

Figure 5.14 Aqueous phase geometry optimised complex **L1** with buttress groups NH_2 and $NHCH_3$, formed with the Be^{2+} cation, with **coh** and **n** apexes at B3LYP/6-311++G(d,p).

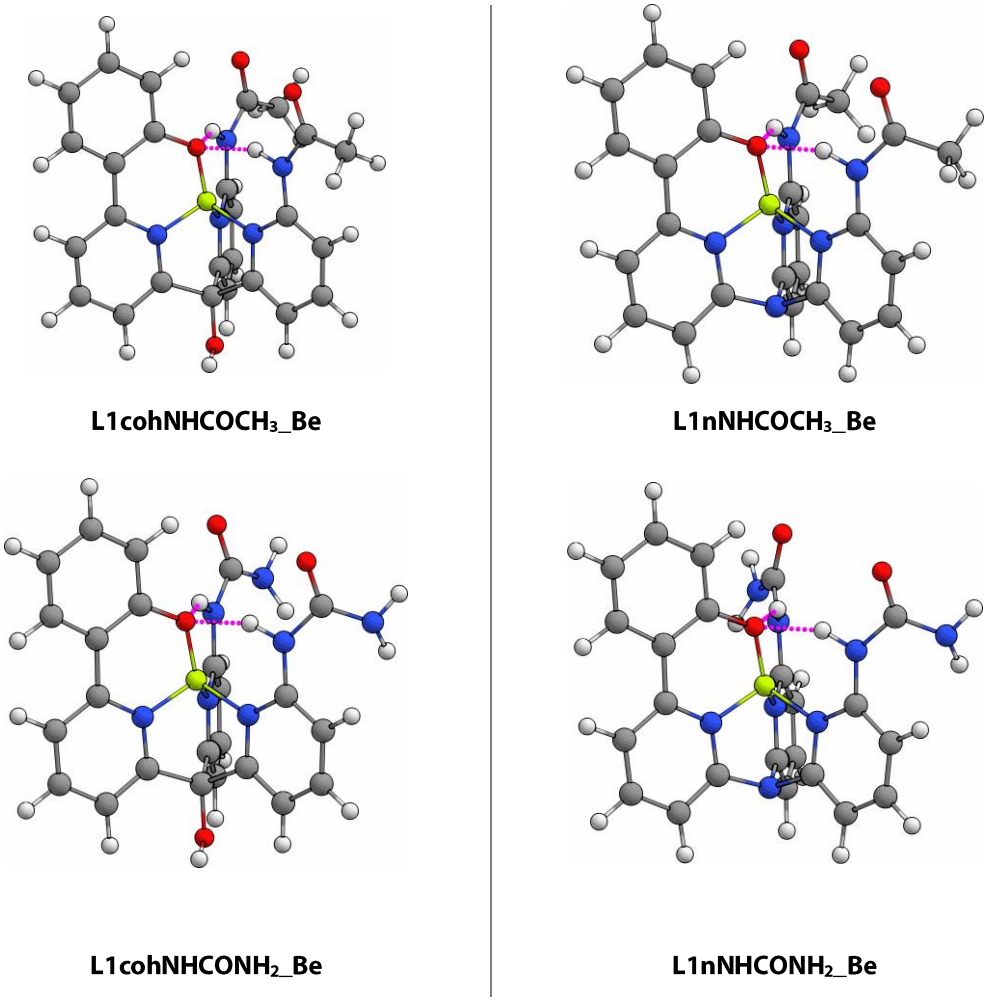

Figure 5.15 Aqueous phase geometry optimised complex **L1** with buttress groups $NHCOCH_3$ and $NHCONH_2$, formed with the Be^{2+} cation, with **coh** and **n** apexes at B3LYP/6-311++G(d,p).

For each apex, a hydrogen-bond occurs between each buttress and the phenolic oxygen. A comparison of these between the **ch**, **coh**, and **n** apexes reveal similar bond lengths between **ch** and **coh** complexes, but significantly longer bond lengths for **n** complexes. This is observed regardless of ligand motif, buttress, or complexed ion. Values for **L1** and **L3** bound to Be^{2+} have been listed (Table 5.15). The longer bond lengths of the **n** apex complexes are attributed to the expansion of the binding site due to the planarity of the apex.

Table 5.15 Hydrogen-bond lengths of **L1** and **L3** with the **NH_2** buttress group.

Ligand	O···H /Å
L1chNH_2	2.115
L1cohNH_2	2.087
L1nNH_2	2.212
L3chNH_2	2.136
L3cohNH_2	2.109
L3nNH_2	2.237

5.3.3 Binding Energies

The binding energy trend for the apexes is noted to be **n** < **coh** < **ch**. This is the same as for the non-buttressed ligands. The nature of the **n** apex group to stretch out its substituents to adopt a more trigonal planar geometry results in longer bond lengths and therefore lower binding energies. Their geometric parameters have been tabulated in Tables 5.16-5.19.

Table 5.16 Calculated binding energies of **NH_2** buttressed complexes with varying apex group.

NH_2		ΔG_{aq} / kJ mol^{-1}		
Ligand	**Apex**	**Al**	**B**	**Be**
1	**ch**	-358.03	-754.55	-383.71
	coh	-335.10	-739.02	-370.20
	n	-286.80	-672.91	-312.92
2	**ch**	-304.23	-691.14	-342.49
	coh	-268.96	-665.52	-322.81
	n	-213.76	-586.70	-251.93
3	**ch**	-390.92	-782.11	-413.29
	coh	-355.63	-758.35	-391.38
	n	-295.74	-677.32	-319.30
4	**ch**	-325.68	-695.02	-331.91
	coh	-306.02	-680.76	-321.97
	n	-249.67	-611.40	-259.59
5	**ch**	-440.36	-841.97	-405.97
	coh	-408.25	-823.18	-392.27
	n	-350.72	-750.96	-328.10

Table 5.17 Calculated binding energies of **$NHCH_3$** buttressed complexes with varying apex group.

$NHCH_3$		ΔG_{aq} / kJ mol^{-1}		
Ligand	**Apex**	**Al**	**B**	**Be**
1	**ch**	-370.41	-765.45	-395.64
	coh	-339.22	-739.34	-372.04
	n	-301.67	-681.52	-322.62
2	**ch**	-297.23	-642.19	-264.11
	coh	-245.38	-567.98	-275.87
	n	-217.30	-555.86	-229.26
3	**ch**	-385.50	-772.91	-406.07
	coh	-330.49	-729.43	-364.20
	n	-317.65	-691.77	-336.37
4	**ch**	-331.96	-669.86	-269.37
	coh	-311.50	-621.11	-247.38
	n	-254.27	-581.44	-194.26
5	**ch**	-439.48	-847.11	-348.42
	coh	-418.40	-793.20	-303.03
	n	-355.85	-720.47	-312.81

Table 5.18 Calculated binding energies of **$NHCOCH_3$** buttressed complexes with varying apex group (* = 5-coordinate, † = 6-coordinate).

$NHCOCH_3$		ΔG_{aq} / kJ mol^{-1}		
Ligand	**Apex**	**Al**	**B**	**Be**
1	**ch**	-298.79	-679.70	-347.84
	coh	-265.09	-653.34	-321.46
	n	-241.77	-608.96	-287.71
2	**ch**	-237.78	-616.08	-296.46
	coh	-232.51	-629.29	-309.30
	n	-255.46*	-513.27	-189.94
3	**ch**	-310.64	-685.80	-354.90
	coh	-284.59	-667.93	-342.06
	n	-242.70	-608.47	-290.80
4	**ch**	-284.90	-618.25	-286.34
	coh	-424.31†	-580.20	-271.61
	n	-395.85†	-539.64	-208.77
5	**ch**	-505.15*	-773.49	-391.01
	coh	-469.50*	-741.05	-362.50
	n	-442.92*	-694.63	-306.07

Table 5.19 Calculated binding energies of **NHCONH$_2$** buttressed complexes with varying apex group (* = 5-coordinate, † = 6-coordinate).

NHCONH$_2$		ΔG_{aq} / kJ mol^{-1}		
Ligand	**Apex**	**Al**	**B**	**Be**
1	**ch**	-308.81	-691.58	-349.35
	coh	-273.70	-661.72	-327.80
	n	-230.06	-605.64	-277.76
2	**ch**	-240.30	-605.40	-271.27
	coh	-347.24*	-619.59	-289.83
	n	-227.05*	-515.51	-194.21
3	**ch**	-435.76	-709.48	-361.54
	coh	-305.05	-681.55	-346.24
	n	-381.61*	-619.22	-294.20
4	**ch**	-300.95*	-585.91	-249.01
	coh	-408.14*	-615.76	-269.22
	n	-438.57†	-561.43	-219.71
5	**ch**	-522.06*	-783.30	-394.16
	coh	-491.73*	-758.09	-371.87
	n	-455.94*	-699.75	-319.47

5.3.4 Comparison

The binding strength of each apex with each buttress is compared below (Figures 5.16-5.19). The alkyl apex gives the highest binding energies. **L4** and **L5** aluminium complexes, especially when they adopt 5- or 6-coordinate geometries, have large increases in their binding energies over that of the analogous beryllium complexes.

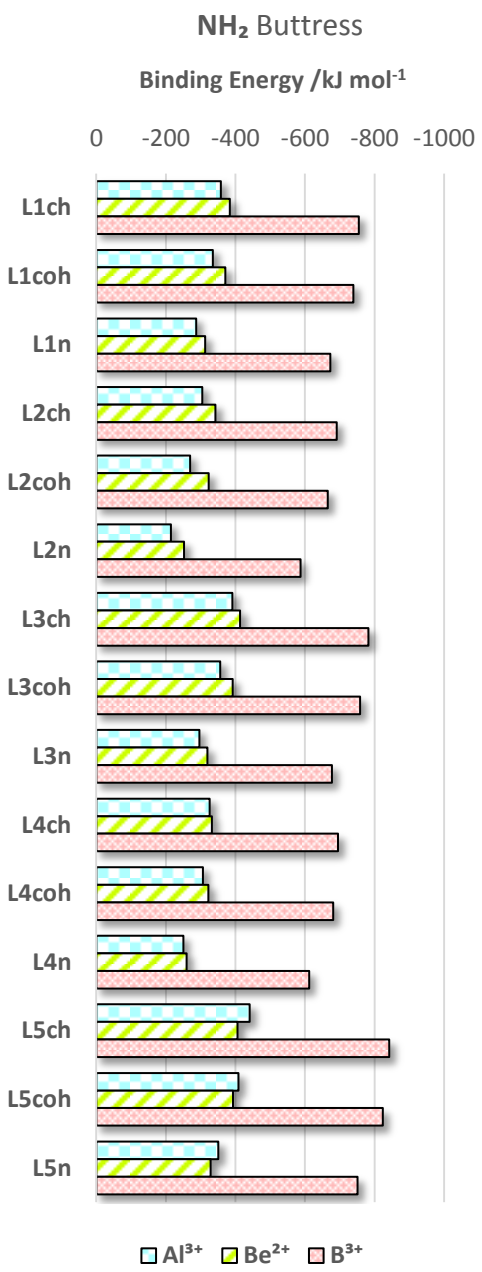

Figure 5.16 Binding energies of **L1**-**L5** with the **NH_2** buttress.

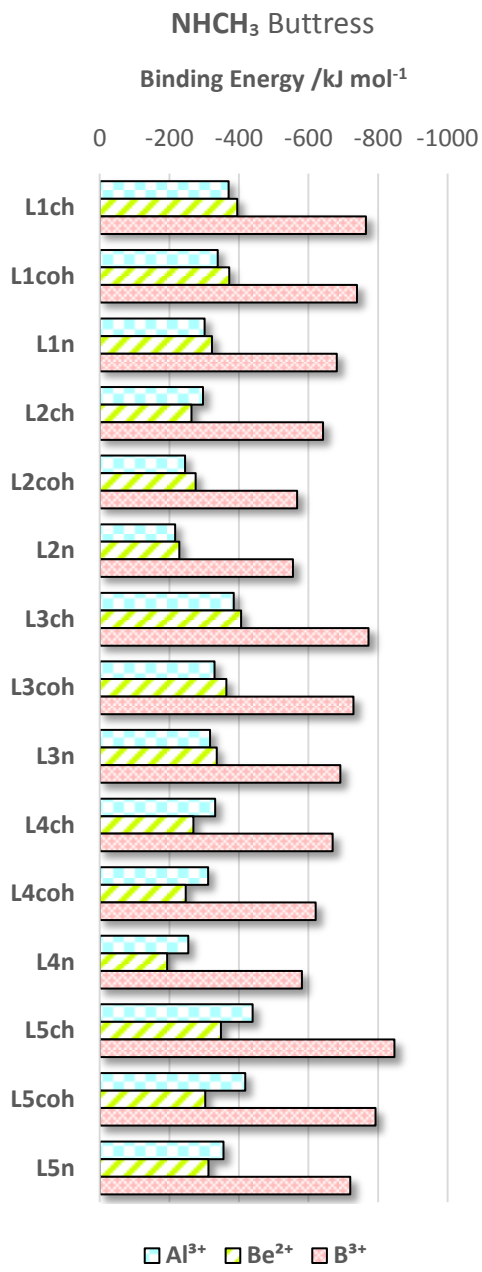

Figure 5.17 Binding energies of **L1**-**L5** with the **$NHCH_3$** buttress.

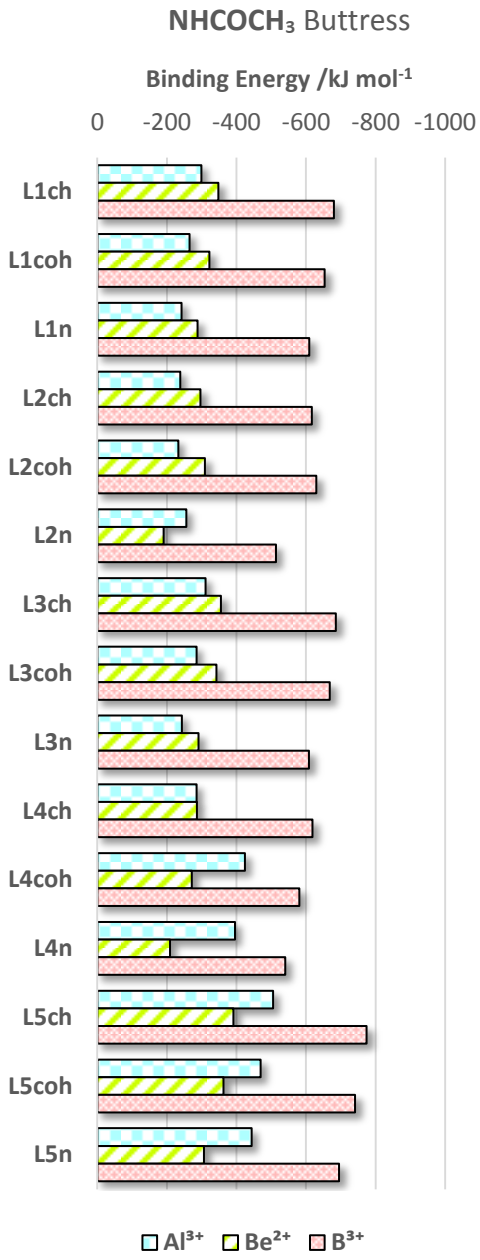

Figure 5.18 Binding energies of **L1**-**L5** with the **NHCOCH$_3$** buttress.

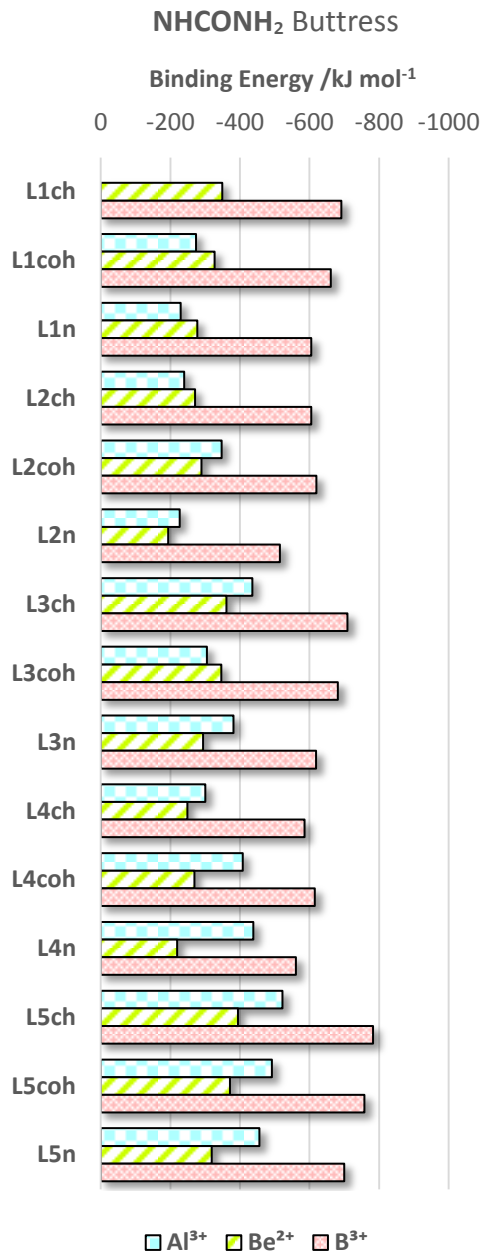

Figure 5.19 Binding energies of **L1**-**L5** with the **NHCONH$_2$** buttress.

5.4 Metal Binding Study

In parallel to the main body of calculations, a focused study on the metal binding of a selection ligands was carried out. Preferably, the study would examine the best of our studied binders, but as these results had not yet been obtained, two of the simplest but well contrasting ligands were chosen. These were **L1chH** and **L1chNH$_2$** (Figure 5.20). Three well-known chelators were used to form the basis of a comparison. These were **EDTA**, **NTP**, and **10-HBQS**. All three of these molecules are known to bind to Be^{2+} and have been used in wet chemistry studies as well as in therapeutic and hazardous qualitative testing (Figure 5.20).[45, 78b, 81]

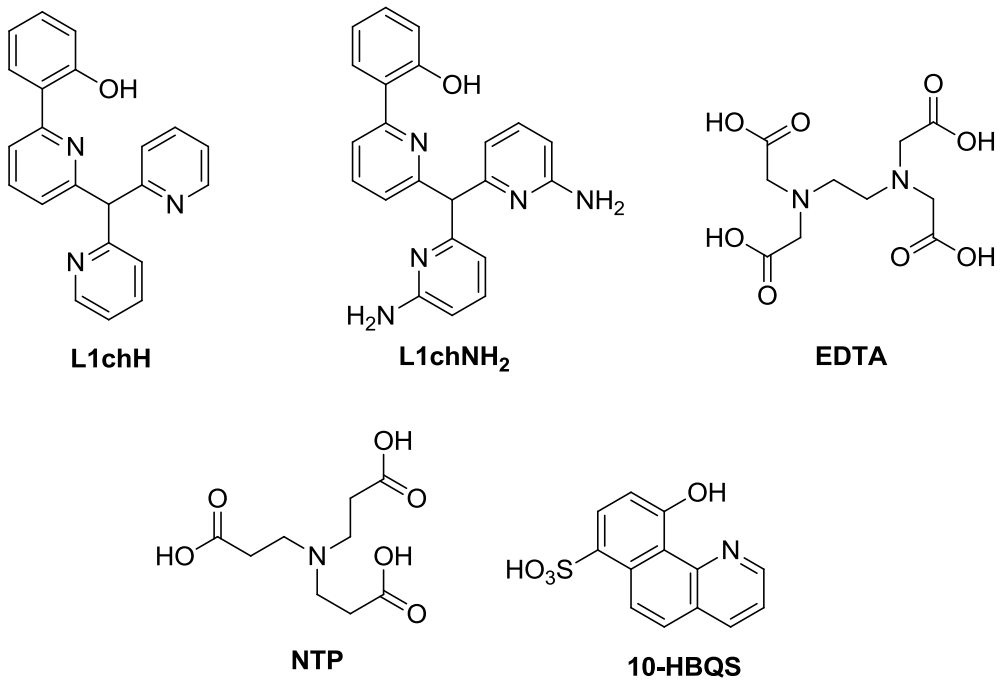

Figure 5.20 Ligands examined in the metal binding study.

A comprehensive list of metal cations was chosen for this study. 18 further metals were chosen in addition to Al^{3+}, B^{3+}, and Be^{2+} (Table 5.20). Each was chosen as they were either commonly found in nature, are essential to human biology, or were well known transition metals.

Table 5.20 Properties of all examined metals in this work.[117]

Cation	Atomic radii (pm)	Ionic radii (Å)	C.N.	Cation	Atomic radii (pm)	Ionic radii (Å)	C.N.
Al^{3+}	125	0.68	6	Fe^{3+}	140	0.55	6
B^{3+}	85	0.25	4	K^{+}	220	1.38	6
Be^{2+}	105	0.41	4	Li^{+}	145	0.76	6
Ca^{2+}	180	1.00	6	Mg^{2+}	150	0.72	6
Co^{2+}	135	0.65	6	Mn^{2+}	140	0.67	6
Co^{3+}	135	0.545	6	Mn^{3+}	140	0.58	6
Cr^{2+}	140	0.73	6	Na^{+}	180	1.02	6
Cr^{3+}	140	0.615	6	Ni^{2+}	135	0.69	6
Cu^{2+}	135	0.73	6	V^{2+}	135	0.79	6
Fe^{2+} *(s)*	140	0.61	6	V^{3+}	135	0.64	6
Fe^{2+} *(t)*	140	0.78	6	Zn^{2+}	135	0.74	6

5.4.1 Ligand Geometries

EDTA adopts the most flexible motif of the selected ligands, owing to the ethylene bridge connecting its two 3° nitrogens (Figure 5.21). This allows a large bite size with up to six donor atoms, suitable for the full encapsulation and chelation of metal cations for a wide range of sizes. Hydrogen bonds (1.758 and 1.859 Å) dictate some pre-organisation in **NTP**, which form a partial cavity. Upon deprotonation of the acid groups, **NTP** has four donor atoms available which will result in adoption of tetrahedral complexes. For the chelator **10-HBQS**, a hydrogen bond exists between its aromatic nitrogen and the proton of the nearby phenol (1.791 Å) which are its two available donor atoms. Its sulfonate residue sits on the other side of the molecule for increased aqueous solubility. The geometries of **L1chH** and **L1chNH$_2$** have already been investigated in this thesis (Figure 2.7, page 54 and Figure 5.2, page 119).

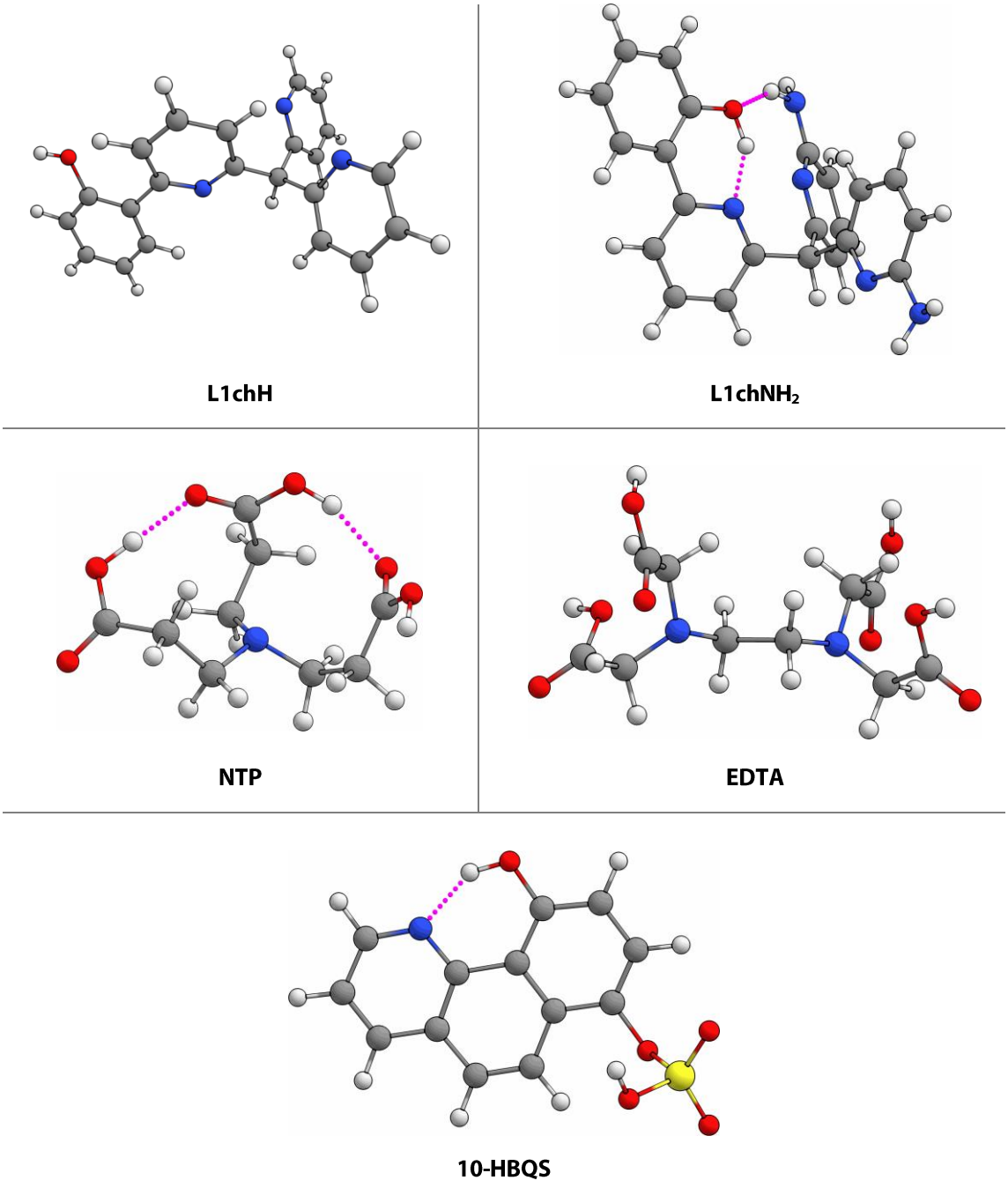

Figure 5.21 Aqueous phase geometry optimised chelators **L1chH**, **L1chNH$_2$**, **NTP**, **EDTA**, and **10-HBQS**, at B3LYP/6-311++G(d,p).

5.4.2 Complex Geometries

As many cations have been investigated, only the most noteworthy will be shown. These are complexes of the B^{3+}, Be^{2+}, and Co^{2+} cations (Figures 5.22-5.23). Their geometric parameters are listed in Tables 5.21-5.24. Because it was found that Al^{3+} was not a good

analogue for Be^{2+} in the previous systems due to its size, charge, and preference for large coordination numbers, it has been substituted for Co^{2+}. Although cobalt(II) is larger than aluminium(III), it has the same charge as beryllium(II), and is known to adopt tetrahedral arrangements.[118]

To boron and beryllium, the complexes have formed tetrahedral-type geometries. **10-HBQS** is unique in that it does not offer all donors, but instead requires water molecules to complete the binding. With a weaker chelation effect, potential for binding strength is not maximised. **NTP** provides close to perfect tetrahedral arrangements for B^{3+} and Be^{2+}, having τ_4 values of 0.98 and 0.97 respectively. This contrasts with **EDTA** (τ_4 = 0.92 and 0.81 respectively), and to a smaller extent, the less hindered **10-HBQS** (τ_4 = 0.93 and 0.91 respectively). In addition, these angle geometries are more favourable than that of **L1chH** (τ_4 = 0.93 and 0.83 respectively) and **L1chNH$_2$** (τ_4 = 0.92 and 0.84 respectively). These known chelators (**NTP**, **EDTA**, and **10-HBQS**) all have on average, significantly shorter bond lengths to stronger donors (carboxylic acids vs pyridyl amines). As noted earlier, **L1chNH$_2$**, in stark contrast to each of these other chelators, has the additional hydrogen bonding present. These, as previously discussed, form a secondary sphere of interactions and as such are complex-stabilising due to the tightening of the binding site (as demonstrated by their bond lengths and τ_4 values).

It was discovered that Co^{2+} takes a different conformation when binding to each of these ligands. To **NTP**, it forms a close to tetrahedral arrangement of donors (τ_4 = 0.75), but its bond lengths are all significantly longer than the B^{3+} and Be^{2+} complexes, which is a consequence of its larger ionic radius. With **EDTA**, an octahedral geometry is found. This is again because its ionic radius is much larger than the other cations, and it is expected that it will have a higher binding energy to **EDTA** than Be^{2+}. A square planar geometry has been found for **10-HBQS_Co**. Its τ_4 value is only 0.10, which is very close to the ideal value for this conformation (Figure 2.1, page 46). And to **L1chNH$_2$**, the conformation is tending towards a seesaw geometry (τ_4 = 0.65 and τ_4' = 0.44). Only one hydrogen bond

exists in the complex (O···H, 2.04 Å). Towards B^{3+} and Be^{2+} a second hydrogen bond exists, but for Co^{2+} this distance is too great (3.72 Å) to describe it as a second hydrogen bond.

An overview of the entire metal study shows that in many cases, the metal adopts an octahedral geometry, for example Fe^{3+}. Alternatively, in the case of Na^{+} or K^{+}, their ionic radii (1.02 and 1.38 Å respectively) are simply too large, therefore these do not fit well into the binding cavity of these chelators. This causes their complexes to have unwieldy conformations.

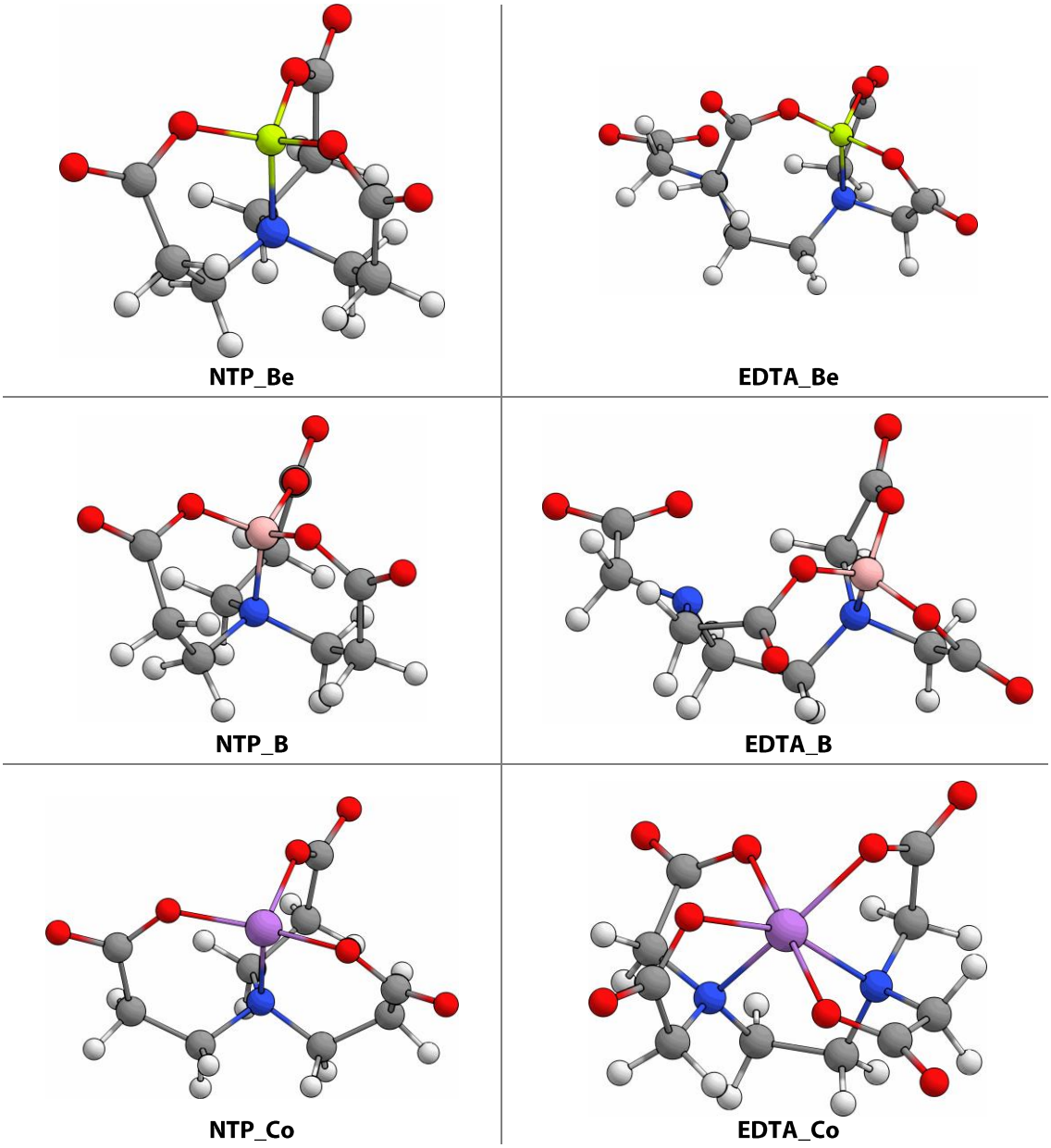

Figure 5.22 Aqueous phase geometry optimised complexes **NTP** and **EDTA**, formed with B^{3+}, Be^{2+}, and Co^{2+}, examined at B3LYP/6-311++G(d,p).

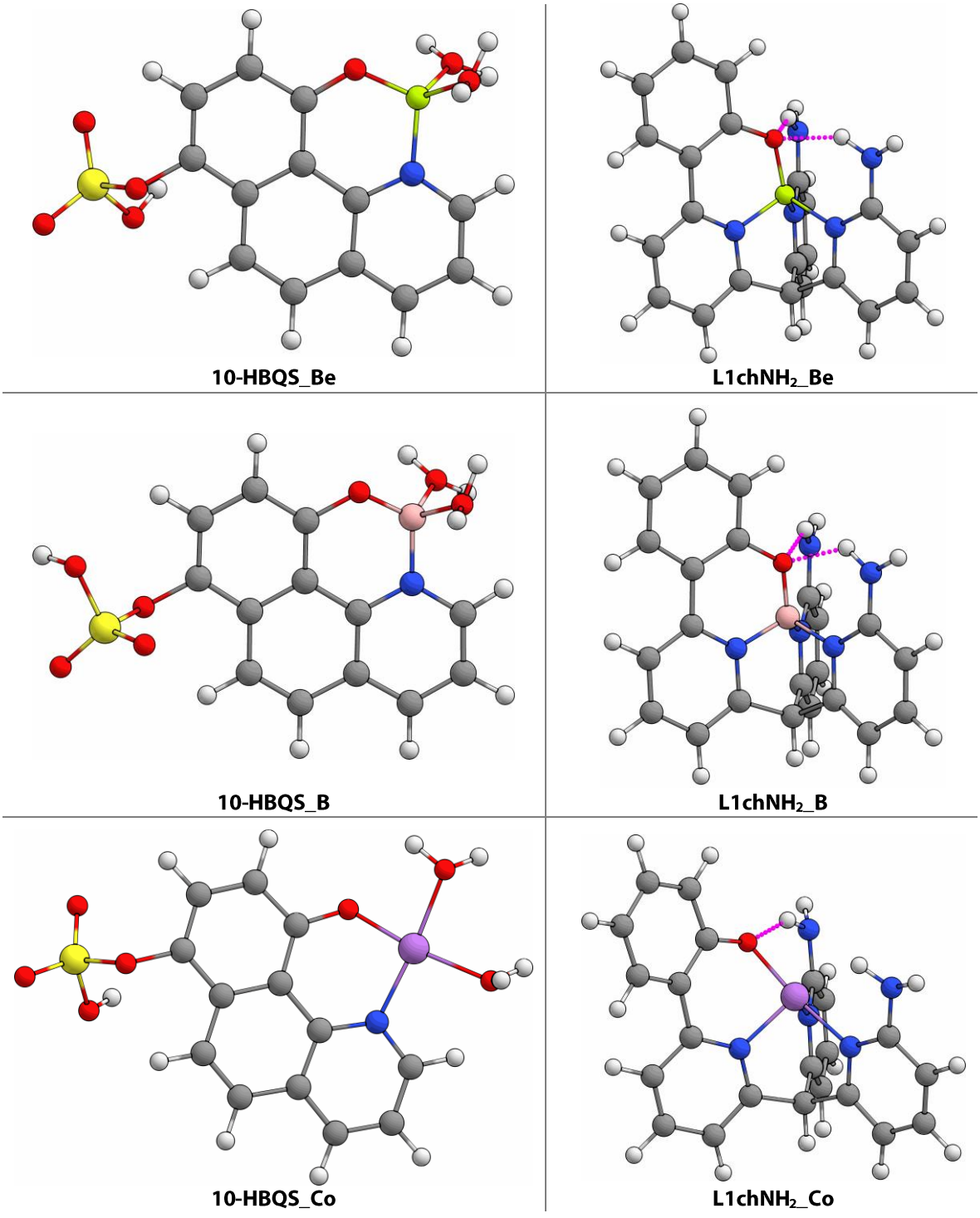

Figure 5.23 Aqueous phase geometry optimised complexes **10-HBQS** and **L1chNH$_2$**, formed with B^{3+}, Be^{2+}, and Co^{2+}, examined at B3LYP/6-311++G(d,p).

Table 5.21 Geometric parameters for **NTP**.

NTP				
		B	**Be**	**Co**
Bond /Å	O_1-M	1.457	1.606	1.922
	O_2-M	1.462	1.618	2.038
	O_3-M	1.460	1.613	1.921
	N-M	1.619	1.791	2.019
Angle /°	O_1-M-O_2	107.8	110.8	101.4
	O_2-M-O_3	108.2	109.6	152.4
	O_3-M-O_1	109.6	111.8	98.5
	O_1-M-N	111.5	109.4	96.3
	O_2-M-N	110.9	107.7	98.0
	O_3-M-N	108.7	107.5	99.6
Index	τ_4	0.98	0.97	0.75

Table 5.22 Geometric parameters for **10-HBQS**.

10-HBQS				
		B	**Be**	**Co**
Bond /Å	O_1-M	1.379	1.531	1.840
	O_2-M	1.561	1.701	2.009
	O_3-M	1.549	1.692	2.022
	N-M	1.528	1.697	1.943
Angle /°	O_1-M-O_2	107.1	107.2	82.6
	O_2-M-O_3	99.4	99.3	172.2
	O_3-M-O_1	111.9	116.8	89.6
	O_1-M-N	116.7	110.1	92.9
	O_2-M-N	112.4	115.0	174.1
	O_3-M-N	107.9	108.3	95.0
Index	τ_4	0.93	0.91	0.10

Table 5.23 Geometric parameters for **EDTA**.

EDTA				
		B	**Be**	**Co**
Bond /Å	O_1-M	1.415	1.584	2.055
	O_2-M	1.465	1.629	2.269
	O_3-M	1.466	1.632	2.055
	O_4-M	-	-	2.269
	N_1-M	1.670	1.876	2.011
	N_2-M	-	-	2.011
Angle /°	O_1-M-O_2	110.0	111.5	-
	O_2-M-O_3	112.6	109.5	-
	O_3-M-O_1	114.2	114.8	-
	O_1-M-N_1	115.9	130.6	-
	O_2-M-N_1	100.7	93.7	-
	O_3-M-N_1	102.5	96.0	-
Index	τ_4	0.92	0.81	-

Table 5.24 Geometric parameters for **L1chNH$_2$**.

L1chNH$_2$				
		B	**Be**	**Co**
Bond /Å	O-M	1.414	1.549	1.858
	N_1-M	1.568	1.697	2.083
	N_2-M	1.597	1.751	1.995
	N_3-M	1.597	1.751	1.951
	O-H_1	2.007	2.115	2.043
	O-H_2	2.007	2.116	-
Angle /°	O-M-N_1	112.3	109.0	92.6
	O-M-N_2	114.8	120.5	99.3
	O-M-N_3	114.8	120.5	168.7
	N_1-M-N_2	105.2	102.0	92.3
	N_1-M-N_3	105.2	102.0	93.1
	N_2-M-N_3	103.5	99.9	90.2
Index	τ_4	0.92	0.84	0.65

5.4.3 Binding Energies

The binding energies for each of the complexes was determined and are shown in Table 5.25 (except in four cases, where global minima could not be located). The strongest binding is found in cases where the metal cation has a low ionic radii and high charge. It

was found that the binding energy is relatively weak when the ionic radius was too large or in the case where hexadentate configurations dominate.

Table 5.25 Calculated binding energies of chelating complexes with each metal.

Chelator	Binding Energy / kJ mol^{-1}											
	Al^{3+}	B^{3+}	Be^{2+}	Ca^{2+}	Co^{2+}	Co^{3+}	Cr^{2+}	Cr^{3+}	Cu^{2+}	Fe^{2+}	Fe^{3+}
L1chH	-326.85	-735.30	-357.47	-198.39	-387.81	-537.10	-198.09	-414.16	-365.71	-	-514.31
$L1chNH_2$	-358.03	-755.78	-389.03	-191.94	-397.20	-541.31	-330.19	-425.13	-384.72	-353.69	-521.98
NTP	-474.56	-806.39	-401.74	-240.20	-371.16	-564.62	-306.04	-482.50	-371.36	-310.48	-559.88
EDTA	-610.97	-817.59	-415.38	-345.30	-439.00	-830.13	-400.95	-645.56	-462.17	-425.77	-730.81
10-HBQS	-190.86	-491.27	-249.71	-156.68	-275.97	-347.90	-195.26	-287.82	-276.76	-193.79	-345.26
	K^{+}	Li^{+}	Mg^{2+}	Mn^{2+}	Mn^{3+}	Na^{+}	Ni^{2+}	V^{2+}	V^{3+}	Zn^{2+}	
L1chH	-93.00	-199.47	-218.63	-130.46	-	-130.71	-343.50	-179.19	-254.00	-328.94	
$L1chNH_2$	-103.12	-216.07	-224.00	-335.73	-	-138.40	-357.43	-263.00	-471.27	-344.42	
NTP	-96.93	-206.10	-270.49	-323.28	-540.78	-133.83	-319.50	-275.09	-529.98	-559.88	
EDTA	-140.13	-225.41	-359.68	-397.16	-700.83	-184.19	-445.58	-395.53	-688.92	-	
10-HBQS	-95.91	-178.82	-145.80	-252.33	-372.74	-125.22	-271.38	-179.72	-323.44	-221.00	

5.4.4 Comparison

Binding energy graphs are displayed showing the entire range of metals (Figure 5.24). **EDTA** is the strongest binder (across the board), with **NTP** coming in a close second. **10-HBQS** has the smallest binding energies in all cases but one. The binding energies for our ligand motifs **L1chH**and **L1chNH$_2$** are typically found between that of **10-HBQS** and **NTP**. The buttress improves the strength of binding in most cases, but sometimes has little effect. In these cases, the geometry is found to be distorted to a seesaw conformation, with only one hydrogen bond present.

The average binding energies were calculated for each ligand (Table 5.26) and compared to their binding energy of the Be^{2+} cation. The complexes of Ca^{2+}, K^{+}, Li^{+}, Mg^{2+}, and Na^{+} were removed as outliers as their corresponding binding strengths were the lowest (likely due to either their ionic radius being too large, or their charge of +1 being too small). On average, all chelators bound to the Be^{2+} cation worse on average than to other metals. The chelators **L1chH** and **L1chNH$_2$** were found to have a binding energy to Be^{2+} just 1.2% or 5.9% below their average. Whereas for the known binders, their energies are 8.6%, 33.0%, or 11.5% below the average binding energy. Although this qualitative comparison is not comprehensive, this does give an idea of how these ligands may behave towards a range of metal cations. Although **EDTA** is the strongest binder for Be^{2+}, it binds better on average to all other metals. This mimics what is found experimentally for **EDTA**, that it binds many metals strongly but less so towards Be^{2+}. This lack of selectivity explains its use in the swipe protocol before application of **10-HBQS** in the detection of beryllium.

Table 5.26 Averaged binding energies of chelating complexes.

	Average Binding Energy	Binding Energy (Be^{2+})
L1chH	-361.63	-357.47
L1chNH$_2$	-411.86	-389.03
NTP	-436.42	-401.74
EDTA	-552.32	-415.38
10-HBQS	-278.34	-249.71

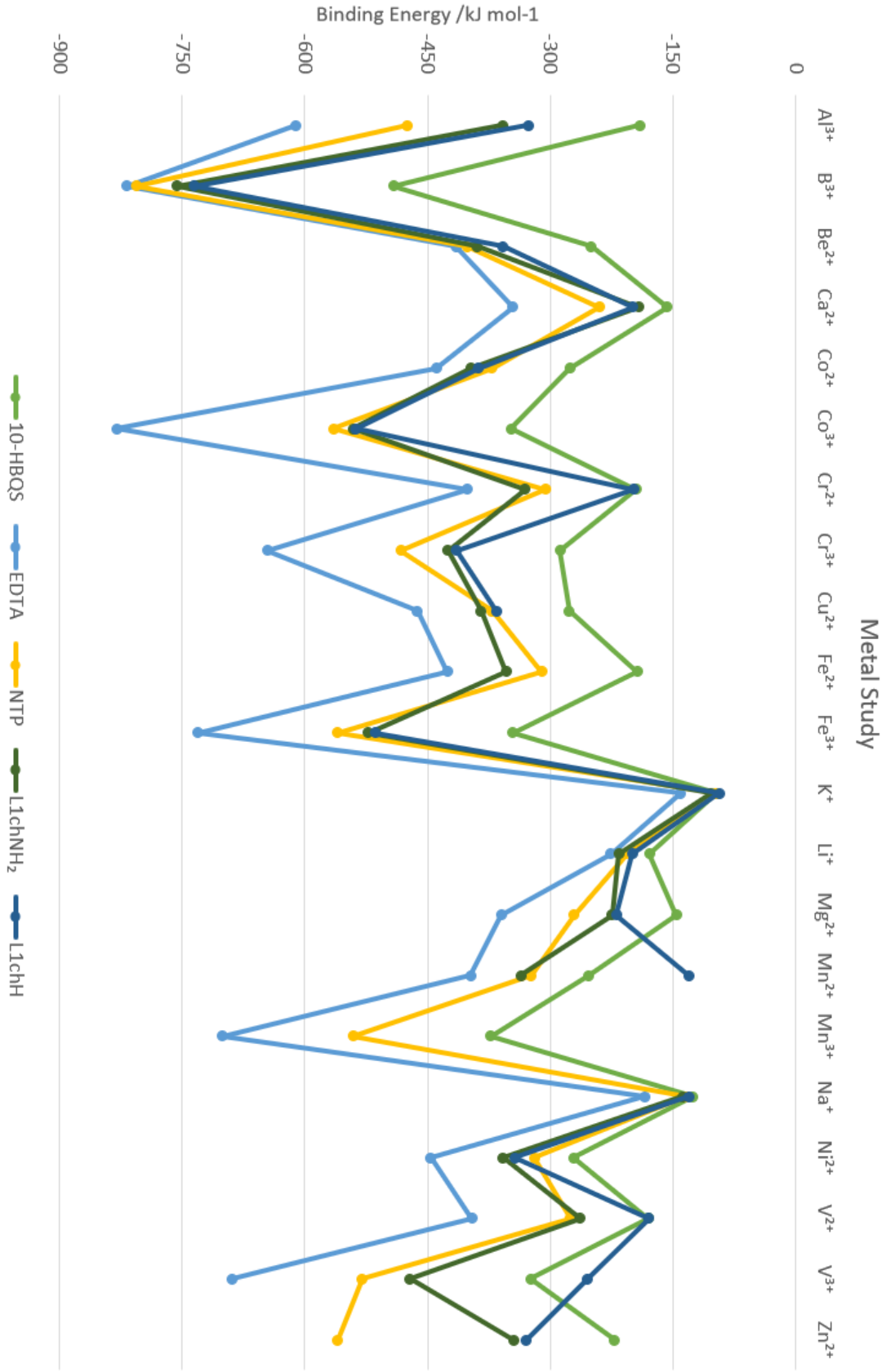

Figure 5.24 Comparison of binding energies of **L1chH**, **L1chNH$_2$**, **NTP**, **EDTA**, and **10-HBQS** to Be^{2+} and a series of commonly found metal cations.

5.5 NCIPlot Study

A non-buttressed and a buttressed ligand, and their beryllium complexes, were selected for further analysis of their intra-molecular non-covalent interactions (Figure 5.25). In particular, identification of secondary coordination spheres would provide a greater insight into their metal binding ability as they can visualise the non-covalent interactions arising from the hydrogen bond donors and acceptors. The NCIPlot software package has been used to visualise these interactions, after these molecules have been optimised using Gaussian 09.[90] NCIPlot creates pictures that are helpful in discussing attractive and repulsive forces throughout a given structure.[119]

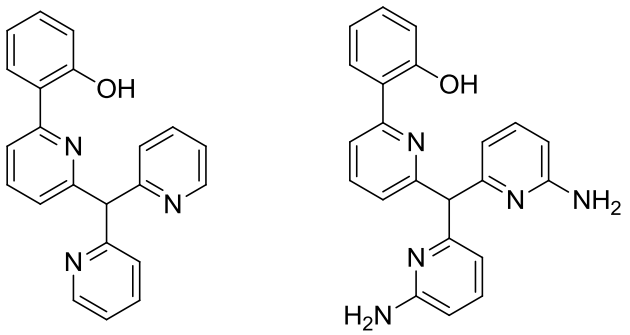

L1chH **L1chNH$_2$**

Figure 5.25 Ligands examined in the NTP study.

In order to quantify non-covalent interactions, NCIPlot analyses the non-covalent interaction index of a molecule. This index corresponds to interactions based on the reduced electron density gradient of a molecule. A plot generated by the index provides data for critical points that are associated with certain intra- or inter-molecular interactions. These critical points are peaks that appear in the reduced density gradient at low densities. They may arise from many situations, including from dispersive forces due to ring strain, and attractive forces due to hydrogen bonding. The eigenvalue λ_2 of the second derivative of the reduced electron density distinguishes attractive (blue) and repulsive interactions (red). The density of a peak determines the strength of its corresponding non-covalent interaction.

5.5.1 Comparison of Non-buttressed Ligands

Visualisation of the isosurfaces of the NCI index allows interactions to be identified by their location, as well as their type. The NCIPlot isosurfaces of **L1chH** and **L1chNH$_2$** are shown in Figure 5.28. The isosurfaces are coloured according to the type of interaction (blue/green = attractive, red/orange = repulsive). The critical points located at the centre of each ring correspond to ring strain, and therefore they are coloured orange and red. In contrast, in both ligands there exist attractive forces between particular atoms. For **L1chH**, these are weak dispersion interactions between the four heteroatoms and neighbouring protons. However, in the isosurface of **L1chNH$_2$**, a number of critical points can be identified that are due to the formation of hydrogen bonds. These are between the phenol oxygen atom and a primary amine proton, as well as the phenol proton and the neighbouring pyridyl nitrogen atoms. Although **L1chH** has some attractive interactions – none of these are hydrogen bonds.

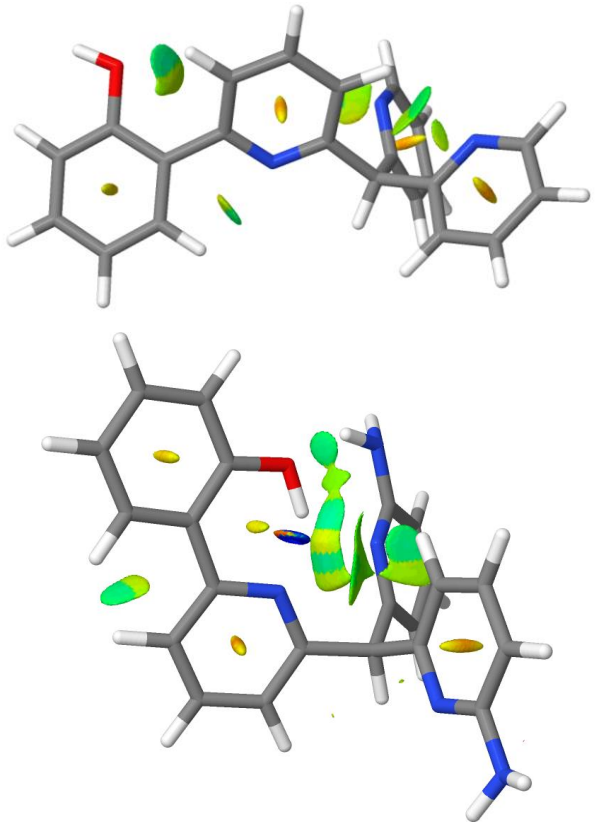

Figure 5.26 Models of L1chH (top) and L1chNH_2 (bottom) showing their NCIPlot surfaces.

These non-covalent interactions can be visualised further by their NCIPlots (Figure 5.27). The sharp blue peaks correspond to attractive interactions, and the sharp red peaks correspond to repulsive interactions. Both types of interactions can be identified in each of the NCIPlots. There are two major differences between them. The first is that the attractive interactions seen in **L1chNH_2** are more dense and closer to the mid-point of the graph. This indicates stronger interactions, which are due to the hydrogen bonds present. The other noticeable change is there are more interactions that are repulsive. This is simple because of the steric strain caused by the more tightly packed ligand geometry.

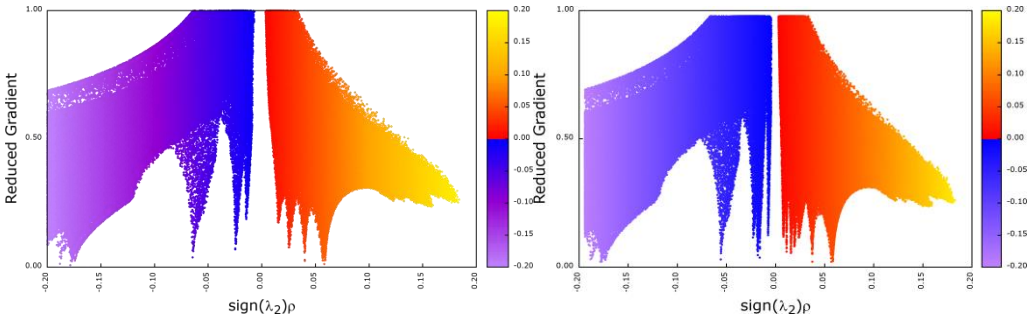

Figure 5.27 NCIPlot for **L1chH** (left), and **L1chNH$_2$** (right).

5.5.2 Comparison of Buttressed Ligands

The NCIPlot isosurfaces for the beryllium complexes L1chH_Be and L1chNH$_2$_Be have been calculated (Figure 5.28). This time, the surfaces are similar because the ligand has formed a tetrahedral cavity for the metal cation in both cases. The globular surface at the metal-core is an artefact due to covalent interactions with the donor atoms and therefore ignored. The only significant difference is that **L1chNH$_2$** has the presence of an attractive interaction between its phenol oxygen and a proton of each of the nearby primary amine protons. These lie at the critical point corresponding to hydrogen bonds. This is in effect visualisation of a second sphere of interaction.

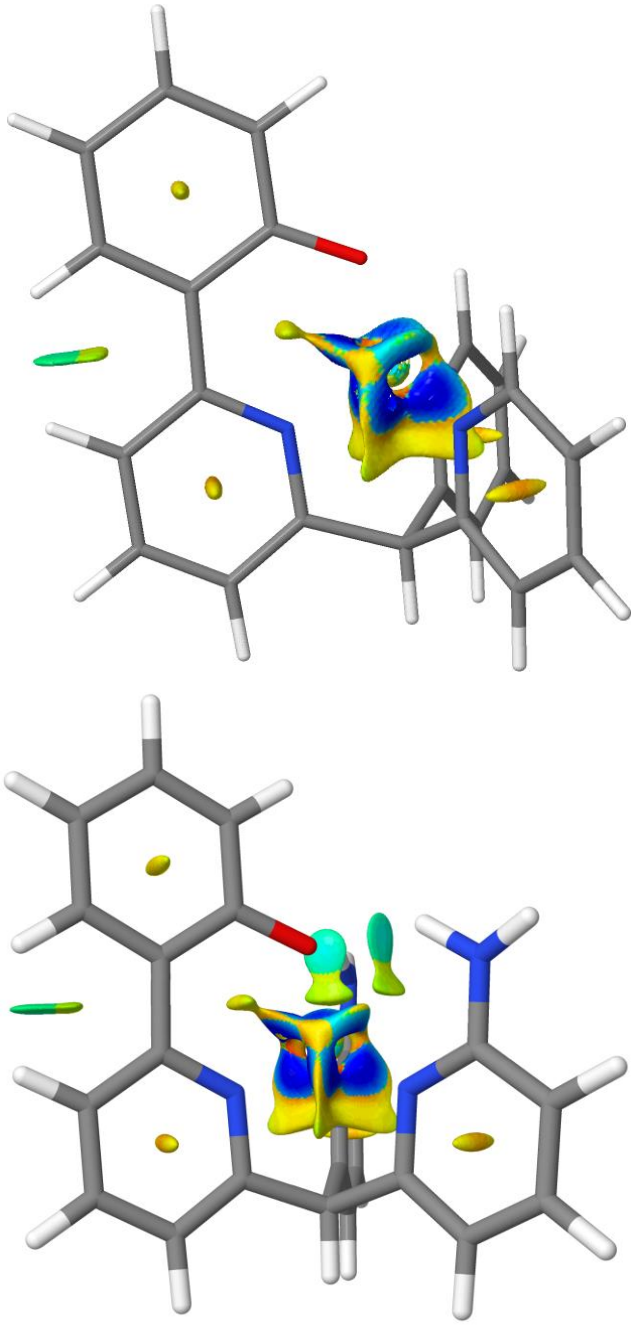

Figure 5.28 Models of **L1chH_Be** (top) and **L1chNH$_2$_Be** (bottom) showing their NCIPlot surfaces.

NCIPlots have been created for each complex (Figures 5.29-5.30). The main notable difference between these and the free ligands is the collection of data found in the top-left portion of the graphs. This is the metal-ligand interaction that is attributed to the covalent bonds to beryllium. A subtle but important detail is the comparison between the large blue peak near the mid-point of each of the graphs. For **L1chNH$_2$**, this peak is denser, and

corresponds to an overlapping of peaks. One of which is due to the hydrogen bonds previously mentioned. These strongly attractive forces correlate well to the higher binding strength seen in the calculated structures for the buttressed complexes relative to the non-buttressed complexes.

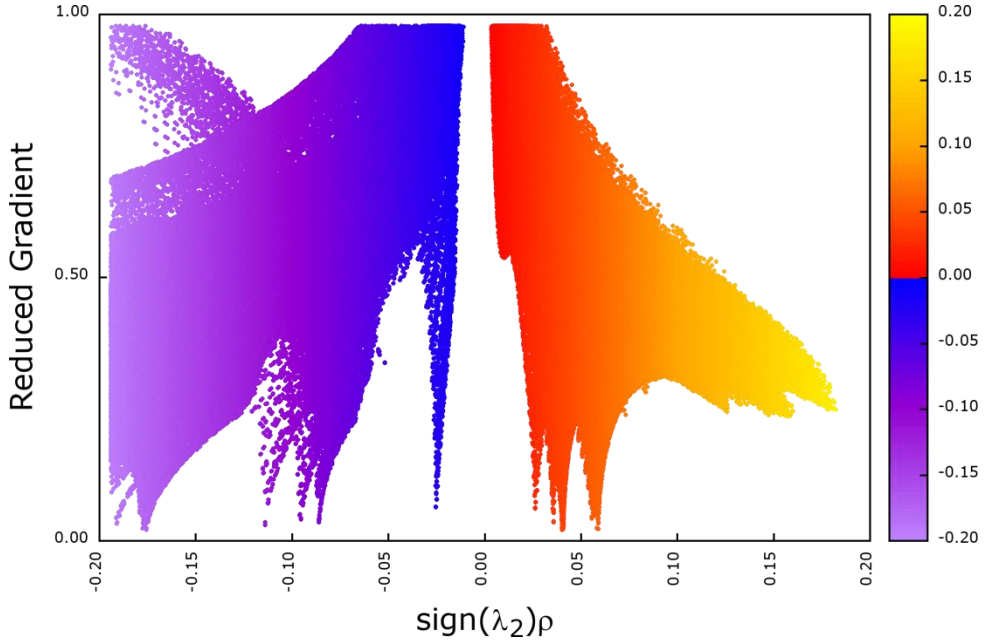

Figure 5.29 NCIPlot for **L1chH_Be**.

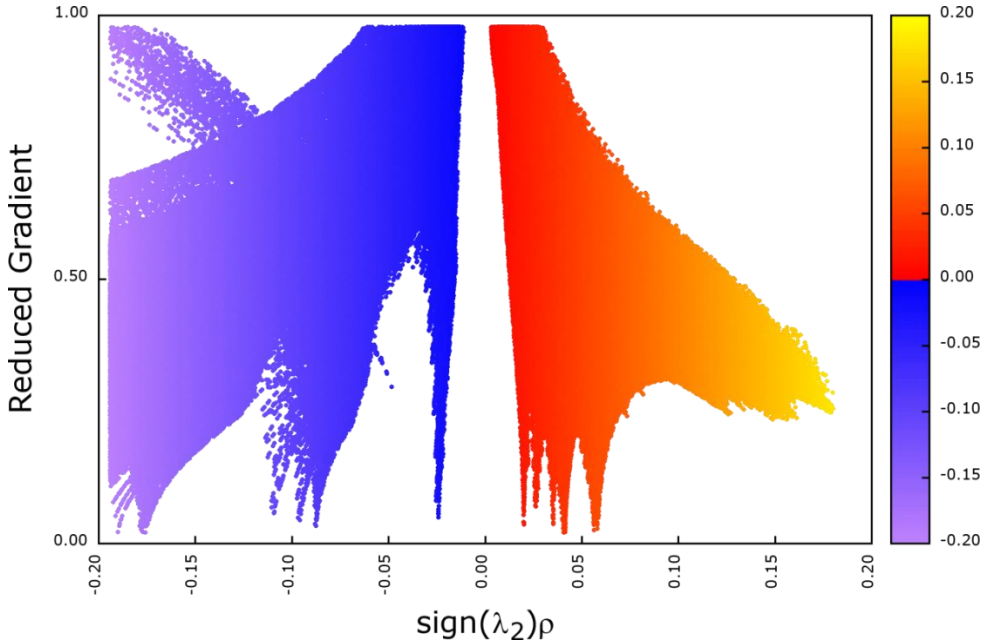

Figure 5.30 NCIPlot for **L1chNH$_2$_Be**.

Figure 5.31 presents NCIPlots at large and small radii centred on the hydrogen bonds visualised in **L1chNH$_2$**. As the radius is decreased, the NCIPlot scans a smaller area of the complex. At a radius of 0.25 Å, only the sharp peak corresponding to the hydrogen bonds remain. In the case of **L1chH**, mapping this same region shows no interactions at all.

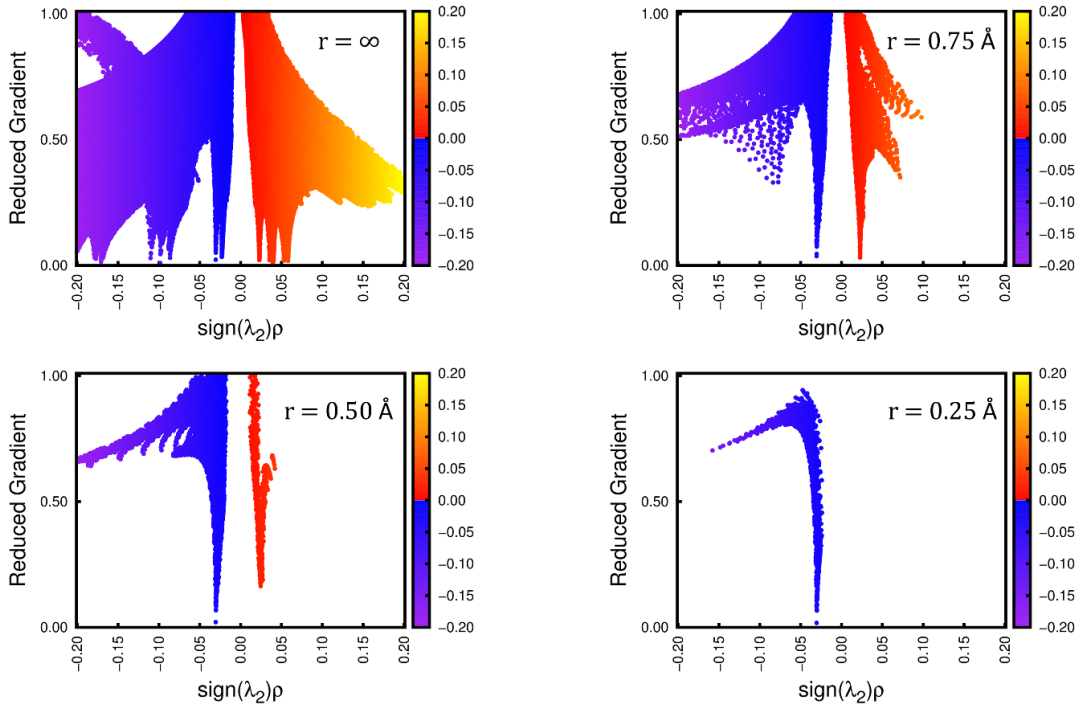

Figure 5.31 NCIPlots at radius r from the critical point of the buttress-phenol hydrogen bond.

5.6 Summary

This chapter has expanded upon the first computational study with extensive modifications. These were buttressing groups appended to the pyridyl arms of the ligands. It was found that in most cases, these groups led to increased binding strength towards cations, and in particular, to Be^{2+}. The general trend found in binding energies was B^{3+} > Be^{2+} > Al^{3+}. The identified ligands that have the most potential to bind strongly and selectively to Be^{2+} are the following (Figure 5.32):

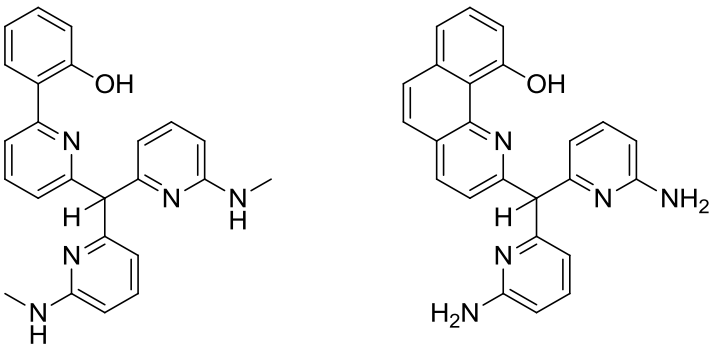

L1chNHCH$_3$ **L3chNH$_2$**

Figure 5.32 These ligands have been identified as the best theoretical and experimental candidates for further studies.

Another investigation was made regarding their apex group, whether the presence of a buttress group would significantly alter their conformation preferences. It was found that they do not, and computationally the preferred apex is **ch**, **coh** and **n** (to a lesser degree).

The wider metal binding study showed our ligands in comparison to known binders. Although it was found that the **L1** motif had weaker binding strength data towards Be^{2+} than other metal cations, it was the case that the amine buttress showed the most significant effect on its ability to chelate. The environment in which the sequestering of Be^{2+} is required must be carefully considered to understand what other metals may compete in the binding. As boron and beryllium are not typically found in the same environments, the binders that have been investigated are potentially good chelators for use with beryllium in the absence of the B^{3+} cation.

NCIPlots and corresponding isosurfaces were used to visualise the attractive and repulsive non-covalent interactions present in unbuttressed and buttressed ligands and complexes. A surface was successfully generated that shows the second sphere of interactions identified as a key for the success of these materials.

5.7 Future Work

Continuation of this project should primarily involve further synthesis towards key targets. However, although there is plenty of work to continue in the synthetic side of this project, several potential areas to expand on computationally have been identified. One such idea is a thorough investigation of the protein binding site that has been found to interact with beryllium in the human body.[120] This protein, HLA-DP2, is the primary candidate for beryllium binding due to the mutations that have been identified as occurring (Figure 5.33).[121] Using a combination of DFT and molecular mechanics (MM) using the ONIOM (our own n-layered integrated molecular orbital and molecular mechanics) computational approach, much could be learnt from the crucial and devastating interaction occurring in the protein when exposed to beryllium. Possible deductions might be made to improve on these or other chelators for therapeutic advances.

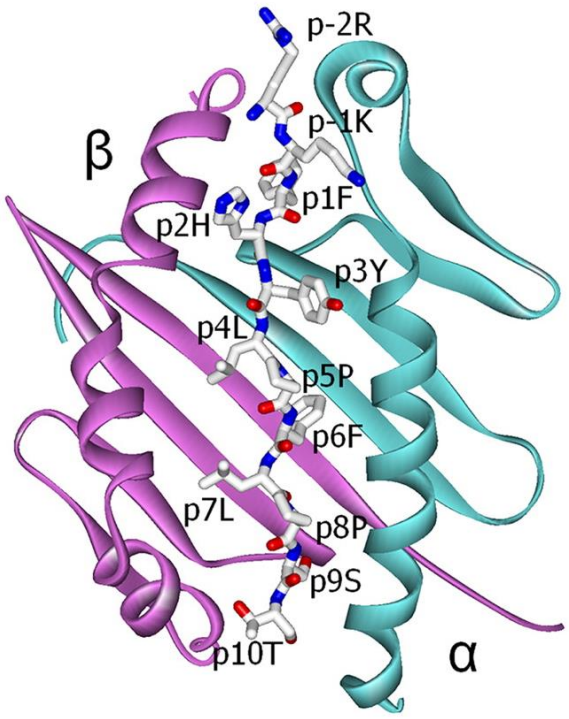

Figure 5.33 Ribbon representation of the HLA-DP2 structure, with the α2 and β2 domains omitted. Individual amino acids in the peptide are labelled.[121]

Another avenue to explore would involve ligands with multiple oxygen donors (Figure 5.34). Although these may be more flexible in nature, it could be the case that amine buttresses would hinder the ligand binding to large metal cations. Multiple layers of buttressing may also be possible.

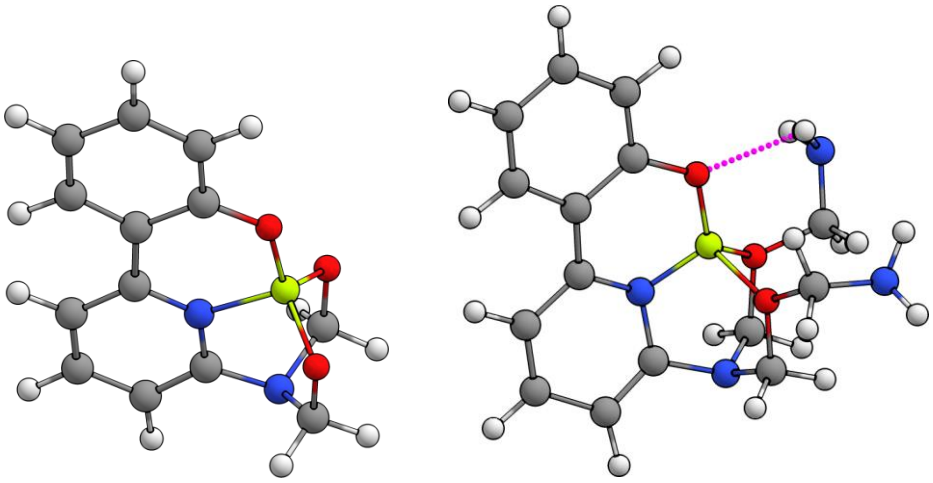

Figure 5.34 Flexible arms with primary alcohols (left) and with ethers and primary amine buttress (right).

It may be worth investigating long oily chains without additional donor atoms. This should help with organic solubility, if that is the desired property, as well as affect the binding strength to each metal in a possibly significant manner.

An experimental metal binding study should be undertaken. The computational results prompt a need for a comprehensive competition study if several non-buttressed and buttressed ligands can be synthesised in large amounts in high purity.

Chapter 6: Synthesis of Buttressed Ligands

"Insanity: doing the same thing over and over again and expecting different results."

– Albert Einstein

6.1 Introduction to Buttress Groups

The following chapter will discuss the synthesis towards a second sphere coordination-enabled ligand (Figure 6.1). This modified ligand incorporates the idea of chemical buttressing into its framework. The hydrogen-donor capable functionality of the pyridyl arms are free to from a secondary sphere of coordination through hydrogen bonds to the phenolic oxygen. It is expected that this modification will lead to a change in the binding strength of the subsequent complexed cation.

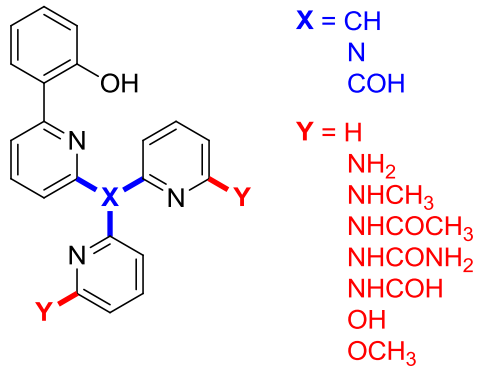

Figure 6.1 Ligand type 1 with buttressing.

Buttressing is a relatively new concept in supramolecular chemistry.[122] It occurs whenever a secondary sphere of coordination exists around the core binding site of a complex, through the use of appendages which support hydrogen bonding. This can increase the binding strength of the system, as well as altering its selectivity.

The primary use of buttressing found in the literature and industrial use is in metal extraction. Synthesising ligands that are more efficient in this task can decrease the

chemical cost of operations significantly, and perhaps even decrease waste. Tasker *et al.* found that secondary sphere interactions between ligands can be used to tune the strength and selectivity of metal extraction.[87, 122-123] This was in part due to the water-immiscible solvents favouring the formation of the buttressing hydrogen bonds. By altering these groups, the selective recovery of different metals is possible.

Introducing hydrogen bond donor capable functional groups to **L1**, such as an NH_2 group, the desired buttressing is achieved. This will have a number of useful effects:

- Pre-organisation of the binding site
- Smaller and more rigid binding pocket
- Metal-specific tuning of the binding site

Because the buttressed ligand is pre-organised before binding, the enthalpy of the system before complexation will be smaller, and therefore a higher binding strength is achieved. Increased selectivity towards beryllium is preferable but will not necessarily eventuate. Competition studies will be required to ascertain how each buttress group alters cation preference. The introduction of hydrogen bond donor functionalities should help to reduce flexibility, leading to a tighter and more rigid binding pocket; therefore, the relative binding strength to smaller cations should be increased. Due to steric constraint, larger metals may be destabilised, or at least less stabilised than their smaller counterparts. The bonds between the metal cation and each donor will be shorter, giving stronger bonds. Lastly, the buttress functional group ideally can be altered to any appropriate hydrogen-donor capable group. This could allow the ligand to be tuned specifically for certain metals.

In order to maximise binding and selectivity, buttressing components will be investigated for these ligand types. The functional group attached to the 6-positions of the two core pyridine rings will provide donors capable of hydrogen bonding to the deprotonated

phenolic oxygen. Examples of groups that could be examined for buttressing potential include amino and amido groups.

6.2 L1cohNH$_2$

6.2.1 First Route towards L1cohNH$_2$

Our initial buttressed target was **L1cohNH$_2$** (Figure 6.2). Initially, a reaction pathway was devised that was analogous to the first route attempted for the synthesis of **L1**. This would form a ligand of the same motif as **L1cohH**, including the tertiary alcohol apex, but with the addition of two amine functionalities. Synthesising this ligand will be more complicated than the previous compounds because of the reactive amino groups.

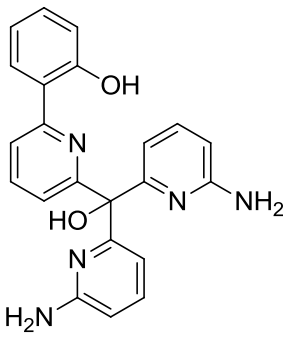

L1cohNH$_2$ 601

Figure 6.2 L1cohNH$_2$.

The first step of the retrosynthetic analysis is similar to Scheme 3.1-Scheme **3.2** (page 80), with the disconnection of the phenol ring from the bis(6-aminopyridin-2-yl)(pyridyl-2-yl)methanol scaffold (Scheme 6.1). Hence disconnection of **601** gives **302** and **602**. To prevent the amino groups from interfering with the Suzuki coupling, protecting groups will be required.

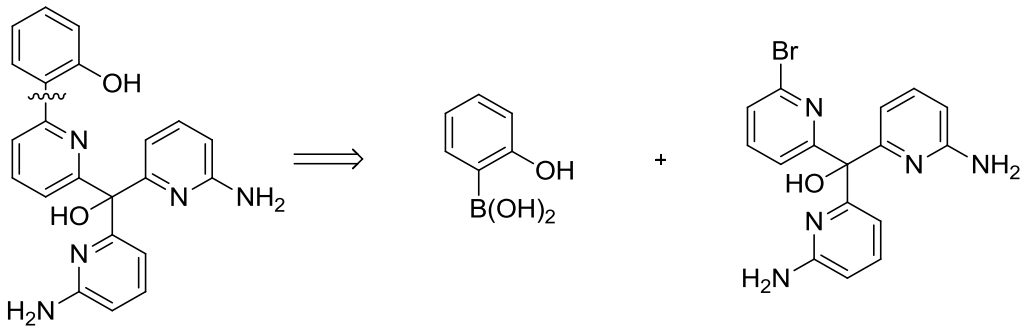

L1cohNH$_2$ 601 **302** **602**

Scheme 6.1 Disconnection of **601**.

Compound **602** can be formed from the reaction of 2,6-dibromopyridine **302** with a suitably protected dipyridyl ketone unit **603** (Scheme 6.2).

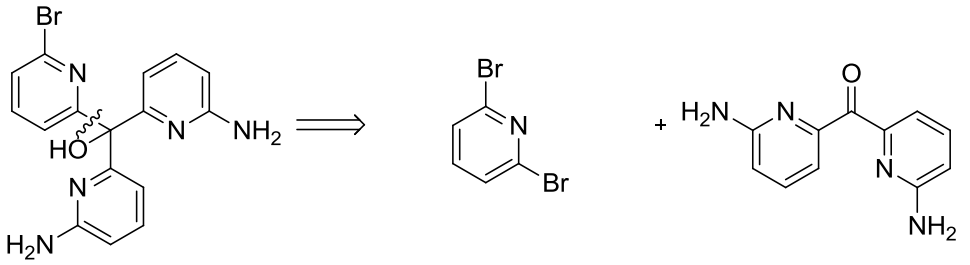

602 **304** **603**

Scheme 6.2 Disconnection of **602**.

As before, disconnection of the dipyridyl ketone gives ethyl chloroformate and a bromopyridine (Scheme 6.3).

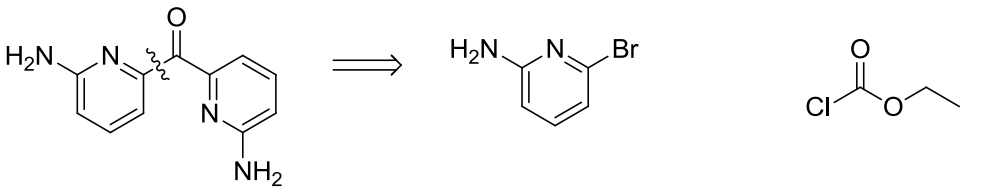

603 **604** Ethyl chloroformate

Scheme 6.3 Disconnection of **603**.

Before starting the forward synthesis, an appropriate protecting group that is stable to both the presence of *n*-BuLi, strong bases, and the Suzuki coupling must be identified. Carbobenzyloxy and *tert*-butyoxycarboynl groups are two of the most common groups typically used, but both can react with *n*-BuLi. The benzyl group provides the simplest solution; it is stable to strong bases and should be inert in the palladium coupling. It can also be removed under a host of different conditions at the end of the synthesis.

The compound 2-amino-6-bromopyrdine **604** was therefore protected (Scheme 6.4). This reaction was carried out on a large scale (~30 g) and catalysed with tetrabutylammonium iodide (TBAI). Excess benzyl bromide was removed through purification by either silica gel chromatography, or recrystallization from 9:1 hexanes:EtOAc, affording a 82% yield with high purity. This new compound was fully characterised by NMR and ESI-MS, confirming its synthesis and purity (Figure A-7).

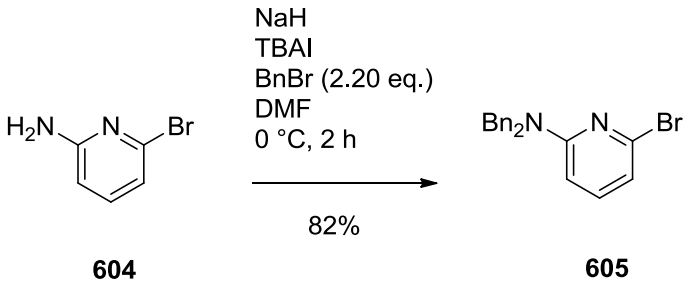

Scheme 6.4 Protection of 2-amino-6-bromopyridine.

Crystals of **605** were grown by slow evaporation from an EtOAc solution and subjected to single crystal X-ray structural determination (Figure 6.3). The compound crystallized in the space group $P2_1/n$ and the model converged to an R_1 of 4.04%. The composition of the simple molecule is as expected, with the two benzyl groups replacing the amine protons. This leaves the amine inert for any subsequent reactions. The reactive bromo atom is available for further reaction.

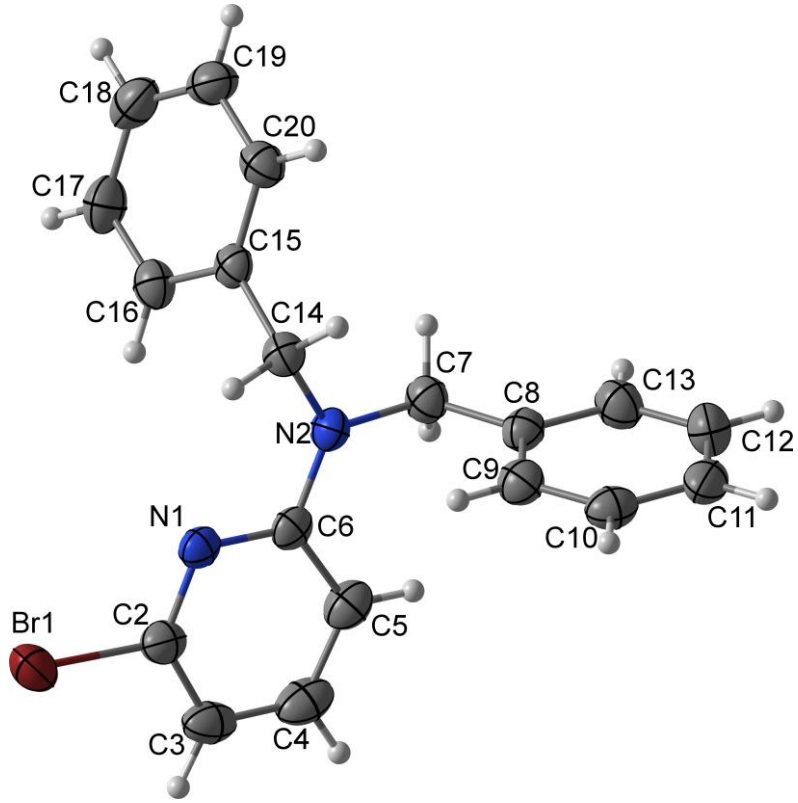

Figure 6.3 X-ray image of the benzyl-protected 2-amino-6-bromopyridine **605**, with thermal ellipsoids at 50% probability level.

The next step in this route, the synthesis of ketone **606**, proved difficult (Scheme 6.5). Bromine-lithium exchange was performed by adding *n*-BuLi dropwise to a solution of compound **605** to form a good nucleophile. Ethyl chloroformate is added, which has two good leaving groups. The first nucleophile attacks the electrophilic carbonyl, expelling the chlorine atom as Cl^-. The second attacks in the same manner, this time a molecule of ethoxide is expelled.

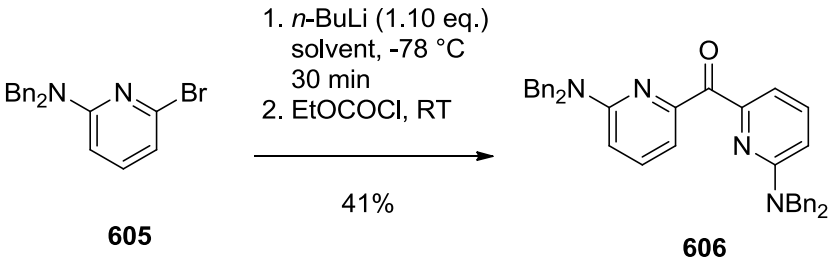

605 **606**

Scheme 6.5 Synthesis of the dipyridyl ketone moiety, **606**.

The general synthetic method was as follows: *n*-butyllithium was added to a solution of **605** dropwise, in dry THF at -78 °C under argon. After 30 minutes of stirring, ethyl chloroformate (EtOCOCl) was added and the solution was allowed to warm to room temperature over two hours. The reaction was then quenched with water. Unfortunately, this first attempt after purification using silica gel chromatography reaction resulted in a low yield (7%). The identity of the desired product **606** was confirmed by assignment of the ^{1}H and ^{13}C NMR spectra, and ESI-MS (Figure A-8). The crude reaction product contained a mixture of starting material, protodebrominated **605**, pyridyl ethyl ether, and a small amount of product. Subsequently, because of this poor yield, numerous attempts were made to improve it. The conditions which were varied include the concentration of reagents, the solvent and its dryness, reaction time, and quenching reagent (Table 6.1).

The typical colour changes observed were the following:

Solution of **605**	-	Clear colourless
Addition of *n*-BuLi	-	Clear yellow or orange
Addition of EtOCOCl	-	Dark green or blue for ~5 minutes
Stirring over 1 hour	-	Clear yellow

Reactions left stirring overnight remained a clear yellow solution. The strength of the *n*-butyllithium solution was tested regularly by titrating it against menthol using 1,10-phenanthroline as the indicator. The compound **605** was left to stir with *n*-BuLi for a specific length of time that ranged from 15 minutes to 1 hour. It did not appear to be the case that this was a significant factor in determining the success of the reaction. Further, the reaction was quenched predominately with water, but weak solutions of hydrochloric acid and acetic acid were also tried. As they did not improve the workup procedure, only water was used in the remaining reaction conditions.

Table 6.1 Conditions for the synthesis of **606**.

Entry	eq. 605	eq. EtOCOCl	eq. *n*-BuLi	Solvent	Time	Quenching reagent	Yield
1	1	0.50	1.15	THF	2 h	H_2O	7%
2	1	0.50	1.10	THF	3 h	H_2O	3%
3	1	0.50	1.10	THF	2 h	H_2O	15%
4	1.05	0.50	1.16	THF	3 h	H_2O	8%
5	1.20	0.50	1.30	THF	3 h	5% HCl	22%
6	1	0.50	1.10	THF	o/n	AcOH	0%
7	1	0.50	1.10	THF	3 h	H_2O	18%
8	1	0.50	1.10	THF	o/n	H_2O	0%
9	1	0.50	1.10	Et_2O	3 h	H_2O	15%
10	1	0.50	1.10	THF	2.5 h	H_2O	41%
11	1	0.50	1.15	THF	o/n	H_2O	0%
12	1	0.50	1.15	THF	3 h	H_2O	0%
13	1	0.50	1.15	THF	2 h	H_2O	36%
14	1	0.50	1.15	THF	2 h	H_2O	37%

The sixth reaction (Table 6.1) was the first that allowed the reaction mixture to stir overnight at room temperature. This resulted in little to no product being observed by ^{1}H NMR. As the solution remained a dark green colour for much longer than expected (~1 h) before leaving it to react overnight, it could have been the case that this reaction failed due to a non-time related cause.

Fresh *n*-butyllithium was used for the ninth attempt (Table 6.1), and the solvent was replaced with diethyl ether. The solubility of the starting material in diethyl ether at room temperature was low, and when the temperature was reduced to -78 °C, **605** precipitated. As the glassware was submerged in a cold bath of isopropyl alcohol and liquid nitrogen, the extent of precipitation was not identified at the time. Nonetheless, the reaction was carried out, and a yield of 15% was obtained. After this attempt, the dryness of the solvent was considered. The THF and diethyl ether used had been dried by being passed through alumina columns. This is typically sufficient for the majority of cases. If this reaction was particularly sensitive to the presence of water, it could be tested by drying the solvent further. This was done by drying THF by distillation over fresh sodium-benzophenone

ketyl. The first case using this THF achieved a yield of 41% - the highest so far obtained. Therefore, any subsequent reactions took advantage of this by also following this additional preparative procedure.

The following attempt, number 11 (Table 6.1), allowed the reaction mixture to stir overnight at room temperature. This resulted in little to no product being observed by ^{1}H NMR, therefore it was concluded that allowing the reaction to continue for too long resulted in either decomposition or additional undesired reactions. Silica gel chromatography was used in an attempt to isolate the various compounds from this reaction (as well as the previous overnight attempts), but any conditions used resulted in streaking or overlap of peaks. Obfuscation in the NMR prevented their identities from being determined. It was decided that the conditions used in reaction 10 were the best, and these were repeated for reactions 12-14. The crude material of reaction 12 was found by NMR to be only starting materials, and so it must be the case that the *n*-BuLi did not function as per normal. The last reactions 13 and 14 gave acceptable yields of 36% and 37% respectively.

During the time spent on developing a good synthetic procedure, crystals of **606** were grown by slow evaporation from DCM/MeOH, and these were subjected to single crystal X-ray structural determination (Figure 6.4). The resulting connectivity provides proof that the synthesis of the desired compound was successful. The asymmetric unit of **606** consists of one half of the molecule. Symmetry elements reproduce the other part of its structure. The crystal space group is orthorhombic (*Fdd*2) and has a modest R_1 value (5.87%). The four benzyl groups lie on one side of the molecule, leaving a sterically hindered underside. The bridging ketone is pointed away from these, leaving room from both above and below for the approach of the nucleophilic reactant. A possible electrostatic attraction exists between the pyridyl nitrogen and a nearby methylene proton (N1···H7a, 2.266(6) Å).

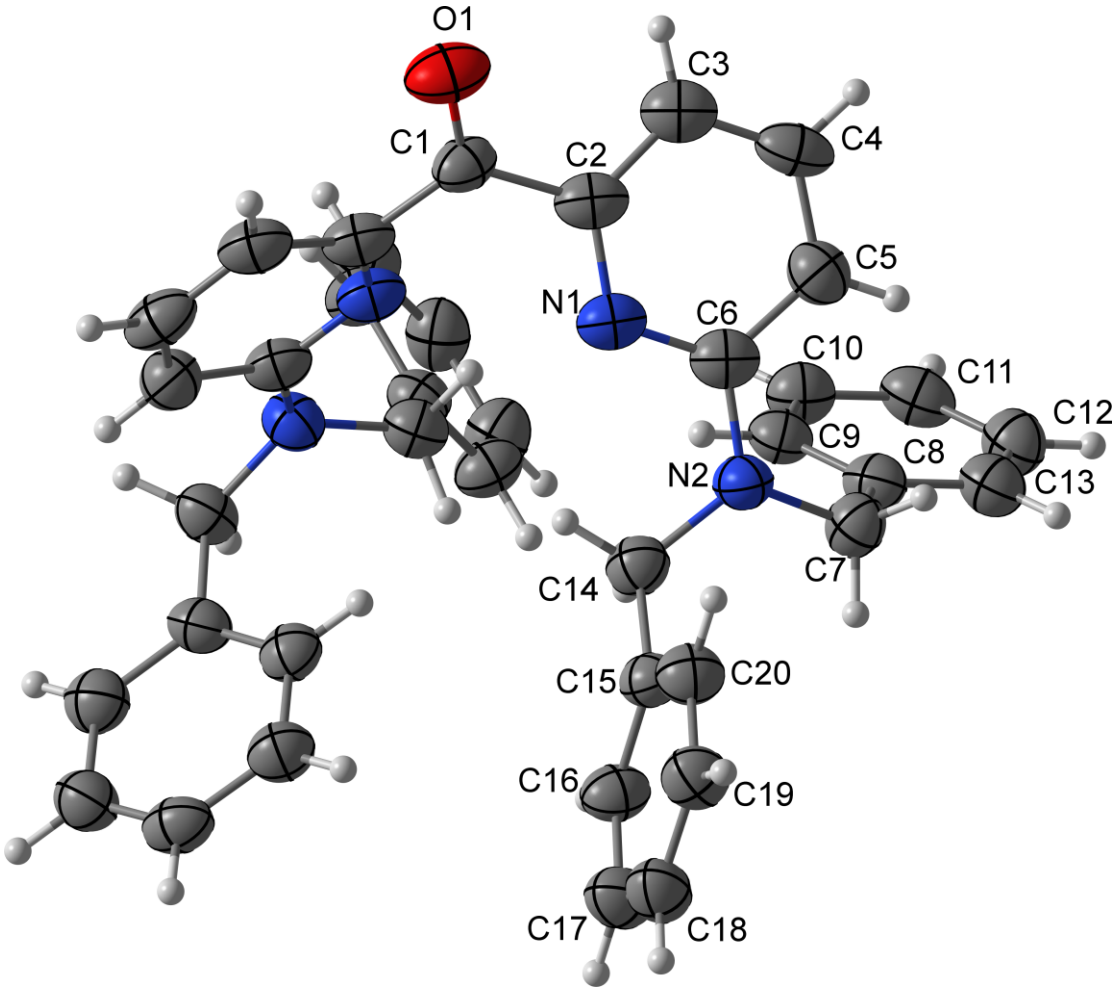

Figure 6.4 X-ray image of **606**, with thermal ellipsoids at 50% probability level.

The addition of 2,6-dibromopyridine to **606** would add the next aromatic ring to the system (Scheme 6.6). Unfortunately, this procedure was unsuccessful. Analysis of the crude product by ^{1}H NMR gave the starting material **606** and 2-bromopyridine. The inability of lithiated **304** to attack the ketone of **606** suggests that the new substituents are prohibiting the reaction from going forward. This could be due to steric bulk, electronics, or that the tertiary nitrogen atoms are behaving as a ligand for the Li^{+} cation.

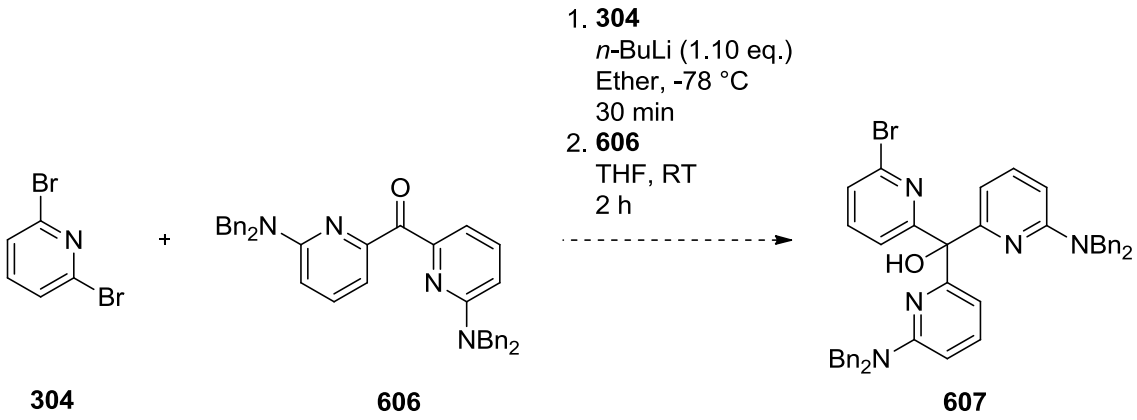

Scheme 6.6 Attempted synthesis of **607**.

To help determine why this reaction did not proceed, smaller protecting groups were investigated. The first was to use methoxymethyl chloride (MOM-Cl) to cap the aryl amine with two hemiaminal groups (Scheme 6.7). Although unprecedented to introduce two MOM groups to an amine, the chemistry to introduce the first is well known. The reaction was carried out, but only the mono-substituted product was identified in the crude product. Resubjecting the material to the same conditions again did not result in any difference. As it is likely that similar reaction conditions have been attempted but not reported in the literature, this line of synthesis was abandoned.

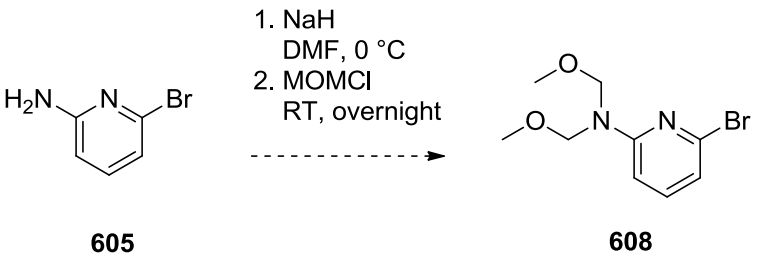

Scheme 6.7 Attempted synthesis of **608**.

Next, the smallest protecting group possible was chosen, to test if size was an issue. A methyl group was chosen to replace the benzyl group (Scheme 6.8). Although these would be very difficult if not impossible to remove once the ligand is synthesised, these would provide a good test for whether this type of reaction could proceed. The synthesis of **609**

followed a similar procedure for making the benzyl-protected analogue. Although compound **609** is known,[124] a new procedure was used to prepare it (Scheme 6.8). The reaction used iodomethane as its source of electrophilic methyl group, giving **609** in a 91% yield. Its synthesis was confirmed by comparison to known literature values (Figure A-9).[124]

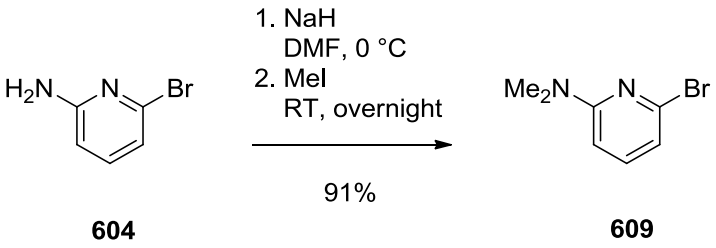

604 **609**

Scheme 6.8 Synthesis of **609**.

The subsequent reaction to synthesise the ketone was carried out successfully in a modest yield of 31 % (Scheme 6.9). ^{1}H NMR analysis was used to prove its synthesis (Figure A-10).

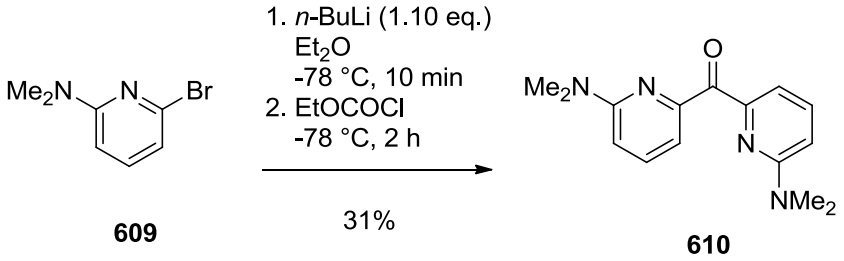

609 **610**

Scheme 6.9 Synthesis of **610**.

In addition to the product being formed, a large fraction of the crude was found to be a side product **611**. The impurity present was the result of a third pyridyl group reacting with the ketone to produce the tertiary alcohol (Figure 6.5). Identification of the impurity **611** was done by ESI-MS. Separation of the ketone and tertiary alcohol was attempted by silica gel chromatography, but the two compounds ran together, allowing for only poor resolution to be achieved. Pure **610** was obtained through this process, but in amounts (10-20 mg) not useful to proceed with. Despite these issues, Scheme 6.9 proved that this

type of reaction when N-substituents are present is possible, at least with less-wieldy protecting groups.

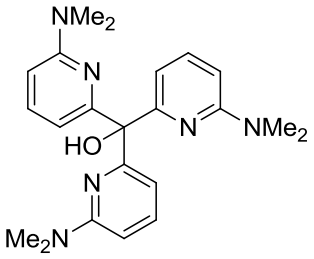

611

Figure 6.5 Impurity in the synthesis of **610**.

The impure mixture was reacted with NaH and ethyl chloroformate. This was in an attempt to chemically alter the polarity of the impurity **611** such that it would interact with the stationary phase to a different degree than **610** (Scheme 6.10). Unfortunately, this reaction did not proceed – the NMR spectrum remained unchanged.

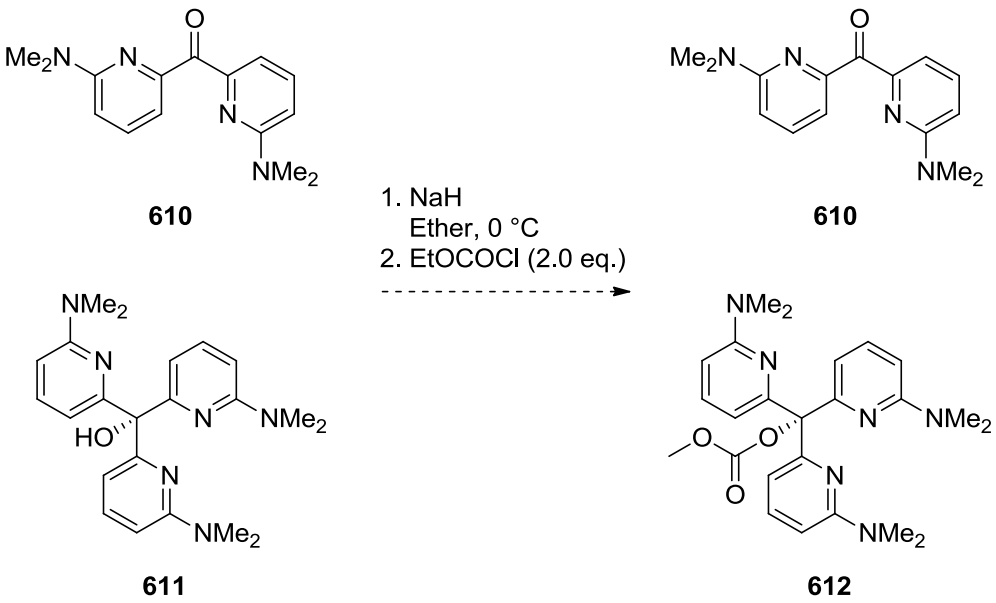

Scheme 6.10 Attempted reaction to help separate 610 from the major impurity 611.

A new method was devised to synthesise pure **610** (Schemes 6.11-6.12). By starting with a thioketone derived from **610**, the formation of the trimodal pyridyl structure may be

prevented. The reaction was attempted only once, giving a yield of 64%. The product was purified by recrystallization from hot diethyl ether. ^{1}H NMR and ESI-MS confirmed that **613** was synthesised.

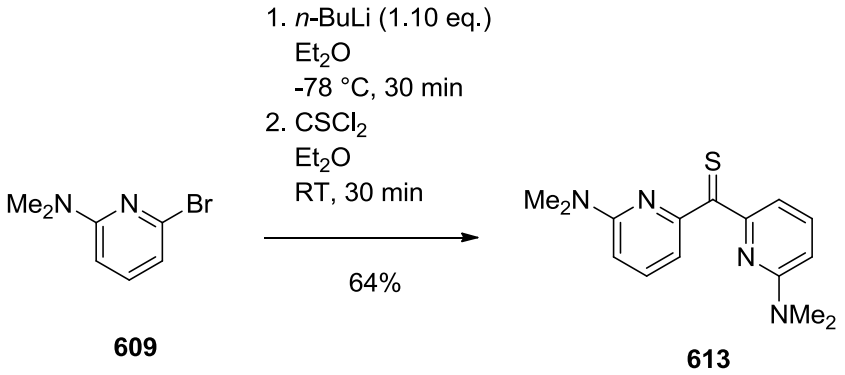

609 **613**

Scheme 6.11 Synthesis of **613**.

The hydrolytic conversion of the thioketone to the ketone was achieved by treatment with hydrogen peroxide and thionyl chloride to give **610** (Scheme 6.12). Pure product was obtained by silica gel chromatography, albeit in poor yields (15%). To confirm its synthesis, the ^{1}H NMR spectrum was compared to the pure material that was recovered from Scheme 6.9, and was found to match exactly.

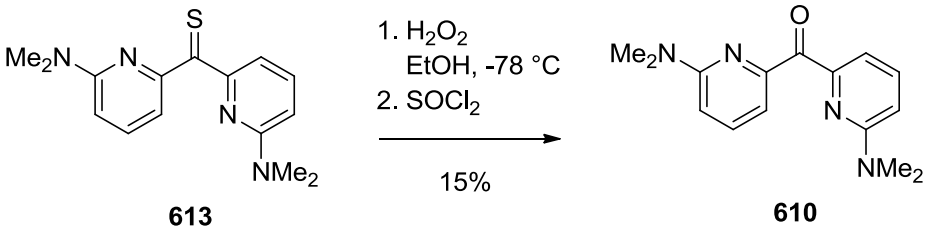

613 **610**

Scheme 6.12 Attempted alternative synthesis of **610**.

A third reaction was attempted to make **610** in a high yield (Scheme 6.13). Triphosgene was employed to form the bridging ketone. Because this compound decomposes to phosgene on heating or reacting with nucleophiles, very careful attention to the appropriate procedures were followed to eliminate any potential health hazards. As it is a solid crystalline material at room temperature, it was found it could be handled safely

with relative ease. Initially, the yield of the reaction was disappointing (17%), with most of the crude material consisting of the starting material **609**. Again, proof of successful synthesis was measured by comparison to prior reactions.

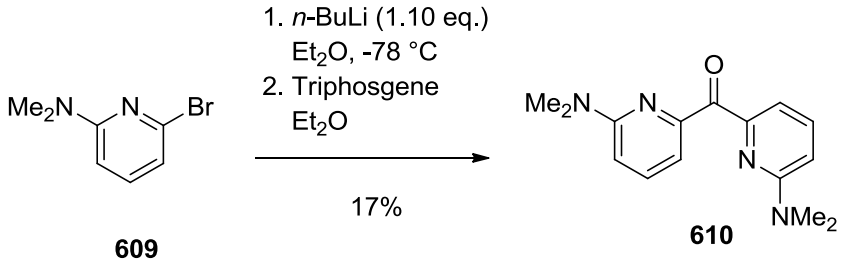

Scheme 6.13 Best synthesis for **610**.

This reaction was repeated as it was thought that the *n*-BuLi used had significantly degraded. The second attempt, with freshly opened *n*-BuLi, proved very successful (88% yield). A new protocol was established in the lab for working with *n*-BuLi, that its concentration would be periodically determined by titration against menthol, using 1,10-phenanthroline as an indicator.[125]

The culmination of the previous syntheses leads to the problematic reaction of combining these two compound types. With a much smaller protecting group on the amino groups, we were hopeful that the reaction would proceed where the benzyl groups did not. Indeed, this was the case with a yield of 23% (Scheme 6.14).

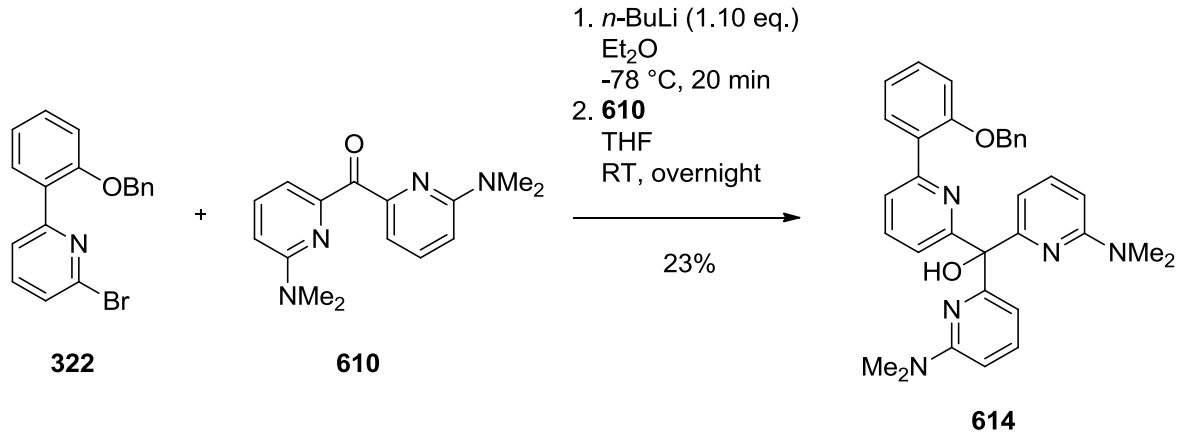

Scheme 6.14 Attempted synthesis of **614**.

Deprotection of the phenol would give a tetradentate ligand capable of binding a small metal (Scheme 6.15). Some unprecedented chemistry may exist that could remove one or multiple methyl groups – this would achieve the first ligand of this type to be capable of forming a secondary coordination sphere. The compound **614** was subjected to hydrogenation with 5% Pd/C in a protic solvent. Analysis of the ^{1}H NMR spectrum of the reaction mixture showed that the starting material had been consumed, due to the disappearance of the C*H*$_2$ signal (5.14 ppm) from the benzyl protecting group, therefore full cleavage of the protecting group is occurring (Figure 6.6). This suggests then that the product is being formed successfully, albeit with a low yield (12%). The rest of the material is unaccounted for. In hindsight it is likely to have remained on the Pd/C.

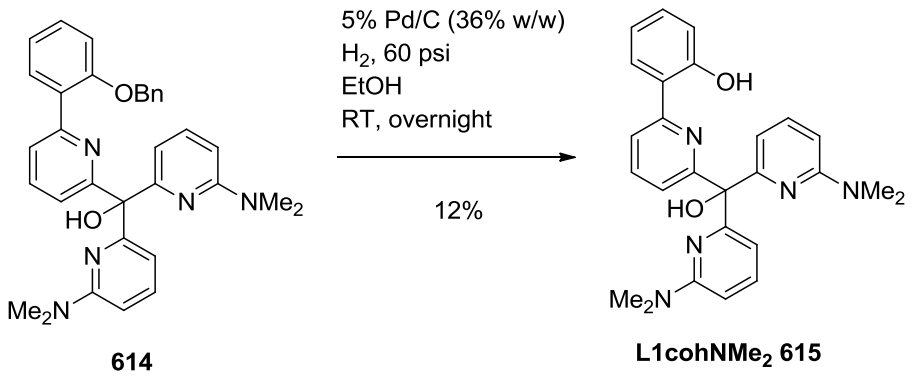

614 **L1cohNMe$_2$ 615**

Scheme 6.15 Deprotection synthesis of **615**.

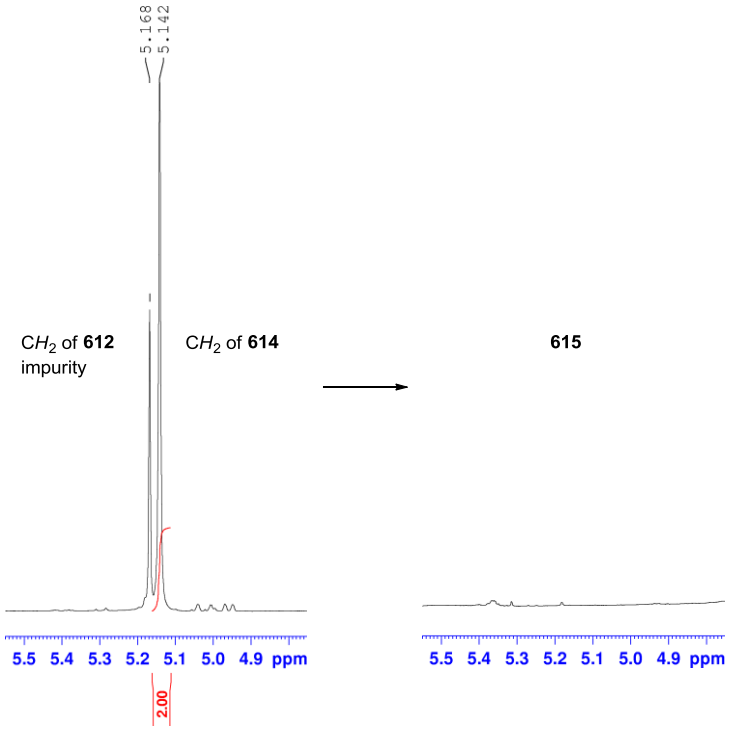

Figure 6.6 ^{1}H NMR comparison of the CH_2 group of the benzyl functionality before and after hydrogenation.

Purification of **615** was attempted by silica gel chromatography and recrystallization. Unfortunately, regardless of conditions, it was not possible to separate it from impurities.

A new approach was required, and so therefore a deviation from this general route was attempted. The same chemistry was used but in a different order. A non-symmetric dipyridyl compound would be first formed, where one pyridine has a bromine group, and the other the benzyl-protected amine (Scheme 6.16). Ethyl 6-bromopicolinate, **616**, was commercially available.

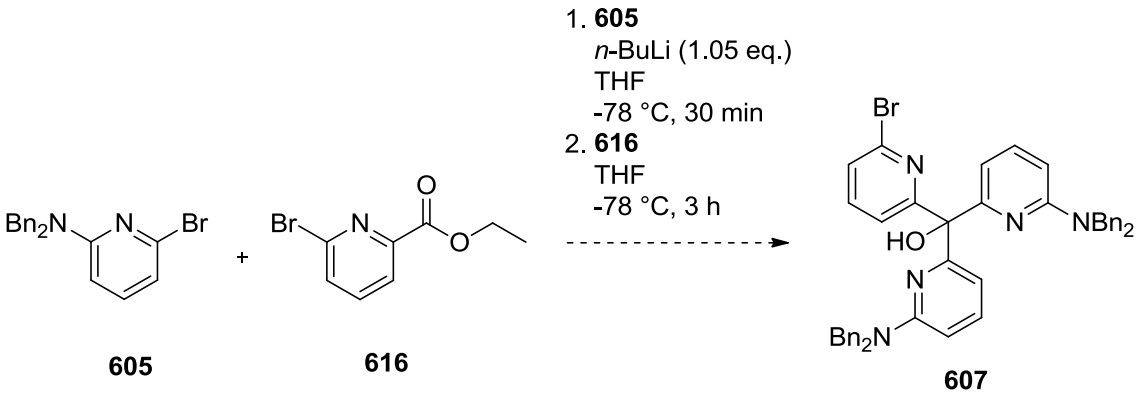

Scheme 6.16 Attempted synthesis of **607**.

The major product of this reaction was found to be the result of only a single addition to the ester (Scheme 6.17), in good yield (57%). The proton and carbon chemical shifts in the spectra of ^{1}H NMR, ^{13}C NMR, COSY, HMBC, and HMQC were fully assigned to prove the identity and purity of **617** (Figure A-11).

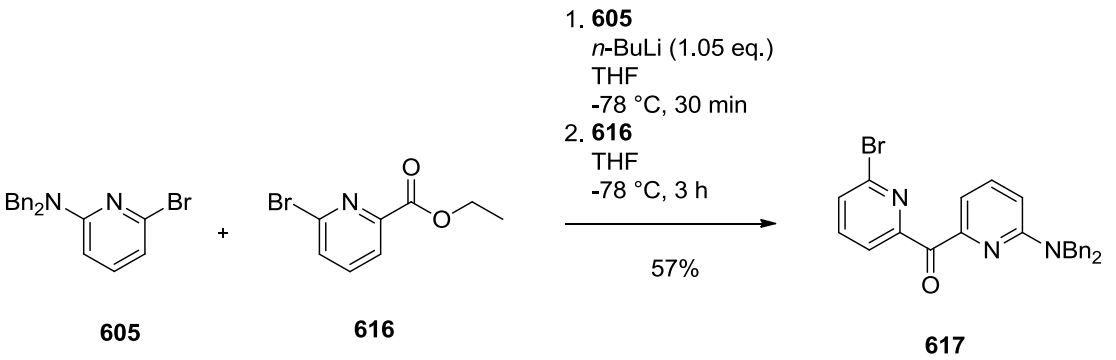

Scheme 6.17 Synthesis of **617**.

Conclusive proof of the successful reaction was obtained by single X-ray structural determination of a purified sample of **617**, which was grown from the slow evaporation of a solution of Et_2O/MeOH (Figure 6.7). Its space group was monoclinic ($P2_1/a$), with an R_1 value of 9.36%. The conformation of the structure showed that the 2-bromopyridyl moiety orientated itself away from the dibenzylamine so to reduce steric strain, and to maximise π-π stacking interactions between the benzyl rings within the intermolecular

packing. A moderate electrostatic attraction possibly exists between one pyridyl nitrogen and an opposing hydrogen (N2···H3, 2.408(8) Å).

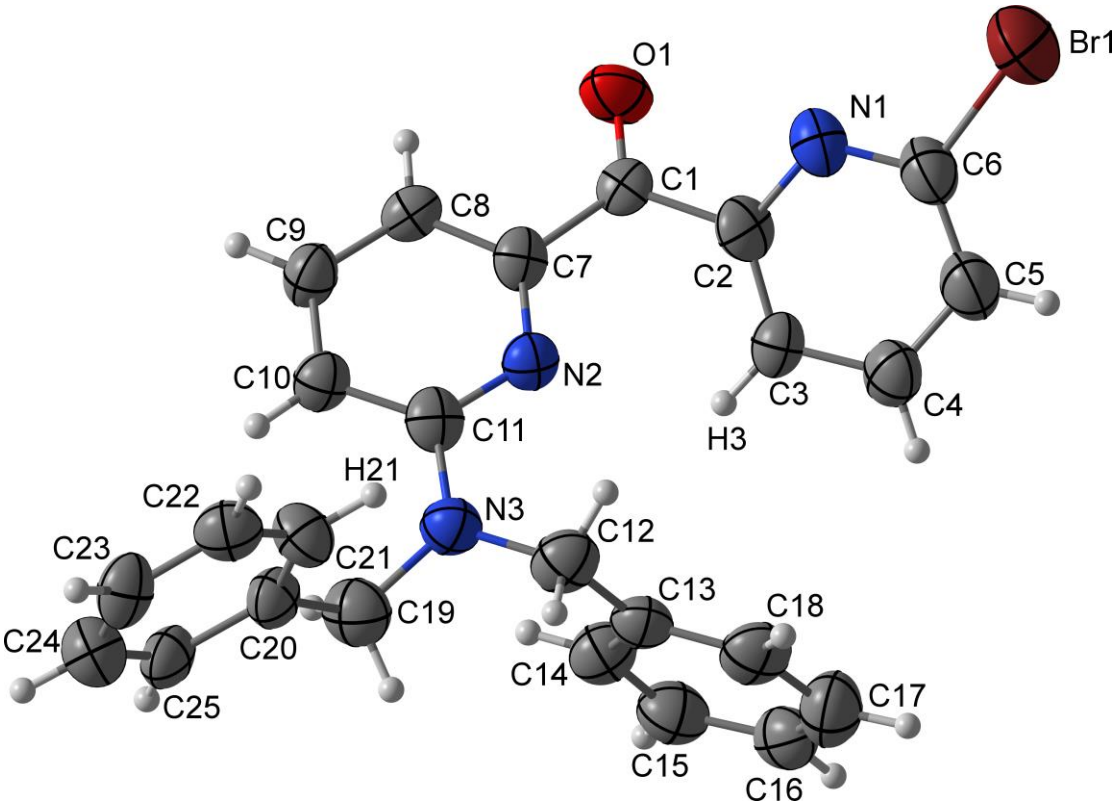

Figure 6.7 X-ray image of **617**, with thermal ellipsoids at 50% probability level.

In this conformation, the ketone remained relatively unhindered to the approach of a second molecule of **605**. A step-wise process towards **607** was attempted by reintroducing lithiated **605** to **617**, but unfortunately the reaction did not proceed, as analysed by ^{1}H NMR and ESI-MS. The reason why could not be deduced, so there is number of possibilities still left to be considered. It is most likely that the reactivity of the mono addition product was too low for the second addition, due to a deactivating effect from the aryl bromo group or tertiary amine.

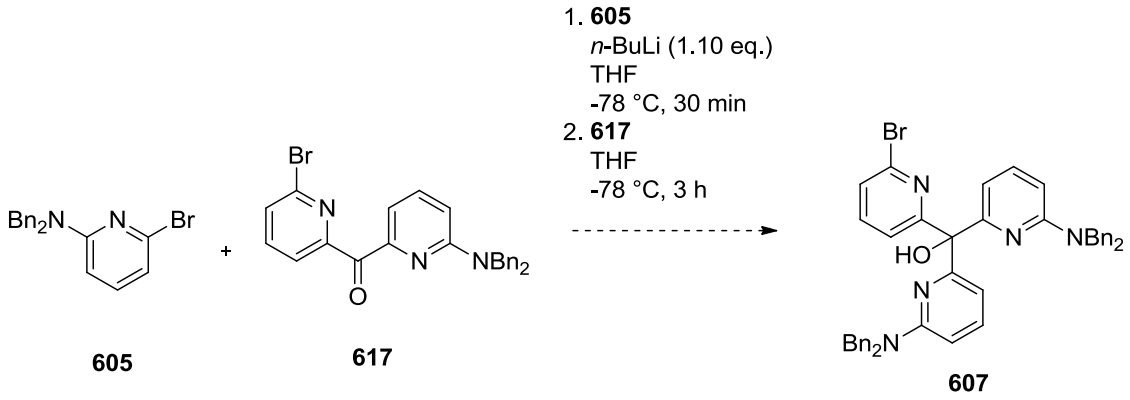

Scheme 6.18 Second attempted synthesis of **607**.

A single attempt to couple **617** with a boronic acid was attempted (Scheme 6.19). The resulting product was a mixture of starting material and unidentifiable compounds. Purification by silica gel chromatography was not simple and did not produce any pure new compounds. This route was given up and another more promising avenue was pursued.

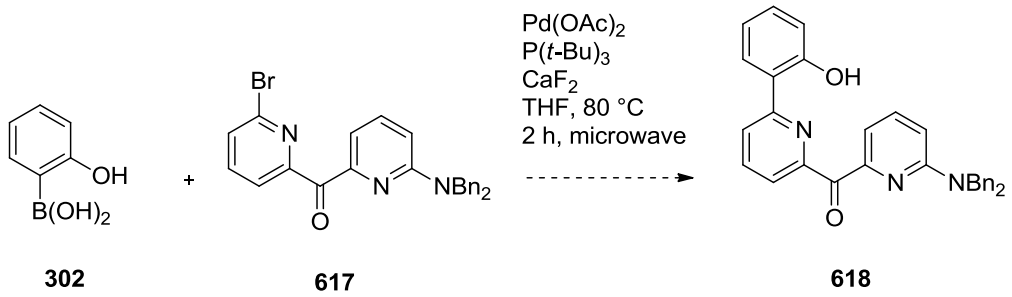

Scheme 6.19 Attempted synthesis of **618**.

6.2.2 Second Route towards L1cohNH$_2$

The previous retrosynthetic plan disconnected the bi-aryl phenol-pyridine fragment (Scheme 6.2). A new plan involved the addition of the aminopyridine to an ester substituted bi-aryl moiety (Scheme 6.20). This would give a phenyl-pyridyl compound with an ester functional group, as well as the previously synthesised protected amino pyridine.

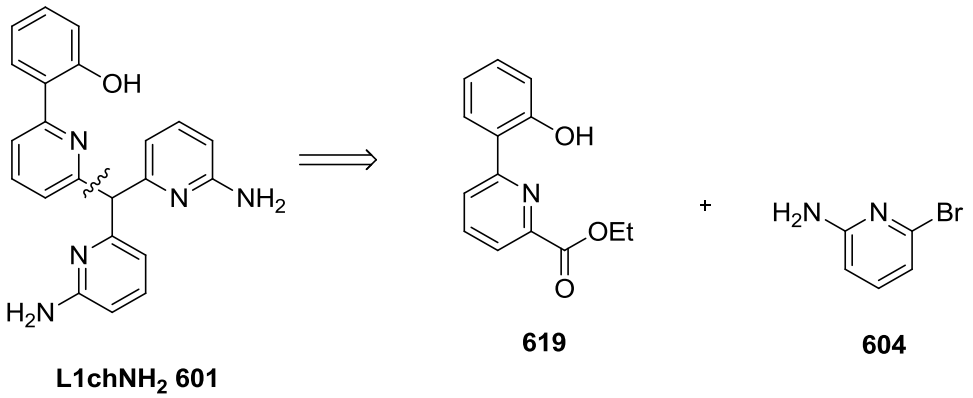

L1chNH$_2$ 601 **619** **604**

Scheme 6.20 New disconnection of **601**.

The compound **619** could be prepared from the following compounds, both of which are commercially available (Scheme 6.21).

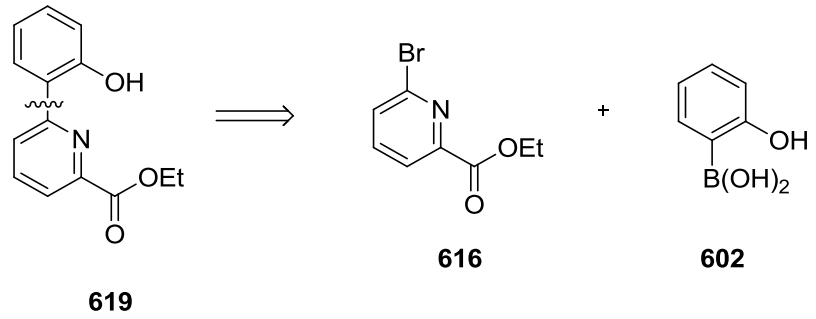

619 **616** **602**

Scheme 6.21 Disconnection of **619**.

This route would take just 2 steps, excluding any required protection and deprotection. A benzyl protecting group is again appropriate here, so **605** will be substituted for **604** here. Similarly, the phenol of the boronic acid **302** was protected as methyl ether (Scheme 6.22) in order to prevent undesirable reactions such as those observed earlier in this chapter (Figure 3.6, page 84).

A Suzuki coupling was used to combine the boronic acid **620** to the first pyridyl unit **616**. This proceeded with a 66% yield, and its identity was confirmed by ^{1}H NMR.

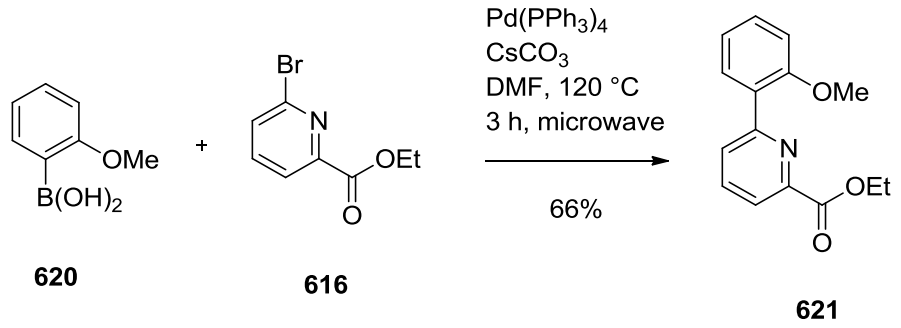

620 **616** **621**

Scheme 6.22 Synthesis of **621**.

It was hoped that reacting **621** with **605** would produce the protected version of the ligand (Scheme 6.23). This did not proceed. Likewise, the addition of just one pyridine unit to **621** was also unsuccessful.

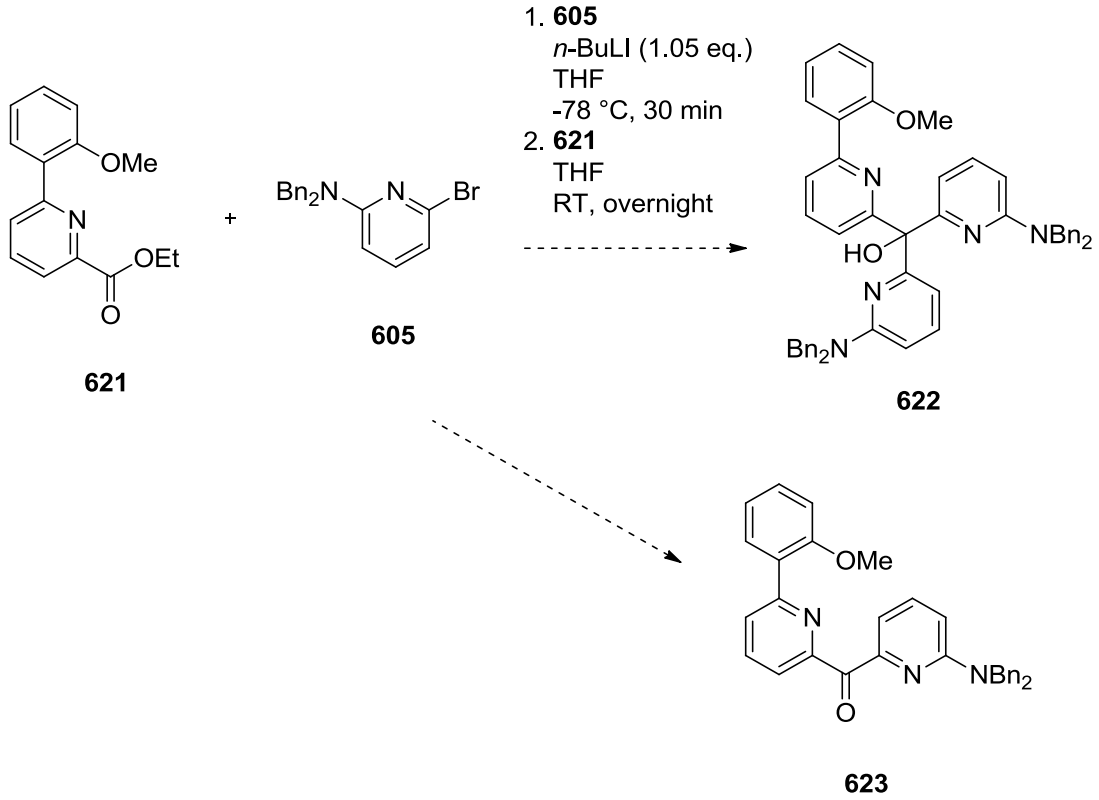

621 **605** **622** **623**

Scheme 6.23 Attempted synthesis of **622** or **623**.

A third approach using known Grignard chemistry was made (Scheme 6.24). Compound **322** was used for this, as it has previously been synthesised as part of the earlier work towards **L1chH**. Analysis of the reaction product gave no sign of any reaction with **606**.

Some protodebrominated pyridine was observed in the ^{1}H NMR spectrum, suggesting some success of Grignard formation.

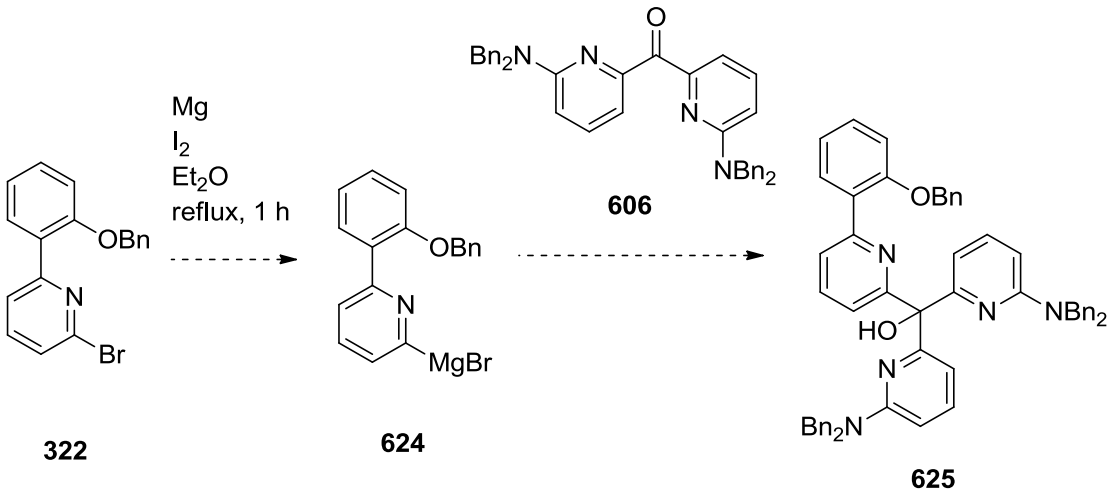

Scheme 6.24 Attempted synthesis of **625**.

The last considered reactions returned to using lithium halogen exchange chemistry (Scheme 6.25). The coupling of **310** to **606** was successful. This gave **622** as a new compound in a 23% yield, albeit with its amine and phenol functionality still protected. The compound **622** was purified by silica gel column chromatography, and its synthesis proven by ^{1}H NMR and ESI-MS.

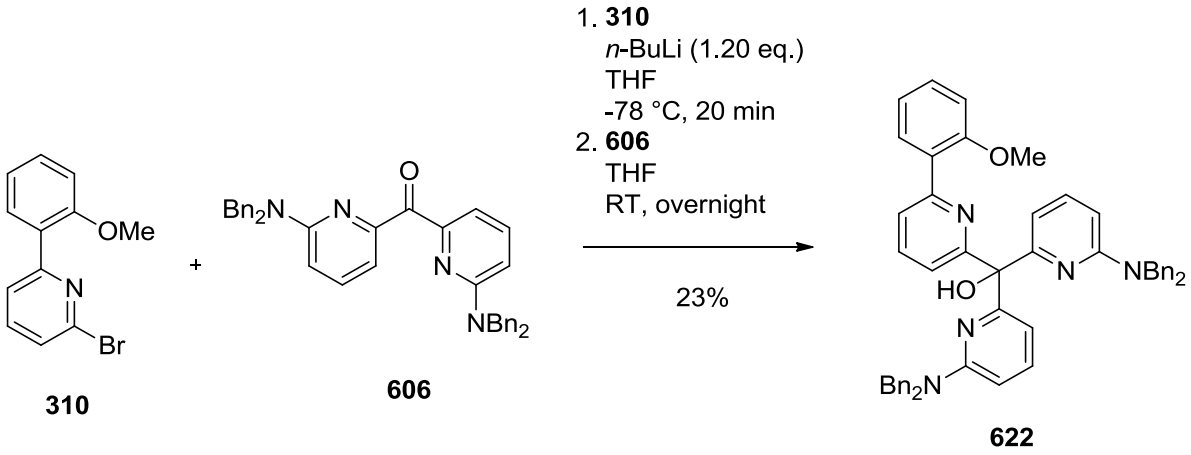

Scheme 6.25 Synthesis of **622**.

The last two steps in this route involved deprotection of the methyl group from the phenol, and the benzyl groups from the amino groups (Scheme 6.26). A standard procedure for deprotection using benzyl tribromide was followed. Silica gel chromatography was used to separate the various compounds formed, but it was not clear from analysis that **626** had been formed. Increasing the quantity of BBr_3 failed in aiding the reaction. Because **622** had seven heteroatoms, in hindsight it would have been advisable to use an excess of 7+ equivalents of boron tribromide.[126] This is because stable chelates can form between boron tribromide and other heteroatoms present in the molecule.

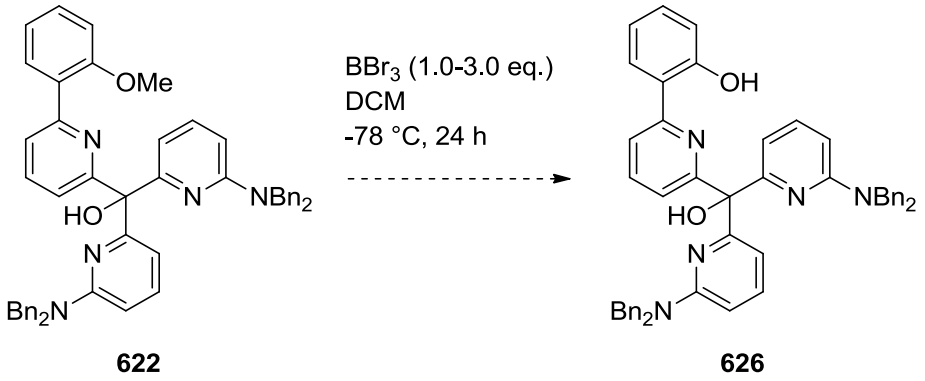

622 **626**

Scheme 6.26 Attempted methyl deprotection of **622**.

An analogous reaction was attempted as above, this time with a benzyl group protecting the phenol (Scheme 6.27). Here THF dried over sodium-benzophenone ketyl was employed, in order to try and repeat the success of the reaction depicted in Scheme 3.18. This reaction worked better (32% yield) than Scheme 6.25 (23% yield). Analysis of the ^{1}H NMR spectrum after silica gel column chromatography identified **625**, and its proton and carbon chemical shifts were assigned (Figure A-12). Due to the presence of **322** in the reaction mixture, it was thought that it was not fully reacting with the *n*-BuLi. Therefore *n*-BuLi was substituted with *t*-BuLi, in an attempt to increase the yield or reaction product purity. However, this only resulted in a busier ^{1}H NMR spectrum and lower yield.

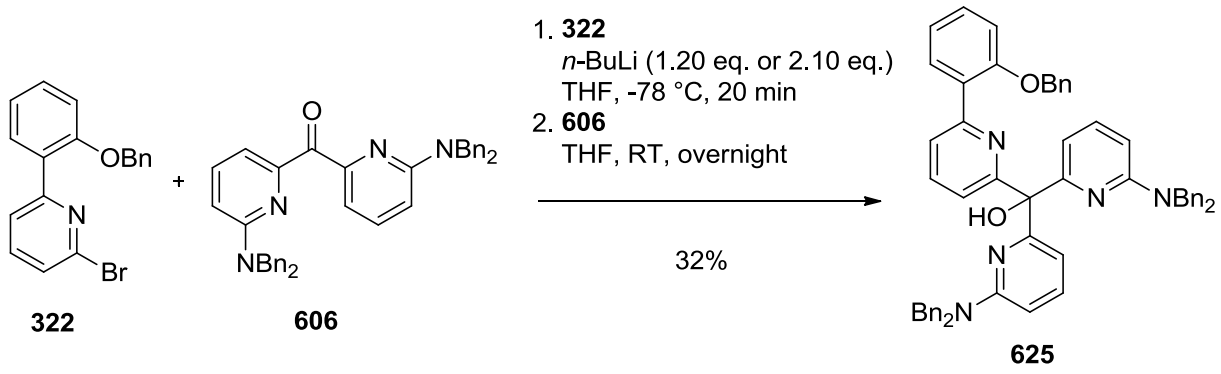

Scheme 6.27 Synthesis of **625**.

Again, deprotection proved troublesome (Schemes 6.28-6.29). It was clear from the ^{1}H NMR spectrum that some of the benzyl groups were being removed, but the extent was obscured by the many peaks in the crude mixture. Silica gel chromatography was used to try and purify each compound into unique fractions. Unfortunately, similarities between the compounds meant that separation was impossible regardless of the solvent system employed. Altering the solvent to pure acetic acid or leaving the reaction mixture to stir for 3 days didn't result in any change in their crude ^{1}H NMR in comparison to the starting materials.

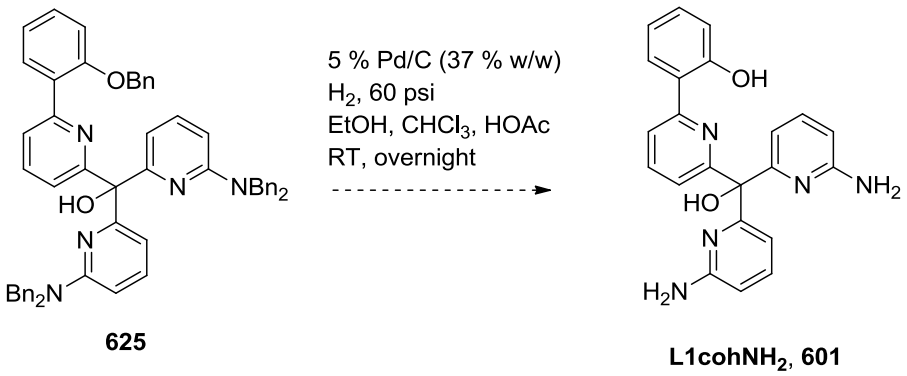

Scheme 6.28 Attempted synthesis of **601**.

Boron tribromide was then tried, but the resulting crude gave very unclear ^{1}H NMR results. Its spectrum contained multiple unidentifiable and overlapping peaks. Either product degradation was occurring, or multiple compounds with varying degrees of

deprotection were being synthesised. Column chromatography was used in an attempt to purify the material but was not successful.

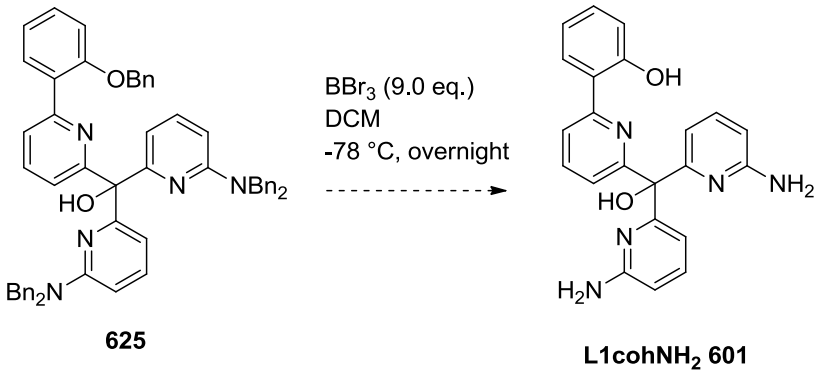

625 **L1cohNH$_2$ 601**

Scheme 6.29 Attempted synthesis of **601**.

6.3 L1nNH$_2$

A second target ligand that includes amino groups capable of buttressing, **L1nNH$_2$**, is shown in Figure 6.8. Using a nitrogen apex will alter the N···Be···N bond angles, which may influence the binding strength.

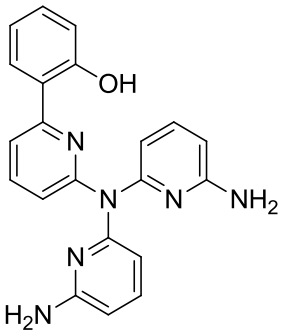

Figure 6.8 Target ligand **L1nNH$_2$ 627**.

Retrosynthetic disconnection of the amino-pyridyl groups results in target compounds **604** and **628**. Such chemistry is well precedent (Scheme 6.30).[52]

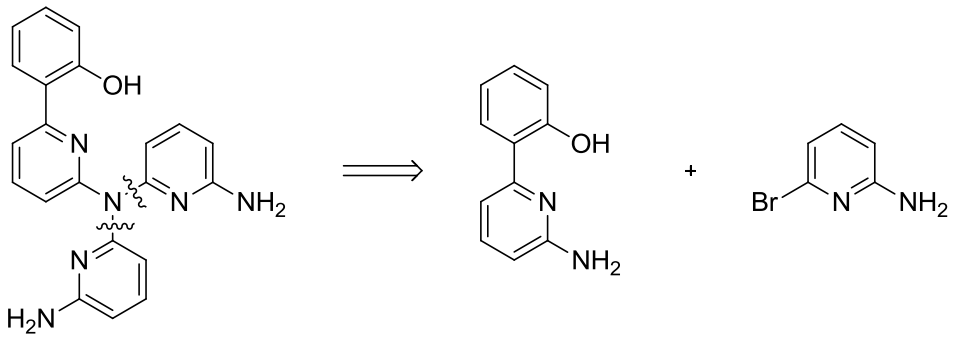

627 **629** **604**

Scheme 6.30 Disconnection of **251**.

Further retrosynthetic analysis of **628** gives a likely disconnection of the phenol ring from the pyridyl unit (Scheme 6.31). The reverse is achieved through a Suzuki reaction. This gives two simple molecules – a boronic acid **302**, and another unit of **604**.

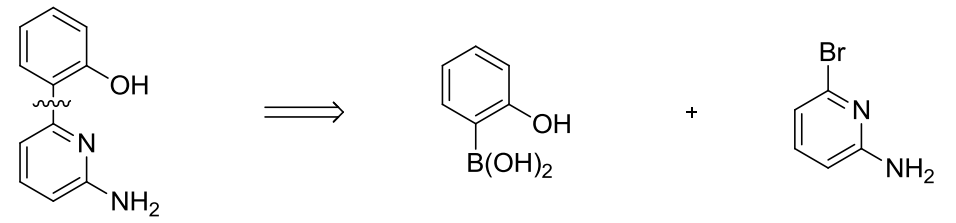

628 **302** **604**

Scheme 6.31 Disconnection of **628**.

As discussed earlier, protecting groups are necessary for each of these reactions to proceed. For the phenol, the free phenol could be protected with a methyl group. And the previously synthesised *N*,*N*-dibenzyl-6-bromopyridin-2-amine **605**, can be used in the second step of this scheme in place of **604**.

The first reaction in this procedure was to perform a Suzuki coupling reaction to form one half of the molecule (Scheme 6.32). This reaction was successful in a high yield (87%). The product **629** contains the first two heteroatoms that will eventually be involved in coordination, and a primary amine available to react with the further arms. This new

compound was characterised by ^{1}H NMR, ^{13}C NMR, COSY, HMBC, HMQC, and ESI-MS (Figure A-13).

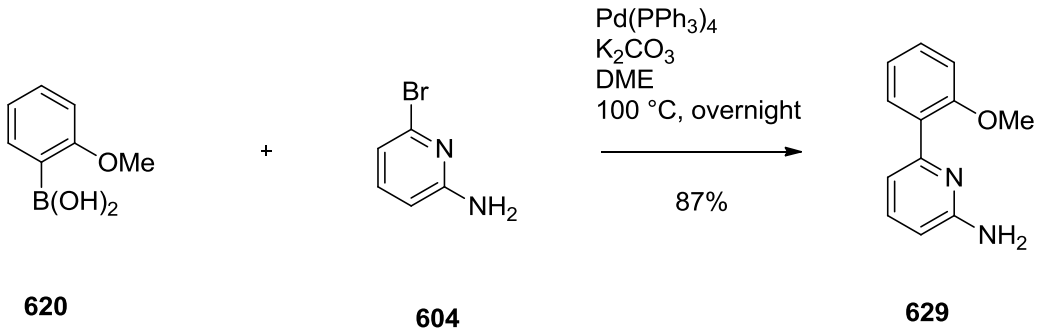

620 **604** **629**

Scheme 6.32 Synthesis of **629**.

This next reaction was attempted under many conditions, as it was not clear for some time if the product was made successfully (Scheme 6.33, Table 6.2). This included three reaction types with the catalyst being copper sulfate, palladium acetate, or bronze powder. Various other conditions were also altered including reagent and solvent concentration, temperature, and microwave use.

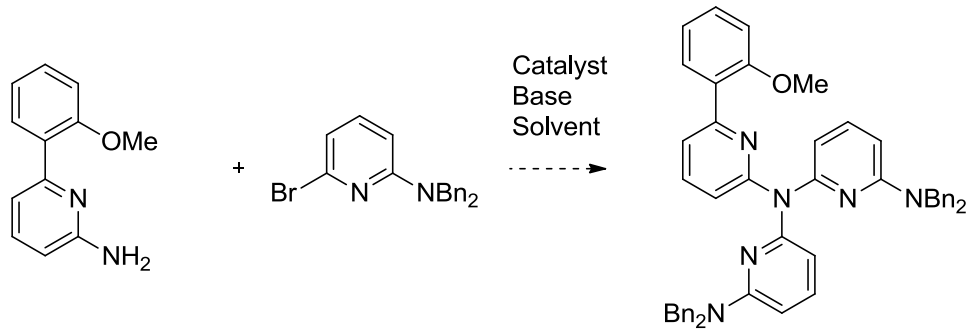

629 **605** **630**

Scheme 6.33 General reaction synthesis of **630**.

Entries 2 and 4 were the most successful, as analysis of their ^{1}H NMR spectra indicated the presence of **630** due to the singlet peak that integrated to 8 protons, corresponding to the methylenes of the benzyl protecting groups. ESI-MS also confirmed the limited success of these reactions. The other entries had varying degrees of success. $Pd(OAc)_2$ was

found to be the best catalyst, but reactions which used it were inconsistent (Entries 4, 6-9). Purifications by silica gel column chromatography were attempted in the more promising cases (2, 4, 5, 6-9), but these failed to obtain **630** in good purity. It was however possible to separate the impurity **633** (Scheme 6.36) from the reaction material, which was the intermediate product wherein only the first pyridyl group had reacted to the apex nitrogen.

Table 6.2 Conditions for the synthesis of **630**.

Entry	Reagents	Base	Solvent	Temperature	Time	Microwave	Product
1	$CuSO_4{\cdot}(H_2O)_6$	6 M KOH	–	160 °C	15 min	✓	x
2	$CuSO_4{\cdot}(H_2O)_6$	6 M KOH	–	160 °C	15 min	✓	✓
3	$CuSO_4{\cdot}(H_2O)_6$	6 M KOH	Diphenyl Ether	160 °C	15 min	–	x
4	$Pd(OAc)_2$, XPhos	K_2CO_3	Dioxane	90 °C	24 h	✓	✓
5	Bronze powder (9:1 Cu:Sn), trace KI, trace KBr	K_2CO_3	*p*-cymene	180 °C	66 h	–	?
6	$Pd(OAc)_2$, XPhos	K_2CO_3	Dioxane	90 °C	24 h	✓	x
7	$Pd(OAc)_2$, XPhos	K_2CO_3	Dioxane	100 °C	24 h	✓	x
8	$Pd(OAc)_2$, XPhos	K_2CO_3	Dioxane	110 °C	24 h	–	?
9	$Pd(OAc)_2$, XPhos	K_2CO_3	Dioxane	110 °C	21 h	–	x

Deprotection of **601** made was attempted with boron tribromide (Scheme 6.34). Due to the number of nucleophilic sites present in the molecule, a large excess of BBr_3 was used.[126] Analysis of the reaction mix was inconclusive.

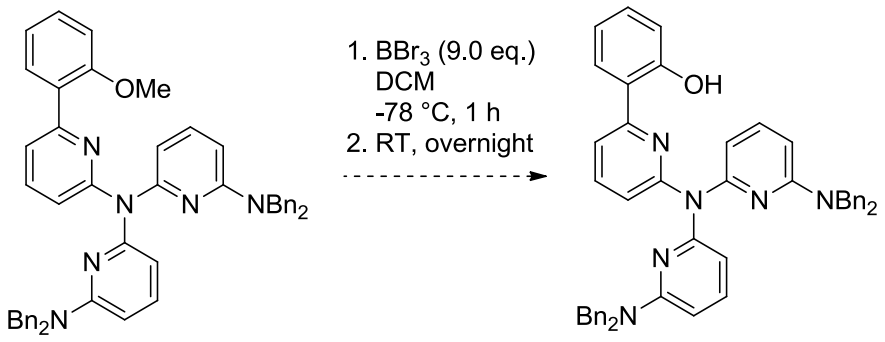

630 **631**

Scheme 6.34 Synthesis of **631**.

Unfortunately, only small quantities (10-20 mg) of unpurified crude **630** or **631** were obtained at any one time. Given the very low yields, only one or two further reactions with the material was realistically possible. Further deprotection of **631**, this time with palladium on carbon as a catalyst, was trialled (Scheme 6.35). It was unclear to what extent this reaction succeeded. Nonetheless, the crude material **631**, without purification, was subjected to reaction conditions for the conversion of its amine buttress into an amide functionality. ESI-MS data suggests that **632** is present in the solution, but its parent ion was of low intensity. Purification was tried by silica gel column chromatography, but separation was not possible. This was due to the mixture of compounds travelling together in every solvent system used, and an insufficient quantity was available for even a small amount to be separated.

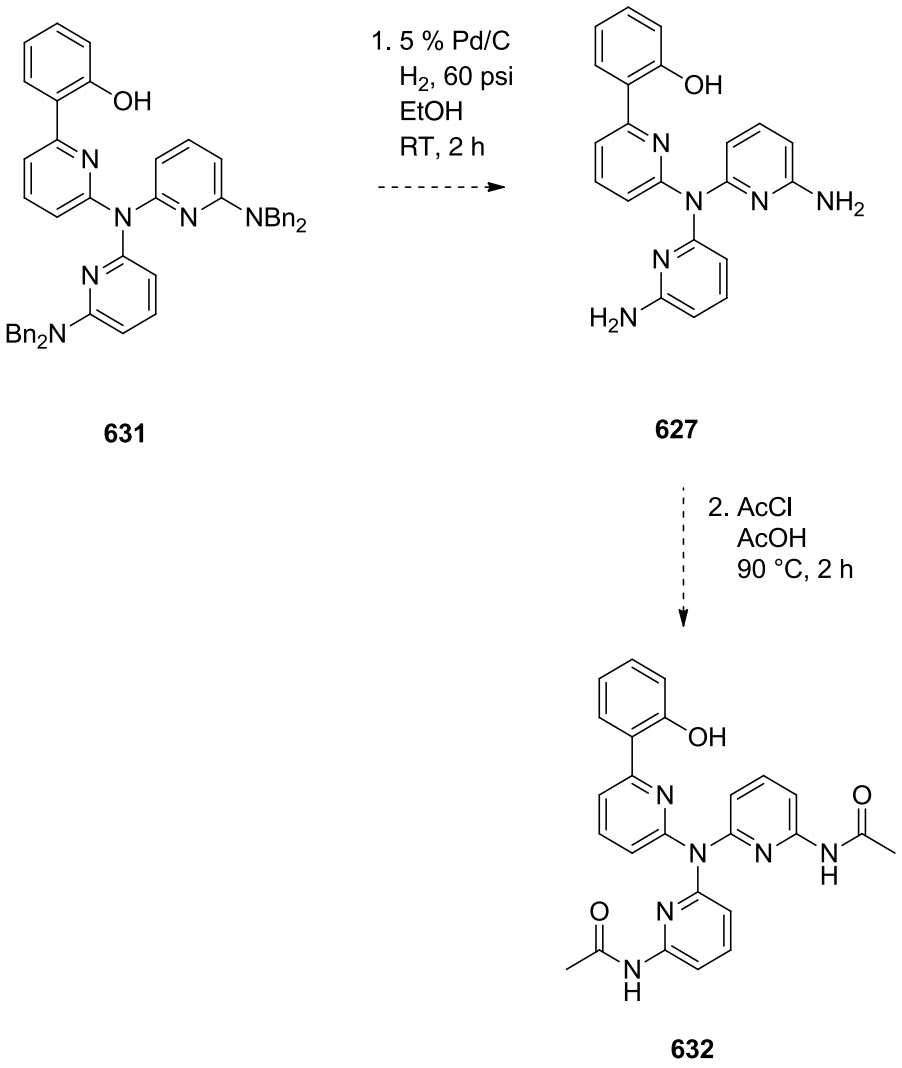

Scheme 6.35 Attempted synthesis of **627** and **632**.

Due to the inconclusive results of all stages of this synthesis, it was decided that we should add the pyridyl arms one at a time (Scheme 6.36). The first pyridyl unit was added successfully to **629** (54% yield). Purification of the product by silica gel column chromatography gave **633**, as determined by a combination of ^{1}H NMR, ^{13}C NMR, and ESI-MS (Figure A-14).

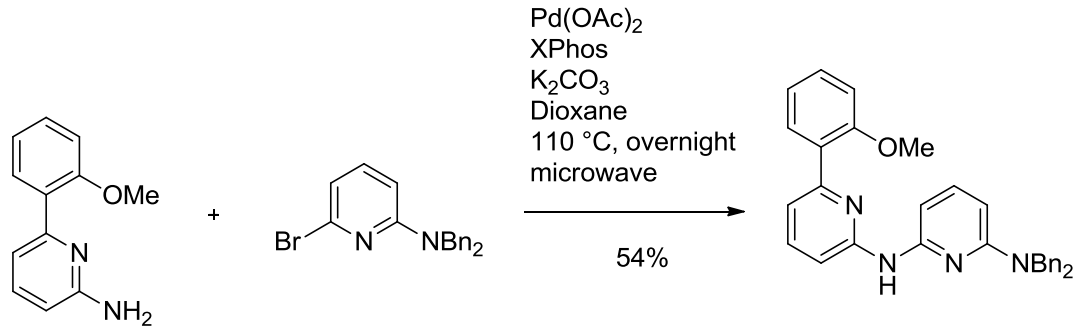

629 **605** **633**

Scheme 6.36 Synthesis of **633**.

The addition of second unit proved problematic (Scheme 6.37). Nine attempts were made using different catalysts, bases, solvents, temperatures, and reaction times, as seen in the table below (Table 6.3).

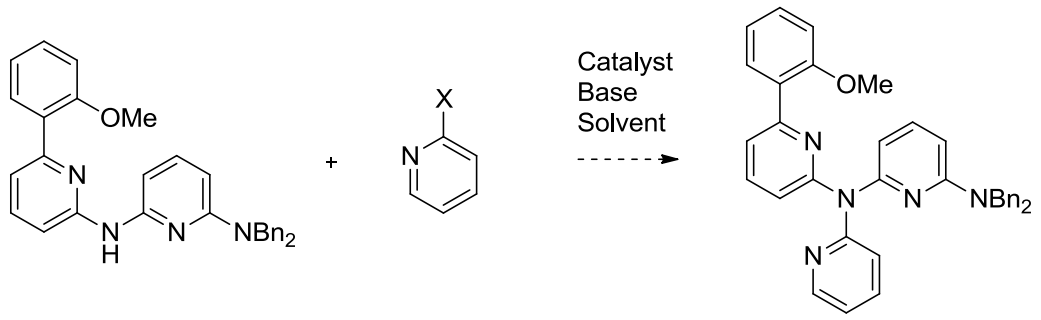

633 **306 / 634** **635**

Scheme 6.37 General reaction synthesis of **635**, where X = Br (**306**), or I (**634**).

Reaction conditions 1-8 were unsuccessful according to their ^{1}H NMR spectra. In the cases of 3 and 5, in which 6 M KOH was used as both the base and solvent, no organic components could be identified by NMR protocols. The most promising condition was 9, in which an iodopyridine **634** replaced the bromopyridine **306**. The latter incorporates a more reactive halide that could increase the chance of product being synthesised. Analysis of the ^{1}H NMR spectrum indicated that a trace of a new, unidentified compound had

been formed. Separation of compounds was attempted via multiple silica gel columns, but all crude material ran together.

Table 6.3 Conditions for the synthesis of **635**.

Entry	X	Reagents	Base	Solvent	Temp.	Time	Microwave	Result
1	Br	$Pd(OAc)_2$, XPhos	K_2CO_3	Dioxane	110 °C	24 h	✓	X
2	Br	$Pd(OAc)_2$, XPhos	*t*-BuOK	Dioxane	90 °C	11 h	✓	X
3	Br	$CuSO_4.(H_2O)_6$	6 M KOH	-	160 °C	15 min	✓	X
4	Br	CuI	$K_3PO_4{\cdot}H_2O$	DMF	130 °C	24 h	–	X
5	Br	$CuSO_4.(H_2O)_6$	6 M KOH	-	160 °C	6.5 h	–	X
6	Br	$Pd(OAc)_2$, dppf	Cs_2CO_3	DMF	100 °C	2 h	✓	X
7	Br	$Pd(dba)_2$, SPhos	NaO*t*Bu	Toluene	110 °C	20 h	–	X
8	Br	Copper powder, trace KBr	Na_2CO_3	Mesitylene	160 °C	19 h	–	X
9	I	$Pd(OAc)_2$, XPhos	K_2CO_3	Dioxane, H_2O	110 °C	15 h	✓	?

6.4 L1nNH_2PhNCO

Due to the problems with the synthesis of buttressed ligands, a new ligand was identified, and its synthesis attempted (Figure 6.9). Taking **633** as a starting material, functionalisation of the central amine with an appropriate donor group was investigated. A compound that would easily react with the secondary amine was desired, that would provide a donor atom in the same position as the previous pyridine moiety. Phenyl isocyanate would work in this case, giving a second oxygen atom that is available in an amide form. The adjacent secondary amine is unlikely to take part in any secondary sphere of coordination as its orientation towards either oxygen atom is unfavourable but could coordinate to a metal if deprotonated.

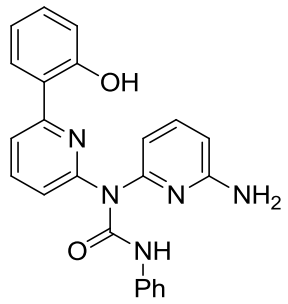

636

Figure 6.9 L1nNH$_2$PhNCO 636.

The retrosynthetic step necessary to procure **636**, would be a disconnection of the phenyl isocyanate from tertiary amine apex group of the main molecule (Scheme 6.38). Addition of the amide can be achieved easily by the introduction of an isocyanate compound.

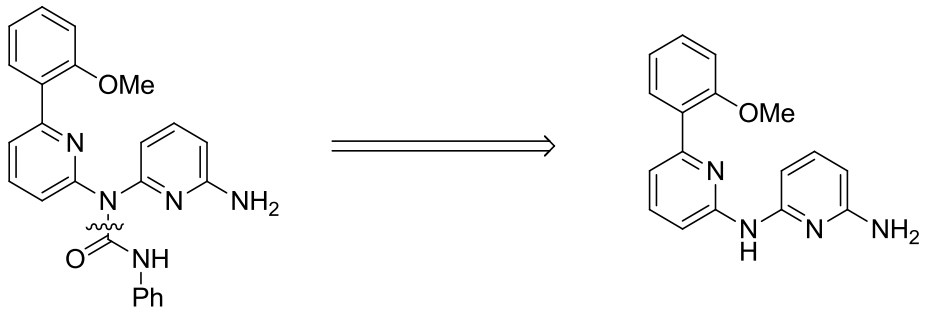

637 **638**

Scheme 6.38 Disconnection of **637**.

A protecting group will be necessary to protect the primary amine. A benzyl protecting group is suitable here, as we already have a supply of **633**. This group can be removed later through one of the previously used methods in this thesis being either palladium on charcoal, or boron tribromide.

The first reaction step was the addition of phenyl isocyanate to the secondary amine of **633** (Scheme 6.39). Stirring these two compounds at room temperature overnight in DCM gave the product **639** in a 79% yield, as identified by its ^{1}H and ^{13}C NMR (Figure A-15). The aromatic protons of the benzyl groups significantly overlapped, so these were

unable to be assigned. Optimisation of the reaction conditions revealed that increasing the excess of phenyl isocyanate was beneficial but that increasing the temperature to reflux had no effect. Silica gel column chromatography was used to separate the product from the excess starting material.

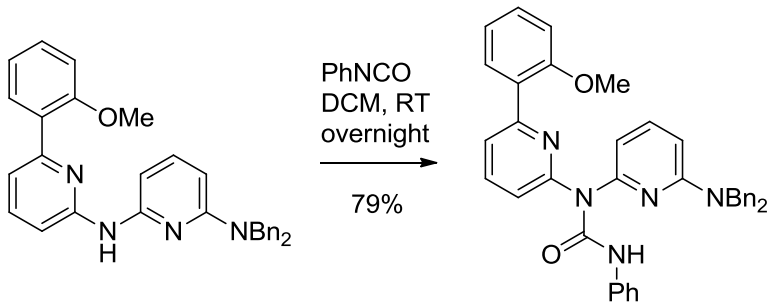

633 **639**

Scheme 6.39 Synthesis of **639**.

Deprotection of **639** was first attempted by hydrogenation (Scheme 6.40). This was unsuccessful. This was repeated but in THF with acetic acid. Inconclusive spectra and yields were initially obtained. The reaction was tried again, this time with acetic acid as the sole solvent, and upon purification some fractions gave noisy NMRs containing new material. Unfortunately, the products could not be identified. ESI-MS was used to clarify the results, but again noise interfered with identification. It is the case then that most starting material remains unreacted.

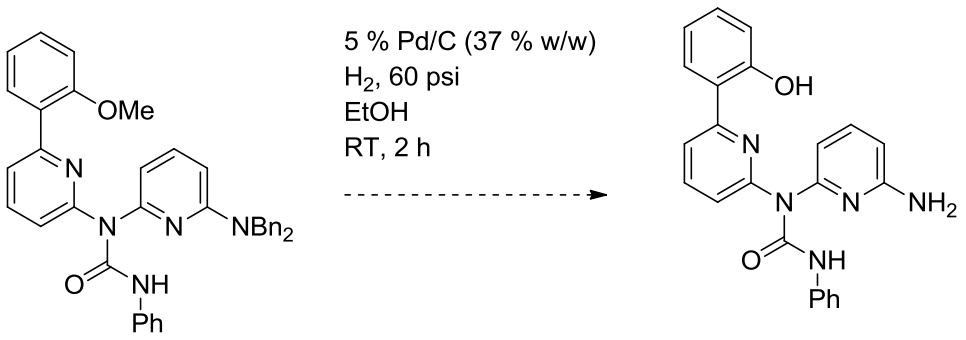

639 **636**

Scheme 6.40 Attempted synthesis of **636**.

Having had previous success with boron tribromide, this was tried next (Scheme 6.41).

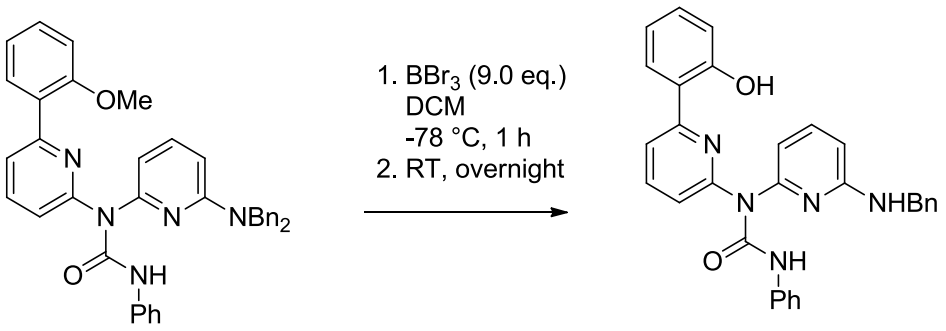

639 **640**

Scheme 6.41 Attempted synthesis towards **640**.

Using BBr_3, cleavage of both the methyl group and one benzyl group was observed, yielding **640**. By ^1H NMR, the *CH*$_3$ peak at 3.86 ppm disappeared (Figure 6.10, Figure A-16). Also, the *CH*$_2$ peak at 4.79 ppm shifted upfield to 4.64 ppm, reduced from an integration of 4H to 2H, and became a doublet. This change in signal is due to each proton of the methylene group being in a different magnetic environment. These factors signified that the new material contained only a single methylene group.

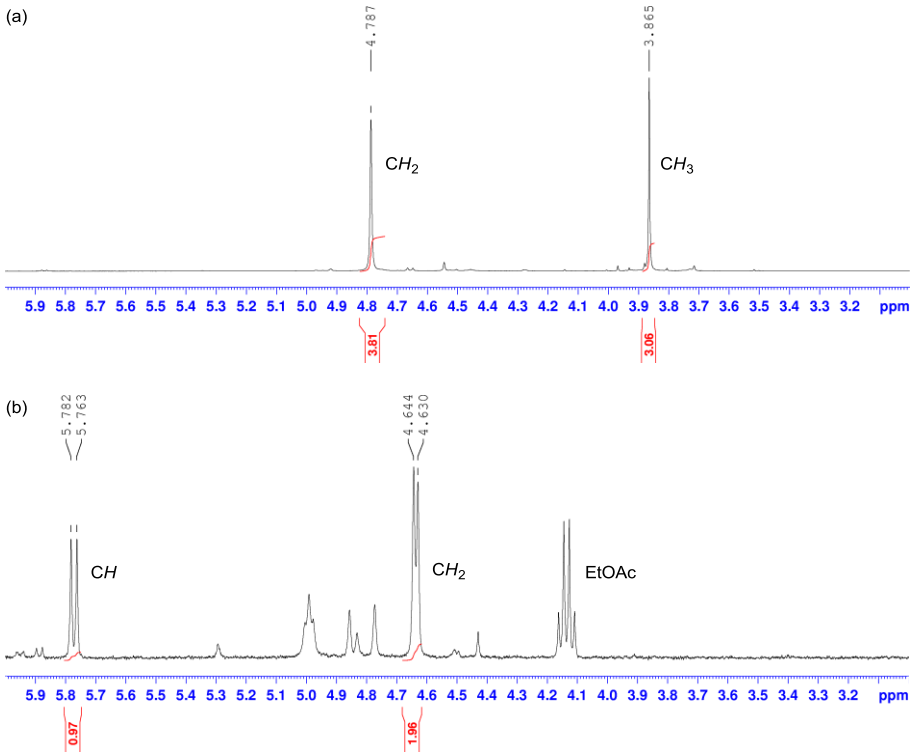

Figure 6.10 ^{1}H NMR spectrum of **639** (a) and **640** (b) from 3-6 ppm.

This deprotection step was attempted several times, increasing the concentration of the BBr_3 each time (up to 12 equivalents), to try to achieve full deprotection. The ^{1}H NMR spectrum of the crude mixture showed potential. New material was synthesised, but purification was not possible. Therefore, the degree of deprotection that had occurred was difficult to determine.

Further hydrogenation was attempted on the partially deprotected ligand **640**, (Scheme 6.42). This was unsuccessful. The same material was resubjected several times in a row with varying solvent mixtures (DCM, MeOH, AcOH), and changes in the ^{1}H NMR spectrum was observed. Column chromatography and recrystallizations were used to try to clean or purify the crude material, but each time was ineffective.

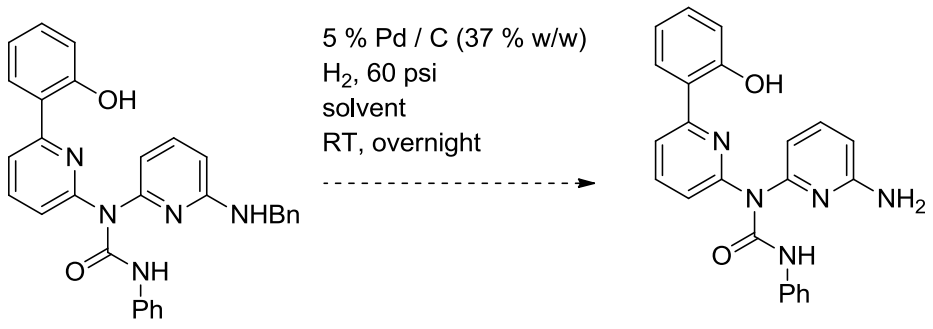

640 **636**

Scheme 6.42 Attempted further deprotection of **640**.

6.5 Summary

This chapter made attempts towards buttressed ligands. These would in theory bind to beryllium in the same manner as **L1cohH**, but with the added benefit of a second sphere of interactions to help stabilise the complex. The second series of procedures came close to procuring **L1cohNH$_2$**. ^{1}H NMR shows that deprotection occurred, but the extent was indeterminable. The chemistry of these compounds resulted in all attempts to purify them with silica gel chromatography in them moving together and streaking. Either a lengthy and systematic approach to the purification of **625** and **L1cohNH$_2$**, or an alternative synthetic route, is required (Scheme 6.44). The ligand **L1nNH$_2$** was further from being made, as the synthetic route produced unclear results when attempting to add the last pyridyl group (Schemes 6.33-6.37). Last, an alternative buttressed ligand design **640** was successfully synthesised. This ligand retains the ability to coordinate to a cation in a tetradentate fashion whilst still having hydrogen bond donors available to form a secondary sphere of coordination.

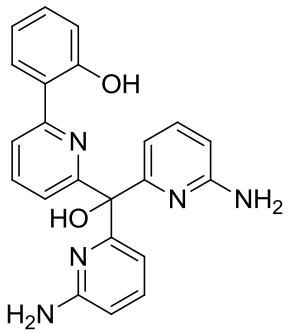

L1cohNH$_2$

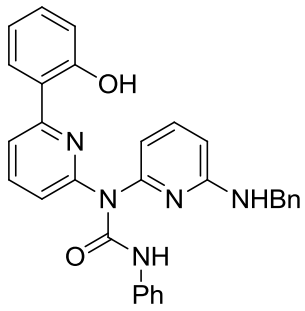

640

Figure 6.11 Potentially synthesised ligand **L1cohNH$_2$** and successfully synthesised ligand **640**.

6.6 Future Work

Alternative routes to buttressed ligands were noted throughout these syntheses, but although interesting, were not attempted. One possible route to another buttressed ligand could expand on the attempted route using MOMCl (Scheme 6.43). After the single addition of MOMCl, the amine could be methylated to give a small, non-sterically demanding, fully protected amine. Later, the methoxymethyl group could be removed by strongly acidic deprotection, leaving -NHMe, which has the potential to support buttressing. Although protecting a 2° methoxymethyl amine with a methyl group is not a type of synthesis that has been reported in the literature, the chemistry appears to be reasonable for an attempt to be made.

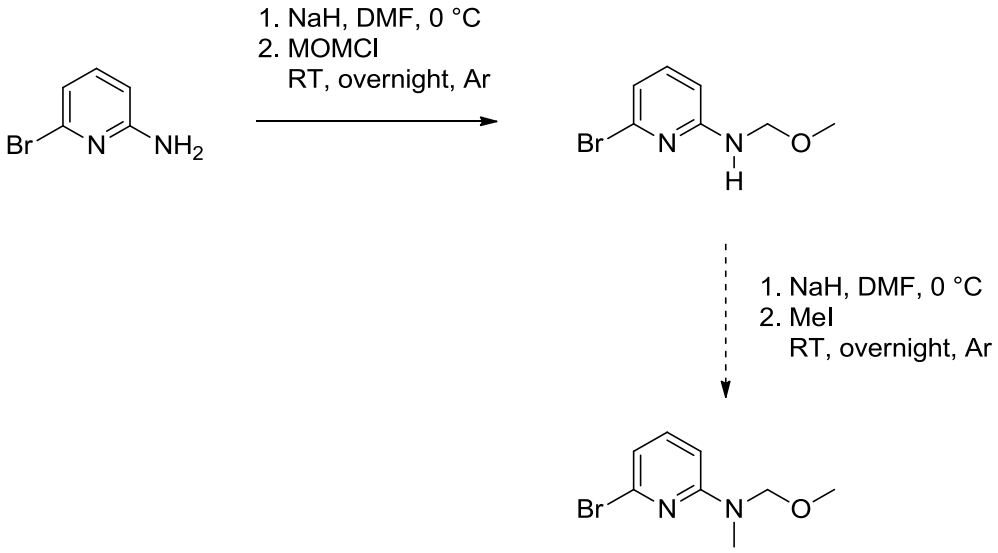

Scheme 6.43 Alternative protecting group methodology.

A modification of Scheme 6.17 could give another potential route (Scheme 6.44). This would give an asymmetric ketone. Followed by coupling with the backbone compound **322**, a new protected ligand is formed. Deprotection of this should result in a spectroscopically clearer reaction mixture than Scheme 6.34, because there are only 3 protecting groups.

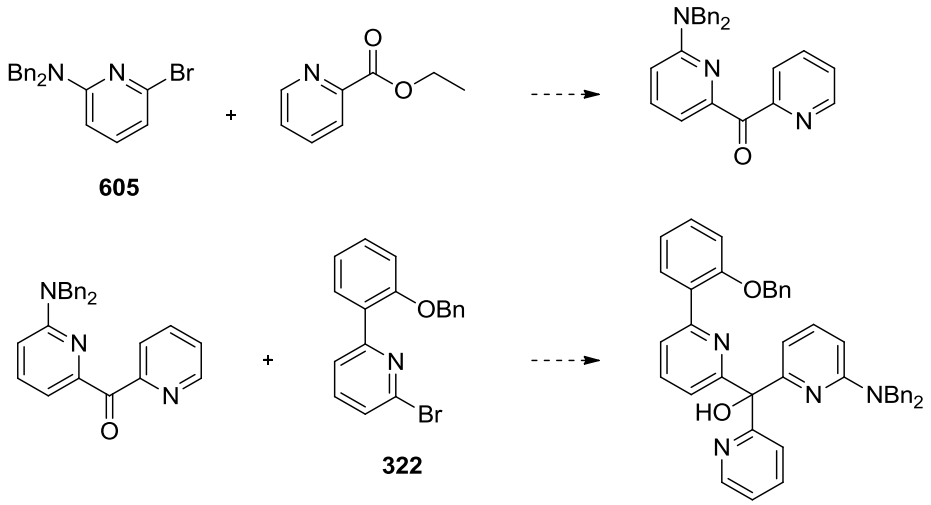

Scheme 6.44 Route to alternative buttressed ligand.

Further experimental plans should be thought out to plan for other buttress components to be added either pre- or post- synthesis.[127] The buttressing could be possibly added by

functionalising dipyridyl ketone in another way (Scheme 6.45). It can have bromine placed in the 6-positions, which will allow a wide range of chemistry to take place.

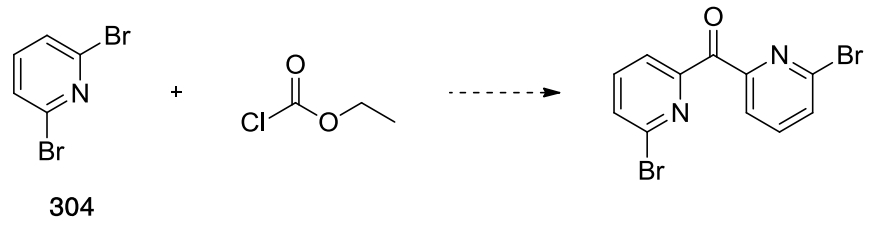

Scheme 6.45 Synthesis of brominated dipyridyl ketone.

This would allow modification of these into many groups, for use in buttressing (Scheme 6.46). There is precedence in the literature for many functional groups to be substituted in the R-position, including the following: CH_3, NH_2 $NHCH_3$, NHCOH, $NHCOCH_3$. Buttresses of interest would include hydrogen bond donors of varying functional groups and sizes, in which the labile proton is positioned to form 6-membered rings with the coordination centre. Also, substituents without this type of functionality, such as bulky alkyl chains or nitro groups, may be investigated. These would provide data on steric and stereoelectronic effects on metal binding abilities.

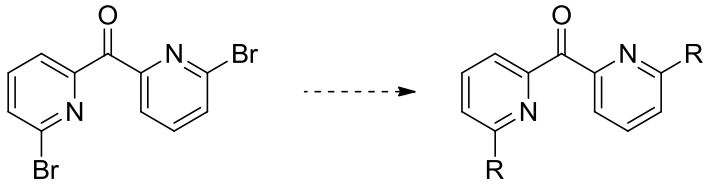

Scheme 6.46 Synthesis of buttress-containing dipyridyl ketone.

Chapter 7: Synthetic Experimental

"Evans boldly put 50 atm. of ethylene in a cell with 25 atm. of oxygen. The apparatus subsequently blew up, but luckily not before he obtained the spectra shown in figure 8."

– A. J. Merer and R. S. Mulliken[128]

7.1 General Experimental

7.1.1 Reagents and Solvents

All starting materials were obtained from commercial sources and used without purification unless otherwise noted. All other reagents and solvents were obtained from commercial sources and used as supplied.

Solvents used in reactions were analytical grade and used directly. If stated as dry, they were subject to further purification as follows: Tetrahydrofuran, dichloromethane, diethyl ether, and toluene were passed through alumina columns on an in-house solvent purification system. In special circumstances, THF was dried via distillation over sodium-benzophenone ketyl.

7.1.2 Synthetic Methods

All reactions were carried out in oven-dried glassware, under an atmosphere of nitrogen or argon, with magnetic stirring. The reaction temperature refers to external oil bath temperature. When a temperature of −78 °C was required, a mixture of isopropyl alcohol and either dry ice or liquid nitrogen was used in a cooling bath. Microwave synthesis was performed using a CEM Discovery Monomode Explorer. All organic extracts were dried over magnesium sulfate and filtered through cotton. The solvents were removed under reduced pressure on a BUCHI or Heidolph rotary evaporator. These were run in tandem

with a Frigomix® 1000 refrigeration unit that cooled the collecting condensers with an ethylene glycol and water mixture at -5 °C. For characterisation purposes, or when strict drying of the compound was required for the next step, the last traces of solvent were removed using a high vacuum oil pump attached to a Schlenk line.

7.1.3 Chromatography

Reactions were followed by TLC on aluminium-backed silica gel 60 F_{254} sheets from E-Merck, visualised by UV light.

Flash column chromatography was performed using Scharlau silica gel 60, 0.04 – 0.06 mm, 230 – 400 mesh. The length of the silica gel column was typically 15 cm and the diameter was varied according to the purification scale. The silica gel slurry was compacted with the specified solvent system of a combination of hexanes, diethyl ether, EtOAc, DCM, or MeOH. The compound was then either wet or dry loaded onto the column and eluted with the specified solvent under positive pressure.

7.1.4 Characterisation

All compounds were characterised by ^{1}H and ^{13}C nuclear magnetic resonance, and electrospray ionisation mass spectrometry. ^{1}H NMR and ^{13}C NMR spectra were recorded on a Bruker Avance 400, 500, or 700 Mhz spectrometer. All chemical shifts are reported relative to residual solvent (^{1}H, ^{13}C). Full NMR assignments were made using their ^{1}H and ^{13}C spectra, including DEPT-90, DEPT-135, HMBC, and HMQC where necessary.

Mass spectra were obtained using a Micromass ZMD 400 electrospray spectrometer run in positive ion mode. High resolution mass spectra (HRMS) were recorded on a ThermoScientific Q Exactive Focus Hybrid Quadrupole-Orbitrap Mass Spectrometer.

New compounds were sent for further characterisation by elemental analysis. Elemental analyses were provided by the Campbell Microanalytical Laboratory, University of Otago. Unfortunately, it was the case that many of the synthesised compounds could not be easily purified by silica gel column chromatography and did not often recrystallize. Therefore, elemental analysis was not able to be carried out on several new compounds and ligands.

X-ray crystal structures were recorded when suitable single crystals were available. This data was collected on several X-ray diffractometers. The majority of structures were obtained using a Rigaku Spider diffractometer equipped with a copper rotating X-ray source and a curved image plate detector, at reduced temperature (other equipment mentioned where necessary). The crystals were mounted in an inert oil, transferred into the cold gas stream of the detector and irradiated with graphite monochromated Cu Kα (k = 1.54178 Å) X-rays. The data was collected by the Crystal Clear program (v.1.4.0) and processed with FS-PROCESS to apply the Lorentz and polarisation corrections to the diffraction spots (integrated 3 dimensionally). The structures were solved by direct methods SHELXS-97 and refined using the SHELXL-97 program. Absorption correction was carried out empirically. Hydrogens were calculated at their ideal positions unless otherwise stated.

7.2 Procedures

301

323 **301**

The benzyl-protected precursor **323** (0.0555 g, 0.125 mmol) in dry DCM (5 mL) was cooled to -78 °C under Ar. Boron tribromide (0.623 mL, 0.623 mmol) was added dropwise to produce a cloudy white solution. The reaction was allowed to warm to RT and stirred overnight, affording a yellow precipitate. The reaction was quenched with H_2O (10 mL) and extracted with DCM (50 mL). The organic layer was washed with brine (50 mL) and water (50 mL), dried over $MgSO_4$, filtered, and evaporated *in vacuo* to afford a yellow oil. The ligand **301** was purified by silica gel column chromatography using 98:2 DCM / MeOH to afford an off-white solid (0.0257 g, 46%). R_f = 0.24 (98:2 DCM / MeOH). ^{1}H NMR (500 MHz, $CDCl_3$) δ 6.89 (t, *J* = 7.48, 1H; c), 6.96 (d, *J* = 8.20, 1H, a), 7.27 (d, *J* = 6.20, 1H; b), 7.28 (d, *J* = 6.20, 2H; j), 7.40 (s, 1H; m), 7.63 (d, *J* = 7.65, 1H; g), 7.74 (d, *J* = 7.44, 1H; d), 7.76 (d, *J* = 8.55, 2H; i), 7.78 (d, *J* = 8.61, 1H; e), 7.83 (t, *J* = 7.85, 1H; f), 7.98 (d, *J* = 8.10, 2H; h), 8.62 (d, *J* = 4.4, 2H; k), 13.11 (br s, 1H, l); ^{13}C NMR (125 MHz, $CDCl_3$) δ 80.3 (12), 117.9 (8), 118.5 (2), 118.8 (4), 119.5 (6), 119.9 (10), 122.8 (16), 122.9 (14), 126.5 (5), 131.2 (3), 137.0 (15), 138.3 (9), 147.6 (17), 156.5 (7), 159.3 (1), 161.0 (13), 161.9 (11). HRMS for $C_{22}H_{18}N_3O_2$ (M^+) 356.1309, expected 356.1305. $C_{22}H_{17}N_3O_2$. ½H_2O (364.40): calc. C, 72.48; H, 4.97; N, 11.57; found C, 72.90; H, 4.94; N, 11.55. Figure A-1.

303

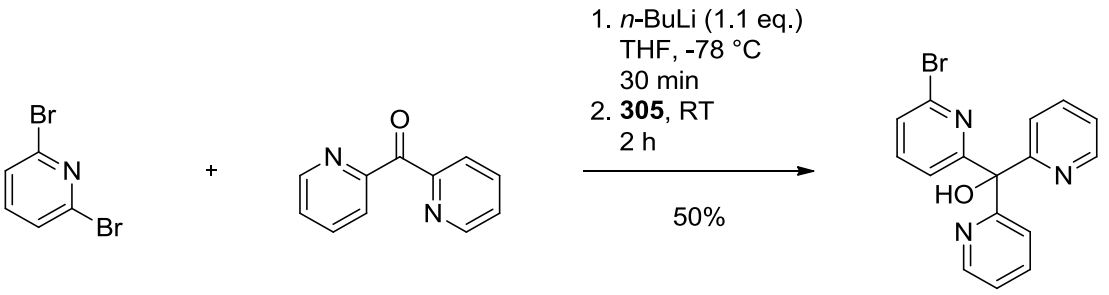

304 **305** **303**

The compound **303** was synthesised by modification of a known literature procedure for a related compound.[129] The dibromopyridine **304** (7.25 g, 30.7 mmol) in diethyl ether (250 mL) was cooled to -78 °C under Ar. *n*-Butyllithium (21.1 mL, 33.8 mmol, as a 1.6 M solution in hexane) was added slowly over 25 minutes to produce a dark orange solution, which was stirred an additional 20 minutes. The dipyridyl ketone **305** (5.21 g, 28.3 mmol) in dry THF (100 mL) was added over the course of 20 minutes to produce a dark brown mixture. After two hours of stirring at -78 °C, the mixture was warmed to 0 °C, acidified to pH 3.5 with 5% HCl (150 mL), basified with saturated aqueous Na_2CO_3 (20 mL), and extracted into $CHCl_3$ (3 × 50 mL). The combined organic layers were dried over $MgSO_4$, filtered, and evaporated *in vacuo* to afford a red oil. The impure product **303** was purified by passage through a plug of silica gel followed by hexanes and diethyl ether washes to provide an orange solid (4.84 g, 14.2 mmol, 50%). The characterisation data agreed with the reported literature.[129] ^{1}H NMR (500 MHz, $CDCl_3$) δ 7.01 (br s, 1H), 7.20 (ddd, J = 6.0, 4.8, 2.4, 2H), 7.36 (dd, J = 8.0, 0.8, 1H), 7.53 (t, J = 7.6, 1H), 7.69 (m, 4H), 7.73 (dd, J = 7.6, 0.8, 1H), 8.53 (dt, J = 4.8, 1.2, 2H); ^{13}C NMR (125 MHz, $CDCl_3$) δ 81.1, 121.9, 122.7, 123.3, 126.9, 136.7, 138.9, 140.4, 148.0, 162.3, 164.7. MS for $C_{16}H_{12}BrN_3O$ (M^+) 343.56.

305

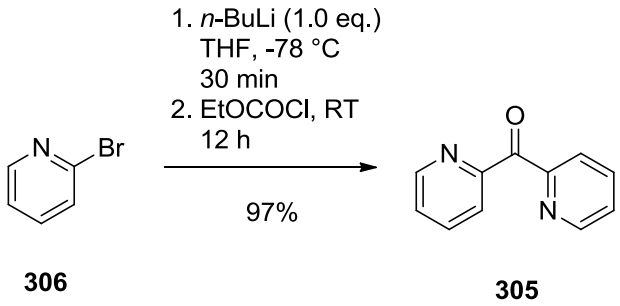

306 **305**

The pyridyl ketone **305** was a known compound, and synthesised by modification of the literature procedure.[106] *n*-Butyllithium (4.0 mL, 6.4 mmol, as a 1.6 M solution in hexane) was added dropwise to a solution of 2-bromopyridine (0.6 mL, 6.33 mmol) in dry THF (10 mL) at −78 °C under an atmosphere of Ar, and stirred for 30 mins. Ethyl chloroformate (0.3 mL, 2.85 mmol) was then added, and the reaction was allowed to warm to room temperature and stirred for an additional 12 h. After this time the reaction was quenched with water (5 mL), and the aqueous layer was extracted with dichloromethane (3 × 10 mL). The combined organic layers were washed with $NaHCO_3$ (15 mL of a sat. aq. solution) and brine (10 mL), dried over $MgSO_4$, filtered, and evaporated *in vacuo* to afford a brown oil. The compound **305** was purified by silica gel column chromatography using EtOAc, providing an orange solid (0.51 g, 97%). R_f = 0.35 (EtOAc). The characterisation data agreed with the reported literature. ^{1}H NMR (500 MHz, $CDCL_3$) δ 7.48 (ddd, *J* = 7.6, 4.8, 1.2, 2H), 7.89 (td, *J* = 7.6, 1.2, 2H), 8.09 (dt, *J* = 7.6, 1.2, 2H), 8.75 (dt, *J* = 4.8, 1.2, 2H); ^{13}C NMR (125 MHz) δ 124.8, 126.0, 136.3, 148.7, 153.8, 192.5. MS for $C_{11}H_8N_2O$ (M^+) 185.10.

307

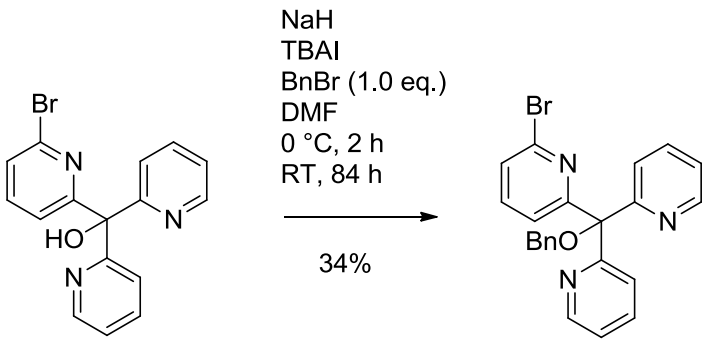

303 **307**

The compound **303** (1.00 g, 2.92 mmol) in dry DMF (20 mL) was cooled to 0 °C under Ar. NaH (0.587 g, 14.6 mmol) was added in portions over 10 minutes. After cessation of H_2 generation, a small crystal of tetrabutylammonium iodide was added. Benzyl bromide (0.348 mL, 2.92 mmol) was added dropwise forming a cloudy solution and stirred for a further 2 hours at 0 °C. The reaction was allowed to warm to RT and stirred for a further 84 hours. The resulting orange solution was quenched with MeOH (10 mL) and concentrated *in vacuo* to remove the DMF. The resulting oil was extracted with DCM (30 mL) and the organic layer was washed with brine (30 mL) and water (30 mL). The aqueous layer was washed further with DCM (30 mL). The combined organic layers were dried over $MgSO_4$, filtered, and evaporated *in vacuo* to afford a pale-yellow oil. The product **307** was purified by silica gel column chromatography using 1:1 hexanes / EtOAc. R_f = 0.22 (1:1 hexanes / EtOAc). The resulting oil was further purified by silica gel column chromatography using 9.9:9.9:0.2 hexanes / EtOAc / TEA to afford a white solid (0.434 g, 34%). R_f = 0.33 (9.9:9.9:0.2 hexanes / EtOAc / TEA). ^{1}H NMR (500 MHz, $CDCl_3$) δ 4.56 (s, 2H; h), 7.20 (dt, *J* = 5.23, 1.48, 2H; k), 7.27 (t, *J* = 6.74, 1H; f), 7.33 (d, *J* = 7.64, 1H; j), 7.36 (d, *J* = 8.04, 1H; a), 7.43 (d, *J* = 7.35, 2H; i), 7.52 (t, *J* = 7.80, 1H; b), 7.68-7.74 (m, 6H; c, d, e), 8.60 (d, *J* = 4.61, 2H; g); ^{13}C NMR (125 MHz, $CDCl_3$) δ 67.2 (12), 88.0 (6), 122.3 (10), 123.5 (8), 124.1 (4), 126.6 (2), 127.2 (16), 127.7 (14), 128.1 (15), 136.3 (9), 138.1 (3), 139.0 (13), 140.6 (1), 148.5 (11), 161.4 (7), 162.6 (5). $C_{23}H_{19}N_3O$ (M^+) 432.17. Figure A-2.

308

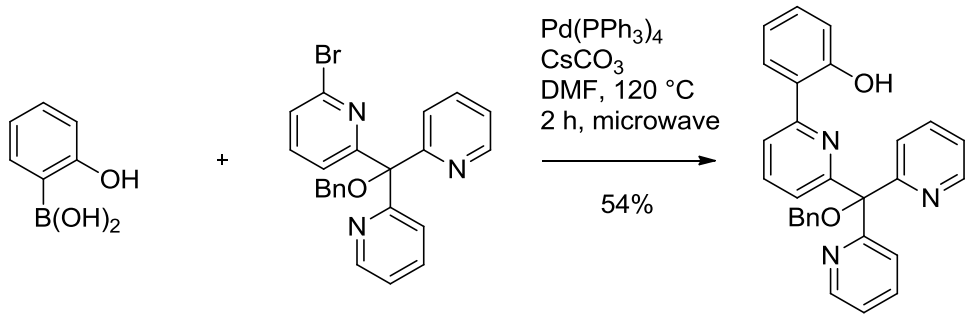

302 **307** **308**

A mixture of **307** (0.100 g, 0.2313 mmol), 2-hydroxyphenylboronic acid **302** (0.064 g, 0.463 mmol), cesium carbonate (0.226 g, 0.694 mmol), tetrakis(triphenylphosphine)palladium(0) (0.027 g, 0.0231 mmol) in dry DMF (4 mL) was stirred and heated in a microwave for 2 hrs at 120 °C. The mixture was allowed to cool to RT and filtered with a 0.45 µm syringe filter. The mixture was extracted with DCM (50 mL) and the organic layer was washed with brine and water alternatively (3 x 50 mL each). The organic layer was dried over $MgSO_4$, filtered, and evaporated *in vacuo* to afford an off-white solid (0.0445 g, 54%). The product **308** was unable to be purified. MS for $C_{29}H_{24}N_3O_2$ (M^+) 447.10.

310

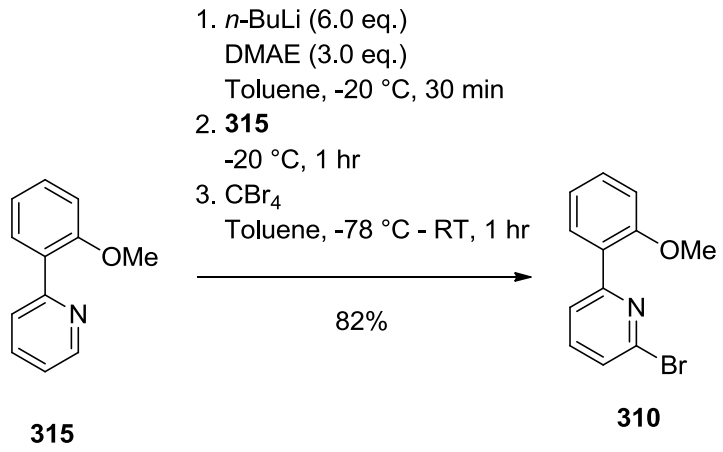

315 **310**

The compound **321** (1.12 g, 4.47 mmol) in dry THF (20 mL) was cooled to 0 °C under Ar. NaH (0.214 g, 8.93 mmol) was added in portions. After cessation of H_2 generation, the reaction was stirred for a further hour at 0 °C. Methyl iodide (0.556 mL, 8.93 mmol) was added dropwise, forming a precipitate, and the reaction was allowed to warm to RT and stirred overnight affording a cloudy yellow solution. The reaction was quenched with water (40 mL). The aqueous layer was washed with $CHCl_3$ (2 x 50 mL) and the combined organic layers were washed with sat. $NaHCO_3$ (50 mL) and brine (50 mL). The organic layer was dried over $MgSO_4$, filtered, and evaporated *in vacuo* to afford a yellow oil. The product **310** was purified by column chromatography using 19:1 hexanes / EtOAc to afford a white solid (0.971 g, 82%). R_f = 0.23 (19:1 hexanes / EtOAc). ^{1}H NMR (500 MHz, $CDCl_3$) δ 3.88 (s, 3H), 7.01 (d, J = 8.35, 1H), 7.11 (dt, J = 7.50, 1.00, 1H), 7.39-7.42 (m, 2H), 7.56 (t, J = 7.80, 1H), 7.88-7.91 (m, 2H). $C_{12}H_{11}BrNO$ (M^+) 264.20. Figure A-3.

311

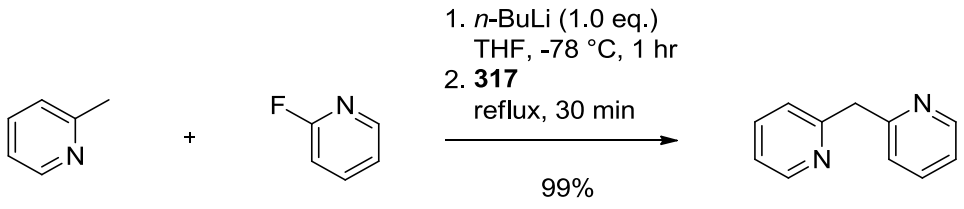

316 317 311

Compound **311** was a known compound and was synthesised according to the literature procedure.[111a] 2-Picoline **316** (0.82 mL, 8.65 mmol) in dry THF (5 mL) was cooled to -78 °C under Ar. *n*-Butyllithium (0.54 mL, 8.65 mmol, as a 1.6 M solution in hexane) was added and the reaction stirred at -78 °C under Ar for 1 hr, slowly warming to -20 °C. 2-Fluoropyridine **317** (0.35 mL, 4.07 mmol) was added and the reaction was heated to reflux for 30 min. The reaction was diluted with DCM (200 mL) and washed with water (4 x 50 mL). The organic layer was dried over $MgSO_4$, filtered, and evaporated *in vacuo* to afford a brown oil. The product **311** was used without further purification (0.685 g, 99%). The characterisation data agreed with the reported literature.[111a] ^{1}H NMR (500 MHz, $CDCl_3$) δ 4.35 (s, 2H), 7.13 (dd, *J* = 7.4, 4.9, 2H), 7.25 (d, *J* = 7.7, 2H), 7.60 (td, *J* = 7.7, 1.8, 2H), 8.57 (dd, *J* = 4.9, 1.8, 2H); ^{13}C NMR (125 MHz, $CDCl_3$) δ 47.0, 121.5, 123.6, 136.7, 149.4, 159.2. $C_{11}H_{10}N_2$ (M^+) 171.19.

315

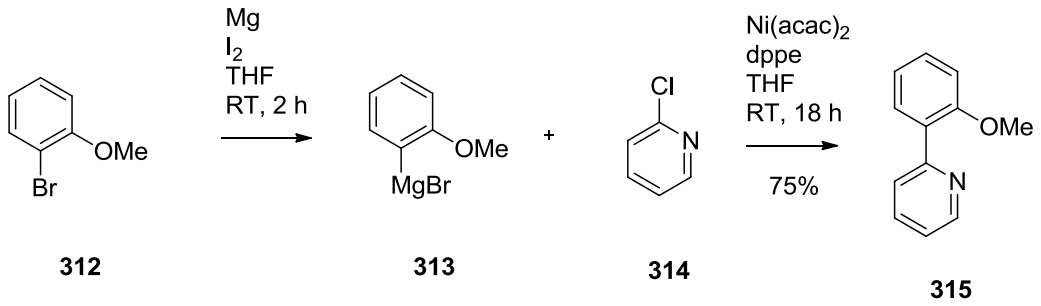

312 **313** **314** **315**

The compound **315** was a known compound and was synthesised according to the literature procedure.[130] Magnesium (0.400 g, 16.5 mmol) was heated under vacuum for a short period, a few crystals of iodine were added and 2-bromoanisole (2.05 mL, 16.5 mmol) in dry THF (50 mL) was added. The mixture was stirred at RT under Ar for 2 hr. 2-Chloropyridine (1.36 mL, 14.5 mmol), nickel acetylacetonate (0.190 g, 0.739 mmol) and 1,2-*bis*(diphenylphosphino)ethane (0.290 g, 0.739 mmol) in dry THF (20 mL) was added to the reaction mixture and then stirred at RT for 18 hr. The reaction was diluted with DCM (200 mL) and washed with water (4 x 50 mL). The organic layer was dried over $MgSO_4$, filtered, and evaporated *in vacuo* to afford a pale-yellow liquid. The product **315** was purified by silica gel column chromatography using 1:4 EtOAc / hexanes (2.01 g, 75%). R_f = 0.14 (1:5 EtOAc / hexanes). The characterisation data agreed with the reported literature.[130] ^{1}H NMR (500 MHz, $CDCl_3$) δ 3.82 (s, 3H), 6.99 (d, *J* = 8.5, 1H), 7.09 (td, *J* = 7.6, 0.9, 1H), 7.19 (ddd, *J* = 7.6, 4.8, 0.9, 1H), 7.36 (td, *J* = 8.5, 1.8, 1H), 7.68 (td, *J* = 8.0, 1.8, 1H), 7.79 (dd, *J* = 7.6, 1.8, 1H), 7.81 (dt, *J* = 8.0, 0.9, 1H), 8.68 (m, 1H); ^{13}C NMR (125 MHz, $CDCl_3$) δ 55.4, 111.2, 120.9, 121.5, 125.0, 128.9, 129.8, 131.0, 135.6, 149.1, 155.9, 156.8. $C_{12}H_{12}NO$ (M^+) 186.63.

319

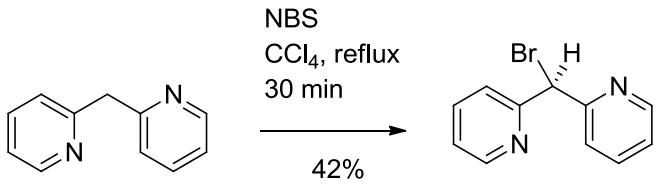

311 **319**

Compound **319** was a known compound and was synthesised according to the literature procedure.[112] The methylene pyridine **311** (0.151 mL, 0.888 mmol) and *N*-bromosuccinimide (0.213 g, 0.903 mmol) in CCl_4 (2 mL) were refluxed for 30 min. The reaction was diluted with DCM (200 mL) and washed with water (200 mL). The organic layer was dried over $MgSO_4$, filtered, and evaporated *in vacuo* to afford a brown oil. The product 2,2'-(Bromomethylene)dipyridine **319** was purified by silica gel column chromatography using 98:2 DCM / MeOH (0.092 g, 42%). R_f = 0.68 (9:1 DCM / MeOH). The characterisation data agreed with the reported literature.[112] ^{1}H NMR (500 MHz, $CDCl_3$) δ 4.36 (s, 1H), 7.18 (ddd, *J* = 7.6, 4.8, 1.6, 2H), 7.69 (td, *J* = 7.6, 1.8, 2H), 7.72 (dt, *J* = 7.6, 1.8, 2H), 8.57 (dd, *J* = 4.8, 1.8, 2H); ^{13}C NMR (125 MHz, $CDCl_3$) δ 54.5, 122.9, 123.5, 136.9, 149.1, 158.3. $C_{11}H_{10}BrN_2$ (M^+) 249.18.

321

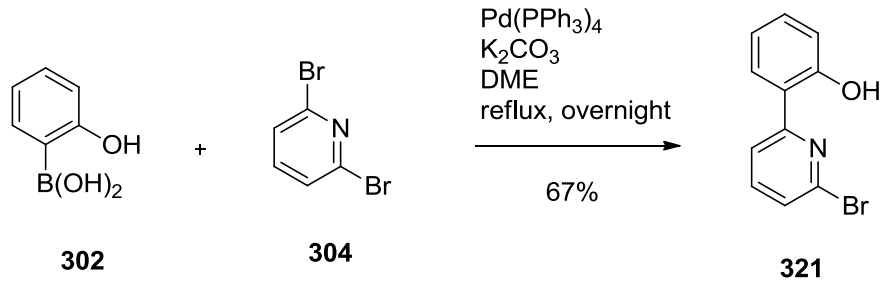

302 **304** **321**

2,6-dibromopyridine (20.0 g, 84.4 mmol) in DME (300 mL) was added to 2-hydroxyboronic acid (11.7 g, 84.4 mmol), tetrakis(triphenylphosphine)palladium(0) (4.88 g, 4.22 mmol), and potassium carbonate (82.9 g, 4.22 mmol) in water (300 mL). The suspension was refluxed overnight at 100 °C under Ar. The organic layer was separated, and the aqueous layer was washed with EtOAc (4 x 50 mL). The combined organic layers were washed with brine and water alternatively (3 x 50 mL each). The organic layer was dried over $MgSO_4$, filtered, and evaporated *in vacuo* to afford a pale-yellow oil. The product **321** was purified by silica gel column chromatography using 9:1 hexanes / EtOAc, loaded with toluene (0.704 g, 67%). R_f = 0.25 (9:1 hexanes / EtOAc). ^{1}H NMR (500 MHz, $CDCl_3$) δ 6.95 (dt, *J* = 7.10, 0.95, 1H; b/d), 7.07 (dd, *J* =8.25, 0.85, 1H; a/c), 7.36 (dt, *J* = 8.48, 1.45, 1H; b/d), 7.43 (d, *J* =7.80, 1H; g), 7.70 (t, *J* = 7.95, 1H; f), 7.76 (dd, *J* = 8.00, 1.35, 1H; a/c), 7.85 (d, *J* = 8.05, 1H; e), 12.72 (br s, 1H; h). ^{13}C NMR (125 MHz, $CDCl_3$) δ 117.9 (8), 118.1 (6), 118.8 (2/4), 119.3 (3/5), 125.5 (10), 126.5 (2/4), 132.2 (3/5), 138.4 (11), 139.7 (9), 158.9 (7), 159.2 (1). $C_{11}H_9BrNO$ (M^+) 250.15. Figure A-4.

322

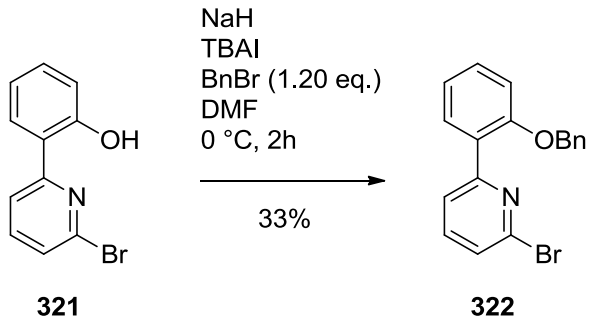

321 **322**

The compound **321** (3.00 g, 12.0 mmol) in dry DMF (25 mL) was cooled to 0 °C under Ar. NaH (2.40 g, 60.0 mmol) was added in portions. After cessation of H_2 generation, a small crystal of TBAI was added. Benzyl bromide (1.71 mL, 14.39 mmol) was added dropwise forming a white precipitate and stirred for a further 2 hours at 0 °C. The reaction was quenched with MeOH (25 mL) and concentrated *in vacuo* to remove the DMF. The resulting brown oil was extracted with EtOAc (125 mL) and the organic layer was washed with brine and water alternatively (5 x 25 mL each). The organic layer was dried over $MgSO_4$, filtered, and evaporated *in vacuo* to afford a yellow oil. The product **322** was purified by silica gel column chromatography using 9:1 hexanes / EtOAc, loaded with toluene (2.05 g, 33%). R_f = 0.46 (9:1 hexanes / EtOAc). ^{1}H NMR (500 MHz, $CDCl_3$) δ 5.17 (s, 2H; h), 7.07 (d, *J* = 8.25, 1H; d), 7.12 (t, *J* = 7.48, 1H; f), 7.34-7.38 (m, 7H; a/c, e, i, j, k), 7.53 (t, *J* = 7.75, 1H; b), 7.90 (m, 2H; a/c, g). ^{13}C NMR (125 MHz, $CDCl_3$) δ 70.7 (12), 113.1 (7), 121.6 (9), 124.0, 125.9, 127.2 (14), 127.9 (6), 128.6 (16), 130.6 (15), 131.5 (10), 136.8 (13), 138.0 (3), 141.4 (1), 157.0 (11), 156.2 (5). HRMS for $C_{18}H_{15}BrNO$ (M^+) 340.0329, expected 340.0332. $C_{18}H_{14}BrNO$ (340.21): calc. C, 63.55; H, 4.15; N, 4.12; found C, 62.99; H, 4.20; N, 4.08. Figure A-5.

323

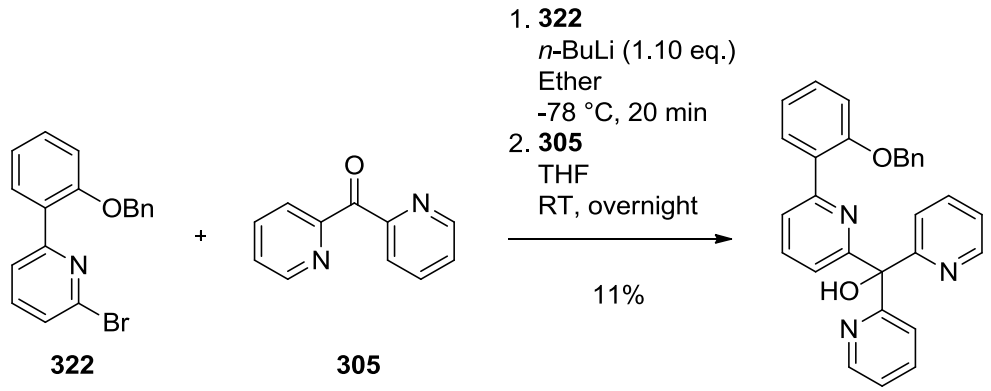

322 305 323

n-Butyllithium was added (1.06 mL, 2.42 mmol, as a 1.6 M solution in hexane) dropwise to a solution of **322** (0.75 g, 2.20 mmol) in dry diethyl ether (15 mL) at -78 °C under Ar and stirred for 30 minutes. The compound **305** (0.406 g, 2.20 mmol) in dry THF (15 mL) was added dropwise, and the solution was allowed to warm to room temperature over 2 hours. The reaction was quenched with 10% aq. K_2CO_3 (w/v) (10 mL) and extracted with chloroform (50 mL). The aqueous layer was separated and washed with chloroform (2 x 25 mL). The organic layers were combined and washed with water (50 mL) and brine (50 mL), dried over $MgSO_4$, filtered, and evaporated *in vacuo* to afford a pale-yellow oil. The product **323** was purified by silica gel column chromatography using 98:2 DCM / MeOH (0.110 g, 11%). R_f = 0.10 (98:2 DCM / MeOH). ^{1}H NMR (500 MHz, $CDCl_3$) δ 5.16 (s, 2H; l), 7.07 (m, 2H; b, d), 7.20 (dt, *J* = 6.23, 1.34, 2H; j), 7.31-7.40 (m, 6H; c, m, n, o), 7.49 (br s, 1H; p), 7.66-7.82 (m, 7H; i, f, h, e/g, a), 7.93 (d, *J* = 7.50, 1H; e/g), 8.58 (d, 2H; k). ^{13}C NMR (125 MHz, $CDCl_3$) δ 70.63 (18), 81.33 (12), 113.08 (5), 121.29 (16), 121.36, 122.18 (14), 122.96 (22), 123.87 (10), 127.15 (20), 127.82 (21), 128.54 (3), 128.97 (6), 129.90 (8), 131.48 (2), 136.26 (9), 136.35 (4, 15), 136.92 (19), 147.95 (17), 153.05 (7), 156.38 (1), 161.10 (11), 163.52 (13). $C_{29}H_{24}N_3O_2$ (M^+) 446.29. Figure A-6.

605

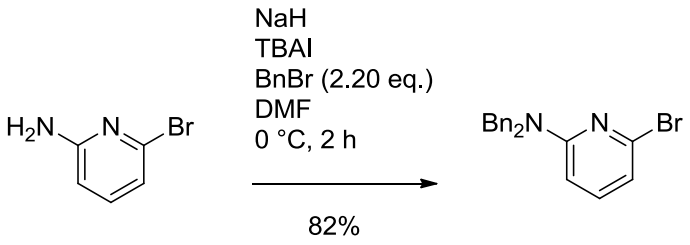

604 **605**

2-Amino-6-bromopyridine **604** (20.0 g, 116 mmol) in dry DMF (200 mL) was cooled to 0 °C under Ar. NaH (23.1 g, 578 mmol) was added in portions. After cessation of H_2 generation, a small crystal of Tetrabutylammonium Iodide was added. Benzyl bromide (30.3 mL, 254 mmol) was added dropwise forming a white precipitate and stirred for a further 2 hours at 0 °C. The reaction was quenched with MeOH (50 mL) and concentrated *in vacuo* to remove the DMF. The resulting red oil was extracted with DCM (200 mL) and the organic layer was washed with brine and water alternatively (3 x 50 mL each). The organic layer was dried over $MgSO_4$, filtered, and evaporated *in vacuo* to afford a clear colourless oil. The product **605** crystallized out providing clear colourless crystals, which were washed with hexanes to remove impurities (33.4 g, 82%). ^{1}H NMR (500 MHz, $CDCl_3$) δ 4.78 (s, 4H; d), 6.35 (d, J = 8.47, 1H; c), 6.76 (d, J = 7.36, 1H; a), 7.21 (t, J = 7.77, 1H; b), 7.26-7.36 (m, 10H; e, g, f); ^{13}C NMR (125 MHz, $CDCl_3$) δ 51.0 (6), 104.2 (4), 115.3 (2), 127.2 (10), 127.3 (8), 128.7 (9), 137.7 (7), 139.5 (3), 140.1 (1), 158.5 (5). $C_{19}H_{18}BrN_2$ (M^+) 353.18. Figure A-7.

606

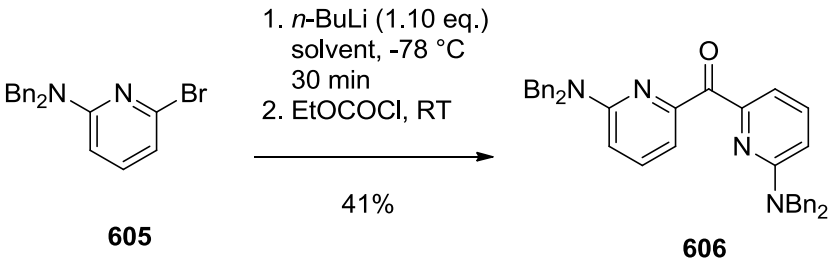

605 **606**

n-Butyllithium (7.10 mL, 16.3 mmol, as a 1.6 M solution in hexane) was added dropwise to a solution of the bromopyridine **605** (5 g, 14.2 mmol) in dry THF (100 mL) at -78 °C under Ar and stirred for 30 minutes. Ethyl chloroformate (674 µL, 7.08 mmol) was added dropwise, and the solution was allowed to warm to room temperature over 2 hours. The reaction was quenched with H_2O (20 mL) and extracted with DCM (3 x 80 mL). The combined organic layers were separated and washed with sat. $NaHCO_3$ (40 mL) and brine (40 mL), dried over $MgSO_4$, filtered, and evaporated *in vacuo* to afford a yellow oil. The product **606** was purified by silica gel column chromatography using 19:1 hexanes / EtOAc, by dry loading the sample (1.66 g, 41%). R_f = 0.16 (19:1 hexanes / EtOAc). ^{1}H NMR (500 MHz, $CDCl_3$) δ 4.80 (s, 8H; d), 6.57 (d, J = 8.64, 2H; c), 7.21-7.30 (m, 22H; e, f, g, a), 7.42 (t, J = 7.96, 2H; b). ^{13}C NMR (125 MHz, $CDCl_3$) δ 51.0 (7), 109.7 (5), 114.0 (3), 127.0 (11), 127.3 (9), 128.5 (10), 137.6 (4), 138.3 (8), 153.0 (2), 157.5 (6), 161.7 (1). HRMS for $C_{39}H_{35}N_4O$ (M^+) 575.2801, expected 575.2805. Figure A-8.

609

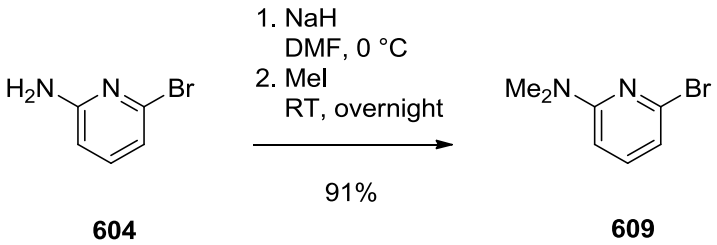

604 **609**

The compound **604** (5.00 g, 28.9 mmol) in dry DMF (50 mL) was cooled to 0 °C under Ar. NaH (3.47 g, 86.7 mmol) was added in portions over 10 minutes. After cessation of H_2 generation, methyl iodide (4.50 mL, 72.3 mmol) was added dropwise, and stirred for a further 2 hours at 0 °C. The reaction was allowed to warm to RT and stirred overnight. The reaction was quenched with water (50 mL) and extracted with isopropyl acetate (50 mL). The organic layer was dried over $MgSO_4$, filtered, and evaporated *in vacuo* to afford a pale-yellow oil. The product **609** was used without any further purification (5.31 g, 91%). ^{1}H NMR (500 MHz, $CDCl_3$) δ 3.05 (s, 6H; d), 6.36 (d, J = 8.43, 1H; c), 6.65 (d, J = 7.45, 1H; a), 7.23 (t, J = 8.14, 1H; b). $C_7H_{10}BrN_2$ (M^+) 201.18. Figure A-9.

610

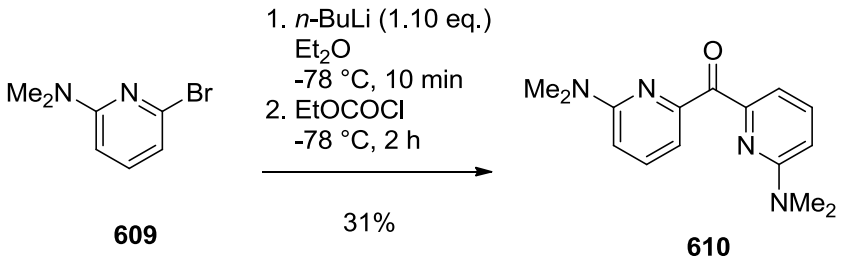

609 **610**

n-Butyllithium (2.53 mL, 2.74 mmol, as a 1.6 M solution in hexane) was added dropwise to a solution of **609** (0.500 g, 2.49 mmol) in dry diethyl ether (10 mL) at -78 °C under Ar and stirred for 5 minutes. Ethyl chloroformate (118 µL, 1.24 mmol) was added dropwise affording a red solution, and was stirred for a further 2 hrs at -78 °C. The reaction was allowed to warm to RT affording cloudy green solution. The reaction was quenched with water (20 mL) and extracted with DCM (25 mL). The organic layer was washed with $NaHCO_3$ (10 mL) and brine (10 mL), dried over $MgSO_4$, filtered, and evaporated *in vacuo* to afford a pale-orange oil. The product **238** was purified by silica column chromatography using 9:1 hexanes / EtOAc (0.104 g, 31%). R_f = 0.23 (9:1 hexanes / EtOAc). ^{1}H NMR (500 MHz, $CDCl_3$) δ 3.11 (s, 12H; d), 6.69 (d, *J* = 8.51, 2H; c), 7.34 (d, *J* = 7.25, 2H; a), 7.23 (dt, *J* = 7.95, 1.06, 2H; b). $C_{15}H_{19}N_4O$ (M^+) 272.07. Figure A-10.

617

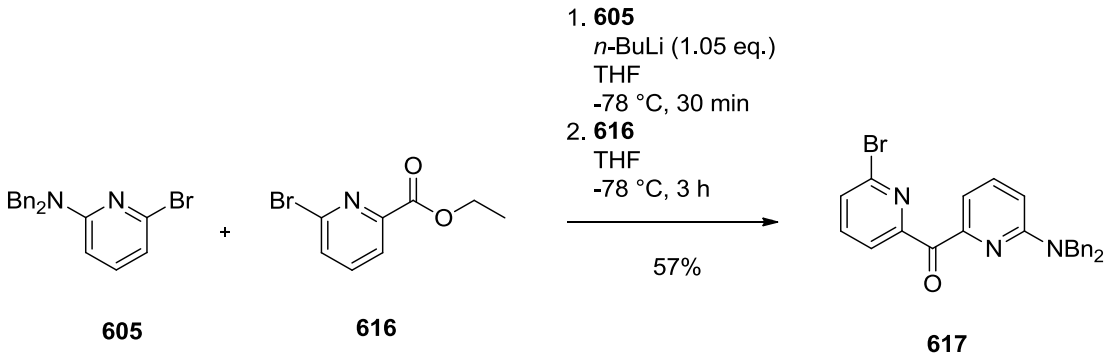

605 616 617

n-Butyllithium was added (1.95 mL, 3.11 mmol, as a 1.6 M solution in hexane) dropwise to a solution of **605** (1.00 g, 2.83 mmol) in dry THF (10 mL) at -78 °C under Ar and stirred for 30 minutes. **616** (0.651 g, 2.83 mmol) in dry THF (10 mL) was added dropwise, and the solution was stirred at -78 °C for 3 hours. The solution was allowed to warm to RT and was stirred overnight. The reaction was quenched with 10% acetic acid (10 mL), and the solution was extracted into EtOAc (3 x 10 mL). The organic layer was washed with brine (10 mL) and water (10 mL). The aqueous layer was washed with $CHCl_3$ (3 x 10 mL). The combined organic layers were combined, dried over $MgSO_4$, filtered, and evaporated *in vacuo*. The product **617** was purified by silica column chromatography using 6:1 hexanes / EtOAc (0.316 g, 57%). R_f = 0.18 (6:1 hexanes / EtOAc). ^{1}H NMR (500 MHz, $CDCl_3$) δ 4.77 (s, 4H; d), 6.70 (d, *J* = 8.45, 1H; c), 7.19 (d, *J* = 7.15, 4H; e), 7.31-7.35 (m, 6H; f, g), 7.37 (t, *J* = 7.80, 1H; i), 7.51 (d, *J* = 7.45, 1H; j), 7.53 (d, *J* = 8.69, 1H; a), 7.60 (t, *J* = 7.78; b), 7.74 (d, *J* = 7.56, 1H; h). $C_{25}H_{21}BrN_3O$ (M^+) 458.20. Figure A-11.

621

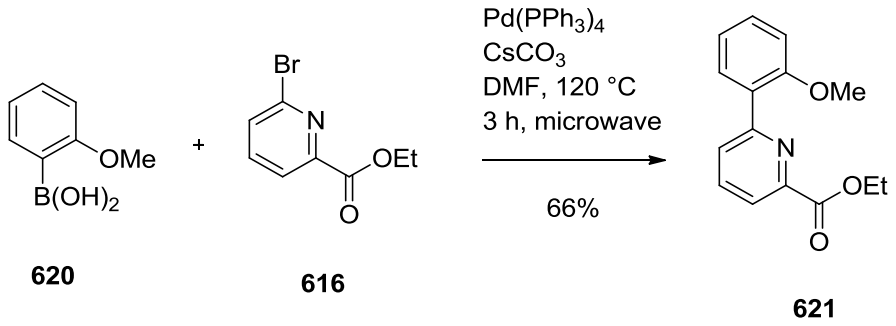

620 **616** **621**

A mixture of **616** (0.250 g, 1.09 mmol), **620** (0.330 g, 2.17 mmol), cesium carbonate (1.06 g, 3.26 mmol), tetrakis(triphenylphosphine)palladium(0) (0.126 g, 0.109 mmol) in dry DMF (10 mL) was stirred and heated in a microwave for 3 hrs at 120 °C under Ar. The mixture was allowed to cool to RT and filtered with a 0.45 μm syringe filter. The mixture was extracted with $CHCl_3$ (50 mL) and the organic layer was washed with brine and water alternatively (5 x 50 mL each). The organic layer was dried over $MgSO_4$, filtered, and evaporated *in vacuo* to afford a pale-yellow oil. The product **621** was purified by column chromatography using 9:1 hexanes / EtOAc to afford a white solid (0.184 g, 66%). R_f = 0.13 (9:1 hexanes / EtOAc). ^{1}H NMR (500 MHz, $CDCl_3$) δ 1.47 (t, *J* = 7.15, 3H), 3.87 (s, 3H), 4.50 (q, *J* = 7.14, 2H), 7.02 (d, *J* = 8.30,), 7.12 (dt, *J* = 7.51, 0.88, 1H), 7.41 (dt, *J* = 7.71, 1.80, 1H), 7.84 (t, *J* = 7.85, 1H), 7.92 (dd, *J* = 7.66, 1.79, 1H), 8.05 (d, *J* = 7.80, 2H). $C_{15}H_{16}NO_3$ (M^+) 258.22.

622

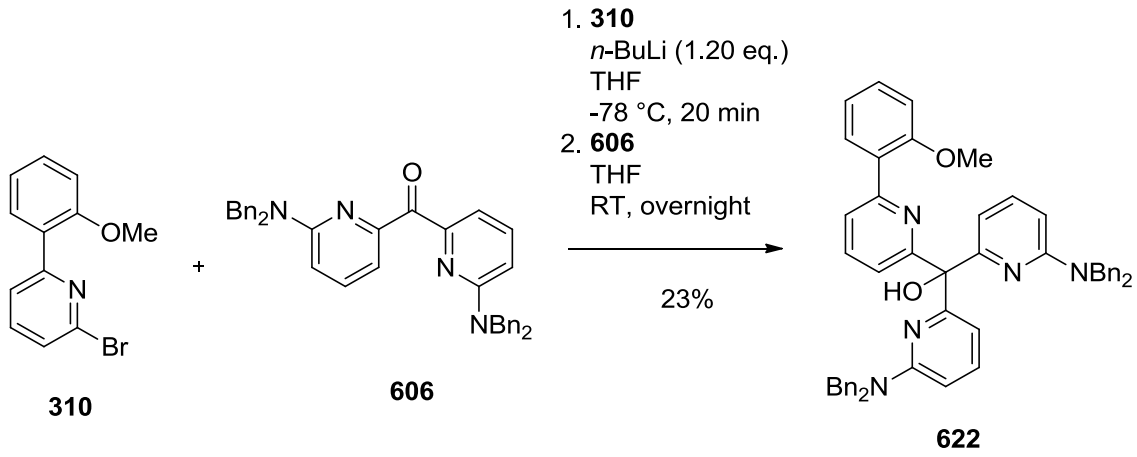

n-Butyllithium (1.14 mL, 1.14 mmol, as a 1.6 M solution in hexane) was added dropwise to a solution of **310** (0.255 g, 0.947 mmol) in dry THF (2.5 mL) at -78 °C under Ar and stirred for 20 minutes. The pyridyl ketone **606** (0.544 g, 0.947 mmol) in dry THF (2.5 mL) was added dropwise affording a lime solution. The reaction was allowed to warm to RT and was stirred overnight to afford a clear orange solution. The reaction was quenched with 25% acetic acid (1 mL) and extracted with EtOAc (50 mL). The organic layer was washed with water (3 x 20 mL) and brine (30 mL). The aqueous layer was washed with $CHCl_3$ (2 x 15 mL). The combined organic layers were dried over $MgSO_4$, filtered, and evaporated *in vacuo* to afford a yellow oil. The product **622** was purified by silica column chromatography using 9:1 hexanes / EtOAc (0.0652 g, 23%). R_f = 0.09 (9:1 hexanes / EtOAc). ^{1}H NMR (500 MHz, $CDCl_3$) δ 3.86 (s, 3H), 4.64-4.71 (m, 8H), 6.32 (d, *J* = 8.35, 2H), 7.01 (d, *J* = 8.15, 1H), 7.40 (d, *J* = 7.40, 3H), 7.12-7.14 (m, 8H), 7.21-7.25 (m, 12H), 7.31 (d, *J* = 7.80, 1H), 7.37 (t, *J* = 7.78, 4H), 7.68 (d, *J* = 7.80, 1H), 7.71 (d, *J* = 7.52, 1H), 7.86 (dd, *J* = 7.64, 1.70, 1H). $C_{51}H_{46}N_5O_2$ (M^+) 760.57.

625

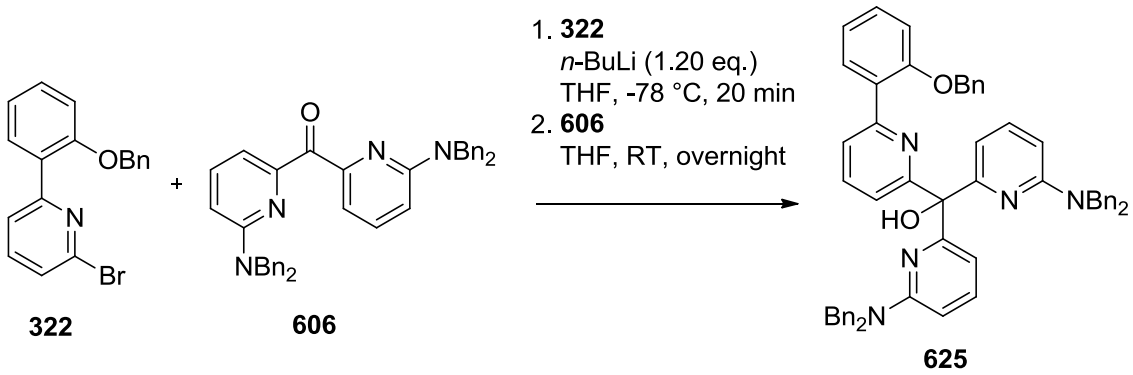

n-Butyllithium (0.70 mL, 1.61 mmol, as a 1.6 M solution in hexane) was added dropwise to a solution of **322** (0.498 g, 1.46 mmol) in dry diethyl ether (20 mL) at -78 °C under Ar and stirred for 30 minutes. **606** (0.8408 g, 1.46 mmol) in dry THF (20 mL) was added dropwise, and the solution was allowed to warm to room temperature over 2 hours. The reaction was quenched with H_2O (10 mL) and extracted with EtOAc (25 mL). The reaction was washed with water (25 mL) and brine (25 mL). The organic layer was dried over $MgSO_4$, filtered, and evaporated *in vacuo*. The product **625** was purified by silica gel column chromatography using 98:2 DCM / MeOH (0.2012 g, 32%). R_f = 0.36 (98:2 DCM / MeOH). ^{1}H NMR (700 MHz, $CDCl_3$) δ 4.67 (q, *J* = 12.19, 16.38, 8H; k), 5.13 (s, 2H; o), 6.33 (d, *J* = 8.39, 2H; h), 7.06-7.10 (m, 4H; j, b), 7.13-7.14 (m, 8H; l/m/n), 7.22-7.25 (m, 13H; f, l/m/n), 7.32-7.40 (m, 9H; d, c, i, s), 7.67 (d, *J* = 8.03; 1H; g), 7.77 (d, *J* = 7.72, 1H; e), 7.89 (1d, *J* = 7.64, 1H; a). ^{13}C NMR (175 MHz, $CDCl_3$) δ 51.1 (18), 70.6 (23), 81.2 (12), 103.8 (14), 111.0 (16), 113.1 (27), 121.3 (26), 122.8 (10), 123.2 (8), 126.8 (22), 126.9, 127.0, 127.1, 127.2, 127.3 (20), 127.7 (25), 128.4 (21), 128.5, 128.6 (6), 129.4, 129.6 (5), 131.7 (2), 135.1 (24), 137.1 (9), 137.8 (15), 138.8 (19), 151.9 (7), 156.3 (1), 156.9 (17), 161.0 (11), 162.3 (13). $C_{57}H_{50}N_5O_2$ (M^+) 837.63. Figure A-12.

629

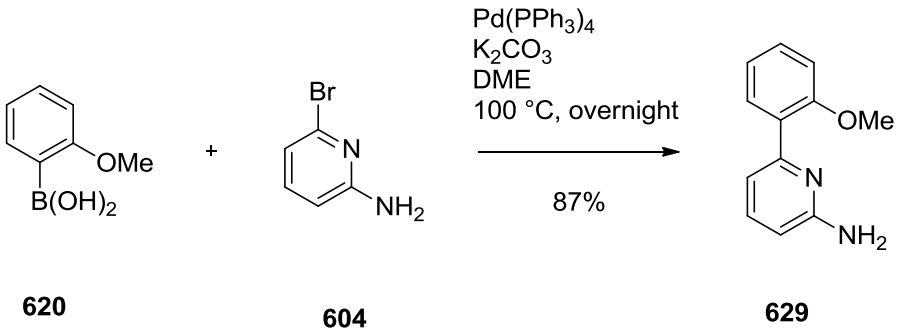

620 **604** **629**

604 (5.00 g, 28.9 mmol) in DME (40 mL) was added to **620** (4.39 g, 28.9 mmol), tetrakis(triphenylphosphine)palladium(0) (1.67 g, 1.45 mmol), and potassium carbonate (28.4 g, 205 mmol) in water (40 mL). The suspension was refluxed overnight at 100 °C under Ar. The reaction mixture was filtered through cotton wool and diluted with EtOAc (50 mL). The organic layer was washed with brine (50 mL) and water (50 mL), dried over $MgSO_4$, filtered, and dried *in vacuo*. The product **629** was used without any further purification (1.01 g, 87%). ^{1}H NMR (500 MHz, $CDCl_3$) δ 3.87 (s, 3H; h), 4.51 (br s, 2H; i), 6.46 (d, *J* = 8.03, 1H; a), 7.00 (d, *J* = 8.49, 1H; g), 7.07 (t, *J* = 7.20, 1H; e), 7.17 (d, *J* = 7.72, 1H; c), 7.36 (dt, *J* = 7.72, 1.80, 1H; f), 7.49 (t, *J* = 7.72, 1H; b), 7.71 (dd, *J* = 7.62, 1.36, 1H; d). ^{13}C NMR (125 MHz, $CDCl_3$) δ 55.7 (12), 106.8 (2), 111.4 (10), 115.5 (4), 120.9 (8), 129.5 (6, 9), 130.9 (7), 137.5 (3), 154.5 (5), 157.0 (11), 158.1 (1). $C_{12}H_{13}N_2O$ (M^+) 201.68. Figure A-13.

633

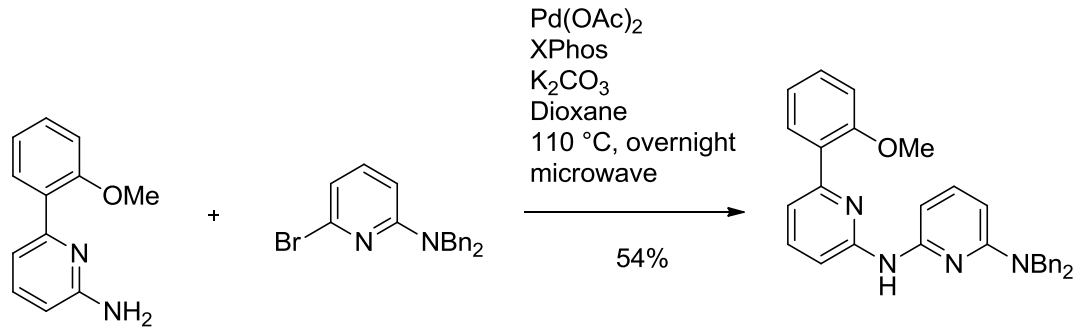

629 **605** **633**

A suspension was formed from **605** (1.76 g, 4.99 mmol), **629** (1.00, 4.99 mmol), palladium(II) acetate (0.112 g, 0.499 mmol), XPhos (0.238 g, 0.499 mmol) and potassium carbonate (1.38 g, 9.99 mmol) in dioxane (20 mL). The suspension was refluxed overnight at 110 °C under Ar. The mixture was allowed to cool to RT and filtered with a 0.45 µm syringe filter. The mixture was extracted with DCM (50 mL) and the organic layer was washed with brine and water alternatively (3 x 50 mL each). The organic layer was dried over $MgSO_4$, filtered, and evaporated *in vacuo* to afford an orange solid. The product **633** was purified by column chromatography using 1:1 hexanes / EtOAc to afford a white solid (1.27 g, 54%). R_f = 0.90 (1:1 hexanes / EtOAc). ^{1}H NMR (500 MHz, $CDCl_3$) δ 3.87 (s, 3H; h), 4.85 (s, 4H; l), 6.09 (d, *J* = 8.26, 1H; k), 6.50 (d, *J* = 7.81, 1H; i), 7.01 (d, *J* = 8.26, 1H; g), 7.09 (dt, *J* = 7.66, 0.93, 1H; e), 7.20 (br s, 1H; p), 7.27-7.39 (m, 14H; m, a, f, j, n), 7.57 (d, *J* = 8.13, 1H; c), 7.75 (dd, *J* = 7.60, 1.70, 1H; d). ^{13}C NMR (125 MHz, $CDCl_3$) δ 51.4 (18), 55.6 (12), 97.5 (16), 98.9 (14), 109.7 (4), 111.5 (10), 117.4 (2), 120.9 (8), 126.9 (20), 126.9, 127.1, 127.3, 128.6 (21), 129.4, 129.6 (6), 130.9 (7), 137.2, 138.7 (19), 139.2, 152.8 (13), 153.5 (1), 154.1 (5), 157.0 (11), 157.7 (17). $C_{31}H_{29}N_4O_2$ (M^+) 474.44. Figure A-14.

639

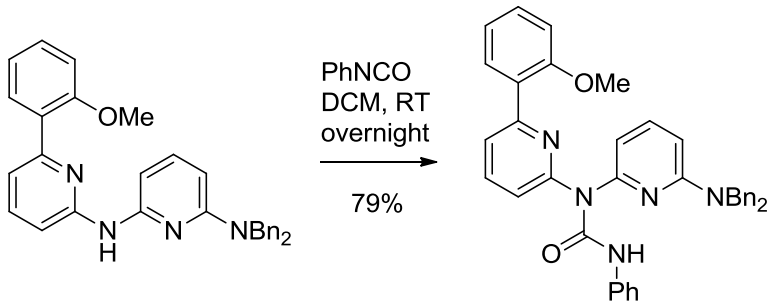

635 **639**

A solution of phenylisocyanate (0.347 mL, 3.17 mmol) was dropwise added to **635** (0.5000 g, 1.06 mmol) in DCM (10 mL). The mixture was stirred overnight at RT. The reaction was extracted with DCM (25 mL), washed with water (2 x 25 mL) and brine (25 mL). The organic layer was separated, dried over $MgSO_4$, filtered, and dried *in vacuo*. The product **639** was purified by column chromatography using 7:3 hexanes / diethyl ether to afford a pale-yellow solid (0.489 g, 79%). R_f = 0.33 (7:3 hexanes / diethyl ether). ^{1}H NMR (500 MHz, $CDCl_3$) δ 3.86 (s, 3H; h), 4.79 (s, 4H; l), 6.44 (d, *J* = 8.51, 1H; k), 6.46 (d, *J* = 7.37, 1H; i), 6.60 (d, *J* = 8.02, 1H; a), 7.00 (tt, *J* = 7.47, 1.08, 1H), 7.07-7.10 (m, 5H), 7.13 (dt, *J* = 7.57, 0.98, 1H), 7.21 (t, *J* = 7.49, 2H; q), 7.25-7.28 (m, 6H; m, r), 7.30-7.32 (m, 8H; n), 7.39 (d, *J* = 7.57, 5H), 7.44-7.47 (m, 1H; f), 7.50 (t, *J* = 8.19, 1H; j), 7.56 (d, *J* = 7.51, 1H; c), 7.62 (t, *J* = 8.19, 1H; b), 7.79 (dd, *J* = 7.55, 1.75, 1H; d), 12.84 (br s, 1H; s). ^{13}C NMR (175 MHz, $CDCl_3$) δ 51.4 (18), 55.7 (12), 104.0 (16), 109.7 (14), 111.5 (10), 114.8 (2), 120.1 (4), 120.4, 120.6 (25), 121.0 (8), 123.0 (27), 123.7 (22), 127.1(20), 127.2 (6), 128.6 (26), 128.7 (21), 129.1, 130.4 (9), 131.1 (7), 137.9 (3), 138.0 (19), 138.4 (24), 138.9 (11), 140.0 (15), 152.0 (13), 153.2 (1), 153.5 (23), 153.7 (5), 154.4, 157.0 (11), 158.6 (17). $C_{38}H_{34}N_5O_2$ (M^+) 593.32. Figure A-15.

640

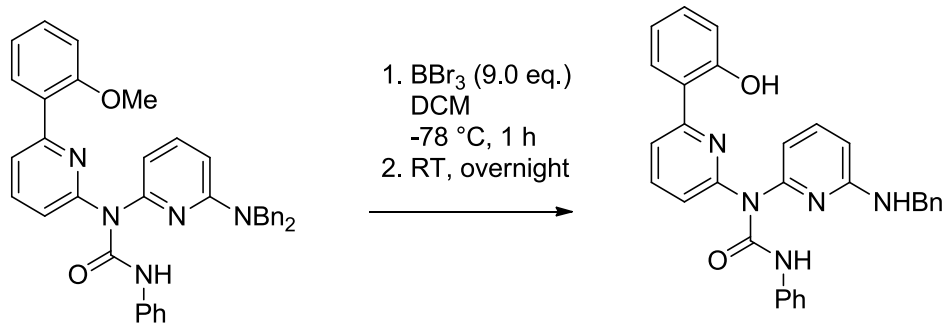

639 **640**

The compound **639** (0.250 g, 0529 mmol) in dry DCM (10 mL) was cooled to -78 °C under Ar. Boron tribromide (4.76 mL, 4.76 mmol) was added dropwise to produce a cloudy white solution. The reaction was allowed to warm to RT and stirred overnight, affording a yellow precipitate. The reaction was quenched with H_2O (10 mL) and extracted with DCM (50 mL). The organic layer was washed with brine (50 mL) and water (50 mL), dried over $MgSO_4$, filtered, and evaporated *in vacuo* to afford a yellow oil. The product **640** was purified by silica gel column chromatography using 9:1 hexanes / EtOAc to afford a pale-yellow solid. R_f = 0.45 (9:1 hexanes / EtOAc). ^{1}H NMR (400 MHz, $CDCl_3$) δ 4.65 (d, *J* = 5.40, 2H), 4.98 (s, 1H), 5.78 (d, *J* = 7.92, 1H), 6.22 (d, *J* = 8.16, 1H), 6.91-6.97 (m, 2H), 7.05 (t, *J* = 7.08, 1H), 7.24-7.41 (m, 6H), 7.49 (d, *J* = 7.56, 1H), 7.82 (d, *J* = 7.68, 1H), 7.88 (d, *J* = 7.88, 1H), 7.98 (t, *J* = 7.90, 1H), 11.20 (s, 1H), 12.87 (s, 1H). $C_{30}H_{26}N_5O_2$ (M^+) 489.11. Figure A-16.

641

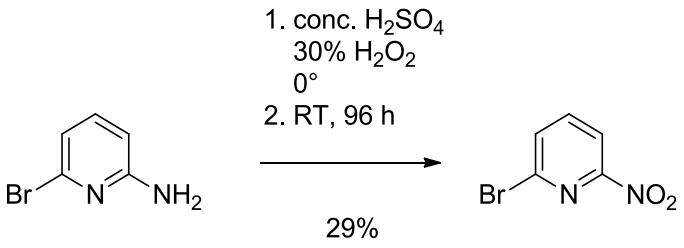

2-Amino-6-bromopyridine (5.00 g, 28.9 mmol) in conc. H_2SO_4 (25 mL) was cooled to 0 °C. Dropwise was added a cooled (5 °C) mixture of 30% hydrogen peroxide (37.5 mL) and conc. sulfuric acid (75 mL) while the temperature was held below 5 °C. The solution was allowed to warm to RT and stirred for a further 96 hrs. The solution was carefully neutralized with 6 M KOH, filtered, and extracted with DCM (200 mL). The organic layer was separated, dried over $MgSO_4$, filtered, and dried *in vacuo*. The product **641** was purified by column chromatography using 3:7 hexanes / DCM to afford a white solid (1.72 g, 29%). R_f = 0.49 (3:7 hexanes / DCM). ^{1}H NMR (500 MHz, $CDCl_3$) δ 7.88 (dd, *J* = 7.76, 1.08, 1H; a), 7.92 (t, *J* = 7.59, 1H; b), 8.23 (dd, *J* = 7.60, 1.05, 1H; c). $C_5H_4BrN_2O_2$ (M^+) 203.05. Figure A-17.

642

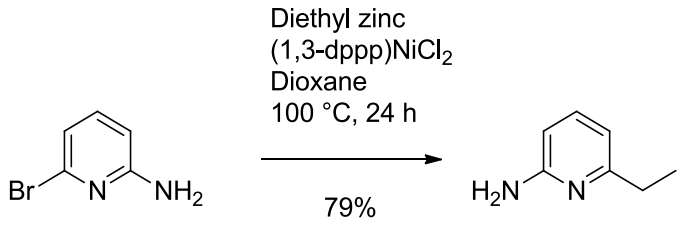

Diethyl zinc in hexanes (82.5 mL, 82.5 mmol) was added dropwise to a solution of 6-bromo-2-aminopyridine and [1,3-bis(diphenylphosphino)propane]nickel(II) chloride in dry dioxane (150 mL). The solution was refluxed for 24 hours at 100 °C under Ar. The reaction was allowed to warm to RT and quenched with MeOH (100 mL) and evaporated *in vacuo*. The resulting grey-green oil was dissolved in a solution of brine (250 mL), DCM (270 mL) and MeOH (30 mL) via sonication. The solution was filtered and washed with 2:1 DCM:MeOH (150 mL). The aqueous layer was washed further with 2:1 DCM:MeOH (100 mL). The combined organic layers were combined, dried over $MgSO_4$, filtered, and evaporated *in vacuo* to afford a brown oil. The product **642** was purified by silica column chromatography using 1:1 hexanes / EtOAc (2.80 g, 79%). R_f = 0.33x (1:1 hexanes / EtOAc). ^{1}H NMR (500 MHz, $CDCl_3$) δ 1.14-1.18 (m, 3H; e), 2.55 (q, J = 7.95, 7.40, 2H; d), 4.73 (br s, 2H; f), 6.21 (d, J = 8.16, 1H; a), 6.40 (d, J = 7.35, 1H; c), 7.23 (t, J = 7.71, 1H; b). $C_7H_{11}N_2$ (M^+) 123.26. Figure A-18.

Chapter 8: Conclusion

"There is an art to flying, or rather a knack. The knack lies in learning how to throw yourself at the ground and miss." – Douglas Adams

Beryllium, an alkali-earth element, is a seemingly simple silver-grey metal. It has had no uses other than for jewellery until the beginning of the 21st century. But now it is indispensable. Its unique combination of low density, extreme stiffness, high thermal conductivities, and transparency to ionizing radiation has resulted in widespread application of beryllium to all major industries. Another of its properties that has been well documented is its toxicity. There are occupational, public health, and environmental concerns that are increasingly necessary to be addressed. Since the literature on the coordination chemistry of beryllium is relatively shallow, there was much to gain by making an investigation into its chelation for safe and effective removal. Therefore, we have taken a two-pronged approach to better understand beryllium coordination: first through computational studies using buttressing chemistry, and second to synthesise the best of these new chelators.

A sequence of calculations was made with complexes of Be^{2+} and other metal cations that explored donor preferences, cavity size preferences, and buttress groups. The theoretical results collected in this thesis illustrate the success of second sphere hydrogen bonding in tuning the binding site of a ligand. The complex geometries show clear trends for the size of the cavity (as influenced by the ligand motif, buttress, and apex group) correlating to binding energy. Buttress groups made available the potential for hydrogen bonds as part of an outer coordination sphere. These interactions between the primary backbone structures and the buttressing groups were observed to be the principal influence on the stabilisation of the electronic ground state of the metal complexes. Summaries of this work can be found on pages 74 and 161.

This work also considered the synthesis of these computationally modelled ligands, and their derivatives. Successful synthesis gave pure non-buttressed and buttressed materials. These were made available for reaction with beryllium salts for X-ray crystallography for further characterisation and study. X-ray data for three unique beryllium complexes were obtained, which agreed well with the calculated geometries. Summaries of this work can be found on pages 101, 115, and 202.

Although this thesis has only studied a small fragment of beryllium chemistry, it has shown that through the addition of buttress groups, ligands can be tuned in their binding to metal cations and could strongly bind to Be^{2+}. Pathways to multiple new ligands have been discovered, giving a strong foundation for future synthetic work in this area. I have my very best hope that the continuation of this research will serve as a witness to New Zealand's strong environmental convictions.

Chapter 9: References

"All papers that you save will never be needed until such time as they are disposed of, when they become essential."

—Paul Dickson

1. Taylor, T. P.; Ding, M.; Ehler, D. S.; Foreman, T. M.; Kaszuba, J. P.; Sauer, N. N., Beryllium in the Environment: A Review. *Journal of Environmental Science and Health Part A: Toxic/Hazardous Substances & Environmental Engineering* **2003,** *38* (2), 439-469.
2. Reedijk, J.; Poeppelmeier, K., *Comprehensive Coordination Chemistry II*. Elsevier: **2003**; p 8400.
3. (a) *Toxicological Profile for Beryllium*; US Agency for Toxic Substances and Disease Registry (ATSDR): Atlanta, GA, **2002**; (b) Jakubke, H.; Heschkeit, J., *Concise Encyclopedia Chemistry*. Walter de Gruyter: Berlin, Germany, **1994**; p 1201; (c) Young, J.; War, M. *Copper Beryllium Alloys – The Value of Occupational Hygiene Principles when Investigating an Occupational Health Issue within Aircraft Maintenance Operations?*; Air New Zealand Limited OSIGH Internal report, **2008**.
4. (a) Rossman, M. D., Chronic Beryllium Disease: A Hypersensitivity Disorder. *Applied Occupational and Environmental Hygiene* **2001,** *16* (5), 615-6618; (b) Saltini, C., Amicosante, M., Beryllium disease. *The American Journal of The Medical Sciences* **2001,** *321* (1), 89-98.
5. Council, N. R., *Health Effects of Beryllium Exposure: A Literature Review*. The National Academics Press: Washington, DC, United States, **2007**; p 108.
6. Weeks, M. E.; Leichester, H. M., *Discovery of the Elements*. Mack Printing Company: Easton, United States, **1968**; p 383.
7. (a) Bussy, A., D'une travail qu'il a entrepris sur le glucinium. *Journal de Chimie Medicale* **1828,** *4*, 456-457; (b) Emsley, J., *Nature's Building Blocks*. Oxford University Press: New York, United States, **2001**; p 538; (c) Wöhler, F., Ueber das Beryllium und Yttrium. *Annalen der Physik und Chemie* **1828,** *89* (8), 577-582.
8. Kane, R.; Sell, H., *Revolution in Lamps: A Chronicle of 50 Years of Progress*. The Fairmont Press, Inc.: Lilburn, United States, **2001**; p 284.
9. Tivon, A. Reproduced by permission of the copyright owner: Photos of emerald, helidor, morganite, and aquamarine gemstones. **2018**
10. Walsh, K. A., *Beryllium Chemistry and Processing*. ASM International: Novelty, United States, **2009**; p 575.
11. Anovitz, L. M.; Mamontov, E.; ben Ishai, P.; Kolesnikov, A. I., Anisotropic dynamics of water ultraconfined in macroscopically oriented channels of single-crystal beryl: A multifrequency analysis. *Physical Review E* **2013,** *88* (5).
12. Frängsmyr, T.; Ekspong, G., *Physics 1981-1990*. World Scientific: Singapore, **1993**; p 741.
13. *Mineral Commodity Summaries 2006*; United States Geological Survey: Reston, United States, **2006**; p 199.
14. Wong, C. Y.; Woollins, J. D., Beryllium Coordination Chemistry. *Coordination Chemistry Reviews* **1994,** *130* (1-2), 243-273.
15. Svilar, M.; Schuster, G.; Civic, T.; Sabey, P.; Vidal, E.; Freeman, S.; Petzow, G.; Aldinger, F.; Jönsson, S.; Welge, P.; Kampen, V.; Mensing, T.; Brüning, T., Beryllium and

Beryllium Compounds. In *Ullmann's Encyclopedia of Industrial Chemistry*, Wiley: Weinheim, Germany, **2013**; pp 1-35.
16. Wright, D. J.; Nichini, F. M.; Stauffer, H. M., Beryllium Window Tubes for Mammographic Examinations. *British Journal of Radiology* **1971,** *44* (522), 480.
17. *Mineral Commodity Summaries 1995*; United States Geological Survey: Pittsburgh, United States, **1995**.
18. Hurley, K.; Sommer, M.; Atteia, J. L.; Boer, M.; Cline, T.; Cotin, F.; Henoux, J. C.; Kane, S.; Lowes, P.; Niel, M.; Vanrooijen, J.; Vedrenne, G., The solar X-Ray / cosmic gamma-ray burst experiment aboard Ulysses. *Astronomy & Astrophysics Supplement Series* **1992,** *92* (2), 401-410.
19. Erb, R. B.; Lee, D. B.; Weston, K. C.; Greenshields, D. H., Proceedings of the 1967 Heat Transfer and Fluid Mechanics Institute. Stanford University Press: Stanford, United States, **1967**.
20. Feinberg, L. D.; Clampin, M.; Keski-Kuha, R.; Atkinson, C.; Texter, S.; Bergeland, M.; Gallagher, B. B., James Webb Space Telescope Optical Telescope Element Mirror Development History and Results. *Space Telescopes and Instrumentation 2012: Optical, Infrared, and Millimeter Wave* **2012,** *8442*.
21. Schirmer, O. F., Structure of Paramagnetic Lithium Center in Zinc Oxide and Beryllium Oxide. *Journal of Physics and Chemistry of Solids* **1968,** *29* (8), 1407-1429.
22. Atlas Technologies. Reproduced by permission of the copyright owner: Photo of a beryllium window. **2018**
23. (a) Kumberger, O.; Schmidbaur, H., Why is Beryllium so Toxic. *Chemie in Unserer Zeit* **1993,** *27* (6), 310-316; (b) Newman, L. S., Beryllium. *Chemical & Engineering News Archive* **2003,** *81* (36), 38.
24. James, D. G.; Zumla, A., *The Granulomatous Disorders*. Cambridge University Press: Cambridge, United Kingdom, **1999**; p 628.
25. Cummings, K. J.; Deubner, D. C.; Day, G. A.; Henneberger, P. K.; Kitt, M. M.; Kent, M. S.; Kreiss, K.; Schuler, C. R., Enhanced Preventive Programme at a Beryllium Oxide Ceramics Facility Reduces Beryllium Sensitisation Among New Workers. *Occupational and Environmental Medicine* **2007,** *64* (2), 134-140.
26. Greenberg, M. I., *Occupational, Industrial, and Environmental Toxicology*. Elsevier - Health Sciences Division: St Louis, United States, **2003**; p 829.
27. Richeldi, L.; Sorrentino, R.; Saltini, C., HLA-DPB1 Glutamate 69: a genetic marker of beryllium disease. *Science* **1993,** *262* (5131), 242-244.
28. Schuler, C. R.; Kitt, M. M.; Henneberger, P. K.; Deubner, D. C.; Kreiss, K., Cumulative Sensitization and Disease in a Beryllium Oxide Ceramics Worker Cohort. *Journal of Occupational and Environmental Medicine* **2008,** *50* (12), 1343-1350.
29. (a) Weber, H.; Engelhardt, W., *Zentralblatt für Gewerbehygiene und Unfallverhütung* **1933,** *10*, 41-47; (b) Van Ordstrang, H.; Hughes, R.; Carmody, M. G., Chemical Pneumonia in Workers Extracting Beryllium Oxide: Report of Three Cases. *Cleveland Clinic Journal of Medicine* **1943,** *10* (1), 10-18.
30. Hosseini, M.; Vaezi, Z.; Ganjali, M. R.; Faridbod, F.; Abkenar, S. D., Fluorescence "Turn-On" Chemosensor for the Selective Detection of Beryllium. *Spectrochimica Acta Part a-Molecular and Biomolecular Spectroscopy* **2011,** *83* (1), 161-164.
31. (a) Chenoweth, M. B., Chelation as a Mechanism of Pharmacological Action. *Pharmacological Reviews* **1956,** *8* (1), 57-87; (b) Shaw, M. J.; Hill, S. J.; Jones, P.; Nesterenko, P. N., Determination of Beryllium in a Stream Sediment by High-Performance Chelation Ion Chromatography. *Journal of Chromatography A* **2000,** *876* (1-2), 127-133.
32. Liao, S.; Shiu, J. G.; Liu, S.; Yeh, S.; Chen, Y.; Chen, C.; Chow, T.; Wu, C., Hydroxynaphthyridine-Derived Group III Metal Chelates: Wide Band Gap and Deep Blue Analogues of Green Alq_3 (Tris(8-hydroxyquinolate)aluminum) and Their

Versatile Applications for Organic Light-Emitting Diodes. *Journal of the American Chemical Society* **2009,** *131* (2), 763-777.

33. (a) Cullen, M. R.; Kominsky, J. R.; Rossman, M. D.; Cherniack, M. G.; Rankin, J. A.; Balmes, J. R.; Kern, J. A.; Daniele, R. P.; Palmer, L.; Naegel, G. P.; McManus, K.; Cruz, R., Chronic beryllium disease in a precious metal refinery. Clinical epidemiologic and immunological evidence for continuing risk from exposure to low level beryllium fume. *American Review of Respiratory Disease* **1987,** *135* (1), 201-208; (b) Sood, A.; Beckett, W. S.; Cullen, M. R., Variable Response to Longterm Corticosteroid Therapy in Chronic Beryllium Disease. *Chest* **2004,** *126* (6), 2000-2007.
34. (a) Mederos, A.; Dominguez, S.; Chinea, E.; Brito, F.; Cecconi, F., Review: New Advances in the Coordination Chemistry of the Beryllium(II). *Journal of Coordination Chemistry* **2001,** *53* (3), 191-222; (b) Mederos, A.; Dominguez, S.; Chinea, E.; Brito, F.; Midollini, S.; Vacca, A., Recent Aspects of the Coordination Chemistry of the Very Toxic Cation Beryllium(II): The Search for Sequestering Agents. *Boletin De La Sociedad Chilena De Quimica* **1997,** *42* (2), 281-295; (c) Schmidbaur, H., Recent Contributions to the Aqueous Coordination Chemistry of Beryllium. *Coordination Chemistry Reviews* **2001,** *215*, 223-241; (d) Tulinsky, A.; Worthington, C. R.; Pignataro, E., Basic Beryllium AcetateL: Part I.. The Collection of Intensity Data. *Acta Crystallographica* **1959,** *12* (9), 623-626.
35. (a) Alderighi, L.; Cecconi, F.; Ghilardi, C. A.; Mederos, A.; Midollini, S.; Orlandini, A.; Vacca, A., Complexes of Beryllium(II) with Substituted Malonates. Crystal Structure of $K_2[Be(C_4H_6(COO)_2)_2]\cdot 2H_2O$. *Polyhedron* **1999,** *18* (25), 3305-3312; (b) Duc, G.; Faure, R.; Loiseleur, H., Crystal-Structure of Potassium bis(malonate)beryllate hemihydrate: $K_2[Be(CO_2CH_2CO_2)_2\cdot(H_2O)_{1/2}$. *Acta Crystallographica Section B-Structural Science* **1978,** *34* (JUL), 2115-2118; (c) Schmidt, M.; Bauer, A.; Schier, A.; Schmidbaur, H., Complexation of Beryllium(II) by Maleic and Succinic Acid. *Zeitschrift Fur Naturforschung Section B-a Journal of Chemical Sciences* **1998,** *53* (7), 727-733; (d) Schmidt, M.; Bauer, A.; Schmidbaur, H., Beryllium Chelation by Dicarboxylic Acids in Aqueous Solution. *Inorganic Chemistry* **1997,** *36* (10), 2040-2043.
36. Plieger, P. G.; Ehler, D. S.; Duran, B. L.; Taylor, T. P.; John, K. D.; Keizer, T. S.; McCleskey, T. M.; Burrell, A. K.; Kampf, J. W.; Haase, T.; Rasmussen, P. G.; Karr, J., Novel Binding of Beryllium to Dicarboxyimidazole-Based Model Compounds and Polymers. *Inorganic Chemistry* **2005,** *44* (16), 5761-5769.
37. (a) Boldog, I.; Rusanov, E. B.; Chernega, A. N.; Sieler, J.; Domasevitch, K. V., Acentric Extended Solids by Self Assembly of 4,4'-Bipyrazolyls. *Angewandte Chemie-International Edition* **2001,** *40* (18), 3543-3546; (b) Burzlaff, H.; Lange, J.; Spengler, R.; Karayannis, M. I.; Veltsistas, P. G., Bis(hexadecylpyridinium) Bis(3,6-dichloro-4,5-dihydroxy-3,5-cyclohexadiene-1,2-dionato-κ_2O_4,O_5)beryllium. *Acta Crystallographica Section C-Crystal Structure Communications* **1995,** *51*, 190-193; (c) Stewart, J. M.; Morosin, B., Crystal and Molecular-Structure of Bis-(2,4-pentanedionato)beryllium. *Acta Crystallographica Section B-Structural Science* **1975,** *31* (APR15), 1164-1168; (d) Vreshch, V. D.; Chernega, A. N.; Howard, J. A. K.; Sieler, J.; Domasevitch, K. V., Two-step construction of molecular and polymeric mixed-metal Cu(Co)/Be complexes employing functionality of a pyridyl substituted acetylacetonate. *Dalton Transactions* **2003,** (9), 1707-1711.
38. (a) Cecconi, F.; Ghilardi, C. A.; Ienco, A.; Mariani, P.; Mealli, C.; Midollini, S.; Orlandini, A.; Vacca, A., Different Complexation Properties of Some Hydroxy Keto Heterocycles Toward Beryllium(II) in Aqueous Solutions: Experimental and Theoretical Studies. *Inorganic Chemistry* **2002,** *41* (15), 4006-4017; (b) Klufers, P.; Mayer, P.; Schuhmacher, J., Polyol-Metal-Complexes. XIII. $Na_2[Be(C_4H_6O_3)_2]\cdot 5H_2O$ and $Na_2[Pb(C_4H_6O_3)_2]\cdot 3H_2O$ - 2 Homoleptic Bis Polyolato Metallates with Beryllium and with Lead. *Zeitschrift Fur Anorganische Und Allgemeine Chemie* **1995,** *621* (8), 1373-1379.

39. (a) Schmidbaur, H.; Kumberger, O., Preparative, X-Ray, and NMR Studies of the Interaction of Beryllium with Salicylic Acid and *o*-Cresotic Acid: Crystal Structures of $(NH_4)_2[Be(C_6H_4OCO_2)_2]\cdot 2.25\ H_2O$ and $Na_3[Be(C_7H_6OCO_2)(OH)(CO_3)Be(C_7H_6OCO_2)]\cdot 8H_2O$. *Chemische Berichte-Recueil* **1993,** *126* (1), 3-9; (b) Schmidbaur, H.; Kumberger, O.; Riede, J., Beryllium salicylate dihydrate. *Inorganic Chemistry* **1991,** *30* (15), 3101-3103.
40. (a) Haddon, R. C.; Chichester, S. V.; Marshall, J. H., Electron Delocalization in 9-Oxidophenalenone Complexes of Boron and Beryllium. *Tetrahedron* **1986,** *42* (22), 6293-6300; (b) Kumberger, O.; Riede, J.; Schmidbaur, H., Preparation and Crystal Structure of $Na_2[Be(o\text{-}C_6H_4O_2)_2]\cdot 5H_2O$. *Chemische Berichte-Recueil* **1992,** *125* (12), 2701-2703.
41. (a) Cecconi, F.; Dominguez, S.; Masciocchi, N.; Midollini, S.; Sironi, A.; Vacca, A., Complexation of Beryllium(II) Ion by Phosphinate Ligands in Aqueous Solution. Synthesis and XRPD Structure Determination of $Be[(PhPO_2)_2CH_2](H_2O)_2$. *Inorganic Chemistry* **2003,** *42* (7), 2350-2356; (b) Cecconi, F.; Ghilardi, C. A.; Midollini, S.; Orlandini, A., Beryllium complexes with mono- and tripodal- phosphinoxide ligands. X-ray crystal structure of $[\{N(CH_2PPh_2O)_3\}Be(OH_2)](ClO_4)_2$. *Inorganic Chemistry Communications* **2000,** *3* (7), 350-353.
42. Irving, R. J.; da Silva, M. A. V. R., Thermochemistry of Beryllium [small beta]-diketonates and Be-O Bond Energies. *Journal of the Chemical Society, Dalton Transactions* **1977,** (5), 413-417.
43. Gottfriedsen, J.; Blaurock, S., [*p*-^{t}Bu-calix[4](OMe)$_2$(OBeCl)$_2$]: The First Structually Characterized Beryllium Calixarene Complex. *Zeitschrift Fur Anorganische Und Allgemeine Chemie* **2005,** *631* (15), 3037-3039.
44. Piispanen, J.; Lajunen, L. H. J., Complex Formation Equilibria of Some Aliphatic α-Hydroxycarboxylic Acids .3. A Study of Beryllium(II) Complexes. *Acta Chemica Scandinavica* **1996,** *50* (12), 1074-1080.
45. Chinea, E.; Dominguez, S.; Mederos, A.; Brito, F.; Arrieta, J. M.; Sanchez, A.; Germain, G., Nitrilotripropionic Acid (NTP) and Other Polyamino Carboxylic Acids as Sequestering Agents for Beryllium(II). X-ray Crystal-Structure of Sodium (nitrilotripropionato)beryllate(II) Trihydrate, $Na[Be(NTP)]\cdot 3H_2O$. *Inorganic Chemistry* **1995,** *34* (6), 1579-1587.
46. Diao, K.; Wang, H.; Qiu, Z., A DFT Study on the Metal Binding Selectivity of 12-Crown-4 and its Heterocyclic Analogs. *Journal of Molecular Structure-Theochem* **2009,** *901* (1-3), 157-162.
47. Cecconi, F.; Chinea, E.; Ghilardi, C. A.; Midollini, S.; Orlandini, A., Complexes of salicylaldehyde and related ligands with beryllium(II) ion. X-ray crystal structures of bis(*N*-isopropylsalicylaldiminato) beryllium(II) and bis(*N*-phenylsalicylaldiminato)beryllium(II). *Inorganica Chimica Acta* **1997,** *260* (1), 77-82.
48. Onyekachi, R. An Investigation of Beryllium Coordination Chemistry Using Electrospray Ionisation Mass Spectrometry. PhD Thesis, University of Waikato, **2018**.
49. (a) Li, Y. Q.; Liu, Y.; Bu, W. M.; Lu, D.; Wu, Y.; Wang, Y., Hydroxyphenyl-pyridine Beryllium Complex ($Bepp_2$) as a Blue Electroluminescent Material. *Chemistry of Materials* **2000,** *12* (9), 2672-2675; (b) Tong, Y. P.; Zheng, S. L.; Chen, X. M., Syntheses, Structures, Photoluminescence, and Theoretical Studies of a Class of Beryllium(II) Compounds of Aromatic N,O-Chelate Ligands. *Inorganic Chemistry* **2005,** *44* (12), 4270-4275.
50. Fisher, B.; Packard, B. S.; Read, E. J.; Carrasquillo, J. A.; Carter, C. S.; Topalian, S. L.; Yang, J. C.; Yolles, P.; Larson, S. M.; Rosenberg, S. A., Tumor localization of adoptively transferred indium-111 labeled tumor infiltrating lymphocytes in patients with metastatic melanoma. *Journal of Clinical Oncology* **1989,** *7* (2), 250-261.

51. Vanniekerk, J. C.; Irving, H.; Nassimbeni, L. R., Crystal-Structure of Bis(2-methyl-8-hydroxyquinolinato)beryllium(II) Dihydrate. *South African Journal of Chemistry* **1979,** *32* (3), 85-88.
52. Shaffer, K. J. Towards Selective Small Cation Chelation. PhD Thesis, Massey University, **2011**.
53. (a) Fleischer, R.; Stalke, D., Syntheses and Structures of $[(THF)_nM\{(NSiMe_3)_2PPh_2\}_2]$ Complexes (M=Be, Mg, Ca, Sr, Ba; *n* =0-2): Deviation of Alkaline Earth Metal Cations from the Plane of an Anionic Ligand. *Inorganic Chemistry* **1997,** *36* (11), 2413-2419; (b) Niemeyer, M.; Power, P. P., Synthesis, ^{9}Be NMR Spectroscopy, and Structural Characterization of Sterically Encumbered Beryllium Compounds. *Inorganic Chemistry* **1997,** *36* (21), 4688-4696.
54. Thiele, K. H.; Lorenz, V.; Thiele, G.; Zonnchen, P.; Scholz, J., $[Be(dad)_2]$: Synthesis and Structure of a Diazabutadieneberyllium Complex. *Angewandte Chemie-International Edition in English* **1994,** *33* (13), 1372-1373.
55. Liu, S. F.; Wu, Q. G.; Schmider, H. L.; Aziz, H.; Hu, N. X.; Popovic, Z.; Wang, S. N., Syntheses, Structures, and Electroluminescence of New Blue/Green Luminescent Chelate Compounds: $Zn(2\text{-py-in})_2(THF)$, $BPh_2(2\text{-py-in})$, $Be(2\text{-py-in})_2$, and $BPh_2(2\text{-py-aza})$ [2-py-in = 2-(2-pyridyl)indole; 2-py-aza = 2-(2-pyridyl)-7-azaindole]. *Journal of the American Chemical Society* **2000,** *122* (15), 3671-3678.
56. Kubiak, R.; Waskowska, A.; Sledz, M.; Jezierski, A., Synthesis, X-ray structures and characterization of beryllium phthalocyanine and (2-ethoxyethanol)-aqua-beryllium phthalocyanine. *Inorganica Chimica Acta* **2006,** *359* (5), 1344-1350.
57. (a) Alder, R. W.; Bowman, P. S.; Steele, W. R. S.; Winterma, D., Remarkable Basicity of 1,8-Bis(dimethylamino)naphthalene. *Chemical Communications* **1968,** *0* (13), 723-724; (b) Raab, V.; Gauchenova, E.; Merkoulov, A.; Harms, K.; Sundermeyer, J.; Kovacevic, B.; Maksic, Z. B., 1,8-Bis(hexamethyltriaminophosphazenyl)naphthalene, HMPN: A Superbasic Bisphosphazene "Proton Sponge". *Journal of the American Chemical Society* **2005,** *127* (45), 15738-15743; (c) Raab, V.; Harms, M.; Sundermeyer, J.; Kovacevic, B.; Maksic, Z. B., 1,8-Bis(dimethylethyleneguanidino)naphthalene: Tailoring the Basicity of Bisguanidine "Proton Sponges" by Experiment and Theory. *Journal of Organic Chemistry* **2003,** *68* (23), 8790-8797; (d) Raab, V.; Kipke, J.; Gschwind, R. M.; Sundermeyer, J., 1,8-Bis(tetramethylguanidino)naphthalene (TMGN): A New, Superbasic and Kinetically Active "Proton Sponge". *Chemistry-a European Journal* **2002,** *8* (7), 1682-1693; (e) Saupe, T.; Krieger, C.; Staab, H. A., 4,5-Bis(dimethylamino)phenanthrene and 4,5-Bis(dimethylamino)-9,10-dihydrophenanthrene: Syntheses and "Proton Sponge" Properties. *Angewandte Chemie-International Edition in English* **1986,** *25* (5), 451-453; (f) Staab, H. A.; Saupe, T.; Krieger, C., 4,5-Bis(dimethylamino)fluorene, a New Proton Sponge. *Angewandte Chemie-International Edition in English* **1983,** *22* (9), 731-732; (g) Zirnstein, M. A.; Staab, H. A., Quino[7,8-*h*]quinoline, a New Type of "Proton Sponge". *Angewandte Chemie-International Edition in English* **1987,** *26* (5), 460-461.
58. Szemik-Hojniak, A.; Rettig, W.; Deperasinska, I., The Forbidden Emission of Protonated Proton Sponge. *Chemical Physics Letters* **2001,** *343* (3-4), 404-412.
59. Shaffer, K. J.; McLean, T. M.; Waterland, M. R.; Wenzel, M.; Plieger, P. G., Structural characterisation of difluoro-boron chelates of quino[7,8-h]quinoline. *Inorganica Chimica Acta* **2012,** *380*, 278-283.
60. 2000-2016: 1559 articles on beryllium chemistry, of which 1040 involve computational methods (Web of Science 7/4/2016).
61. (a) Duley, S.; Goyal, P.; Giri, S.; Chattaraj, P. K., Bonding, Reactivity and Aromaticity in Some Beryllocene Derivatives. *Croatica Chemica Acta* **2009,** *82* (1), 193-205; (b) Velazquez, A.; Fernandez, I.; Frenking, G.; Merino, G., Multimetallocenes. A Theoretical Study. *Organometallics* **2007,** *26* (19), 4731-4736.

62. (a) Wang, Q. Y.; Tong, Y. C.; Xu, X. J., A theoretical study of the binding mechanisms of atomic platinum on Be^-, B^-, N^-, O^-Doped (6,6) single-walled carbon nanotubes. *Structural Chemistry* **2015,** *26* (3), 815-822; (b) Durgun, E.; Jang, Y. R.; Ciraci, S., Hydrogen Storage Capacity of Ti-Doped Boron-Nitride and B/Be-Substituted Carbon Nanotubes. *Physical Review B* **2007,** *76* (7).
63. (a) Borocci, S.; Bronzolino, N.; Grandinetti, F., From OBeHe to $H_3BOBeHe$: Enhancing the stability of a neutral helium compound. *Chemical Physics Letters* **2005,** *406* (1-3), 179-183; (b) Pan, S.; Saha, R.; Chattaraj, P. K., On the stability of noble gas bound 1-tris(pyrazolyl)borate beryllium and magnesium complexes. *New Journal of Chemistry* **2015,** *39* (9), 6778-6786.
64. (a) Sulka, M.; Pitonak, M.; Cernusak, I.; Urban, M.; Neogrady, P., Ab initio study of many-body decomposition of the interaction energy in small beryllium clusters Be_{3-6}. *Chemical Physics Letters* **2013,** *573*, 8-14; (b) Brito, B. G. A.; Hai, G. Q.; Candido, L., Correlation effects on aromaticity of Be_3^{2-} Cluster: A quantum Monte Carlo study. *Chemical Physics Letters* **2013,** *586*, 108-110.
65. (a) Yanez, M.; Mo, O.; Alkorta, I.; Elguero, J., Can Conventional Bases and Unsaturated Hydrocarbons Be Converted into Gas-Phase Superacids That Are Stronger than Most of the Known Oxyacids? The Role of Beryllium Bonds. *Chemistry-a European Journal* **2013,** *19* (35), 11637-11643; (b) Brea, O.; Mo, O.; Yanez, M.; Alkorta, I.; Elguero, J., Creating σ-Holes through the Formation of Beryllium Bonds. *Chemistry-a European Journal* **2015,** *21* (36), 12676-12682.
66. (a) Leroy, C.; Schuster, J. K.; Schaefer, T.; Müller-Buschbaum, K.; Braunschweig, H.; Bryce, D. L., Linear Dicoordinate Beryllium: a ^{9}Be Solid-State NMR Study of a Discrete Zero-Valent s-block Beryllium Complex. *Canadian Journal of Chemistry* **2018**; (b) Plieger, P. G.; John, K. D.; Keizer, T. S.; McCleskey, T. M.; Burrell, A. K.; Martint, R. L., Predicting ^{9}Be Nuclear Magnetic Resonance Chemical Shielding Tensors Utilizing Density Functional Theory. *Journal of the American Chemical Society* **2004,** *126* (44), 14651-14658; (c) Shaffer, K. J.; Davidson, R. J.; Burrell, A. K.; McCleskey, M. T.; Plieger, P. G., Encapsulation of the Be^{II} Cation: Spectroscopic and Computational Study. *Inorganic Chemistry* **2013,** *52* (7), 3969-3975.
67. (a) Scott, B. L.; McCleskey, T. M.; Chaudhary, A.; Hong-Geller, E.; Gnanakaran, S., The Bioinorganic Chemistry and Associated Immunology of Chronic Beryllium Disease. *Chemical Communications* **2008,** (25), 2837-2847; (b) Scott, B. L.; Wang, Z. L.; Marrone, B. L.; Sauer, N. N., Potential Binding Modes of Beryllium with the Class II Major Histocompatibility Complex HLA-DP: A Combined Theoretical and Structural Database Study. *Journal of Inorganic Biochemistry* **2003,** *94* (1-2), 5-13; (c) Petukh, M.; Wu, B. H.; Stefl, S.; Smith, N.; Hyde-Volpe, D.; Wang, L.; Alexov, E., Chronic Beryllium Disease: Revealing the Role of Beryllium Ion and Small Peptides Binding to HLA-DP2. *Plos One* **2014,** *9* (11); (d) Silveira, L. J.; McCanlies, E. C.; Fingerlin, T. E.; Van Dyke, M. V.; Mroz, M. M.; Strand, M.; Fontenot, A. P.; Bowerman, N.; Dabelea, D. M.; Schuler, C. R.; Weston, A.; Maier, L. A., Chronic Beryllium Disease, HLA-DPB1, and the DP Peptide Binding Groove. *Journal of Immunology* **2012,** *189* (8), 4014-4023.
68. (a) Cukrowski, I.; Mangondo, P., Interacting Quantum Fragments-Rooted Preorganized-Interacting Fragments Attributed Relative Molecular Stability of the Be^{II} Complexes of Nitrilotriacetic Acid and Nitrilotri-3-propionic Acid. *Journal of Computational Chemistry* **2016,** *37* (15), 1373-1387; (b) Pavlov, M.; Siegbahn, P. E. M.; Sandstrom, M., Hydration of Beryllium, Magnesium, Calcium, and Zinc Ions Using Density Functional Theory. *Journal of Physical Chemistry A* **1998,** *102* (1), 219-228; (c) Vyas, N.; Ojha, A. K., A Study on Interaction of Be^{++}, Mg^{++} and Ca^{++} with Phenylalanine: Binding Energies, Metal Ion Affinities and IR Signature of Complex Stability. *Vibrational Spectroscopy* **2011,** *56* (1), 42-50.
69. Ding, J.; Lin, L.; Hang, W.; Yan, X. M., Beryllium uptake and related biological effects studied in THP-1 differentiated macrophages. *Metallomics* **2009,** *1* (6), 471-478.

70. McCleskey, T. M.; Ehler, D. S.; Keizer, T. S.; Asthagiri, D. N.; Pratt, L. R.; Michalczyk, R.; Scott, B. L., Beryllium Displacement of H^+ from Strong Hydrogen Bonds. *Angewandte Chemie-International Edition* **2007,** *46* (15), 2669-2671.
71. (a) Bowerman, N. A.; Falta, M. T.; Mack, D. G.; Kappler, J. W.; Fontenot, A. P., Mutagenesis of Beryllium-Specific TCRs Suggests an Unusual Binding Topology for Antigen Recognition. *Journal of Immunology* **2011,** *187* (7), 3694-3703; (b) Fontenot, A. P.; Keizer, T. S.; McCleskey, M.; Mack, D. G.; Meza-Romero, R.; Huan, J. Y.; Edwards, D. M.; Chou, Y. K.; Vandenbark, A. A.; Scott, B.; Burrows, G. G., Recombinant HLA-DP2 Binds Beryllium and Tolerizes Beryllium-Specific Pathogenic $CD4^+$ T Cells. *Journal of Immunology* **2006,** *177* (6), 3874-3883; (c) Bill, J. R.; Mack, D. G.; Falta, M. T.; Maier, L. A.; Sullivan, A. K.; Joslin, F. G.; Martin, A. K.; Freed, B. M.; Kotzin, B. L.; Fontenot, A. P., Beryllium Presentation to $CD4^+$ T Cells is Dependent on a Single Amino Acid Residue of the MHC Class II β-Chain. *Journal of Immunology* **2005,** *175* (10), 7029-7037.
72. Xie, Y. M.; Schaefer, H. F.; Jemmis, E. D., Characteristics of novel sandwiched beryllium, magnesium, and calcium dimers: $C_5H_5BeBeC_5H_5$, $C_5H_5MgMgC_5H_5$, and $C_5H_5CaCaC_5H_5$. *Chemical Physics Letters* **2005,** *402* (4-6), 414-421.
73. Cukrowski, I.; Mangondo, P., Interacting Quantum Fragments-Rooted Preorganized-Interacting Fragments Attributed Relative Molecular Stability of the Be-II Complexes of Nitrilotriacetic Acid and Nitrilotri-3-propionic Acid. *Journal of Computational Chemistry* **2016,** *37* (15), 1373-1387.
74. Aaseth, J.; Crisponi, G.; Anderson, O., *Chelation Therapy in the Treatment of Metal Intoxication*. Elsevier Science: San Diego, United States, **2016**; p 388.
75. Agency for Toxic Substances and Disease Registry. Medical Management Guidelines for Blister Agents: Lewisite (L) and Mustard-Lewisite Mixture (HL). https://www.atsdr.cdc.gov (accessed Jan 29, 2018).
76. Basinger, M. A.; Johnson, J. E.; Burka, L. T.; Jones, M. M., Antidotes for Acute Beryllium Sulfate Intoxication in Mice. *Research Communications in Chemical Pathology and Pharmacology* **1982,** *36* (3), 519-522.
77. (a) Mathur, S.; Flora, S. J. S.; Mathur, R.; Kannan, G. M.; Gupta, S. D., Beryllium-Induced Biochemical-Alterations and their Prevention Following Coadministration of Meso-2,3-Dimercaptosuccinic Acid or 2,3-Dimercaptopropane Sulfonate in Rats. *Journal of Applied Toxicology* **1994,** *14* (4), 263-267; (b) Mathur, S.; Flora, S. J. S.; Mathur, R.; Gupta, S. D., Mobilization and Distribution of Beryllium over the Course of Chelation-Therapy with Some Polyaminocarboxylic Acids in the Rat. *Human & Experimental Toxicology* **1993,** *12* (1), 19-24.
78. (a) Johri, S.; Shrivastava, S.; Sharma, P.; Shukla, S., Analysis of Time-Dependent Recovery from Beryllium Toxicity Following Chelation Therapy and Antioxidant Supplementation. *Indian Journal of Experimental Biology* **2004,** *42* (8), 798-802; (b) Sharma, P.; Johri, S.; Shukla, S., Beryllium-Induced toxicity and its Prevention by Treatment with Chelating Agents. *Journal of Applied Toxicology* **2000,** *20* (4), 313-318.
79. Nirala, S. K.; Bhadauria, M.; Mathur, R.; Mathur, A., Amelioration of beryllium induced alterations in hepatorenal biochemistry and ultramorphology by co-administration of tiferron and adjuvants. *Journal of Biomedical Science* **2007,** *14* (3), 331-345.
80. Cash, R.; Shapiro, R. I.; Levy, S. H.; Hopkins, S. M., Chelating Agents in the Therapy of Beryllium Poisoning. *New England Journal of Medicine* **1959,** *260* (14), 683-686.
81. Matsumiya, H.; Hoshino, H.; Yotsuyanagi, T., A novel fluorescence reagent, 10-hydroxybenzo[*h*]quinoline-7-sulfonate, for selective determination of beryllium(II) ion at pg cm^{-3} levels. *Analyst* **2001,** *126* (11), 2082-2086.
82. Agrawal, A.; Cronin, J.; Tonazzi, J.; McCleskey, T. M.; Ehler, D. S.; Minogue, E. M.; Whitney, G.; Brink, C.; Burrell, A. K.; Warner, B.; Goldcamp, M. J.; Schlecht, P. C.; Sonthalia, P.; Ashley, K., Validation of a Standardized Portable Fluorescence

Method for Determining Trace Beryllium in Workplace Air and Wipe Samples. *Journal of Environmental Monitoring* **2006,** *8* (6), 619-624.
83. Adams, L.; Agrawal, A.; Cronin, J. P.; Ashley, K., Optical Molecular Fluorescence Determination of Ultra-Trace Beryllium in Occupational and Environmental Samples Using Highly Alkaline Conditions. *International Journal of Environmental Analytical Chemistry* **2017,** *97* (3), 264-275.
84. Plieger, P. G.; John, K. D.; Burrell, A. K., Encapsulating beryllium - Synthesis, characterisation and modelling of a chiral binaphthyldlimine-Be(II) complex. *Polyhedron* **2007,** *26* (2), 472-478.
85. Stoessel, P.; Joosten, D.; Breuning, E. Electronic Device Containing Metal Complexes. WO2011066898, **2010**.
86. Cram, D. J.; Cram, J. M., *Container Molecules and Their Guests*. Royal Society of Chemistry: Thomas Graham House, United Kingdom, **1997**; p 223.
87. (a) Healy, M. R.; Roebuck, J. W.; Doidge, E. D.; Emeleus, L. C.; Bailey, P. J.; Campbell, J.; Fischmann, A. J.; Love, J. B.; Morrison, C. A.; Sassi, T.; White, D. J.; Tasker, P. A., Contributions of Inner and Outer Coordination Sphere Bonding in Determining the Strength of Substituted Phenolic Pyrazoles as Copper Extractants. *Dalton Transactions* **2016,** *45* (7), 3055-3062; (b) Forgan, R. S.; Roach, B. D.; Wood, P. A.; White, F. J.; Campbell, J.; Henderson, D. K.; Kamenetzky, E.; McAllister, F. E.; Parsons, S.; Pidcock, E.; Richardson, P.; Swart, R. M.; Tasker, P. A., Using the Outer Coordination Sphere to Tune the Strength of Metal Extractants. *Inorganic Chemistry* **2011,** *50* (10), 4515-4522.
88. (a) Ali, S. K. M.; Maity, D. K.; De, S.; Shenoi, M. R. K., Ligands for Selective Metal Ion Extraction: A Molecular Modeling Approach. *Desalination* **2008,** *232* (1-3), 181-190; (b) Carson, I.; MacRuary, K. J.; Doidge, E. D.; Ellis, R. J.; Grant, R. A.; Gordon, R. J.; Love, J. B.; Morrison, C. A.; Nichol, G. S.; Tasker, P. A.; Wilson, A. M., Anion Receptor Design: Exploiting Outer-Sphere Coordination Chemistry To Obtain High Selectivity for Chloridometalates over Chloride. *Inorganic Chemistry* **2015,** *54* (17), 8685-8692.
89. Boys, S. F.; Bernardi, F., Calculation of Small Molecular Interactions by Differences of Separate Total Energies - Some Procedures with Reduced Errors. *Molecular Physics* **1970,** *19* (4), 553-566.
90. Frisch, M. J.; Trucks, G. W.; Schlegel, H. B.; Scuseria, G. E.; Robb, M. A.; Cheeseman, J. R.; Scalmani, G.; Barone, V.; Mennucci, B.; Petersson, G. A.; Nakatsuji, H.; Caricato, M.; Li, X.; Hratchian, H. P.; Izmaylov, A. F.; Bloino, J.; Zheng, G.; Sonnenberg, J. L.; Hada, M.; Ehara, M.; Toyota, K.; Fukuda, R.; Hasegawa, J.; Ishida, M.; Nakajima, T.; Honda, Y.; Kitao, O.; Nakai, H.; Vreven, T.; Montgomery, J., J. A.; Peralta, J. E.; Ogliaro, F.; Bearpark, M.; Heyd, J. J.; Brothers, E.; Kudin, K. N.; Staroverov, V. N.; Keith, T.; Kobayashi, R.; Normand, J.; Raghavachari, K.; Rendell, A.; Burant, J. C.; Iyengar, S. S.; Tomasi, J.; Cossi, M.; Rega, N.; Millam, J. M.; Klene, M.; Knox, J. E.; Cross, J. B.; Bakken, V.; Adamo, C.; Jaramillo, J.; Gomperts, R.; Stratmann, R. E.; Yazyev, O.; Austin, A. J.; Cammi, R.; Pomelli, C.; Ochterski, J. W.; Martin, R. L.; Morokuma, K.; Zakrzewski, V. G.; Voth, G. A.; Salvador, P.; Dannenberg, J. J.; Dapprich, S.; Daniels, A. D.; Farkas, O.; Foresman, J. B.; Ortiz, J. V.; Cioslowski, J.; Fox, D. J. *Gaussian 09, Revision D.01*, Gaussian, Inc.: Wallingford CT, **2013**.
91. Dennington, R.; Keith, T. A.; Millam, J. M. *Gauss View, Version 5*, Semichem Inc.: Shawnee Mission, KS, **2009**.
92. Andrienko, G. A. *ChemCraft. V. 1.8 (Build 536b)*, **2016**.
93. (a) Yang, L.; Powell, D. R.; Houser, R. P., Structural variation in copper(I) complexes with pyridylmethylamide ligands: structural analysis with a new four-coordinate geometry index, τ_4. *Dalton Transactions* **2007,** (9), 955-964; (b) Okuniewski, A.; Rosiak, D.; Chojnacki, J.; Becker, B., Coordination polymers and molecular structures among complexes of mercury(II) halides with selected 1-benzoylthioureas. *Polyhedron* **2015,** *90*, 47-57.

94. (a) Becke, A. D., Density-Functional Thermochemistry .3. The Role of Exact Exchange. *Journal of Chemical Physics* **1993,** *98* (7), 5648-5652; (b) Lee, C. T.; Yang, W. T.; Parr, R. G., Development of the Colle-Salvetti Correlation-Energy Formula into a Functional of the Electron-Density. *Physical Review B* **1988,** *37* (2), 785-789; (c) Vosko, S. H.; Wilk, L.; Nusair, M., Accurate Spin-Dependent Electron Liquid Correlation Energies for Local Spin-Density Calculations - a Critical Analysis. *Canadian Journal of Physics* **1980,** *58* (8), 1200-1211; (d) Stephens, P. J.; Devlin, F. J.; Chabalowski, C. F.; Frisch, M. J., Ab-Initio Calculation of Vibrational Absorption and Circular-Dichroism Spectra Using Density-Functional Force-Fields. *Journal of Physical Chemistry* **1994,** *98* (45), 11623-11627.
95. Bucher, G., DFT Calculations on a New Class of C_3-Symmetric Organic Bases: Highly Basic Proton Sponges and Ligands for Very Small Metal Cations. *Angewandte Chemie-International Edition* **2003,** *42* (34), 4039-4042.
96. (a) Kruse, H.; Goerigk, L.; Grimme, S., Why the Standard B3LYP/6-31G*Model Chemistry Should Not Be Used in DFT Calculations of Molecular Thermochemistry: Understanding and Correcting the Problem. *Journal of Organic Chemistry* **2012,** *77* (23), 10824-10834; (b) Lima, F. C. A.; Viana, R. B.; Carneiro, J. W. M.; Comar, M.; da Silva, A. B. F., Coordination Ability of Polyether and Polyamine Ligands: A Density Functional Theory Study of First- and Second-Row Transition Metals. *Journal of Computational and Theoretical Nanoscience* **2013,** *10* (9), 2034-2040; (c) Liu, J. H.; Xia, X. L.; Li, Y.; Wang, H. J.; Li, Z. Y., Theoretical Study on the Interaction of Glutathione with group IA (Li^+, Na^+, K^+), IIA (Be^{2+}, Mg^{2+}, Ca^{2+}), and IIIA (Al^{3+}) Metal Cations. *Structural Chemistry* **2013,** *24* (1), 251-261; (d) Makrlik, E.; Toman, P.; Vanura, P., Complexation of the Ammonium Cation with Dibenzo-18-crown-6: Extraction and DFT Study. *Acta Chimica Slovenica* **2013,** *60* (1), 193-197; (e) Makrlik, E.; Vanura, P.; Bohm, S.; Ruzza, P., Experimental and Theoretical Study on Interaction of the Potassium Cation with Antamanide. *Chemical Physics* **2014,** *433*, 85-88; (f) Mandal, S.; Das, G.; Askari, H., Interactions of *N*-acetyl-l-cysteine with Metals (Ni^{2+}, Cu^{2+} and Zn^{2+}): an Experimental and Theoretical Study. *Structural Chemistry* **2014,** *25* (1), 43-51; (g) Myradalyyev, S.; Limpanuparb, T.; Wang, X. Q.; Hirao, H., Comparative Computational Analysis of Binding Energies Between Several Divalent Frst-Row Transition Metals (Cr_2^+, Mn_2^+, Fe_2^+, Co_2^+, Ni_2^+, and Cu_2^+) and Ligands (Porphine, Corrin, and TMC). *Polyhedron* **2013,** *52*, 96-101.
97. Perera, L. C. The Good Without the Bad: Selective Chelators for Beryllium Encapsulation. PhD Thesis, University of Auckland, **2017**.
98. Mederos, A.; Dominguez, S.; Medina, A. M.; Brito, F.; Chinea, E.; Bazdikian, K., Equilibria in aqueous solution between Be(II) and nitrilotriacetic, methyl-*C*-nitrilotriacetic, nitrilodiaceticpropionic, nitriloaceticdipropionic and nitrilotripropionic acids. *Polyhedron* **1987,** *6* (6), 1365-1373.
99. Goerigk, L.; Grimme, S., A thorough benchmark of density functional methods for general main group thermochemistry, kinetics, and noncovalent interactions. *Physical Chemistry Chemical Physics* **2011,** *13* (14), 6670-6688.
100. Bardwell, D. A.; Jeffery, J. C.; Ward, M. D., Coordination Chemistry of Mixed Pyridine-Phenol Ligands - Polynuclear Complexes of 6-(2-Hydroxyphenyl)-2,2'-Bipyridine with Ni^{II}, Cd^{II}, Mn^{II} and $Mn^{II}Mn^{III}$. *Journal of the Chemical Society-Dalton Transactions* **1995,** (18), 3071-3080.
101. Hattori, Y.; Ogaki, T.; Ishimura, M.; Ohta, Y.; Kirihata, M., Development and Elucidation of a Novel Fluorescent Boron-Sensor for the Analysis of Boronic Acid-Containing Compounds. *Sensors* **2017,** *17* (10).
102. Fard, M. A.; Behnia, A.; Puddephatt, R. J., Platinum(II) complexes of pyridine–amine ligands with phenol substituents: isotactic supramolecular polymers. *Canadian Journal of Chemistry* **2018,** *97* (3), 238-243.
103. Desimoni, G.; Faita, G.; Quadrelli, P., Pyridine-2,6-bis(oxazolines), helpful ligands for asymmetric catalysts. *Chemical Reviews* **2003,** *103* (8), 3119-3154.

104. (a) Kelly, J. Scientific Methadologies Applied to Cultural Heritage, Inc. http://www.smatch-international.org/structure.htm; (b) Fulp, A. B.; Seconi, D.; Spear, K. L.; Wang, X. Polycyclic pyridines as potassium ion channel modulators. WO2005100340A3, **2004**; (c) Toshihiro, I.; Seiji, I. Organic electroluminescent devices and metal complex compounds WO2004108857A1, **2007**; (d) Sahu, S.; Widger, L. R.; Quesne, M. G.; de Visser, S. P.; Matsumura, H.; Moenne-Loccoz, P.; Siegler, M. A.; Goldberg, D. P., Secondary Coordination Sphere Influence on the Reactivity of Nonheme Iron(II) Complexes: An Experimental and DFT Approach. *Journal of the American Chemical Society* **2013,** *135* (29), 10590-10593.
105. Knight, J. C.; Amoroso, A. J.; Edwards, P. G.; Singh, N.; Ward, B. D., Shaping and enforcing coordination spheres: probing the ability of tripodal ligands to favour trigonal prismatic geometry. *Dalton Transactions* **2016,** *45* (26), 10630-10642.
106. Gass, I. A.; Gartshore, C. J.; Lupton, D. W.; Moubaraki, B.; Nafady, A.; Bond, A. M.; Boas, J. F.; Cashion, J. D.; Milsmann, C.; Wieghard, K.; Murray, K. S., Anion Dependent Redox Changes in Iron Bis-terdentate Nitroxide {NNO} Chelates. *Inorganic Chemistry* **2011,** *50* (7), 3052-3064.
107. Yasuda, M.; Onishi, Y.; Ueba, M.; Miyai, T.; Baba, A., Direct reduction of alcohols: Highly chemoselective reducing system for secondary or tertiary alcohols using chlorodiphenylsilane with a catalytic amount of indium trichloride. *Journal of Organic Chemistry* **2001,** *66* (23), 7741-7744.
108. Dai, W. P.; Xiao, J.; Jin, G. Y.; Wu, J. J.; Cao, S., Palladium- and Nickel-Catalyzed Kumada Cross-Coupling Reactions of gem-Difluoroalkenes and Monofluoroalkenes with Grignard Reagents. *Journal of Organic Chemistry* **2014,** *79* (21), 10537-10546.
109. Haetzelt, A.; Nordskog, A.; Erpenbach, S.; Sundermeyer, J.; Gaertner, F. Washing or cleaning agent with optionally in situ produced transition metal complex. DE102009047037A1, **2011**.
110. Golden, J. H.; Facendola, J. W.; Sylvinson, M. R. D.; Baez, C. Q.; Djurovich, P. I.; Thompson, M. E., Boron Dipyridylmethene (DIPYR) Dyes: Shedding Light on Pyridine-Based Chromophores. *Journal of Organic Chemistry* **2017,** *82* (14), 7215-7222.
111. (a) Dyker, G.; Muth, O., Synthesis of methylene- and methine-bridged oligopyridines. *European Journal of Organic Chemistry* **2004,** (21), 4319-4322; (b) Sumby, C. J., Ruthenium(II) Complexes of New Chelating Indolizino [2,3-b] pyrazine- and Indolizino[2,3-b] quinoxaline-Derived Ligands: Syntheses, Electrochemistry and Absorption Spectroscopy. *Australian Journal of Chemistry* **2008,** *61* (11), 894-904; (c) Hagel, M.; Liu, J. H.; Muth, O.; Rivera, H. J. E.; Schwake, E.; Sripanom, L.; Henkel, G.; Dyker, G., p-quinoid compounds by nucleophilic aromatic substitution with hydride as leaving group. *European Journal of Organic Chemistry* **2007,** (21), 3573-3582; (d) Ye, M. C.; Zhou, J.; Tang, Y., Trisoxazoline/Cu(II)-promoted Kinugasa reaction. Enantioselective synthesis of beta-lactams. *Journal of Organic Chemistry* **2006,** *71* (9), 3576-3582.
112. Vedernikov, A. N.; Fettinger, J. C.; Mohr, F., Synthesis and reactivity of dimethyl platinum(IV) hydrides in water. *Journal of the American Chemical Society* **2004,** *126* (36), 11160-11161.
113. Shaibu, B. S.; Kawade, R. K.; Liu, R. S., Regioselective synthesis of 2-(2-hydroxyaryl)pyridines from the reactions of benzynes with pyridine N-oxides. *Organic & Biomolecular Chemistry* **2012,** *10* (34), 6834-6839.
114. (a) Reglinski, J.; Kennedy, A. R.; Steel, G., Tetradentate Schiff base beryllium complexes. *New Journal of Chemistry* **2015,** *39* (4), 2437-2439; (b) Chinea, E.; Dominguez, S.; Mederos, A.; Brito, F.; Arrieta, J. M.; Sanchez, A.; Germain, G., Nitrilotripropionic Acid (Ntp) and Other Polyamino Carboxylic-Acids as Sequestering Agents for Beryllium(Ii) - X-Ray Crystal-Structure of Sodium (Nitrilotripropionato)Beryllate(Ii) Trihydrate, Na[Be(Ntp)]Center-Dot-3h(2)O. *Inorganic Chemistry* **1995,** *34* (6), 1579-1587.

115. (a) Guo, S.; Liang, X. X.; Xia, M. J.; Liu, L. J.; Fang, Z.; Huang, Q.; Wu, R. F.; Wang, X. Y.; Lin, Z. S.; Chen, C. T., Structural Design of Two Fluorine-Beryllium Borates BaMBe2(BO3)(2)F-2 (M = Mg, Ca) Containing Flexible Two-Dimensional [Be3B3O6F3], Single Layers without Structural Instability Problems. *Inorganic Chemistry* **2017,** *56* (19), 11451-11454; (b) Guo, S.; Liang, F.; Liu, L. J.; Xia, M. J.; Fang, Z.; Wu, R. F.; Wang, X. Y.; Lin, Z. S.; Chen, C. T., LiSr3Be3B3O9F4: a new ultraviolet nonlinear optical crystal for fourth-harmonic generation of Nd:YAG lasers. *New Journal of Chemistry* **2017,** *41* (11), 4269-4272; (c) Yan, X.; Luo, S. Y.; Lin, Z. S.; Yue, Y. C.; Wang, X. Y.; Liu, L. J.; Chen, C. T., LaBeB3O7: a new phase-matchable nonlinear optical crystal exclusively containing the tetrahedral XO4 (X = B and Be) anionic groups. *Journal of Materials Chemistry C* **2013,** *1* (22), 3616-3622; (d) Li, H. M.; Ju, J.; Lin, J. H., Synthesis and crystal structure of layered beryllium polyborate H2BeB4O8. *Chinese Journal of Inorganic Chemistry* **2002,** *18* (8), 764-768.

116. Diyabalanage, H. V. K.; Ganguly, K.; Ehler, D. S.; Collis, G. E.; Scott, B. L.; Chaudhary, A.; Burrell, A. K.; McCleskey, T. M., Three-coordinate ligand for physiological beryllium imaging by fluoreseuce. *Angewandte Chemie-International Edition* **2008,** *47* (38), 7332-7334.

117. Shannon, R. D., Revised Effective Ionic-Radii and Systematic Studies of Interatomic Distances in Halides and Chalcogenides. *Acta Crystallographica Section A* **1976,** *32* (Sep1), 751-767.

118. Katzin, L. I., Energy Value of Octahedral-Tetrahedral Coordination Change. *Journal of Chemical Physics* **1961,** *35* (2), 467-742.

119. (a) Johnson, E. R.; Keinan, S.; Mori-Sanchez, P.; Contreras-Garcia, J.; Cohen, A. J.; Yang, W. T., Revealing Noncovalent Interactions. *Journal of the American Chemical Society* **2010,** *132* (18), 6498-6506; (b) Contreras-Garcia, J.; Johnson, E. R.; Keinan, S.; Chaudret, R.; Piquemal, J. P.; Beratan, D. N.; Yang, W. T., NCIPLOT: A Program for Plotting Noncovalent Interaction Regions. *Journal of Chemical Theory and Computation* **2011,** *7* (3), 625-632.

120. (a) Pious, D.; Dixon, L.; Levine, F.; Cotner, T.; Johnson, R., Hla Class-Ii Regulation and Structure - Analysis with Hla-Dr3 and Hla-Dp Point Mutants. *Journal of Experimental Medicine* **1985,** *162* (4), 1193-1207; (b) Amicosante, M.; Sanarico, N.; Berretta, F.; Arroyo, J.; Lombardi, G.; Lechler, R.; Colizzi, V.; Saltini, C., Beryllium binding to HLA-DP molecule carrying the marker of susceptibility to berylliosis glutamate beta 69. *Human Immunology* **2001,** *62* (7), 686-693.

121. Dai, S. D.; Murphy, G. A.; Crawford, F.; Mack, D. G.; Falta, M. T.; Marrack, P.; Kappler, J. W.; Fontenot, A. P., Crystal structure of HLA-DP2 and implications for chronic beryllium disease. *Proceedings of the National Academy of Sciences of the United States of America* **2010,** *107* (16), 7425-7430.

122. Turkington, J. R.; Bailey, P. J.; Love, J. B.; Wilson, A. M.; Tasker, P. A., Exploiting outer-sphere interactions to enhance metal recovery by solvent extraction. *Chemical Communications* **2013,** *49* (19), 1891-1899.

123. Wilson, A. M.; Bailey, P. J.; Tasker, P. A.; Turkington, J. R.; Grant, R. A.; Love, J. B., Solvent extraction: the coordination chemistry behind extractive metallurgy. *Chemical Society Reviews* **2014,** *43* (1), 123-134.

124. Agarwal, P. K.; Saifuddin, M.; Kundu, B., Regioselective intramolecular electrophilic substitution reactions involving pi-deficient pyridine substrates: a new entry to pyridoquinazolines and benzo[*h*][1,6]naphthyridines. *Tetrahedron* **2010,** *66* (4), 862-870.

125. Duhamel, L.; Plaquevent, J. C., Method for Simple Titration of Organolithium Reagents in Ethers or Hydrocarbons Using Metalation of N-Benzylidenebenzylamine as Colored Reaction. *Journal of Organic Chemistry* **1979,** *44* (19), 3404-3405.

126. Suzuki, A.; Hara, S.; Huang, X., Boron Tribromide. In *Encyclopedia of Reagents for Organic Synthesis*, **2006**.

127. (a) Gilman, H.; Diehl, J., Novel Reduction of Ketones by Diphenylsilane. *Journal of Organic Chemistry* **1961,** *26* (12), 4817-4820; (b) Dupre, A. S. The roles of silanes as coupling reagents and in deoxygenative alkylations. PhD Thesis, **2003**.
128. Merer, A. J.; Mulliken, R. S., Ultraviolet Spectra and Excited States of Ethylene and Its Alkyl Derivatives. *Chemical Reviews* **1969,** *69* (5), 639-656.
129. Bigi, J. P.; Hanna, T. E.; Harman, W. H.; Chang, A.; Chang, C. J., Electrocatalytic reduction of protons to hydrogen by a water-compatible cobalt polypyridyl platform. *Chemical Communications* **2010,** *46* (6), 958-960.
130. Parmentier, M. L.; Gros, P.; Fort, Y., Pyridino-directed lithiation of anisylpyridines: new access to functional pyridylphenols. *Tetrahedron* **2005,** *61* (13), 3261-3269.

Appendix A: Experimental Spectra

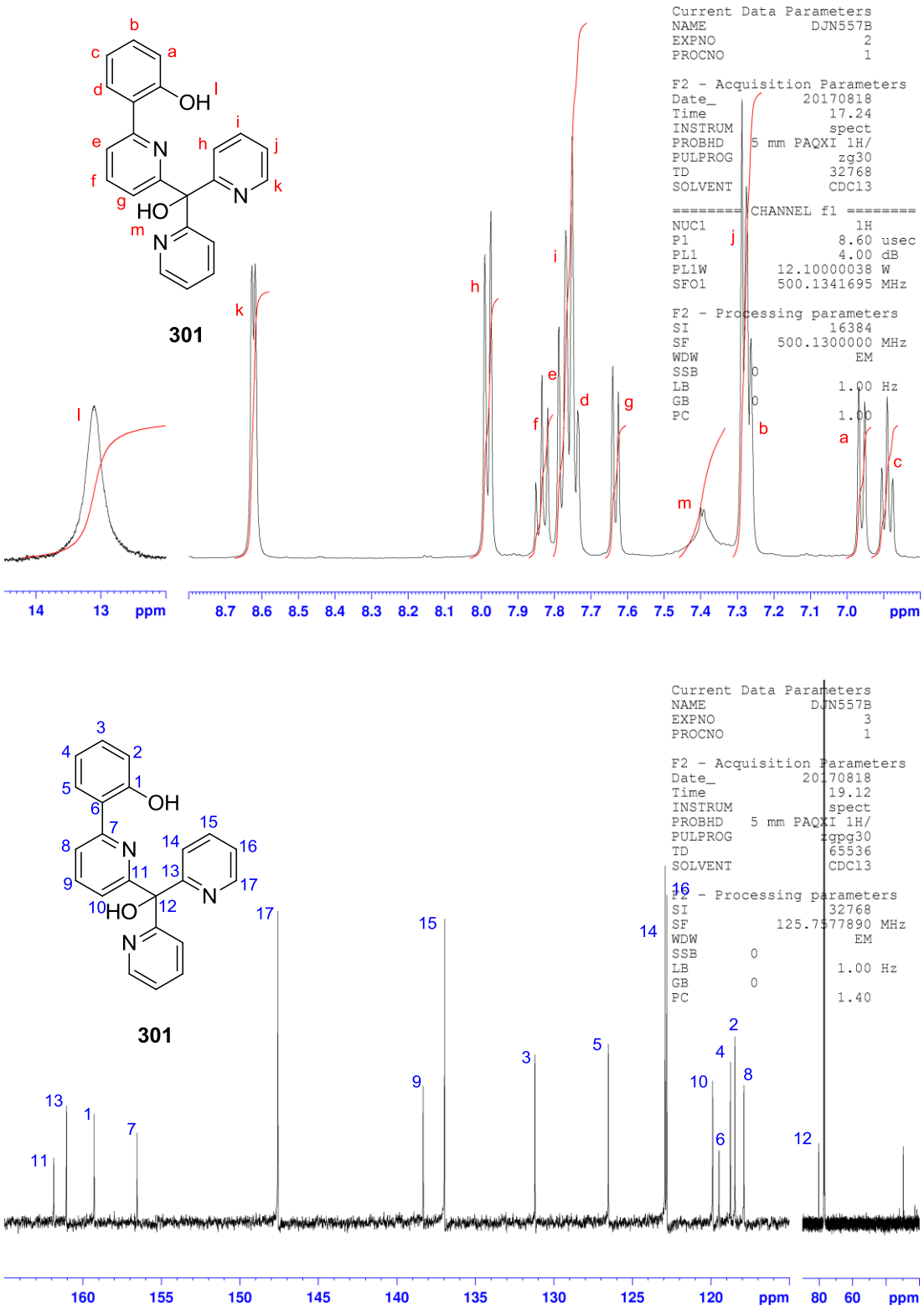

Figure A-1 Assigned ^{1}H and ^{13}C spectra for **301**.

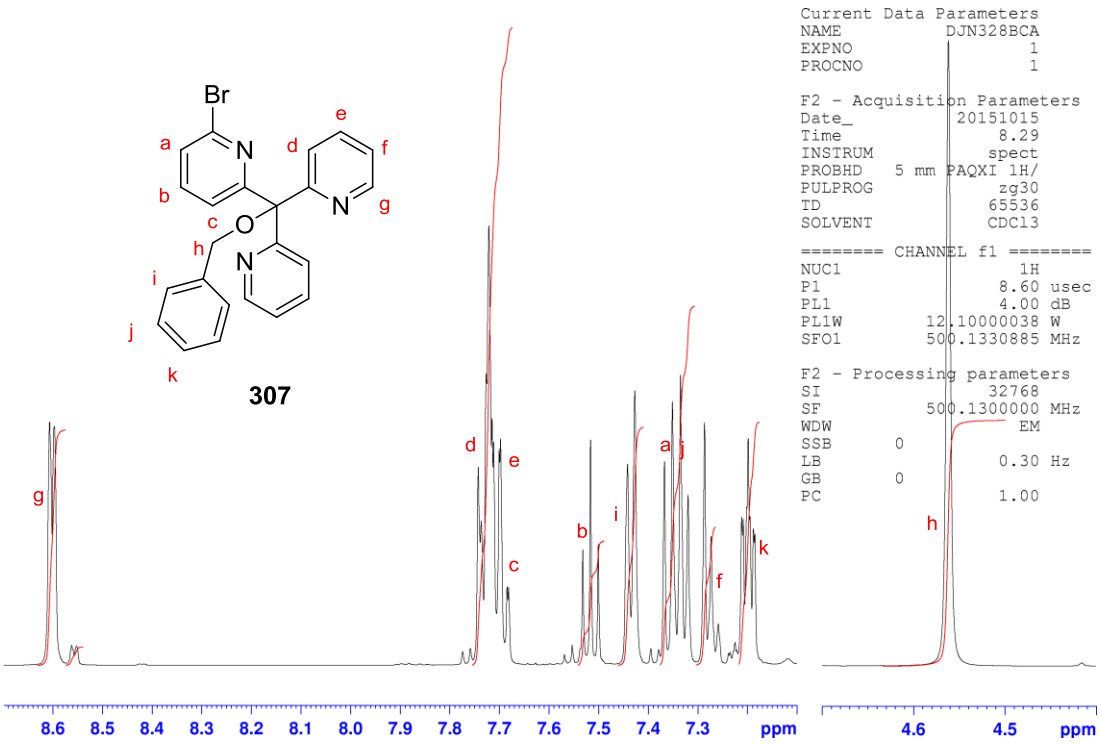

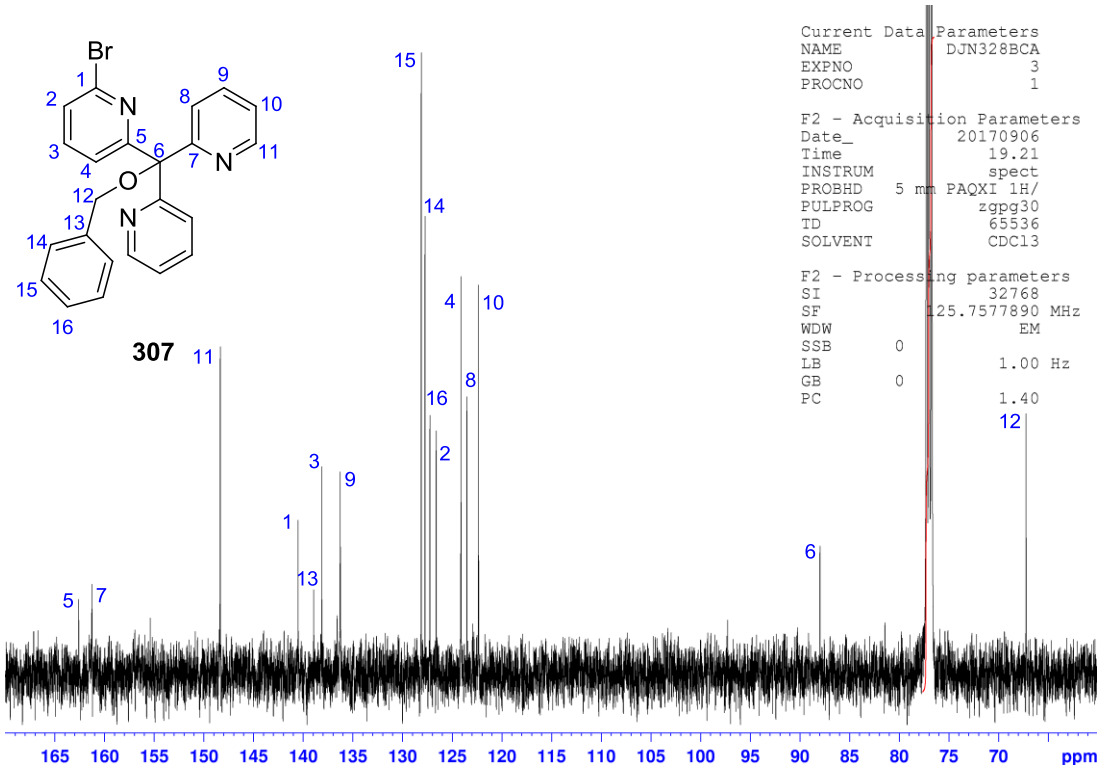

Figure A-2 Assigned ^{1}H and ^{13}C spectra for **307**.

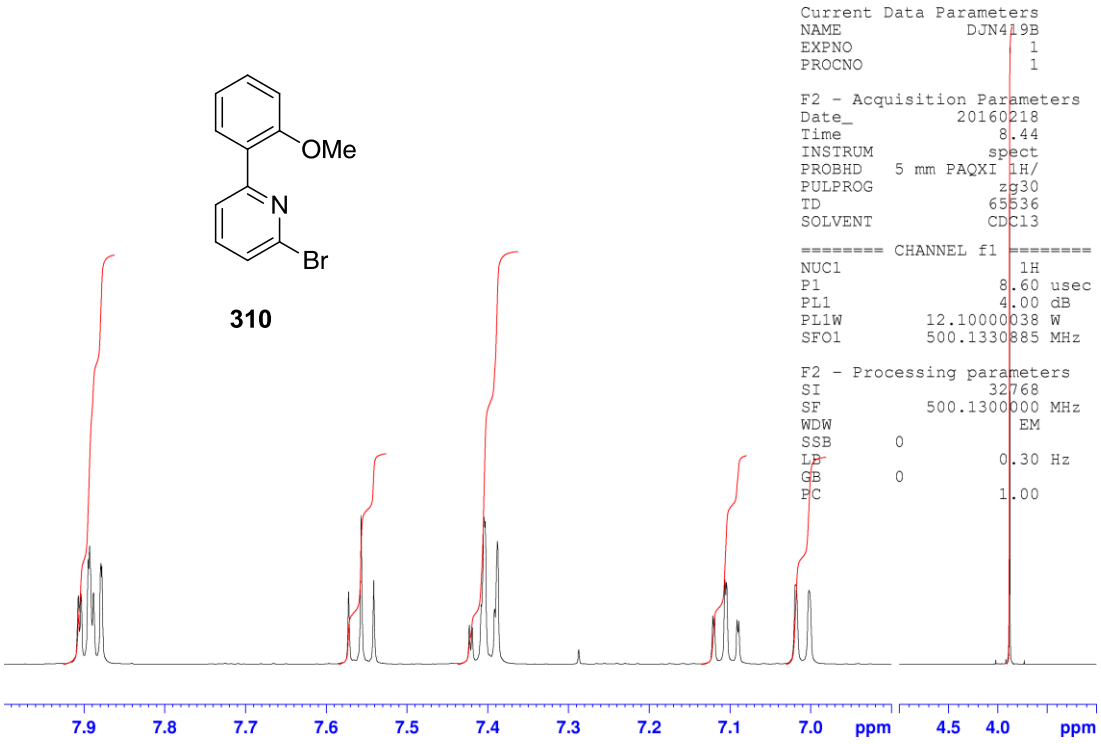

Figure A-3 ^{1}H spectrum for **310**.

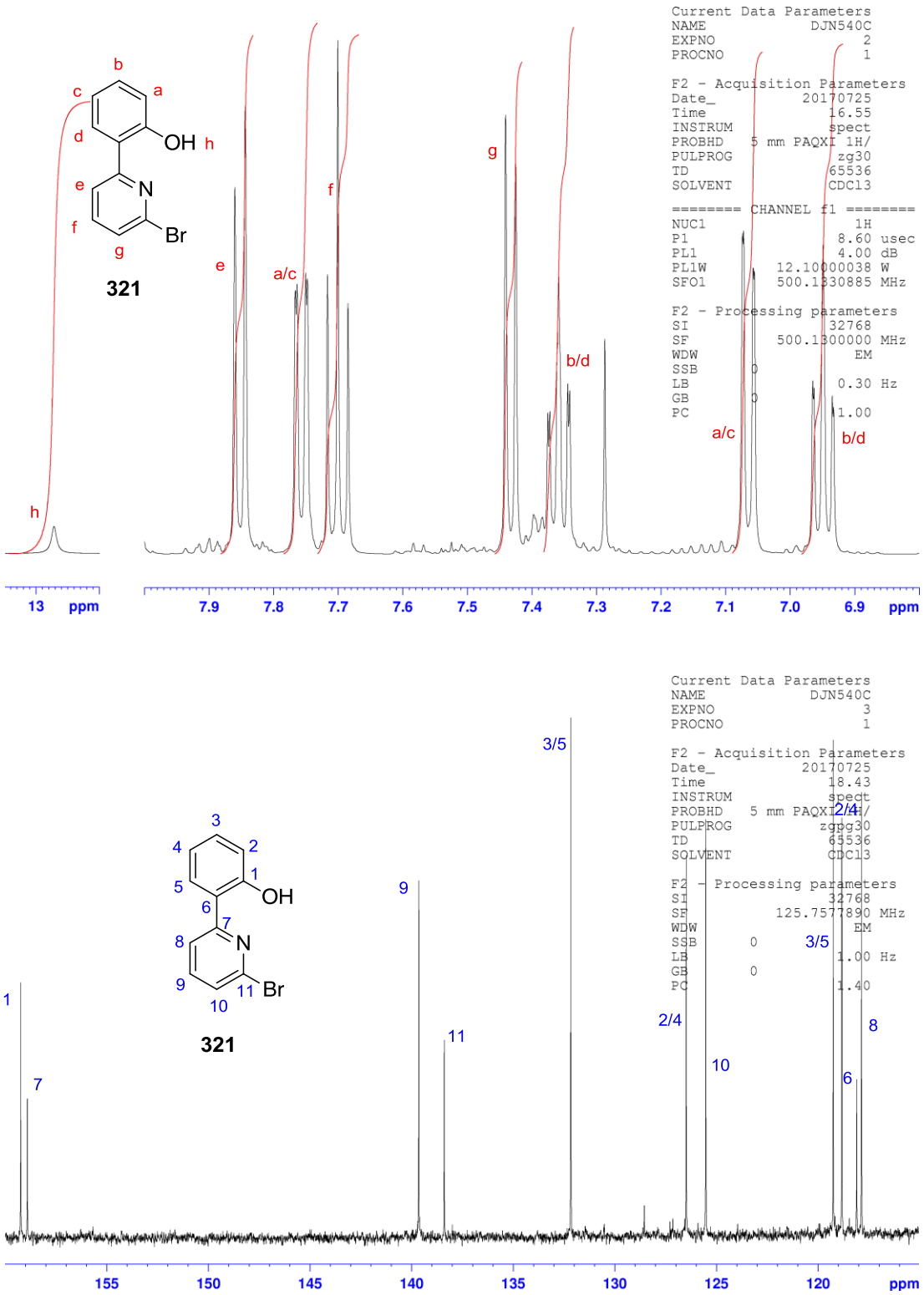

Figure A-4 Assigned ^{1}H and ^{13}C spectra for **321**.

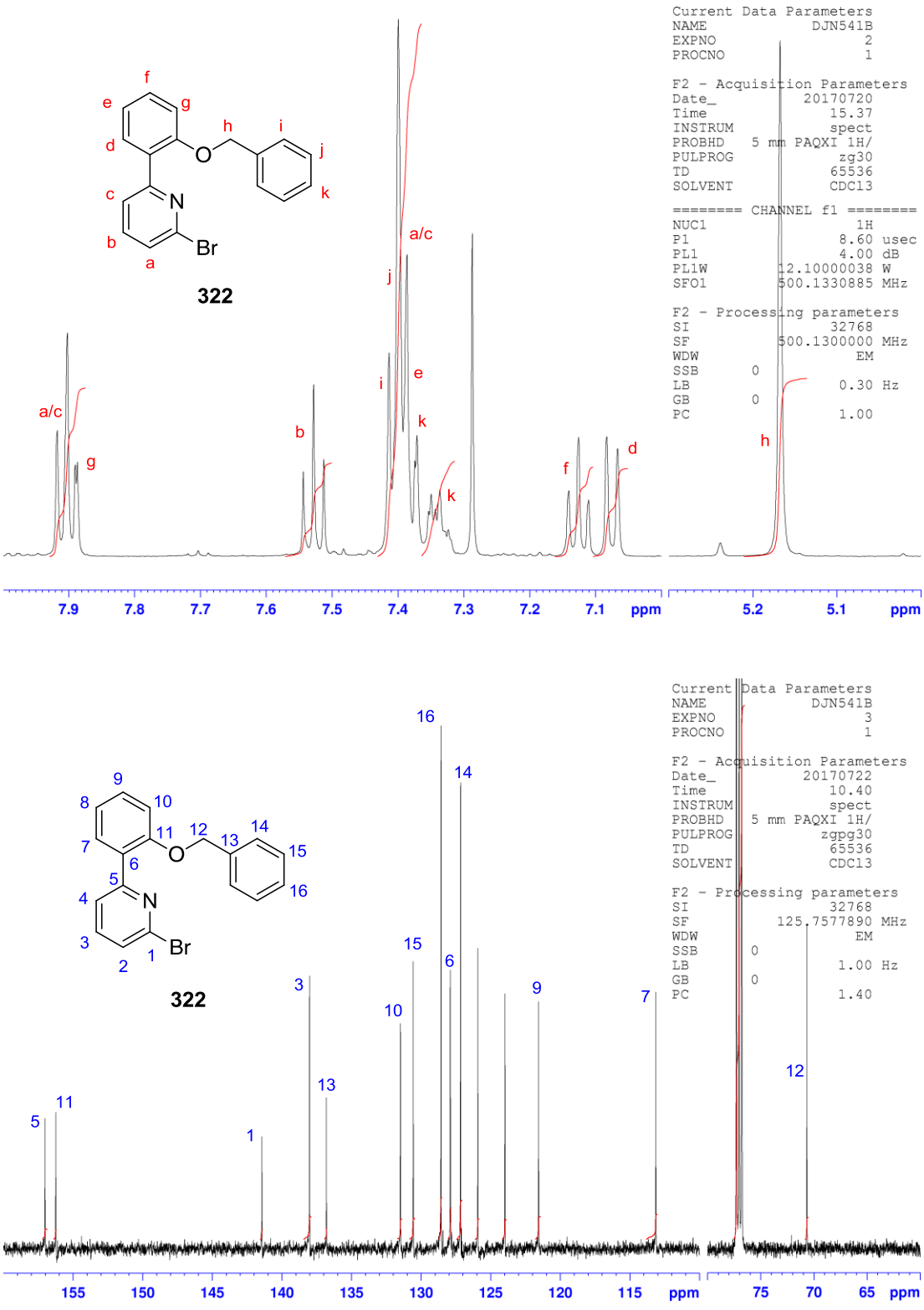

Figure A-5 Assigned ^{1}H and ^{13}C spectra for **322**.

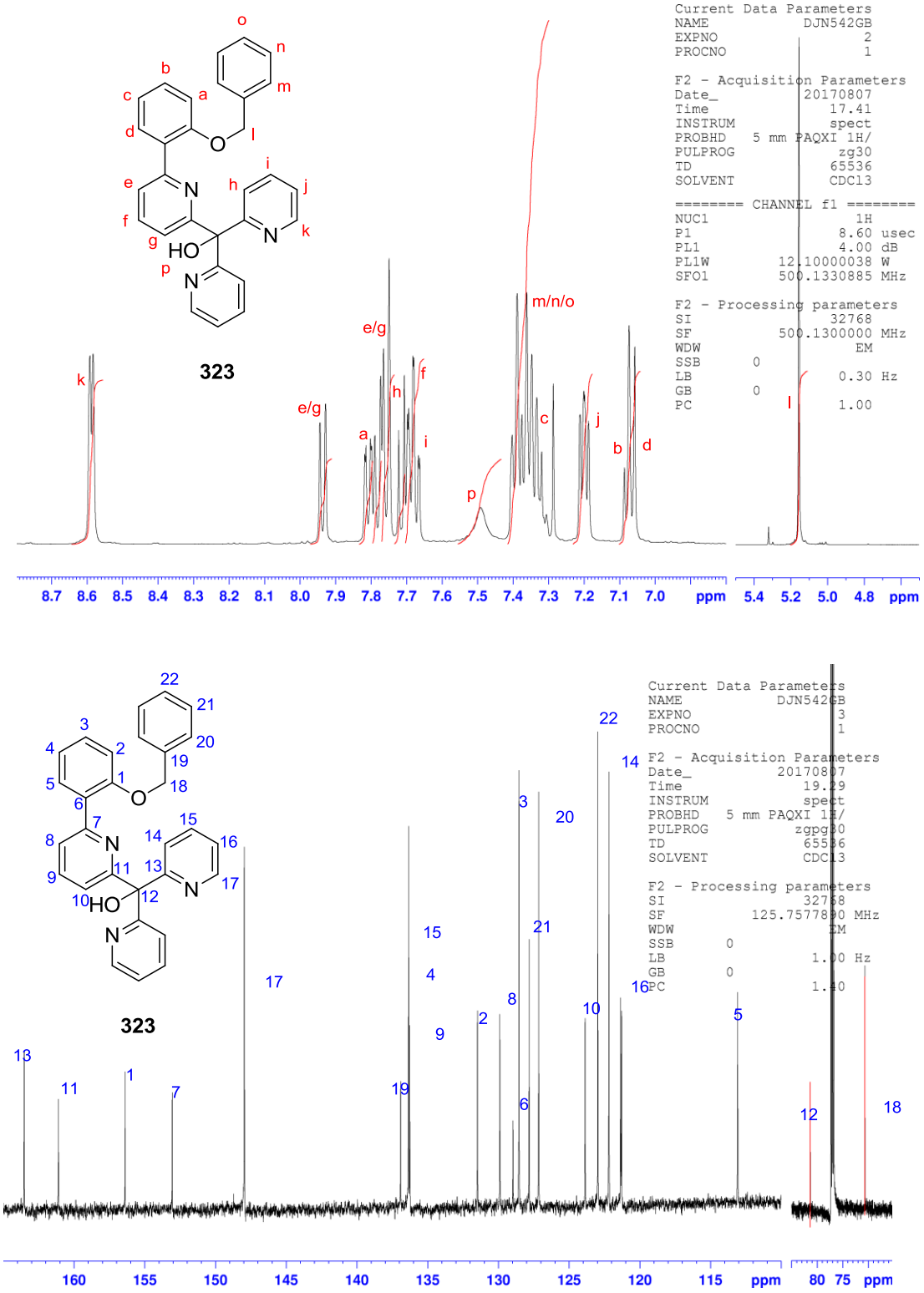

Figure A-6 Assigned ^{1}H and ^{13}C spectra for **323**.

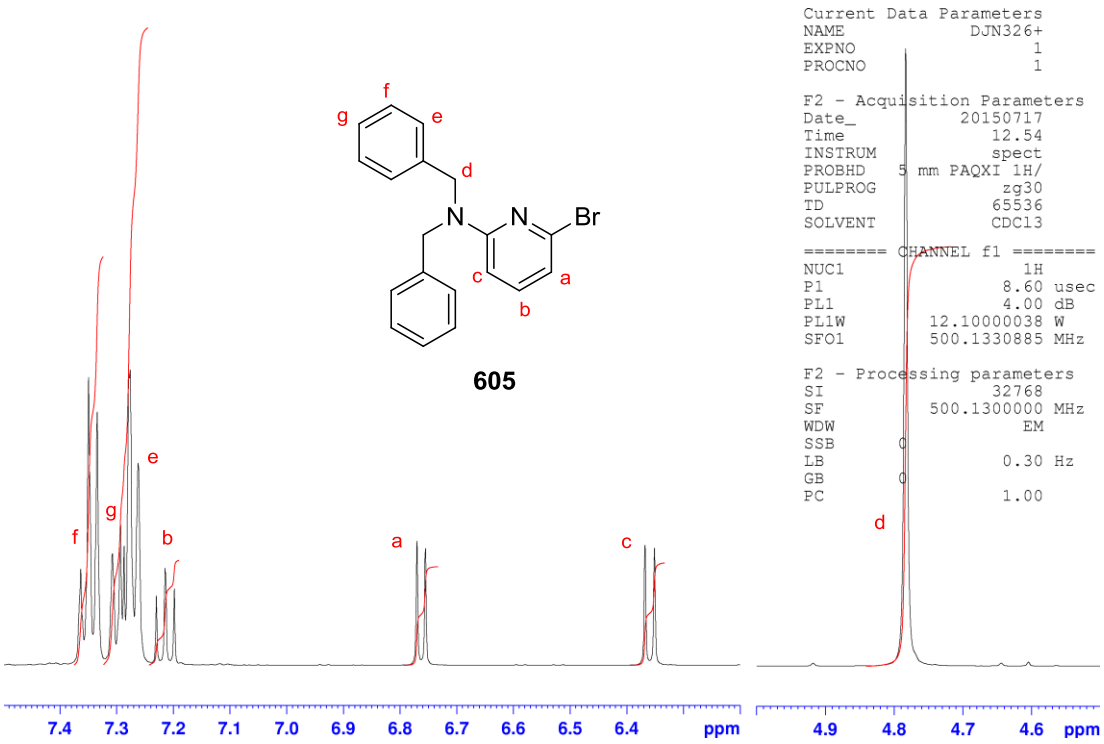

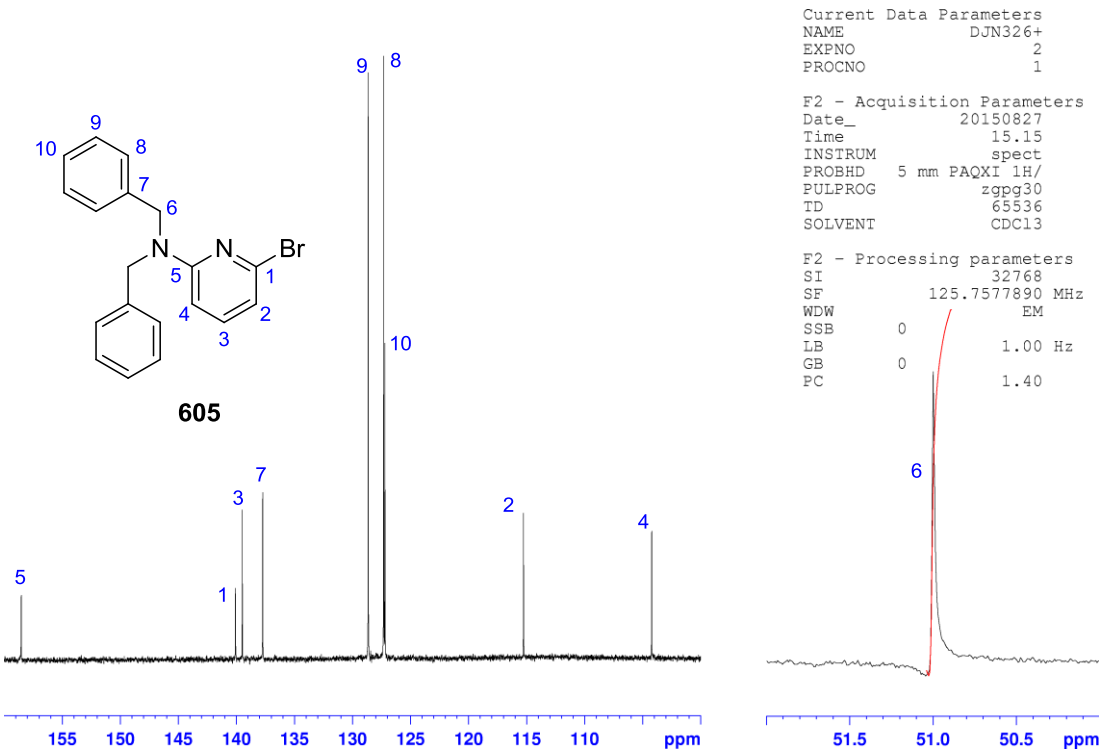

Figure A-7 Assigned ^{1}H and ^{13}C spectra for **605**.

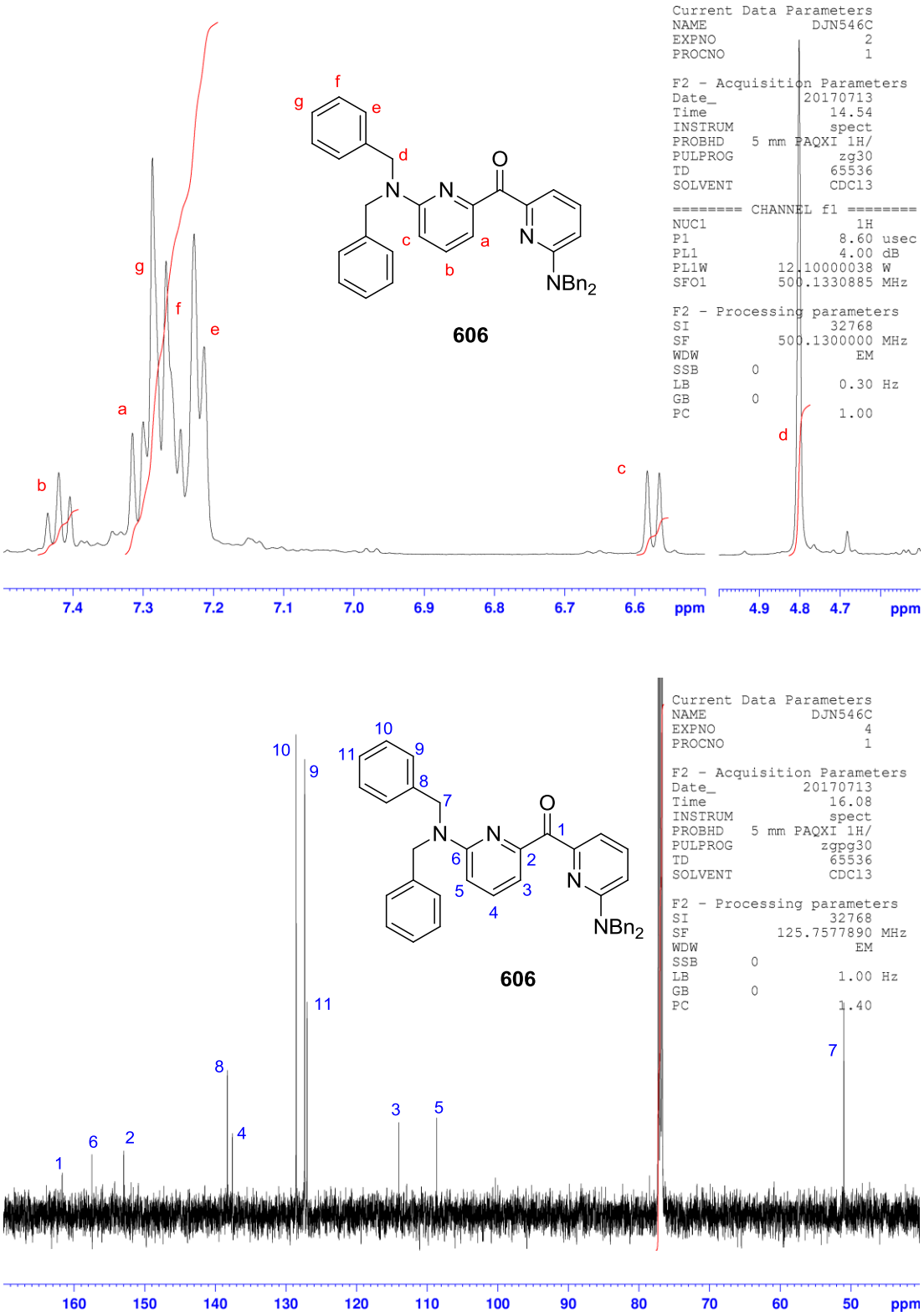

Figure A-8 Assigned ^{1}H and ^{13}C spectra for **606**.

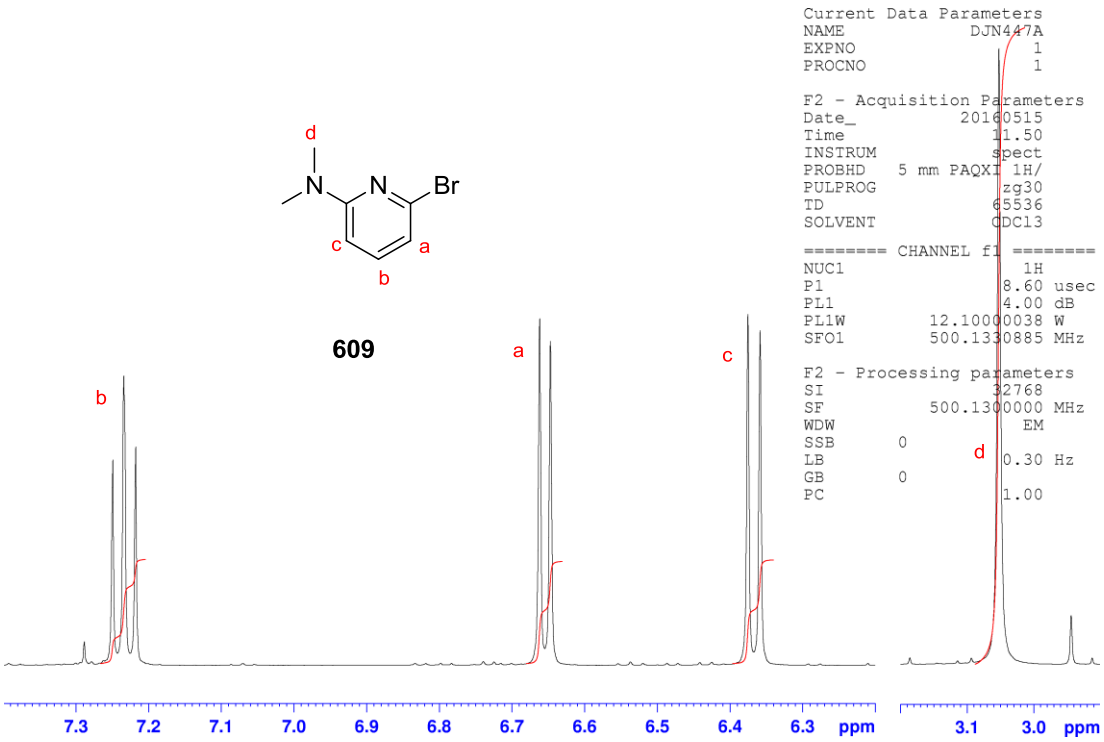

Figure A-9 Assigned ^{1}H spectrum for **609**.

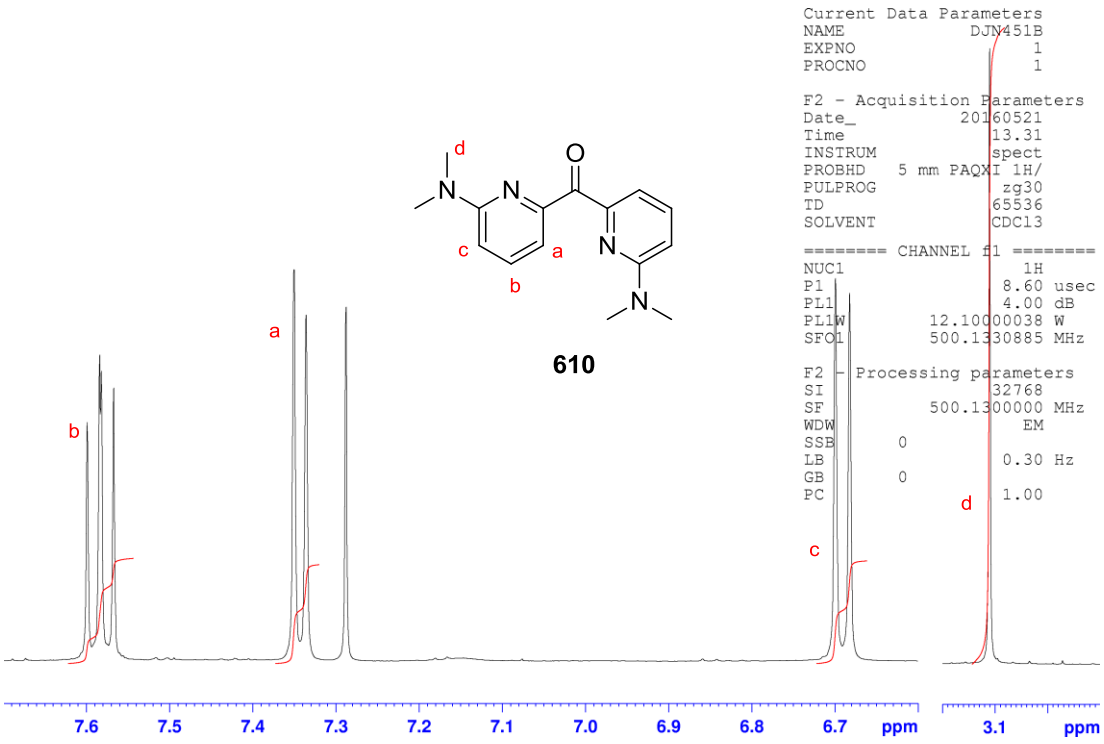

Figure A-10 Assigned ^{1}H spectrum for **610**.

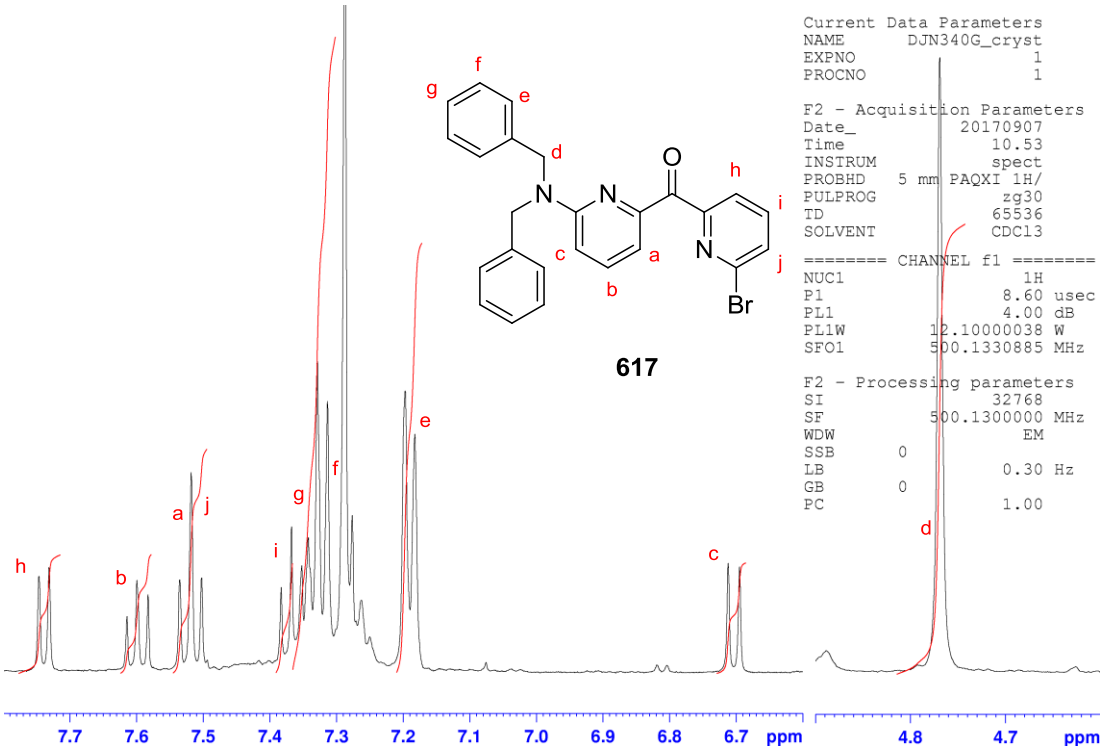

Figure A-11 Assigned ^{1}H spectrum for **617**.

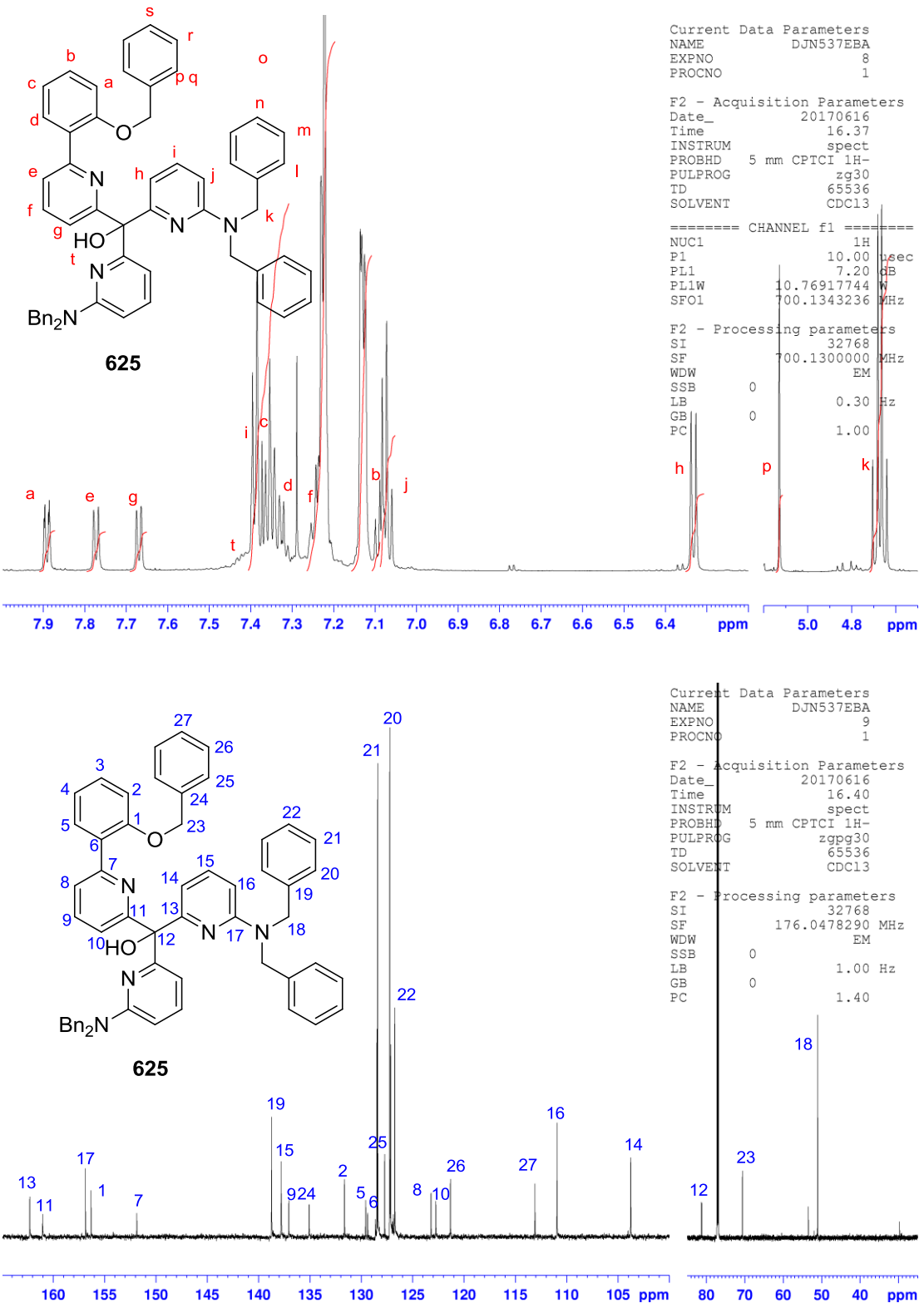

Figure A-12 Assigned ^{1}H and ^{13}C spectra for **625**.

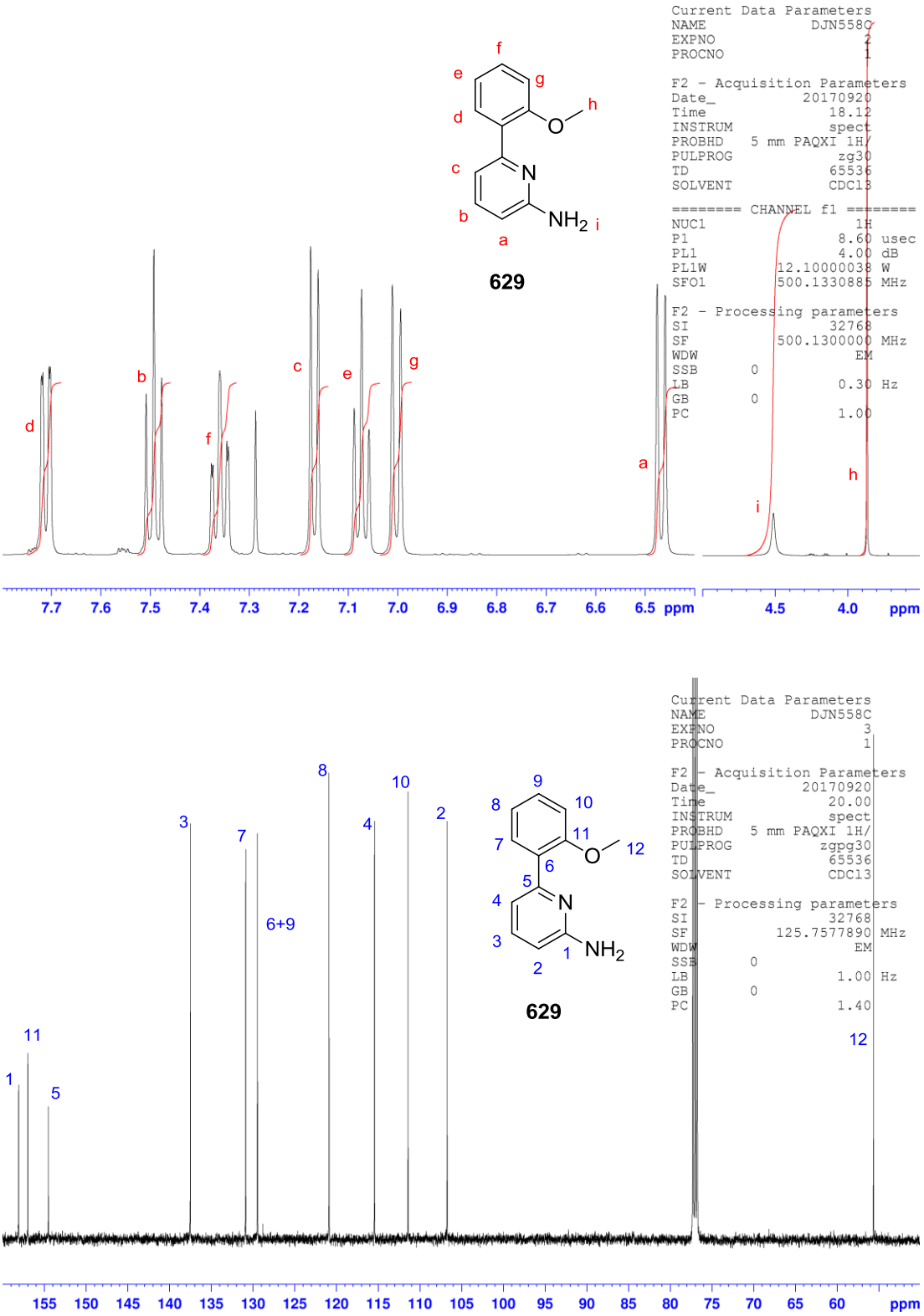

Figure A-13 Assigned ^{1}H and ^{13}C spectra for **629**.

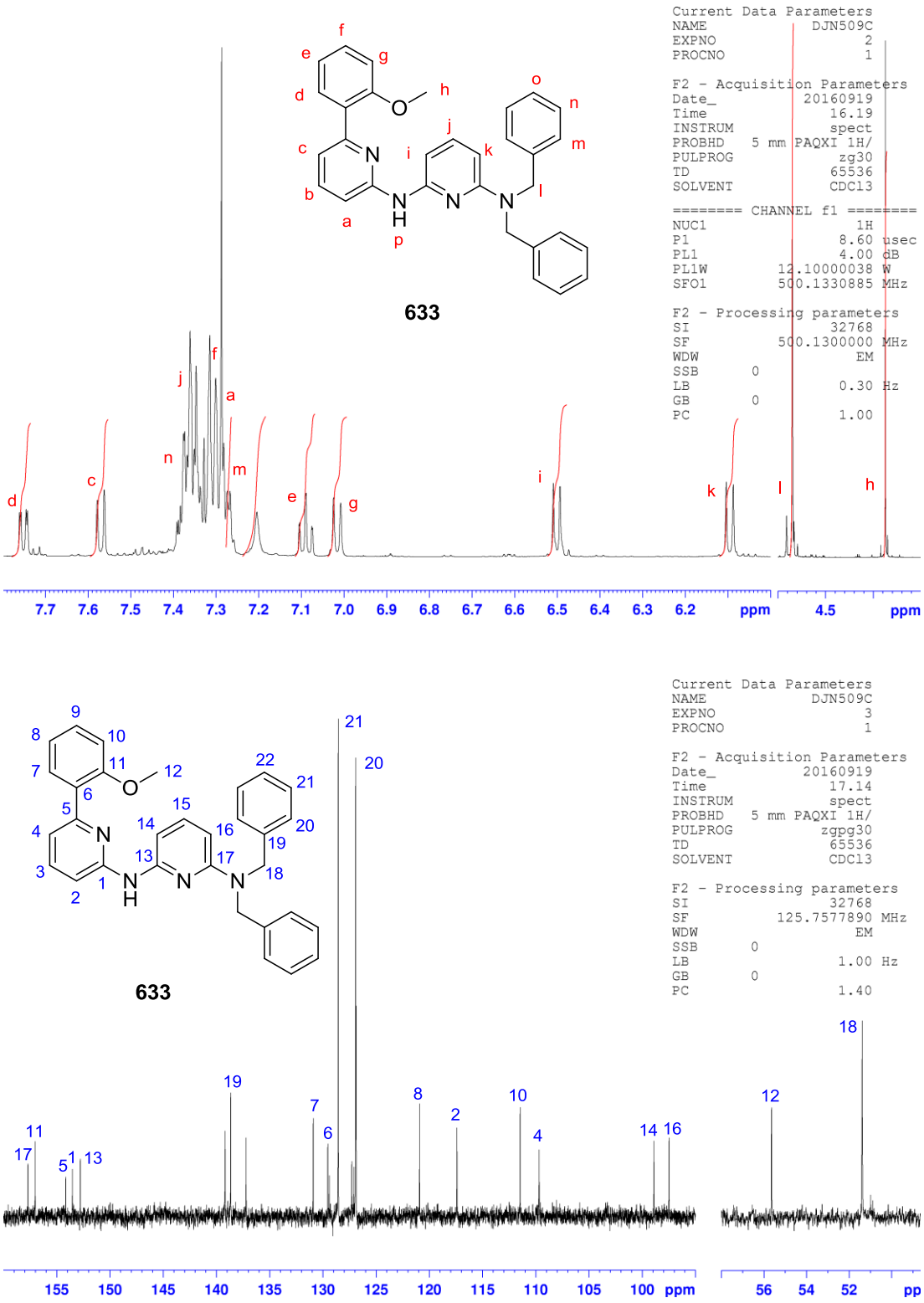

Figure A-14 Assigned ^{1}H and ^{13}C spectra for **633**.

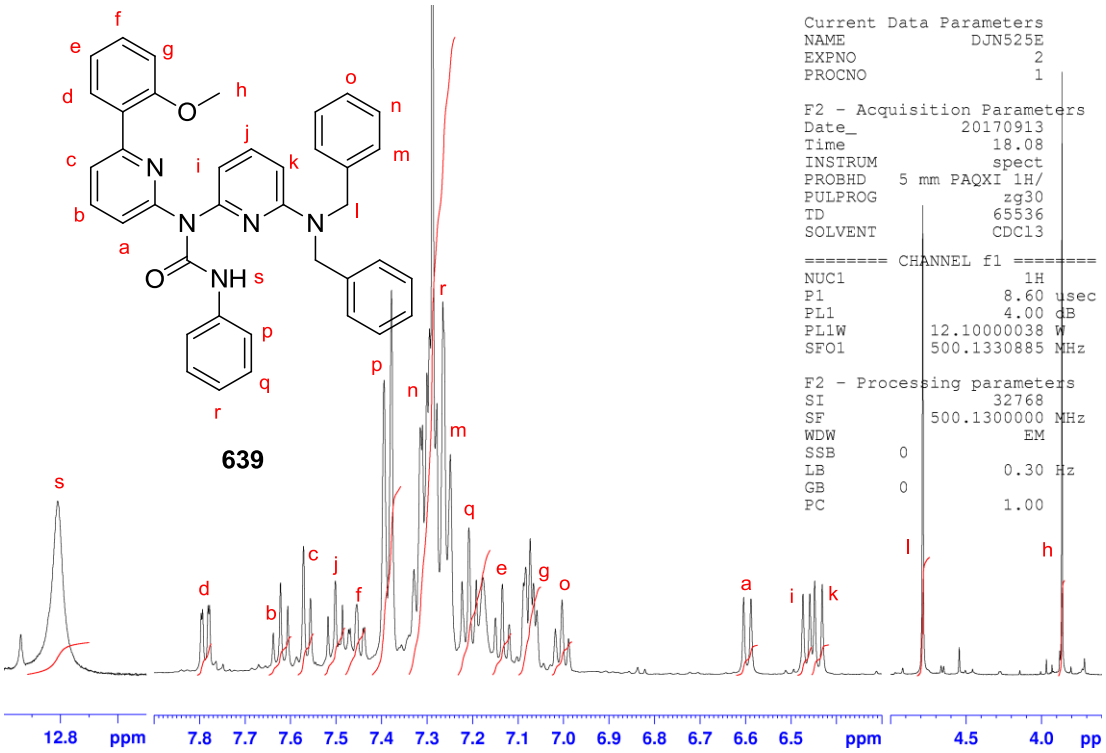

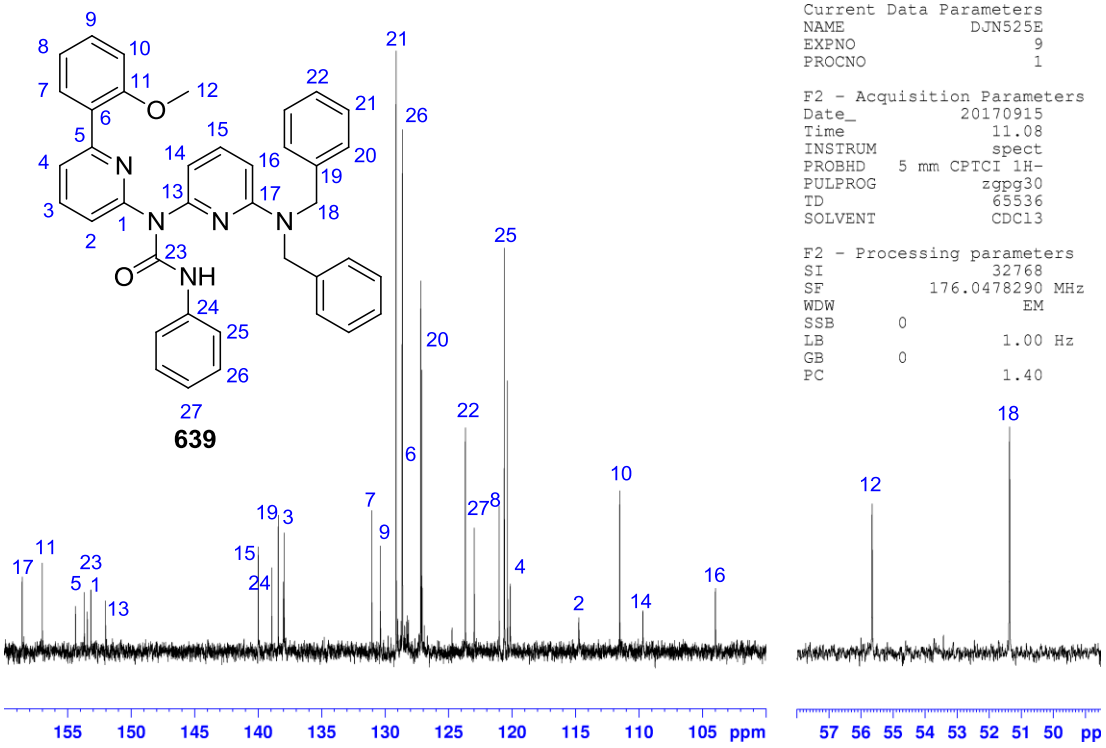

Figure A-15 Assigned ^{1}H and ^{13}C spectra for **639**.

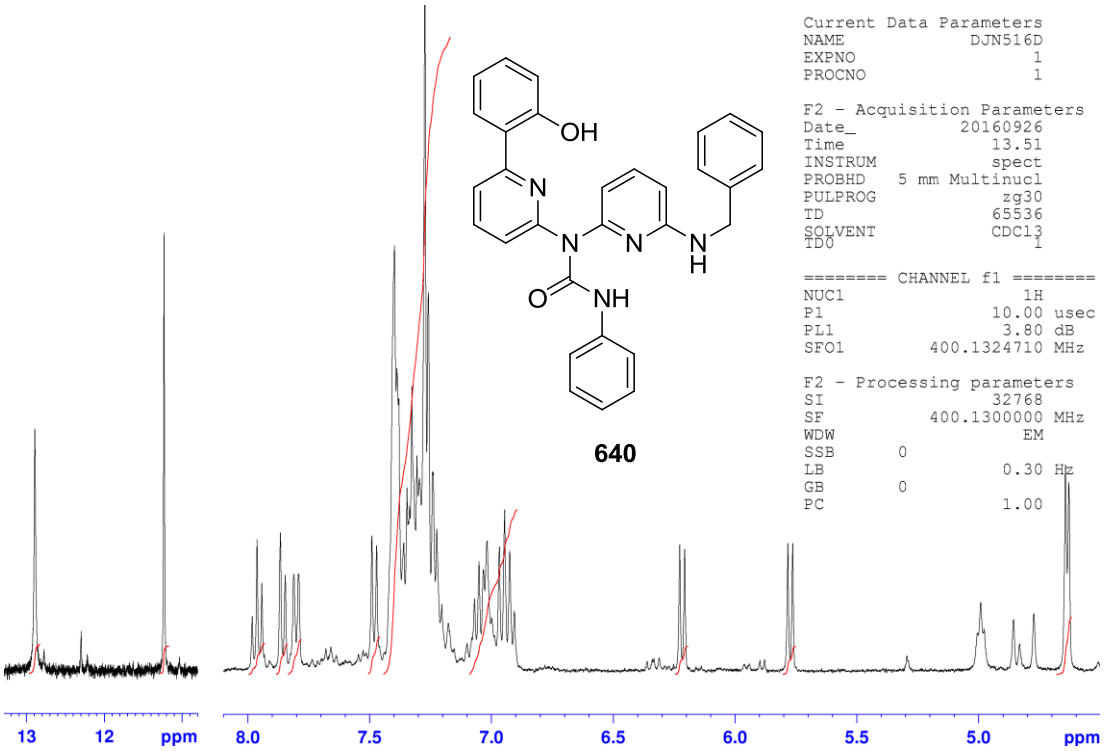

Figure A-16 ^{1}H spectrum for **640**.

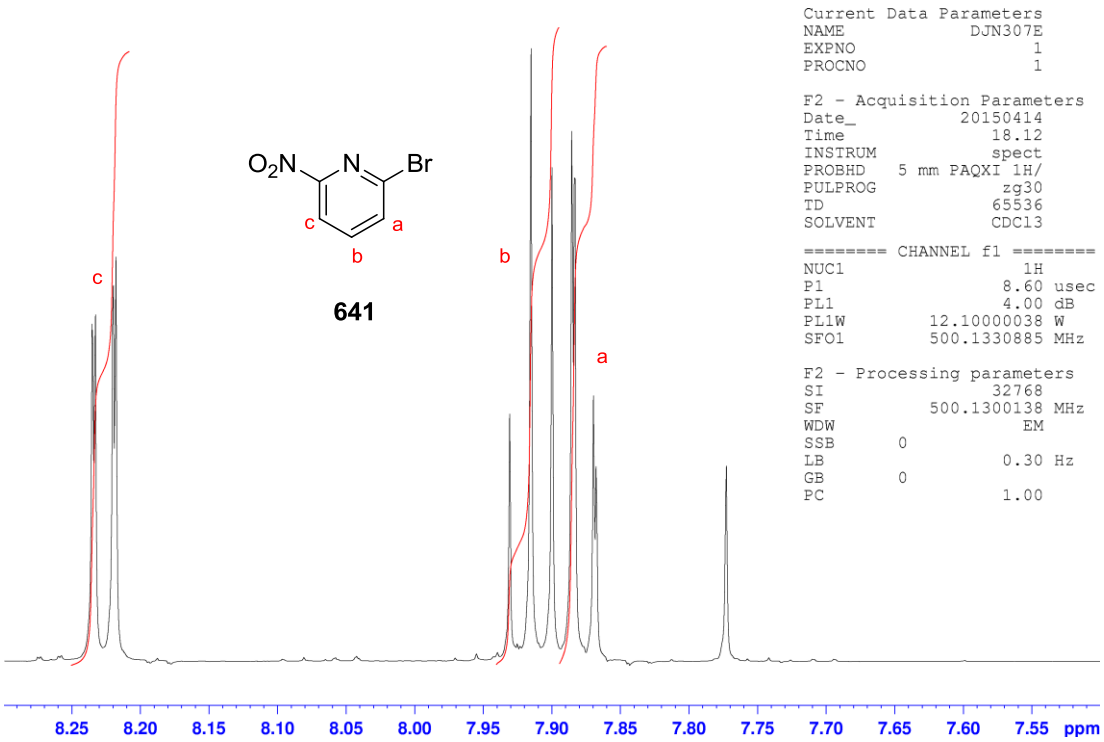

Figure A-17 Assigned ^{1}H spectrum for **641**.

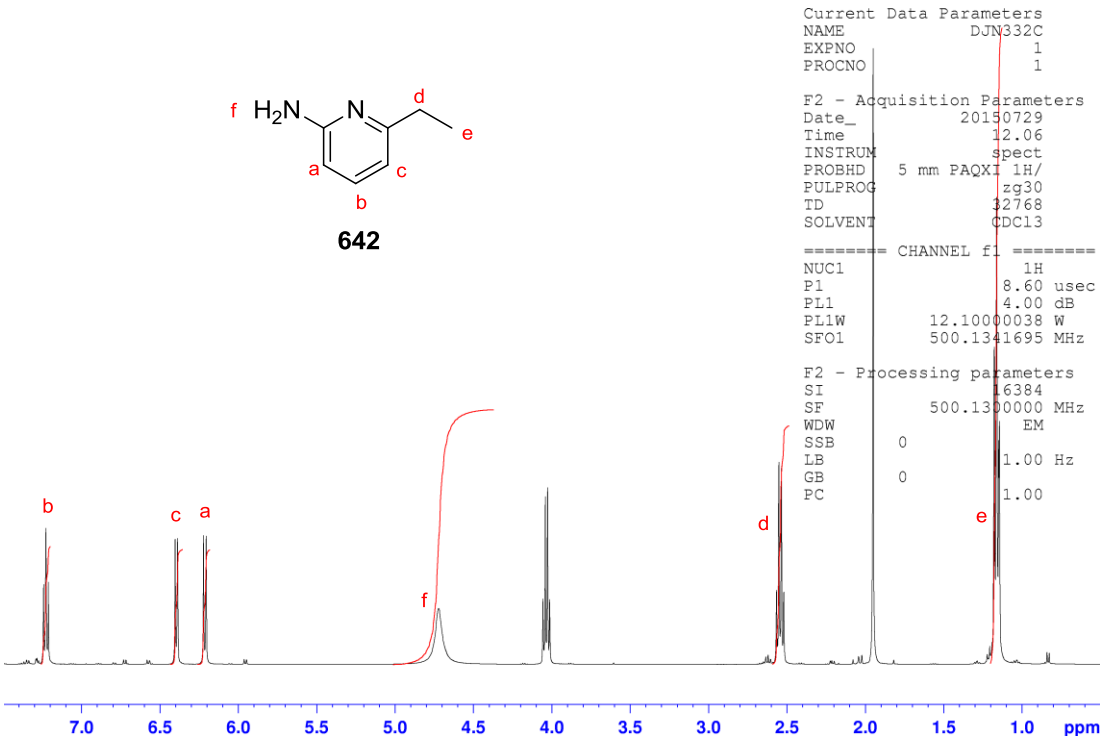

Figure A-18 Assigned ^{1}H spectrum for **642**.

Appendix B: Crystallographic Details

Table B-1 X-ray data summary for **L1cohH 301** and **303**.

	L1cohH 301	**303**
Empirical formula	$C_{22}H_{17}N_3O_2$	$C_{16}H_{12}N_3OBr$
Formula weight /gmol^{-1}	355.38	342.20
Temperature /K	100(2)	123
Crystal system	orthorhombic	monoclinic
Space group	*Pbca*	$P2_1/a$
a /Å	8.3056(17)	13.0181(7)
b /Å	17.493(4)	7.9532(6)
c /Å	23.398(5)	14.1568(10)
α /°	90	90
β /°	90	106.655(8)
γ /°	90	90
Volume /Å^3	3399.6(12)	1404.24(17)
Z	8	4
ρ_{calc} /gcm^{-3}	1.389	1.619
M /mm^{-1}	0.091	4.008
F(000)	1488	688
Crystal size /mm^3	-	0.3 × 0.04 × 0.04
Radiation	MoKα (λ = 0.71073)	CuKα (λ = 1.54187)
2θ range for data collection /°	3.482 to 53.762	13.056 to 130.176
Index ranges	-10 ≤ h ≤ 9, -22 ≤ k ≤ 15, -26 ≤ l ≤ 29	-15 ≤ h ≤ 15, -6 ≤ k ≤ 9, -16 ≤ l ≤ 16
Reflections collected	28116	13846
Independent reflections	3658 [R_{int} = 0.0202, R_{sigma} = 0.0089]	2372 [R_{int} = 0.1165, R_{sigma} = 0.1319]
Data/restraints/parameters	3658/0/312	2372/0/194
Goodness-of-fit on F^2	1.042	0.983
Final R indexes [I>=2σ (I)]	R_1 = 0.0341, wR_2 = 0.0902	R_1 = 0.0555, wR_2 = 0.1057
Final R indexes [all data]	R_1 = 0.0369, wR_2 = 0.0927	R_1 = 0.1012, wR_2 = 0.1265
Largest diff. peak/hole /eÅ^{-3}	0.28/-0.23	0.86/-0.72
Flack parameter	-	-

Table B-2 X-ray data summary for **306** and **307**.

	306	**307**
Empirical formula	$C_{28}H_{20}B_2BrN_3O_4$	$C_{23}H_{18}BrN_3O$
Formula weight /gmol^{-1}	564.00	432.31
Temperature /K	158	138
Crystal system	monoclinic	orthorhombic
Space group	$P2_1/n$	$P2_12_12_1$
a /Å	8.0404(4)	9.8259(6)
b /Å	27.9360(15)	17.9955(14)
c /Å	11.3896(8)	21.8207(15)
α /°	90	90
β /°	104.261(7)	90
γ /°	90	90
Volume /Å^3	2479.5(3)	3858.4(5)
Z	4	8
ρ_{calc} /gcm^{-3}	1.913	1.488
M /mm^{-1}	3.142	3.048
F(000)	1392	1760
Crystal size /mm^3	0.5 × 0.2 × 0.02	0.15 × 0.15 × 0.05
Radiation	CuKα (λ = 1.54187)	CuKα (λ = 1.54187)
2θ range for data collection /°	13.01 to 124.774	13.086 to 144.25
Index ranges	-9 ≤ h ≤ 6, -32 ≤ k ≤ 32, -13 ≤ l ≤ 13	-11 ≤ h ≤ 9, -22 ≤ k ≤ 21, -26 ≤ l ≤ 26
Reflections collected	22733	37662
Independent reflections	3851 [R_{int} = 0.1027, R_{sigma} = 0.1299]	7400 [R_{int} = 0.1072, R_{sigma} = 0.1627]
Data/restraints/parameters	3851/228/332	7400/18/505
Goodness-of-fit on F^2	1.286	1.047
Final R indexes [I>=2σ (I)]	R_1 = 0.1424, wR_2 = 0.3573	R_1 = 0.0768, wR_2 = 0.1424
Final R indexes [all data]	R_1 = 0.2189, wR_2 = 0.4182	R_1 = 0.1798, wR_2 = 0.2029
Largest diff. peak/hole /eÅ^{-3}	3.01/-0.63	1.02/-1.19
Flack parameter	-	-0.012(13)

Table B-3 X-ray data summary for **325** and **401**.

	325	**401**
Empirical formula	$C_{22}H_{18}N_4O$	$C_{22}H_{16}N_3O_2BeCl$
Formula weight /gmol^{-1}	354.4	398.84
Temperature /K	123	97(2)
Crystal system	orthorhombic	triclinic
Space group	*Pbca*	*P*-1
a /Å	14.1939(5)	10.9118(3)
b /Å	14.3618(7)	12.7415(4)
c /Å	17.1111(12)	13.9822(4)
α /°	90	78.973(2)
β /°	90	74.209(2)
γ /°	90	89.425(2)
Volume /Å^3	3488.1(3)	1834.26(10)
Z	8	4
ρ_{calc} /gcm^{-3}	1.35	1.444
M /mm^{-1}	0.685	0.233
F(000)	1488	824
Crystal size /mm^3	0.6 × 0.4 × 0.2	-
Radiation	CuKα (λ = 1.54187)	MoKα (λ = 0.71073)
2θ range for data collection /°	13.372 to 144.152	3.086 to 53.198
Index ranges	-17 ≤ h ≤ 16, -14 ≤ k ≤ 17, -20 ≤ l ≤ 21	-13 ≤ h ≤ 13, -12 ≤ k ≤ 16, -15 ≤ l ≤ 17
Reflections collected	26124	23785
Independent reflections	3385 [R_{int} = 0.0582, R_{sigma} = 0.0461]	7403 [R_{int} = 0.0477, R_{sigma} = 0.0637]
Data/restraints/parameters	3385/0/246	7403/0/525
Goodness-of-fit on F^2	1.13	0.956
Final R indexes [I>=2σ (I)]	R_1 = 0.0493, wR_2 = 0.1144	R_1 = 0.0454, wR_2 = 0.1212
Final R indexes [all data]	R_1 = 0.0688, wR_2 = 0.1343	R_1 = 0.0670, wR_2 = 0.1269
Largest diff. peak/hole /eÅ^{-3}	0.23/-0.29	0.43/-0.32
Flack parameter	-	-

Table B-4 X-ray data summary for **402** and **403**.

	402	**403**
Empirical formula	$C_{20}H_{20}BBeBrClN_3O_3$	$C_{20}H_{18}BeN_2O_3$
Formula weight /gmol^{-1}	405.66	343.37
Temperature /K	97.15	100(2)
Crystal system	monoclinic	orthorhombic
Space group	$P2_1/c$	*Pbca*
a /Å	10.4093(6)	18.7418(4)
b /Å	23.9150(13)	7.84050(10)
c /Å	11.4333(7)	22.6676(3)
α /°	90	90
β /°	90.656(2)	90
γ /°	90	90
Volume /Å^3	2846.0(3)	3330.89(9)
Z	6	8
ρ_{calc} /gcm^{-3}	1.42	1.369
M /mm^{-1}	0.229	0.741
F(000)	1266	1440
Crystal size /mm^3	-	0.30 × 0.10 × 0.08
Radiation	MoKα (λ = 0.71073)	CuKα (λ = 1.54178)
2θ range for data collection /°	4.93 to 61.41	7.8 to 158.858
Index ranges	-14 ≤ h ≤ 14, -33 ≤ k ≤ 34, -16 ≤ l ≤ 16	-23 ≤ h ≤ 22, -9 ≤ k ≤ 8, -28 ≤ l ≤ 24
Reflections collected	98896	55562
Independent reflections	8717 [R_{int} = 0.0735, R_{sigma} = 0.0524]	3585 [R_{int} = 0.0184, R_{sigma} = 0.0064]
Data/restraints/parameters	8717/0/361	3585/0/308
Goodness-of-fit on F^2	1.088	1.029
Final R indexes [I>=2σ (I)]	R_1 = 0.0735, wR_2 = 0.1727	R_1 = 0.0320, wR_2 = 0.0849
Final R indexes [all data]	R_1 = 0.1003, wR_2 = 0.1850	R_1 = 0.0330, wR_2 = 0.0858
Largest diff. peak/hole /eÅ^{-3}	0.95/-0.84	0.30/-0.19
Flack parameter	-	-

Table B-5 X-ray data summary for **605** and **606**.

	605	**606**
Empirical formula	$C_{19}H_{17}BrN_2$	$C_{39}H_{34}N_4O$
Formula weight /gmol^{-1}	353.25	574.7
Temperature /K	123	123
Crystal system	monoclinic	orthorhombic
Space group	$P2_1/n$	$Fdd2$
a /Å	9.3170(2)	19.4346(8)
b /Å	9.9902(2)	37.244(3)
c /Å	17.5701(12)	8.5836(4)
α /°	90	90
β /°	91.725(7)	90
γ /°	90	90
Volume /Å^3	1634.66(12)	6213.1(6)
Z	4	8
ρ_{calc} /gcm^{-3}	1.435	1.229
M /mm^{-1}	3.393	0.583
F(000)	720	2432
Crystal size /mm^3	0.15 × 0.13 × 0.09	0.3 × 0.3 × 0.25
Radiation	CuKα (λ = 1.54187)	CuKα (λ = 1.54187)
2θ range for data collection /°	10.074 to 130.1	9.498 to 143.9
Index ranges	-10 ≤ h ≤ 10, -11 ≤ k ≤ 11, -18 ≤ l ≤ 20	-23 ≤ h ≤ 21, -45 ≤ k ≤ 42, -10 ≤ l ≤ 10
Reflections collected	20692	8339
Independent reflections	2713 [R_{int} = 0.0686, R_{sigma} = 0.0485]	2810 [R_{int} = 0.0863, R_{sigma} = 0.0942]
Data/restraints/parameters	2713/0/199	2810/1/201
Goodness-of-fit on F^2	1.119	1.144
Final R indexes [I>=2σ (I)]	R_1 = 0.0400, wR_2 = 0.1004	R_1 = 0.0699, wR_2 = 0.1493
Final R indexes [all data]	R_1 = 0.0455, wR_2 = 0.1047	R_1 = 0.1240, wR_2 = 0.2109
Largest diff. peak/hole /eÅ^{-3}	0.61/-0.45	0.28/-0.27
Flack parameter	-	0.1(5)

Table B-6 X-ray data summary for **617**.

	617
Empirical formula	$C_{25}H_{20}N_3OBr$
Formula weight /gmol^{-1}	458.35
Temperature /K	148
Crystal system	monoclinic
Space group	$P2_1/a$
a /Å	9.9701(8)
b /Å	17.3553(11)
c /Å	12.5250(9)
α /°	90
β /°	104.678(7)
γ /°	90
Volume /Å^3	2096.5(3)
Z	4
ρ_{calc} /gcm^{-3}	1.452
M /mm^{-1}	2.84
F(000)	936
Crystal size /mm^3	0.15 × 0.1 × 0.02
Radiation	CuKα (λ = 1.54187)
2θ range for data collection /°	15.492 to 130.16
Index ranges	-11 ≤ h ≤ 7, -20 ≤ k ≤ 20, -14 ≤ l ≤ 14
Reflections collected	19836
Independent reflections	3542 [R_{int} = 0.2865, R_{sigma} = 0.4322]
Data/restraints/parameters	3542/239/271
Goodness-of-fit on F^2	0.851
Final R indexes [I>=2σ (I)]	R_1 = 0.0936, wR_2 = 0.1117
Final R indexes [all data]	R_1 = 0.3501, wR_2 = 0.1759
Largest diff. peak/hole /eÅ^{-3}	0.37/-0.39
Flack parameter	-

Appendix C: Coordinates and CIF Reports

Found in the attached supplementary data are Cartesian coordinates for the calculated ligand and complex geometries in the form of xyz files. Also can be found are CIF reports.

Appendix D: Naming System and Ligands

A comprehensive and systematic naming convention was developed for the suite of ligands and complexes discussed throughout this thesis for ease of understanding:

LxY_M

Where:

L = Ligand type	e.g. L1
x = Apex group (lower case)	e.g. ch
Y = Buttress group (upper case)	e.g. NH_2
M = Metal species bound (if present)	e.g. Be

For example, **L1chNH$_2$** would be the following ligand (Figure D-1):

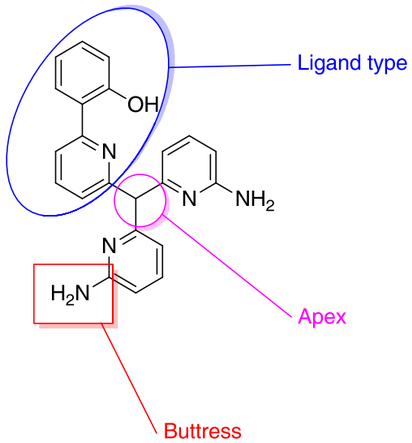

Figure D-1 Ligand **L1chNH$_2$**.

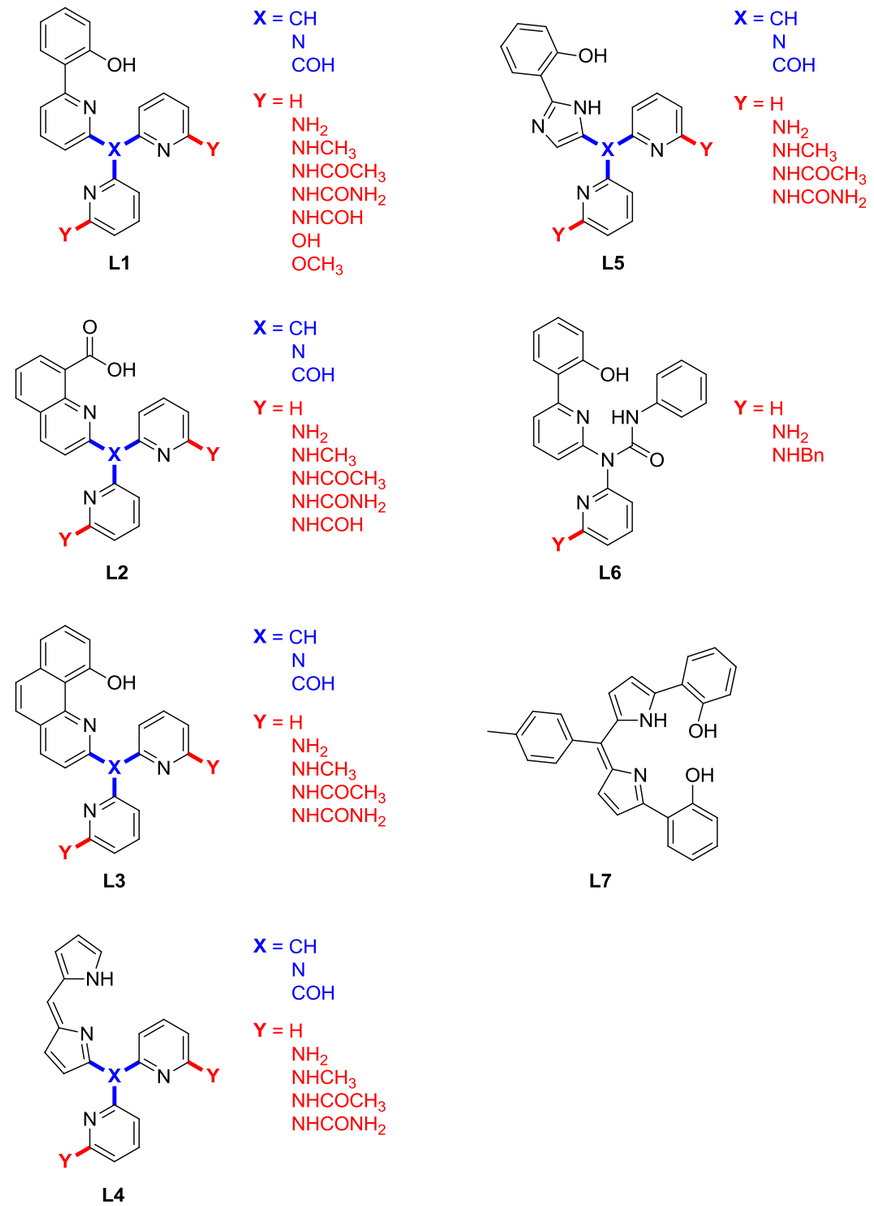

Figure D-2 Ligands examined in the binding energy study. In blue, X denotes the apex group; in red, Y denotes the buttress group (when Y ≠ H).